FUNDAMENTAL INSIGHTS OF PLANAR AND SUPPORTED CATALYSTS

by

Cory A Milligan

A Thesis

Submitted to the Faculty of Purdue University

In Partial Fulfillment of the Requirements for the degree of

Doctor of Philosophy

Davidson School of Chemical Engineering

West Lafayette, Indiana

May 2019

THE PURDUE UNIVERSITY GRADUATE SCHOOL
STATEMENT OF COMMITTEE APPROVAL

Dr. Fabio Ribeiro, Chair
Davidson School of Chemical Engineering
Dr. Dmitry Zemlyanov
Birck Nanotechnology Center
Dr. Jeffrey Miller
Davidson School of Chemical Engineering
Dr. Jeffrey Greeley
Davidson School of Chemical Engineering

Approved by:
Dr. John Morgan
Head of the Graduate Program

To my family and loved ones
who supported me in this journey

ACKNOWLEDGMENTS

I owe much of my success during my Ph.D. to my advisor Fabio Ribeiro. I was lucky to have Dmitry Zemlyanov as a mentor during my time at Purdue. His technical expertise and general life advice allowed me to learn all the complexities of performing valuable UHV experiments, while balancing my personal life. If not for his expert tutelage I would not have become the scientist I am today. I also owe much of my basic UHV knowledge to Michael Detwiler, who took me under his wing when I first joined Purdue. Ron Reifenberger was always a welcome guest in the lab. His love for STM was contagious and provided valuable outside perspective on my projects. Nick Delgass became a valuable resource during my Ph.D. and his enthusiasm for all things science is truly inspiring.

I was fortunate to collaborate with a large variety of researchers. Jeffrey Greeley along with his students and post-docs, specifically Tej Choksi, Paulami Majumdar, Ranga Seemakurthi, Zhenhua Zheng, and Pushkar Ghanekar, helped me to provide strong theoretical validation to my experimental results. Jeffrey Miller and his students, specifically Zhenwei Wu and Evan Wegener, who helped me to relate my surface science experiments to their technical systems. I would like to especially thank Yanran Cui for teaching me how to measure kinetics and operate non-UHV equipment. There are many additional collaborators I need to thank for my success as a student, but the list is too long to include here.

I could not have completed my Ph.D. without the love and support of my family and loved ones. Christina Anson has been supportive of me ever since I showed any interest in continuing my education. I look forward to our time together now that we will both be finished with school, finally.

TABLE OF CONTENTS

LIST OF TABLES

LIST OF FIGURES

ABSTRACT

Author: Milligan, Cory, A. PhD
Institution: Purdue University
Degree Received: May 2019
Title: Fundamental Insights on Model and Supported Catalysts
Committee Chair: Fabio Ribeiro

A fundamental understanding of heterogeneous catalysis requires analysis of model catalytic surfaces in tandem with complex technical catalysts. This work was divided in three areas, 1- preparation and characterization of model surfaces synthesized by vapor deposition techniques, 2- kinetic evaluation of model catalysts for formic acid decomposition and dry methane reforming, 3- characterization and kinetic evaluation of technical catalysts for the water gas shift reaction.

In the first project, model PdZn intermetallic surfaces, a relevant catalyst for propane dehydrogenation, were prepared using an ALD approach. In this work, model surfaces were synthesized by exposing Pd(111) and Pd(100) surfaces to diethylzinc at ca. 10^{-6} mbar. Several different surface structures were identified by careful control of the deposition temperature of the substrate. Modifications in the adsorption properties of these surfaces towards carbon monoxide and propylene coincided with the structure of the PdZn surface layer.

In the second project, formic acid decomposition kinetics were evaluated on model Pt catalysts. Formic acid decomposition was found to be structure-insensitive on Pt(111), Pt(100), and a polycrystalline foil under standard reaction conditions. CO selectivity remained < 1% for conversions <10%. Additionally, inverse Pd-Zr model catalysts were prepared by ALD of zirconium-t-butoxide (ZTB). Depending on treatment conditions, either ZrO_xH_y or ZrO_2 overlayers or Zr as sub-nanometer clusters could be obtained. The activity of the model catalyst surface towards dry reforming of methane if the initial state of the zirconium is metallic.

In the third project, Au/Fe_3O_4 heterodimer catalysts were characterized for their thermal stability. In-situ TEM and XPS characterization demonstrates that the gold nanoparticles transform into gold thin films that wet the Fe_3O_4 surface as the reduction of the oxide proceeds. DFT calculations show that the adhesion energy between the Au film is increased on a partially reduced Fe_3O_4 surface. Additionally, Pt/Nb_2CT_x catalysts were characterized and kinetics

evaluated for the water gas shift reaction. XPS and TEM characterization indicates that a Pt-Nb surface alloy is formed under moderate reduction temperatures, $350^{O}C$. Water-gas shift reaction kinetics reveal that the alloy-MXene interface exhibit high H_2O activation ability compared to a non-reducible support or bulk niobium carbide.

CHAPTER 1. INTRODUCTION

The selectivity and rate of heterogeneous catalysts can depend on several factors, including atomic structure and composition of the catalyst. An individual nanoparticle has different regions of planes, steps and corners. The atoms present in these regions all have a different degree of coordination to other atoms and thus lead to different chemistry then the other domains. This complexity makes identifying the active site of a specific catalyst extremely difficult. The field of surface science breaks down these complexities to truly understand what happens on the surface of a catalyst. By taking a metal single crystal that is cut along one of its primary crystallographic axis's the surface chemistry on each plane of the nanoparticle can be studied in a piecewise manner.

By placing the single crystal in an ultra-high vacuum environment with base pressures below 10^{-11} mbar it is possible to create an atomically flat surface that will remain clean for extended periods of time. This surface can then be exposed to different probe molecules (CO, O_2, H_2) to understand how and where these molecules interact with the surface. Kinetic measurements can even be conducted on these single crystal surfaces at normal reaction conditions to determine if the reaction is structure sensitive or insensitive. The information gained from these studies helps simplify the complex nature of heterogeneous catalysts and can allow for a more rational design of future catalysts.

1.1 Propane Dehydrogenation

Propane dehydrogenation is the process of turning propane into propylene. Propylene is a significantly valuable chemical feedstock where the majority of the demand is accounted for by the polypropylene industry.[1] As part of recent technological advancements in horizontal drilling and hydraulic fracturing, large natural gas reserves in the United States are now mineable. These natural gas deposits, termed shale gas, contains a significant amount of propane (ca. 5%).[2] As propane is significantly less economically valuable than propylene, a selective process of turning propane into propylene is desirable. Significant research is being conducted for finding an optimal catalyst to perform this chemical transformation. [3, 4] One promising class of catalysts for this are intermetallic catalysts using Pt or Pd as base constituents.[5]

Chapter 2 details the synthesis and characterization of PdZn model surfaces used to analyze relevant chemical properties toward PDH.

1.2 Formic Acid Decomposition

Formic acid is a significant byproduct of many biomass upgrading processes. Within the upgrading process many other reaction steps require external hydrogen input. If a process can be conducted internally where formic acid is selectively decomposed to H_2 and CO_2, as opposed to H_2O and CO, this external requirement can be mitigated. On monometallic Pt catalysts, this decomposition is reported to be nearly 100% selective towards H_2. [6, 7] Fundamental understanding of this decomposition process is required to allow for rational design of catalysts to allow for an increased efficiency and lower catalyst cost. Chapter 3 focuses on the kinetic measurements of formic acid decomposition on Pt single crystals and polycrystalline foils.

1.3 Dry Reforming of Methane

Dry reforming of methane is the process of converting CO_2 and CH_4 into syngas (CO and H_2). The reaction process is initiated by the decomposition of methane into H_2 and elementary carbon followed by the Boudouard reaction to form CO. Monometallic Pd catalysts are known for their ability to activate methane, but poor ability to activate CO_2.[8] Due to this, significant research has been conducted to add an additional active phase to Pd catalysts, where the secondary phase would active the CO_2 and the Pd would active the methane.[9] Chapter 4 details the ALD synthesis of model ZrO_x/Pt(111) model catalysts for the dry methane reforming reaction.

1.4 Water-Gas Shift

Steam reforming of methane is an important chemical process for the production of H_2. The chemical processes that demand a H_2 feedstock often require a pure feed, without CO.[10, 11] Thus a process to remove the CO product is required. This is commonly done in industry by use of the water-gas shift (WGS) reaction. In this process water and carbon monoxide into carbon dioxide and hydrogen.

$$CO + H_2O \Leftrightarrow H_2 + CO_2 \quad (1)$$

In this reaction the conversion is equilibrium controlled, where higher conversions are favored at lower temperatures [12]. However, at lower temperatures the reaction proceed slower and thus would require large reactors. Thus, in industry WGS is performed in series where first the feed is sent to a high temperature shift reactor, where the feed is quickly converted towards its equilibrium conversion and then sent to a low temperature shift reactor where the conversion is completed. The research presented here focuses exclusively on the low temperature shift reaction (below 300^{o}C).

One of the more interesting components of WGS research is the influence the support on the reaction. This influence has been speculated to be due to a variety of reasons [13-16]. The most obvious of the reasons is the direct participation of the support in the reaction. Nobel metals ae well known for their ability to adsorb carbon monoxide, but their inability to adsorb and activate water is similarly well known [17]. Oxides on the other hand are known for their ability to adsorb water, but inability to adsorb carbon monoxide [18]. Thus it has been established that for water gas shift, there is a so called three phase boundary where each component of the catalyst activates a different reactant and the reaction occurs at the interface of the two. This has been directly proven for the case of gold supported on Al_2O_3 and TiO_2, where the rate or reaction is proportional to number of interface sites [19]. Because of this interesting type of active site, the need to keeping gold nanoparticles as small as possible is of great importance for maximizing catalyst performance. Chapter 5 details the thermal stability of Au/Fe_3O_4 heterodimer catalysts that have been explored for WGS reaction.

The influence of the WGS catalyst support can influence the reaction in indirect ways, also. One of which is the reactive metal support interaction (RMSI) [20]. RMSI is the phenomena where the supported metal nanoparticle forms a bimetallic particle due to incorporation of the support metal [21]. The alloy formation induces a significant electronic and geometric change in the parent metal that induces a significant change in the adsorption strength of relevant adsorbates[5]. Chapter 6 focuses on the reactive metal support interaction (RMSI) that takes place during WGS reactions on Pt/Nb_2CT_x MXene catalysts.

CHAPTER 2. SURFACE-CONTROLLED ADSORPTION PROPERTIES OF PDZN NEAR-SURFACE ALLOYS

2.1 Abstract

PdZn catalysts has demonstrated high potential in methanol steam reforming, water-gas shift reaction and propane dehydrogenation. In order to understand the reaction mechanisms, β_1-PdZn surface alloys were produced on Pd(111) and Pd(100) single crystal substrates via vapor deposition of diethylzinc. Thermal stability of the surface alloys were investigated by XPS, LEED, and STM. Several other alloy phases were observed for the ZnPd(111) system depending on the preparation conditions. On Pd(111), atomically resolved STM images show a transition from a PdZn p(2×1) row-like structure to the β_1-PdZn(111) surface to a zig-zag like structure when annealed to increasingly higher temperatures. Similarly, a transition from the β_1-PdZn(001) to the β_1-PdZn(010) structure was observed when deposition was performed on a Pd(100) single crystal. Adsorption of carbon monoxide (as a test molecule) and propylene was investigated by HREELS under a variety of conditions. CO was found to bind exclusively in the linear position for the β_1-PdZn(010) surface, while complete destabilization was CO was observed on all other β_1 alloy surfaces. At sub-ambient temperatures, 130 K, propylene was found to no longer adsorb on any of the β_1 surfaces.

2.2 Introduction

The catalyst of interest in this study, PdZn alloy, first gained popularity in its application for methanol steam reforming where it was found that Pd on ZnO had a 97% selectivity towards steam reforming. [22] It was later discovered that under reducing conditions hydrogen spill over from the Pd reduces the ZnO support and generates a PdZn alloy, which was responsible for this improved selectivity. [23] This surface has also been studied for water-gas shift and propane dehydrogenation. [21, 24]

Palladium on SiO_2 has been shown to be a poor PDH catalyst as there is rapid deactivation and only an 11% propylene selectivity and an 89% hydrogenolysis selectivity. However, by alloying palladium with zinc to create β1-PdZn nanoparticles, as verified by synchrotron XRD, on SiO_2 the catalytic performance is enhanced. The propylene selectivity

increases to >98% at 15% conversion and remains stable for several hours on stream. Since hydrogenolysis has previously been shown to be a structure sensitive reaction (requiring ensemble sites of multiple Pd atoms) and PDH has been shown to be a structure insensitive reaction (requiring a reaction site with only a single atom) the change to the selectivity has been attributed to geometric changes of the surface caused by Zn alloying. [5] As alloying occurs, the surface becomes populated by inactive zinc atoms and also increases the bulk Pd-Pd bond distance from 2.80 A to 2.93 A. As the most stable crystallographic surfaces for PdZn ((111), (110) and (100)) still contain adjacent Pd atoms, the vast change in selectivity is primarily attributed to the elongation of the Pd-Pd bond. [25]

In this study, intermetallic Pd-Zn surfaces were synthesized by UHV chemical vapor deposition (UHV-CVD) of Zn onto Pd(111) and Pd(100). PdZn model surfaces have been studied extensively in literature for the application for methanol steam reforming, however here we are studying this surface for propane dehydrogenation. [22, 23] To probe relevant chemical and structural information about these surfaces we coupled surface sensitive structural probes, scanning tunneling microscopy (STM) and low energy electron diffraction (LEED), with surface sensitive chemical probes, high resolution electron energy loss spectroscopy (HREELS) and x-ray photoelectron spectroscopy (XPS). We found that the structure of PdZn surfaces influence the adsorption properties of carbon monoxide and propylene.

2.3 Experimental

Experiments were performed in an Omicron Surface Analysis Cluster at the Birck Nanotechnology Center at Purdue University. The Cluster consists of a preparation chamber and a μ-metal analysis chamber with base pressures of $1x10^{-9}$ and $5x10^{-11}$ mbar, respectively. The preparation chamber contains Ar+ sputtering, resistive sample heating, and leak valves for gas or precursor dosing from a gas manifold. The analysis chamber contains XPS, HREELS, STM, LEED, and resistive sample heating. In both chambers the temperature of the sample is measured by k-type thermocouples connected to the sample holder. A Pd(111) and Pd(100) single crystal with 9.0 mm diameter and 1.0 mm thickness (MaTecK) with orientation accuracy of < 0.5° was used. The single crystals were cleaned by repeated cycles of Ar+ sputtering and annealing in vacuum at 1000K and in oxygen at 623K. The cleanliness of the sample was monitored by XPS,

LEED, HREELS, and STM. Zn was deposited on the single crystals by vapor deposition using diethylzinc as the precursor (≥52 wt. % Zn basis, Sigma-Aldrich).

HREELS data were acquired with an ELS5000 (LK Technologies). Electrons were collected in the specular direction with primary beam energies of 5 eV. The FWHM of the elastic peak was between 2.5-3.0 meV (20-24 cm-1) and the peak intensity was above 10^5 cps for all spectra reported. All HREELS spectra have been normalized to the elastic peak intensity. LEED patterns were acquired using an Omicron rear-view LEED optics with primary electron energies between 30-170 eV.

XPS data were collected using non-monochromatic Mg Kα X-rays (1253.6 eV) at an X-ray gun power of 150 W. High-resolution core level spectra were obtained at constant pass energy of 20 eV with an energy spacing of 0.05 eV. Electrons were collected at a 45° photoemission angle with respect to the surface normal. No energy scale correction was foreseen by the analyzer manufacturer (the electron energy analyzer – Omicron EAC 125 and the analyzer controller – Omicron EAC 2000); therefore, it was possible only to set the Pd 3d5/2 peak, of clean Pd(111), at 335.1 eV by changing the spectrometer work function. XPS data were analyzed using CasaXPS (version 2313Dev64) software.

STM images were collected with an Omicron ambient temperature UHV STM/AFM. W tips were made via electrochemical etching followed by electron bombardment in UHV. Images were collected using a constant current scanning mode. Images were analyzed using WSxM software. [26]

2.4 Results

2.4.1 PdZn Alloy Structure

To prepare the surface for deposition, the Pd(111) single crystal was cleaned by several cycles of sputtering and annealing (in both UHV and O2 environments). Surface cleanliness was verified by scanning for potential contaminants (O, C, Zn, and Al) in XPS and by collecting a p(1x1) LEED pattern. The preparation chamber was conditioned for deposition by exposing the system to diethylzinc at pressures of $1x10^{-7}$ mbar for 10 minutes, prior to transferring in the single crystal. During deposition the Pd(111) sample temperature was held between 300K and 750K, while the DEZ, at room temperature, was exposed through a leak valve. An exposure of

450L was used for surface temperatures between 300K and 473K, and an exposure of 2500L was used for all higher temperatures. The increase in exposure was required in order to keep the quantity of Zn deposited on the surface relatively constant (3-5 ML equivalent) due to the increasing mobility of zinc into the palladium bulk at elevated temperatures. DEZ was found to adsorb dissociatively at all temperatures. Hydrocarbon fragments mainly desorbed, even at room temperature, as the carbon content was below the limit of detection. However, weak HREELS peaks were observed at room temperature, which can be attributed to products of the C_2H_5 ligand (ethane and ethylene) as shown in Figure 4.2. At room temperature, zinc is found to not readily alloy with the Pd(111) substrate and rather grows as a pure metallic zinc thin film as characterized by a very minimal shift in the Pd $3d_{5/2}$ and Zn $2p_{3/2}$ peaks from their well-established reference positions. From LEED the only observed reflects are the (1x1) reflects corresponding to the Pd(111) substrate so it is shown that the Zn film grows pseudomorphically.

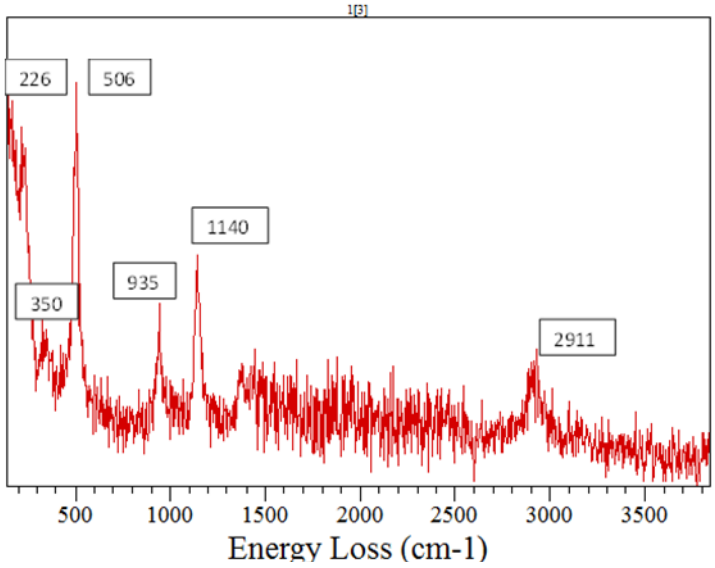

Figure 2.1 HREELS spectra of DEZ fragments on
Pd(111) after 450L DEZ deposition at room temperature.

By annealing the surface prepared by room temperature deposition of diethylzinc to 373K, or by performing the deposition at 373K, the zinc being to intermix with the Pd(111) substrate creating an ordered PdZn alloy. Following deposition, two components of the Pd $3d_{5/2}$ peak can be distinguished at 336.1 and 335.2 eV corresponding to a PdZn intermetallic and pure Pd, respectively. Zinc was characterized by a single Zn $2p_{3/2}$ peak at 1021.3 eV, which is shifted only

by 0.3 eV in respect to the binding energy (BE) for bulk Zn. [27]. From the relative peak areas of the shifted Pd $3d_{5/2}$ peak and the Zn $2p_{3/2}$ peak the ratio of Zn to Pd in the intermetallic near surface region is calculated to be 1.0-1.1 immediately after deposition. For these calculations all of the Zn detected by XPS is taken into account due to the peak shape being consistent with that of a single Zn component. [27] LEED collected on this surface shows a well-defined p(2x1) structure on three rotationally symmetric domains as shown in Figure 10a. This surface would be characterized by alternating rows of Pd and Zn while maintaining the FCC structure of Pd(111), where the Pd-Pd bond distance is the same as the Pd-Zn bond distance.

By performing the DEZ deposition at 473K yet another different surface structure is observed by LEED, as shown in Figure 10b. This LEED pattern, while qualitatively similar to the P(2x1) structure, has two observable differences. The first is the apparent doubling of the (1x1) reflects, and the second is the shifting of one set of fractional reflects towards smaller k-space. This reconstruction would be consistent with the changing of the P(2x1) FCC structure to the (111) surface of the tetragonal β1-PdZn alloy surface. While the atomic structure of both of these surfaces appears qualitatively similar, the key difference is the distance between adjacent Pd atoms on the surface is now larger than the distance between adjacent Pd and Zn atoms. This β1-PdZn(111) surface is confirmed by STM, Figure 11, where linear rows of atoms are observed where a unit cell of 2.8 Å by 4.2 Å is observed. It is important to note that STM probes a convolution of the local density of states (LDOS) and topography of a surface. Thus for a heterogeneous surface populated by atoms of very different density of states, it is possible that only one of the two elements can be observed even if they reside in the same plane. Previous DFT calculations show that under the applied voltage conditions, the LDOS of palladium is much larger than zinc, thus only the palladium atoms would be seen in STM while the zinc atoms would be STM invisible. [28] By XPS the Zn 2p3/2 peak is positioned at 1021.25 eV, slightly further towards lower binding energy than the previous case, and the Pd 3d5/2 peak now appears as a single broad symmetric peak positioned at 335.9 eV. The Zn/Pd ratio is shown to still be close to 1:1.

By taking the surface prepared by deposition at 473K and annealing to temperatures of 523K-573K yet another reconstruction occurs. As shown in Figure 13, an intricate and complex LEED pattern emerges (Note the difference in kinetic energy of incident electrons from previous LEED patterns). Identification of such a complex LEED pattern is difficult without the aid of

dynamic LEED. This LEED pattern appears to be the same as the pattern reported by Gabasch et al. where the identification of the surface was suggested to be a rectangular ($4\sqrt{3}/3$ x 6) superstructure. [29] However, this identification becomes questionable when observed by STM. As shown in Figure 2.3, the surface undergoes a complex reconstruction into a zig-zag type structure. It is apparent that this zig-zag structure grows in three rotationally identical planes. By taking the Fast Fourier Transform (FFT) of all three domains of the surface, a pattern similar that observed in LEED is seen. Similar to LEED, FFT shows symmetry in k-space (inverse real space) so reflects seen closer to the center are related to larger periodicity. The Zn $2p_{3/2}$ peak again shift to lower binding energy, centered now at 1021.05 eV. While the Pd $3d_{5/2}$ peak becomes a single asymmetric peak positioned at 335.5 eV. The Zn/Pd ratio is measured to be 0.6:1.0. However, based on STM images it is still likely that the surface maintains a 1:1 ratio, indicating a diffusion of Zn into deeper layers of Pd.

The preparation conditions for a model ZnPd(001) surface was conducted much the same as for the ZnPd(111) surface. 450L of Diethylzinc was exposed to a freshly cleaned Pd(100) single crystal held at a temperature of 373K. A very minimal amount of residual carbon is left on the surface and no evidence of hydrocarbon fragments from the DEZ precursor is seen by HREELS. XPS on the surface shows a Zn $2p_{3/2}$ located at 1021.2 eV and a Pd $3d_{5/2}$ peak located at 335.8 eV, indicating alloy formation. LEED conducted on this surface shows a symmetry identical to the unmodified Pd(100) substrate. Along with atomically resolved STM (shown in Figure 2.3), showing a square symmetry with atomic distances of 3.3 Å by 3.3 Å, this surface is identified to be a Zn or Pd terminated B1-PdZn(001) surface.

Similar to when using the Pd(111) substrate, this surface reconstructs upon annealing to 473K. By XPS zinc is observed on the surface with a Zn $2p_{3/2}$ peak position of 1021.36 eV, a shift of 0.4 eV from bulk zinc. The Pd $3d_{5/2}$ peak is also seen to shift to a position of 336.05 eV. Performing STM, Figure 14, on this surface shows that a well ordered alloy is produced. Again due to local density of states differences, only the palladium atoms are able to be imaged. [30] An observed rectangular unit cell with Pd-Pd distances of 3.9 Å by 3.4 Å is observed. Based on the Pd/Zn atomic ratio and the periodicity of the surface, it is concluded that the (010) surface of the tetragonal β1-PdZn unit cell is produced.

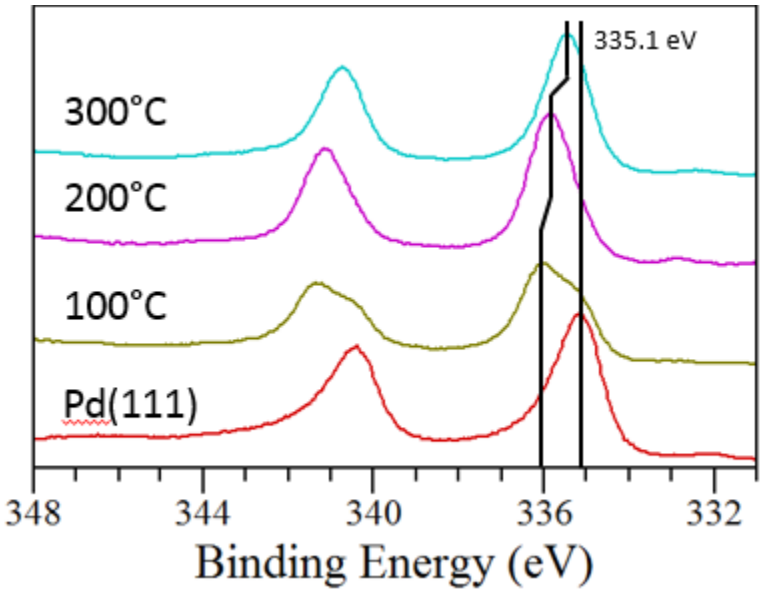

Figure 2.2 XPS spectra of the Pd 3d regions following 450L of diethylzinc exposure with substrate temperatures between 100°C and 300°C

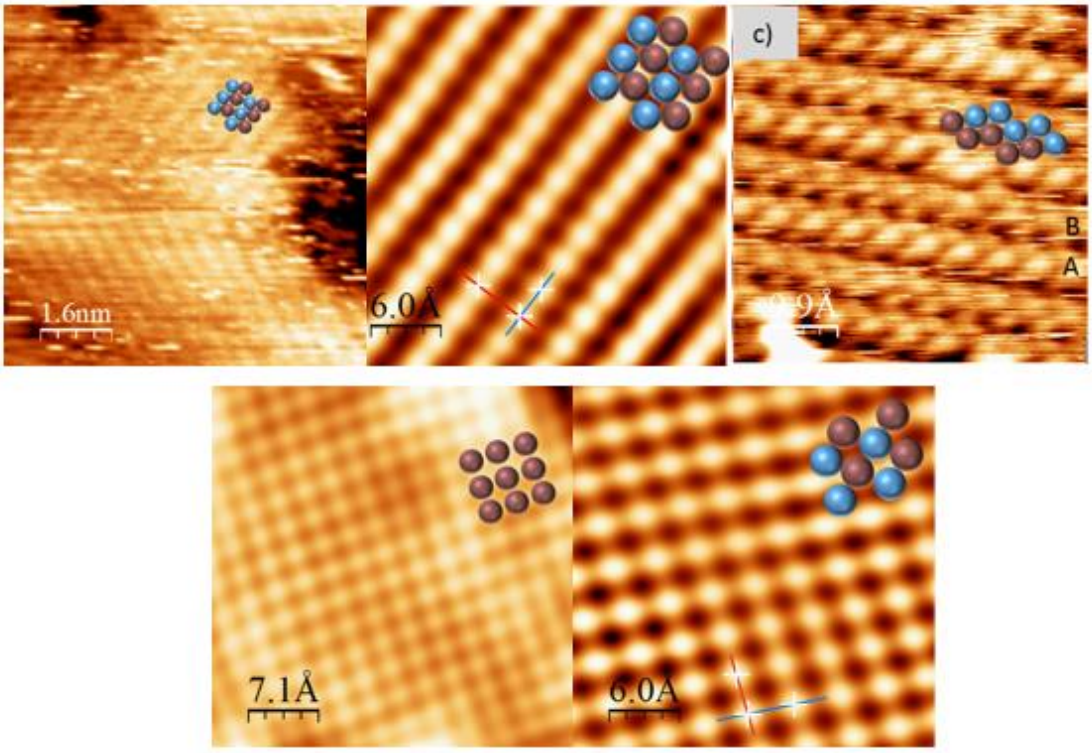

Figure 2.3 STM images of five structually distinct PdZn surface alloys. a) p(2x1), b) B1PdZn(111), c) Zig-Zag, d) B1PdZn(001), e) B1PdZn (010)

In total five different structurally distinct model PdZn surfaces are able to be synthesized and fully characterized by this UHV-CVD method of preparation. Three of these surfaces corresponding to low index surfaces of the B1-PdZn crystal structure.

2.4.2 Carbon Monoxide Adsorption

As it was shown above for the technical catalyst, carbon monoxide changes from bridge to linear adsorption while Pd alloys with Zn. Five PdZn surface structures were tested towards CO adsorption at 130 K (5 L); the HREELS spectra of the stretching CO vibration region are shown in Figure 2.4. For reference, HREELS spectra from CO_{ads} on the Pd(111) and Pd(100) surfaces were also collected.

On the pure Pd(111) surface, CO mainly adsorbs in a 3-fold site (the loss at 1870 cm^{-1}), a bridge (1940 cm^{-1}) and linear (2090 cm^{-1}); a high frequency peak at 2150 cm^{-1} can be attributed to adsorption on defect sites. On the Pd(100) surface, CO only adsorbs in a bridge site (1940 cm^{-1}). No CO adsorption was detected on PdZn(111)-p(2×1) and β_1-PdZn(001), whereas CO adsorbs in the bridge (1940 cm^{-1}) and linear (2090 cm^{-1}) configurations on "zig-zag" surface. Only linearly adsorbed CO was observed on β_1-PdZn(010). On the β_1-PdZn(111) surface very weak (relative to pure Pd(111) and (100)) peaks can be seen in the range of linear (2080 cm^{-1}) and 3-fold (1860 cm^{-1}) adsorption. The slight shift towards lower vibrational frequencies can be attributed to either a change in adsorption site or a dipole-dipole effect (low coverage). In HREELS the relative area of a vibrational signal can give information about the relative coverage of that species. The ratio area under the curves of the β_1-PdZn(111) and clean Pd(111) surface is ~0.05. Taking both the relative intensity and lower peak position it is likely that any adsorbed carbon monoxide is present at very low coverages on defect sites such as step edges. On the β_1-PdZn(010) surface the only measurable adsorption is seen on a linear site with a similar intensity of the pure Pd(100) surface.

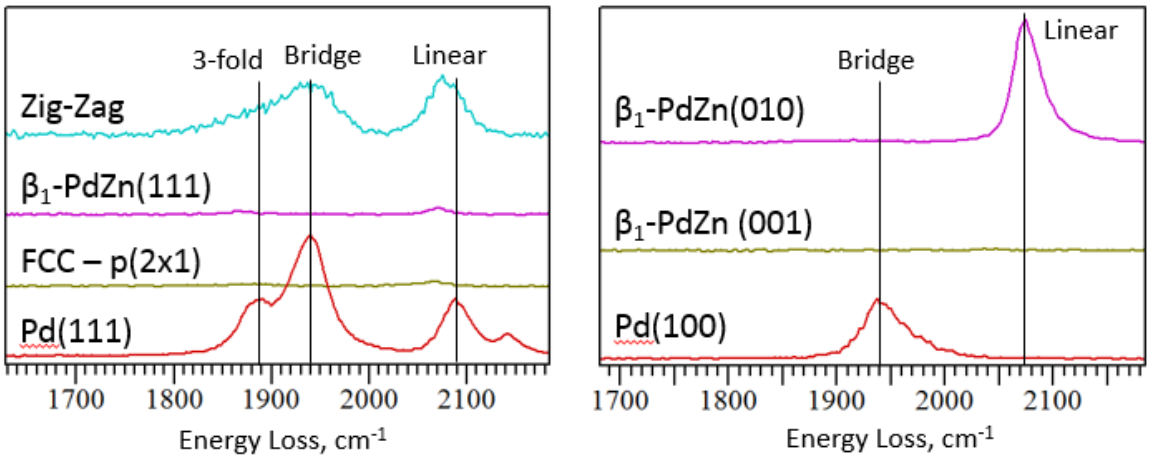

Figure 2.4 HREELS spectra on model PdZn alloy surfaces following 5L exposure of CO at 130K.

These results are consistent with the adsorption of CO on the supported nanoparticle catalysts seen by Gallagher et al. [24] Taking the results obtained on the model PdZn surfaces it is possible to draw conclusions about what surfaces may be present on the supported nanoparticle system. It is likely the bulk of the linear signal is caused by adsorption on the (010) facet. Based on the surfaces tested the bulk of the remaining bridging and 3-fold adsorption would be attributed to adsorption on low index sites (edges or corners) similar to step edges on the planar surfaces. Due to the lack of any adsorption on the (111) and (001) surfaces it is not likely that these surfaces dominate the nanoparticle, but the presence of these surfaces cannot be completely discounted.

Further analysis on the two PdZn surface structures, Zig-Zag and β_1-PdZn(010), that still allow for carbon monoxide adsorption were conducted under a variety of adsorption conditions. These conditions were 1) in-situ at room temperature at pCO=$5x10^{-9}$ mbar 2) ex-situ at room temperature following a 3 Langmuir exposure and 3) ex-situ at 120K following a 3 Langmuir exposure.

As shown in Figure 2.5 CO is unstable on the B1-PdZn(010) surface at 300K with a system pressure of $5x10^{-11}$ mbar. This desorption temperature is significantly lower than that seen on Pd(100), where it has been shown the CO is stable until 450K [31]. Indicating a significant decrease in the adsorption energy of CO on this surface. Linear bound CO is seen to repopulate the surface as the background pressure is increased to $5x10^{-9}$ mbar. The slight

decrease in the vibrational frequency from 2072 cm^{-1} to 2032 cm^{-1} is likely due to a decrease in the surface coverage in CO, decreasing the dipole-dipole interactions.

A similar trend is seen on the zig-zag surface where under ultra-high vacuum conditions the only stable adsorption site is the 3-fold adsorption site. Indicating that this adsorption site binds CO significantly stronger than bridging and linear bound CO. Upon increasing the base pressure of CO to $5x10^{-9}$ mbar the bridging (1893 cm^{-1}) and linear bound (2047 cm^{-1}) being to become partially occupied. Again these peaks are ca. 30 cm^{-1} than the peaks at 140K indicating a lower absolute coverage. These results indicate that the change in prefered adsorption site of carbon monoxide is not soleley a structural phenomena. The significant decrease in adsorption energy of CO indicate a significant electronic change in the surface Pd atoms. More broadly these results indicate the importance of have a sufficently low base pressure for conducting adsorption experiments.

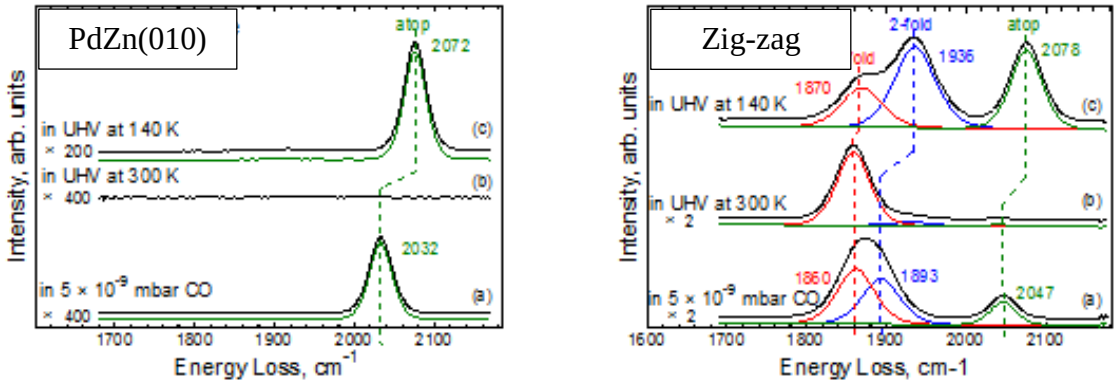

Figure 2.5 HREELS spectra on the Zig-Zag and PdZn(001) surface after a series of deposition conditions.

2.4.3 Propylene Adsorption

The site isolation (distance between adjacent Pd atoms) could be a reason for the good catalytic behavior of ZnPd catalyst for PDH. The poor stability and low selectivity of monometallic Pd catalysts in PDH was supposed to be due to further dehydrogenation of strongly adsorbed propene and eventually coking the surface. [5] The alloying of palladium with zinc results in increasing the distance between adjacent Pd atoms that destabilizes the propene and effectively halts any further dehydrogenation reaction. To test this hypothesis, propene was

adsorbed on Pd(111) and Pd(100) along with their ZnPd surface alloys at 140 K as shown in Figure 2.6. The key result is that on both Pd(111) and Pd(100) propene adsorbs in di-sigma bounded fashion. This conclusion was drawn from the absence of C=C vibrations at ca. 1660 cm^{-1}. [32] It is remarkable that all surface except for the zig-zag surface result in the inability to adsorb propylene under these conditions. The only adsorption features seen on these surfaces is CO that is adsorbed on the B1-PdZn(010) surface.

These results indicate that the low index surface of the PdZn alloy catalyst will be unable to readsorb the desired product, propylene. This demonstrates that these surfaces would be selective towards propylene, as this surface species is required for further dehydrogenation and hydrogenolysis. There is also an apparent correlation in the ability for a surface to adsorb multiply coordinated CO and their ability to adsorb propylene. This result indicates that CO adsorption could be used as a first pass screening technique for future catalyst synthesis.

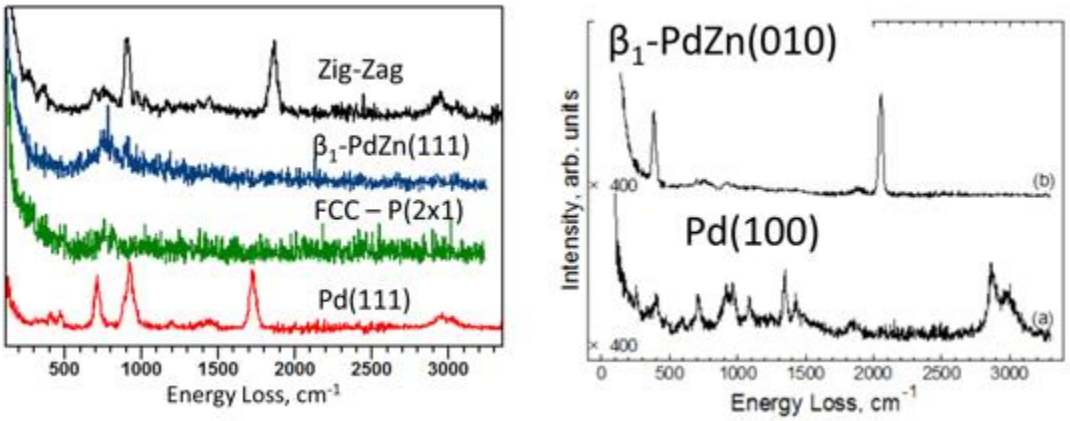

Figure 2.6 HREELS spectra of PdZn model surfaces following 5L exposure of propylene at 130K

2.5 Conclusions

A novel technique has been demonstrated for depositing metallic Zn onto Pd single crystals. This technique has several benefits over the traditional method, namely ease of application and controllability. Zinc is shown to readily alloy with Pd(111) and can create a variety of surface structures. The formation of these surfaces has been confirmed by a variety of techniques including atomically resolved STM. It has been shown by HREELS investigations that there is surface sensitivity to both CO adsorption and propylene adsorption for these surfaces.

All three surfaces corresponding to low index B1-PdZn surfaces show an inability to adsorb propylene, the desired product in propane dehydrogenation. These results explain why the selectivity of PdZn catalysts are superior to monometallic catalysts for this reaction.

CHAPTER 3. KINETICS OF GAS PHASE FORMIC ACID DECOMPOSITION ON PLATINUM SINGLE CRYSTAL AND POLYCRYSTALLINE SURFACES

3.1 Abstract

Formic acid dehydrogenation turnover rates (TORs) were measured on Pt(111), Pt(100), and polycrystalline Pt foil surfaces at a total pressure of 800 Torr between 413 – 513 K in a batch reactor connected to an ultra-high vacuum (UHV) system. The TORs, apparent activation energies, and reaction orders are not sensitive to the structure of the Pt surface, within the precision of the measurements. CO introduced into the batch reactor depressed the formic acid dehydrogenation TOR and increased the reaction's apparent activation energies on Pt(111) and Pt(100), consistent with behavior predicted by the Temkin equation. Two reaction mechanisms were explored which explain the formic acid decomposition mechanism on Pt, both of which include dissociative adsorption of formic acid, rate limiting formate decomposition, and quasi-equilibrated hydrogen recombination and CO adsorption. No evidence was found that catalytic supports used in previous studies altered the reaction kinetics or mechanism.

3.2 Introduction

Conversion of biomass to liquid fuels and valuable chemicals requires a large hydrogen input. Formic acid, a byproduct of many of these upgrading reactions, can catalytically decompose to produce H_2 and CO_2 or H_2O and CO. On Pt, reported dehydrogenation selectivity is near 100% [6, 7]. In this study, the formic acid dehydrogenation kinetics on Pt(111), Pt(100), and a Pt foil were measured at a total pressure of 800 Torr and temperatures between 413 – 513 K. TORs did not vary on the surfaces tested within the precision of the measurements. In this work, we compare the results obtained here to other formic acid decomposition studies on Pt in the literature and discuss simple reaction mechanisms for formic acid dehydrogenation.

3.3 Methods and Materials

Kinetics were measured in a gas phase 1.4 L stainless steel batch reactor connected to a UHV chamber via a welded metal bellows transfer arm allowing for sample transfer between the

two chambers in vacuum. This apparatus has been described previously [33, 34]. The batch reactor was pumped with a turbomolecular pump in order to reach pressures < 1 x 10^{-6} Torr for sample transfer to the UHV chamber. The UHV chamber was equipped with an ion gun (PHI 04-161) and resistive heating of sample, a PHI 15-255G double pass cylindrical mirror electron energy analyzer with a build-in electron gun and a Mg x-ray source for x-ray photoelectron spectroscopy (XPS) and Auger electron spectroscopy (AES), and low energy electron diffraction (LEED) (OCI Vacuum Microengineering BDL800IR-ISH-FIX). The UHV chamber was also equipped with a UTI-100C quadrupole mass spectrometer. The base pressure of the UHV chamber was ~ 5x10^{-10} Torr.

3.3.1 Pt Single Crystal and Foil Samples

Pt(100) and Pt(111) single crystals (Princeton Scientific) with orientation accuracy < 0.1° were spot welded to the sample holder via stainless steel pins on each side of the crystal. Current was passed directly through the pins for resistive heating. A Eurotherm 2408 temperature controller controlled crystal temperature which was measured by a K-type thermocouple spot welded to the side of the single crystal or back of the foil. Each sample was remounted and the thermocouple leads were re-welded several times during a campaign of kinetic experiments.

Samples were prepared before each series of experiments by repeated cycles of Ar^+ sputtering (5 x 10^{-5} Torr Ar, 1-2 keV electrons), O_2 treatment (1 x 10^{-6} to 2 x 10^{-5} Torr, 773-1073 K), and annealing in vacuum at 1073 K. Samples were checked for contaminants by AES or XPS after cleaning to confirm that no contaminants were present on the sample surface other than C or O, which were unavoidable from residual formic acid vapor and background CO and H_2O. A detailed discussion of sample cleanliness is given in the results section. Single crystal samples were checked by LEED to ensure that the expected surface construction was present. Hexagonal (111)-(1x1) and square (100)-(1x1) diffraction patterns were observed on the Pt(111) and (100) crystals after the standard cleaning procedure, respectively. For Pt(100), as noted, residual contamination lifted the hexagonal reconstruction [35].

3.3.2 Kinetic Experiments and Kinetic Data Analysis

Reaction gases and vapors were introduced to the batch reactor one by one via stop valves on the gas manifold which was pumped by a scroll pump after dosing each gas. An MKS

Baratron pressure transducer with ± 0.1 Torr accuracy was used to monitor the amount of gas introduced to the reactor. Formic acid (Thermo Scientific, 99+%) and water (Millipore, 18.2 MΩ resistivity) were introduced from the vapor space in sealed glass containers containing 1-2 mL of the liquid. Each liquid was degassed before reaction by several cycles of freeze-pump-thaw. Other gases used were CO (Research purity, Matheson, 99.998%), H_2 (Praxair, UHP, 99.999%), and N_2 (Research grade, Airgas, 99.9997%). Gas dosing order was typically formic acid, water (if dosed), H_2, CO, and balance N_2 for a total pressure of 800 Torr. For some runs CO was dosed before H_2, but this did not have a measureable impact on the CO_2 turnover rate (TOR). After dosing, gases were circulated in two loops by two bellows pumps (Metal Bellows, MB-21). One circulation loop included a Nicolet Nexus 670 Fourier transform infrared (FTIR) spectrometer with a gas cell for analysis. Gases were permitted to mix for approximately 5 minutes before data collection began to ensure a well-mixed system.

3.3.3 Kinetic Experiments

CO_2 TORs were calculated by measuring the CO_2 evolution monitored by the gas phase asymmetric stretching mode IR peak at 2349 cm^{-1}. A data point from 25 averaged spectra was collected approximately every 10 s using Omnic version 7.2a data acquisition software. CO_2 concentration was related to absorbance using a calibration curve prepared by measuring the CO_2 absorbance peak area for several dilutions of a 500 ± 2% ppm CO_2 in N_2 gas mixture. The batch reactor walls were kept at room temperature during all experiments. Bulk reaction gas temperature change due to heating of the sample in the 140-240 ºC range was negligible, as the formic acid dimer to monomer ratio remained constant during reaction. This was possible because the recirculation flow kept the volume of heated gas near the sample small and the heat added to the gas by the sample was lost through the walls of the reactor and recirculation system.

CO_2 TORs were calculated by numerically differentiating batch reactor data and were normalized to the calculated geometric Pt atom density of the front face of each single crystal: 1.5×10^{15} and 1.3×10^{15} Pt atoms cm^{-2} for Pt(111) and (100), respectively. Pt atom density on the Pt foil surface was assumed to be 1.5×10^{15} cm^{-2}. The backsides of each sample were assumed to be inactive because they were neither polished nor sputter cleaned. Reported TORs were collected following cleaning of the sample and then after at least one run ≥ 30 min. The

TOR usually dropped considerably after this first run then remained roughly constant for subsequent runs. A detailed discussion is given in the results section.

Activation energy and reaction order runs were performed multiple times on different days in the stable kinetic regime. For activation energy measurements, temperature was varied over the relevant temperature range dwelling at each point for 2 to 5 minutes. Temperatures were varied randomly, and at least the final point was collected at the same temperature as the first point in order to account for catalyst deactivation and hysteresis. Because reactions were run in batch mode, gases were recharged for each point for an order collection experiment. Concentrations for reaction order experiments were varied randomly and the first point was always repeated at the end of the series to account for catalyst deactivation and hysteresis. Formic acid reaction orders are plotted against the natural log of effective formic acid monomer concentration which takes into account the presence of dimer in the gas phase. The partial pressures of the formic acid monomer, P_m, and dimer, P_d, fractions are expressed in Equation 1:

$$K = \frac{{P_m}^2}{P_d} = 10^{\left(10.755 - \frac{3090}{T}\right)}\ Torr \qquad (1)$$

where K is the equilibrium constant [36, 37] and T is the temperature in degrees Kelvin. Equation 1 was used to calculate the partial pressures of monomer and dimer present in the gas phase.

3.3.4 *Ex situ* Characterization

AES spectra were collected using 3 keV incident electrons in differential mode using a PHI lock-in amplifier. XPS spectra were collected using a non-monochromated Mg source (hν = 1253.6 eV) with constant pass energy = 50 eV. The binding energy scale was calibrated using Au $4f_{7/2}$ and Cu $2p_{3/2}$ peaks at 83.8 eV and 932.4 eV, respectively, taken from a sputter cleaned sample containing Au and Cu foils. The fwhm of the Au $4f_{7/2}$ line was 1.36 eV. Spectra were analyzed using CasaXPS version 2.3.16 PR 1.6 (Casa Software Ltd.). To calculate coverage from XPS results, we followed Fadley's approach, [38] which assumes a non-attenuating adlayer at fractional coverage. Coverage (Θ), measured in monolayers (ML), is the ratio between the number of adsorbed species and the number of surface Pt atoms on (111) plane, and is expressed in Equation 2:

$$\Theta = \frac{N_l(\theta)}{\frac{d\sigma_l}{d\Omega}} \times \frac{\frac{d\sigma_s}{d\Omega}}{N_s(\theta)} \times \frac{\text{Instrument Function}(E_s)}{\text{Instrument Function}(E_l)} \times \frac{\Lambda_e^{subst}(E_s)}{d_s} \times cos\theta \qquad (2)$$

where $N_l(\theta)$ and $N_s(\theta)$ are the photoemission peak areas of the adlayer and the substrate at the given photoemission angle, θ, with respect to the surface normal; $\text{Instrument Function}(E_s)$ and (E_l) includes the acceptance solid angles of the electron analyzer and the effective analyzed areas for the photoelectrons from substrate and adlayer; $d\sigma_l/d\Omega$ and $d\sigma_s/d\Omega$ are differential cross-sections for the photoemission peaks of the adlayer and the substrate, which are calculated using tabulated Scofield cross-sections [39] and the Reilman asymmetry parameters; [40] $\Lambda_e^{subst}(E_s)$ is the electron attenuation length (EAL) of the photoelectrons originating from the substrate atom that have traveled through the substrate material; and ds is the interlayer distance of the substrate. The EAL was calculated by NIST SRD-82. [41]

3.4 Results

3.4.1 Analysis of the Gas Phase IR Spectra

Figure A.1 and Figure A.2 in the supplementary information show FTIR spectra before and after 52 minutes of reaction on Pt(100) at 473 K respectively. Assignments for formic acid monomer and dimer peaks are given in Table A.1 in the supplementary information. The only observed product of formic acid decomposition was CO_2, evident from the increase in absorbance of the asymmetric CO_2 stretching peak at 2349 cm^{-1}. CO and H_2O, dehydration products, were not observed above the limit of detection. CO could not be quantified in any kinetic experiments for which CO was co-fed. For experiments where CO was not co-fed, no intensity change was observed in the C=O stretching region at 2143 cm^{-1}. The limit of detection for CO was about 0.5 ppm. For all experiments, dehydrogenation selectivity was > 99%. Asymmetric stretching features of water between 1400-1700 cm^{-1} were present in background spectra barely above the noise level due to impurity of the formic acid (99+% pure), these were not quantified, and did not change during reaction.

3.4.2 System Validation

To ensure that measured rates resulted from formic acid decomposition on the Pt surface, two blank experiments were performed. In the first, the CO_2 TOR was measured on a piece of 316 stainless steel (SS) foil spot welded between the two heating leads. The areal rate at 493 K on the 316 stainless steel blank was approximately 5 x 10^{-10} moles CO_2 cm^{-2} s^{-1}, while the measured areal rates on Pt(111) and Pt(100) under the same conditions were greater than 6 x 10^{-9} and 8 x 10^{-9} moles CO_2 cm^{-2} s^{-1}, respectively. The areal rate of 5 x 10^{-10} moles CO_2 cm^{-2} s^{-1} represents a maximum rate on surfaces other than the active Pt for a reaction with catalyst present, as the blank was replaced with the actual catalyst, so only decomposition on the stainless steel heating pins would lead to an error in the rate measurement on SS surfaces.

In the second validation experiment the background activity of the batch reactor was measured with a Pt catalyst present. With Pt(111) loaded, the reactor was charged with gases used under standard conditions except for formic acid (15 Torr H_2, 15 Torr CO, 800 Torr total, balance N_2). At 493 K, the measured CO_2 formation TOR on Pt(111) was approximately 0.05 molecules CO_2 $(Pt\ atom)^{-1}$ s^{-1}. Under the same conditions with 5 Torr formic acid present, the average TOR on Pt(111) was 2.6 ± 0.6.

The rate reported throughout this work is the rate of formation of CO_2. Direct calibration and measurement of CO_2 peak area instead of using formic acid peaks (both monomer and dimer contributions) is a more straightforward route for calculation of the decomposition TOR. The formic acid decomposition TOR was measured for comparison to the CO_2 TOR for an experiment with 1 Torr initial pressure of formic acid (P_{H2} = 15 Torr, Total Pressure 800 Torr, balance N_2). The CO_2 TOR calculated for this run at 473 K was 1.80 molecules CO_2 $(Pt\ atom)^{-1}$ s^{-1}. The decomposition TOR of formic acid was measured to be 1.77 molecules formic acid $(Pt\ atom)^{-1}$ s^{-1}, calculated by the decrease in the ν(C-O) peaks for monomer and dimer at 1106 and 1218 cm^{-1}, respectively, where concentrations of monomer and dimer were calculated using Equation 1, indicating that the generation of CO_2 can be fully attributed to formic acid decomposition. Additionally, the dehydrogenation rates of the formic acid monomer and ½ dimer for this experiment were both equal to ~0.6 s^{-1} (resulting in the total overall rate of 1.8 s^{-1} reported above by adding 2 times the dimer TOR to the monomer TOR), indicating that formic acid dimers readily decomposed forming two monomers near or on the hot catalytic surface.

Internal heat and mass transfer limitations were not present, as the single crystals and Pt foil were non-porous. Based on the data shown below in Figure 3.4 and data gathered previously on this system, external heat and mass transfer limitations also do not affect the rate. Smeltz et al. measured a TOR of 0.34 ± 0.02 s^{-1} for NO oxidation on Pt(111) using the same reactor system at 573 K, and verified that the rate of mass transfer to the surface was at least one order of magnitude higher than the rate of reaction using reaction gas mixtures of < 100 ppm for NO and NO_2 [34]. Since the gas concentrations in this study were much higher (with the exception of CO_2) and thus would accentuate diffusion because of the steeper gradient at the surface but the TORs observed at 413 K under the conditions used in Figure 3.4 on Pt(100) were similar to those for NO oxidation (red line, TOR = 0.37 s^{-1}), we conclude that the external diffusion rate well exceeds the reaction rate. Further evidence is given by the observation that, in the same activation energy run, TORs as high as 3.45 s^{-1} were measured, and all points fell on the same line.

The variability in TOR due to the mounting position of the thermocouple on the Pt single crystals was found to be much less than the day-to-day variability in measured TOR, as the TOR at standard conditions and other kinetic parameters (activation energy, reaction orders) were collected several times over the course of several months during which time the sample was remounted many times.

3.4.3 Rate Stabilization

Supported catalysts in flow reactors are typically subjected to long stabilization periods under reaction conditions before kinetic measurements begin. This approach is not possible for batch reactors. Therefore, the TOR was permitted to stabilize during several consecutive runs before collecting TORs reported for kinetic parameters. For kinetic experiments on low surface area metal single crystals, the factor most affecting TOR variability is likely to be contamination of the surface by species left after reaction from either the decomposition mechanism itself or transport of external contaminants in the reaction chamber to the crystal surface. These external contaminants may arise from chamber or sample holder contamination, contamination of the reaction gases, or diffusion of contaminants from the bulk of the single crystal to the surface.

Contamination was monitored before and after experiments using XPS and/or AES. Prior to reaction, C and O were already present on the Pt surfaces. Transfer to the reactor introduced

both C and O on the surface of the single crystal. Due to poor control of C and O contamination before a reaction, TORs collected on a surface initially completely C- and O-free (according to AES) were not reproducible. Nominal C and O coverages increased on all catalysts after the first ~30 minutes of reaction following cleaning, and then remained constant for subsequent reactions. From XPS, stabilized coverages of C and O ranged between 1-3 ML and 0.4-0.6 ML, respectively, on Pt(111) and Pt(100) surfaces. Typical C and O coverages during several consecutive reactions are plotted in Figure 3.1.

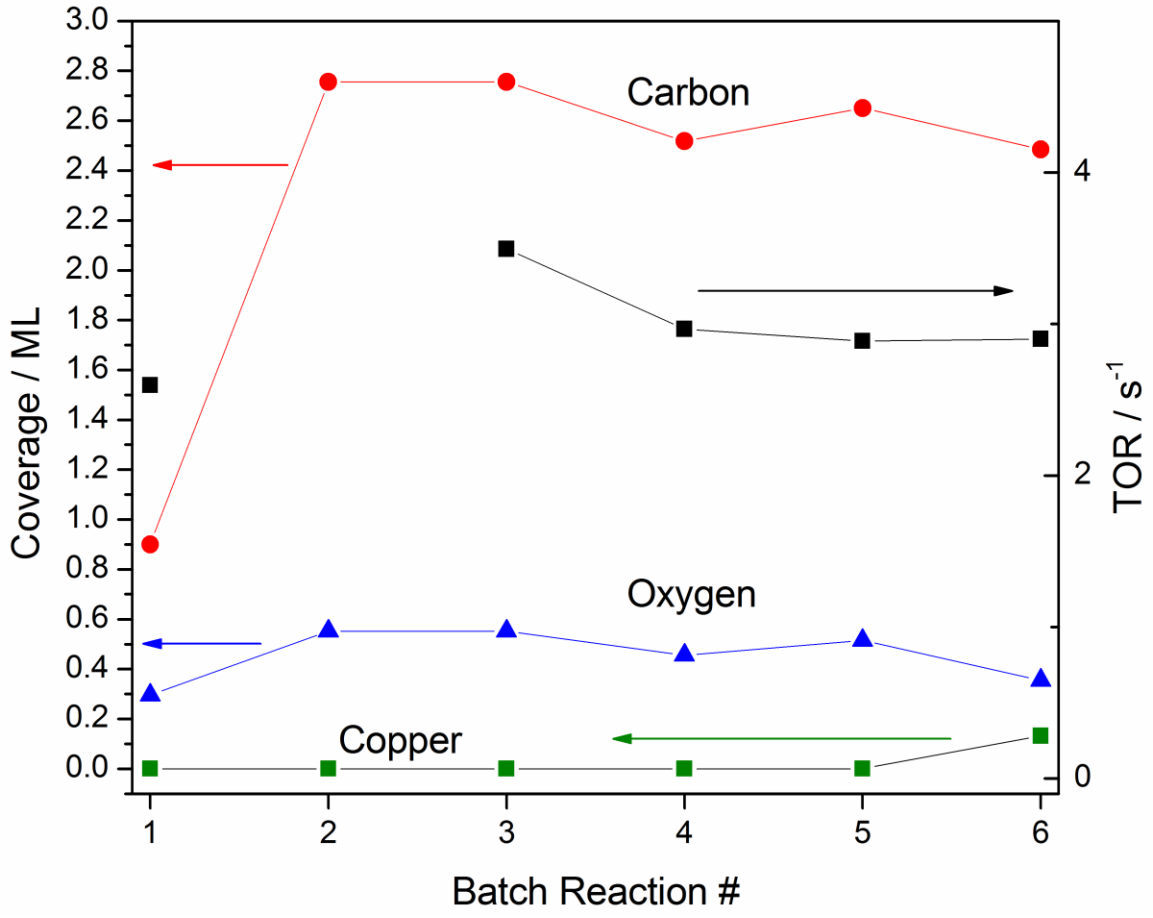

Figure 3.1 Carbon (red circles), oxygen (blue triangles), and copper (green squares) contaminant coverages calculated from XPS plotted against batch reaction number for a series of consecutive reactions on Pt(111). Also plotted on the right y-axis is the CO2 TOR (black squares). Reaction conditions were 5 Torr HCOOH, 15 Torr H_2, 15 Torr CO, 800 Torr total (balance N_2), T = 493 K.

Other contaminants detected after some reactions were Cu and S. Cu is most likely associated with migration of Cu from the sides of the single crystal from spot welding with Cu electrodes, as the amount of Cu present after several runs qualitatively tracked with the number

of times a single crystal had been spot welded to the sample holder. Above the limit of detection for both AES and XPS, Cu does not affect the TOR more than the run-to-run variability of the rate. From XPS, Cu coverage did not exceed 0.2 ML. However, it should be noted that if the Cu were affecting the rate, it might not need to migrate to the front side of the crystal. In fact, trace Cu was detected on the stainless steel blank sample, which may explain at least some of the background activity of this sample.

S contamination was sometimes observed by AES, but was detected by XPS only once after a reaction with contaminated water. From the high resolution XPS region scan following this reactions, the S coverage was approximately 0.2 ML. From this core level spectrum, the limit of detection was calculated to be approximately 0.07 ML using standard procedures of error calculation in the CasaXPS software. S coverage estimation for small amounts of sulfur is difficult from AES alone due to overlap of Pt NNN and S LMM peaks at a kinetic energy of ca. 150 eV, so from this method typical S contamination coverages were estimated to be $\leq$ 0.07 ML for all runs.

In general, the TOR qualitatively tracks most closely to the coverages of carbon and oxygen. For runs occurring within the first ~30 minutes of cleaning, the rate is usually higher than for subsequent runs for which carbon and oxygen coverages have stabilized. The TOR decreases by about 2 times between the first run and subsequent runs when the rate has stabilized (see Figure 3.2). This type of deactivation is not unprecedented in this system [34]. Uncorrected peak-to-peak intensity ratios from AES support this assertion. In Figure 3.2, TORs are plotted for several consecutive batch reactions on Pt(100), and AES peak intensity ratios for the labeled points are given in Table 3.1. Qualitatively, the rate does not track with S or Cu for the points labeled, as the difference in S_{152}/Pt_{168} and Cu_{920}/Pt_{168} intensity ratios are large before and in a few runs after cleaning, yet the rate is nearly the same.

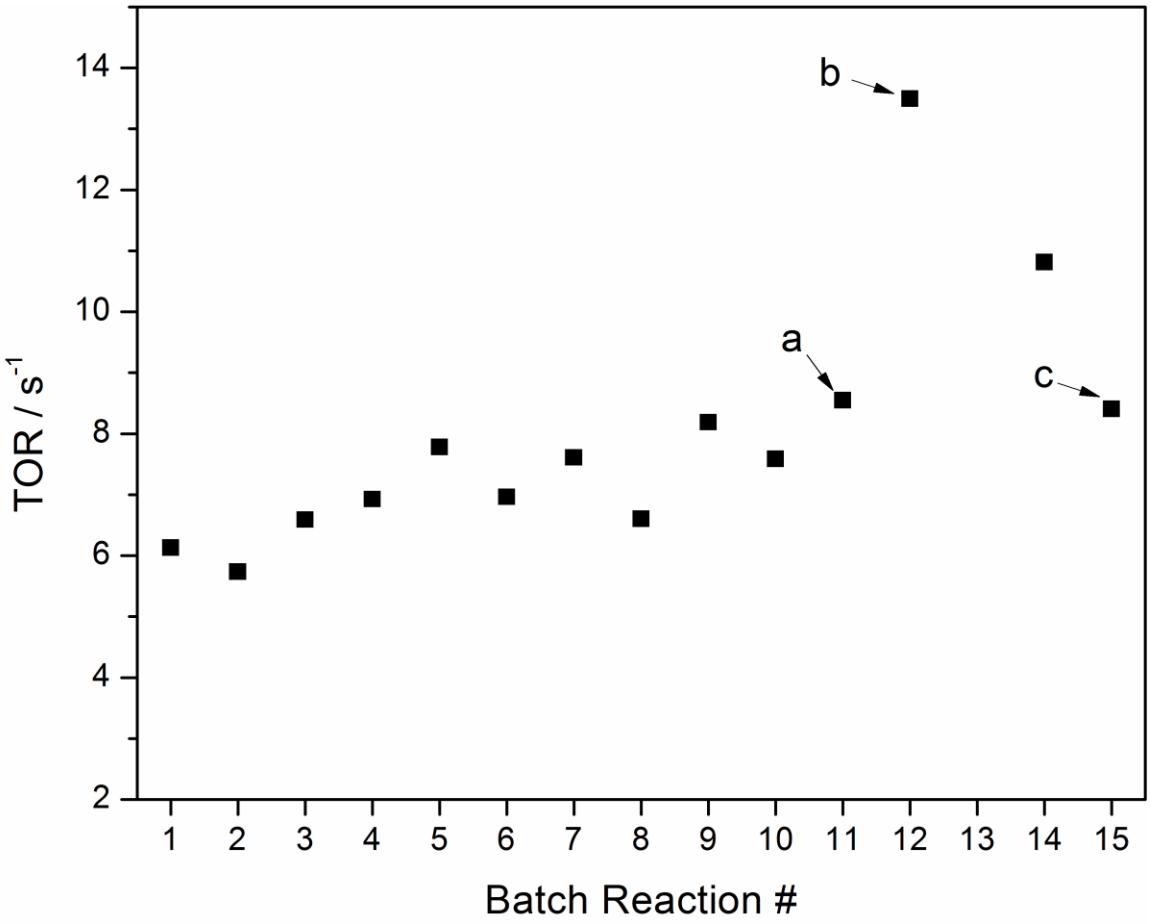

Figure 3.2 CO2 TOR for a series of consecutive batch reactions on Pt(100). The sample was cleaned by Ar+ sputtering and annealing at 1073 K at the point labeled (b). Reaction conditions were 5 Torr HCOOH, 15 Torr H2, 15 Torr CO, 800 Torr total (balance N2), T = 503.

Table 3.1 Uncorrected AES peak intensity ratios from spectra correspsonding to the labelled points in Figure 3.2.

Point	C_{272}/Pt_{168}	O_{510}/Pt_{168}	S_{152}/Pt_{168}	Cu_{920}/Pt_{168}
a	2.3	0.6	3.5	0.4
b	0.1	0.1	0.0	0.0
c	2.1	0.5	1.3	0.1

Within a run, the initial rate was stable as evidenced by a plot of CO_2 concentration versus time, shown in Figure 3.3. Numerically differentiating the data and converting to a TOR yields a slope standard error that is approximately 3 orders of magnitude smaller than the TOR, a

typical slope standard error for a plot of CO_2 concentration versus time within a run. This error, usually on the order of 0.005 s^{-1}, is negligible compared to the day-to-day and run-to-run variability in TOR (± 0.6 and ± 1.0 s^{-1} for Pt(111) and Pt(100), respectively).

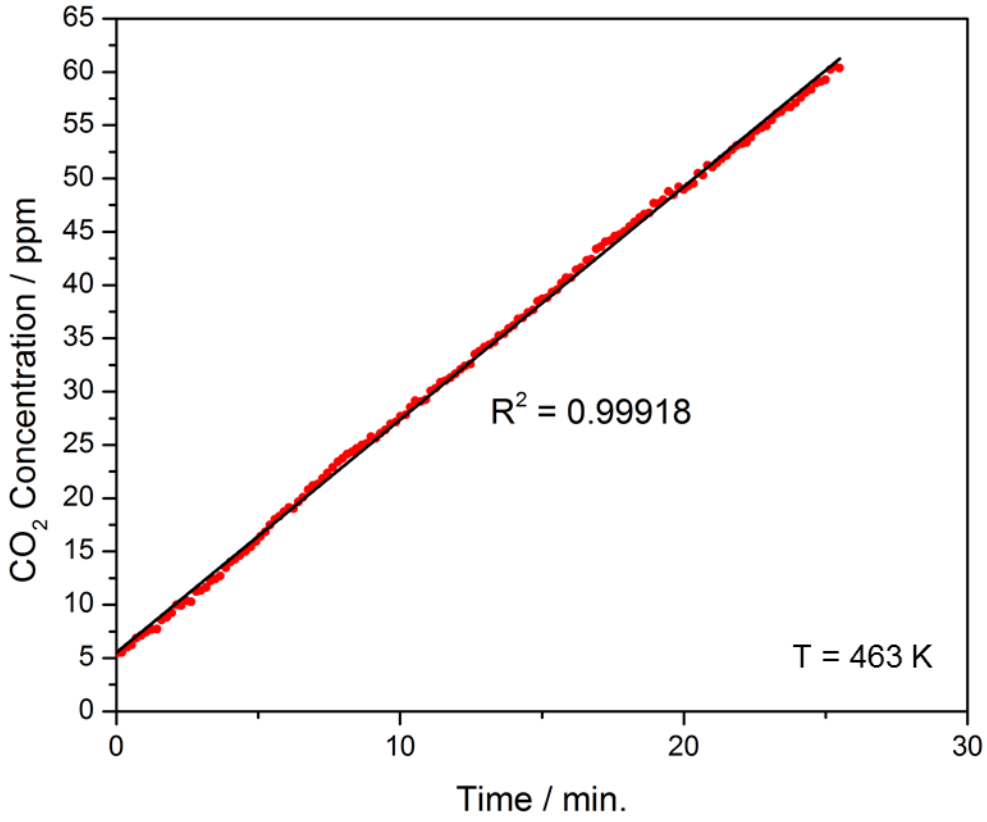

Figure 3.3 Plot of CO2 concentration versus time for a typical batch reaction.

Conversion of formic acid was kept below 10%, usually between 1-5%, for each run to ensure that the change in concentration of each gas phase species is much smaller than that species' total concentration.

3.4.4 Kinetics

As discussed above, turnover rates (TORs) for Pt(111) and Pt(100) are normalized to the calculated number of Pt atoms on ideal Pt(111) and (100)-(1x1) surfaces, equal to 1.5 x 10^{15} and 1.3 x 10^{15} atoms cm^{-2}, respectively. Normalized TORs, apparent activation energies, and reaction orders for experiments carried out at standard conditions (5 Torr FA, 15 Torr H_2, 15 Torr CO, 800 Torr total, balance N_2, T = 493 K) are summarized in Table 3.2. The error in TOR on all catalysts was large on a day-to-day basis: average TORs for Pt(111) and Pt(100) were 2.6 ± 0.6

and 3.7 ± 1.0 molecules CO_2 Pt atom^{-1} s^{-1}, respectively. The areal rate on Pt foil was measured to be (7.5 ± 5.0) x 10^{-9} moles CO_2 cm^{-2} s^{-1}, compared to (6.4 ± 1.5) x 10^{-9} and (8.1 ± 2.2) x 10^{-9} for Pt(111) and (100), respectively.

Table 3.2 Kinetic parameters for formic acid decompositon at standard reaction condtions (5 Torr HCOOH, 15 Torr H2, 15 Torr CO, 800 Torr total, balance N2, T = 493 K). * The TOR on Pt foil assumes an atomic surface density of 1.5x1015 atoms cm-2.

			Reaction Orders				
Catalyst	TOR at 493 K/ s^{-1}	E_{app} / kJ mol^{-1}	HCOOH	CO	H_2	H_2O	CO_2
Pt(111)	2.6 ± 0.6	102 ± 14	0.43 ± 0.03	-0.40 ± 0.03	~0	~0	~0
Pt(100)	3.7 ± 1.0	86 ± 11	0.35 ± 0.10	-0.35 ± 0.03	~0	~0	-
Pt Foil	3 ± 2*	94 ± 12	0.35 ± 0.15	-0.43 ± 0.05	~0	-	-

Table 3.3 Kinetic parameters for formic acid decomposition with low initial CO concentrations. Standard conditions were 5 Torr HCOOH, 2-15 Torr H2, 2 Torr CO, 800 Torr total (balance N2), T= 463 K. * Error is the standard error of the slope for a single order exper

Catalyst	TOR at 463 K/ s^{-1}	E_{app} / kJ mol^{-1}	HCOOH Order	CO Order	H_2 Order
Pt(111)	2.3 ± 0.8	67 ± 11	0.55 ± 0.9*	~0	~0
Pt(100)	2.4 ± 1.0	65 ± 7	(not collected)	~0	~0

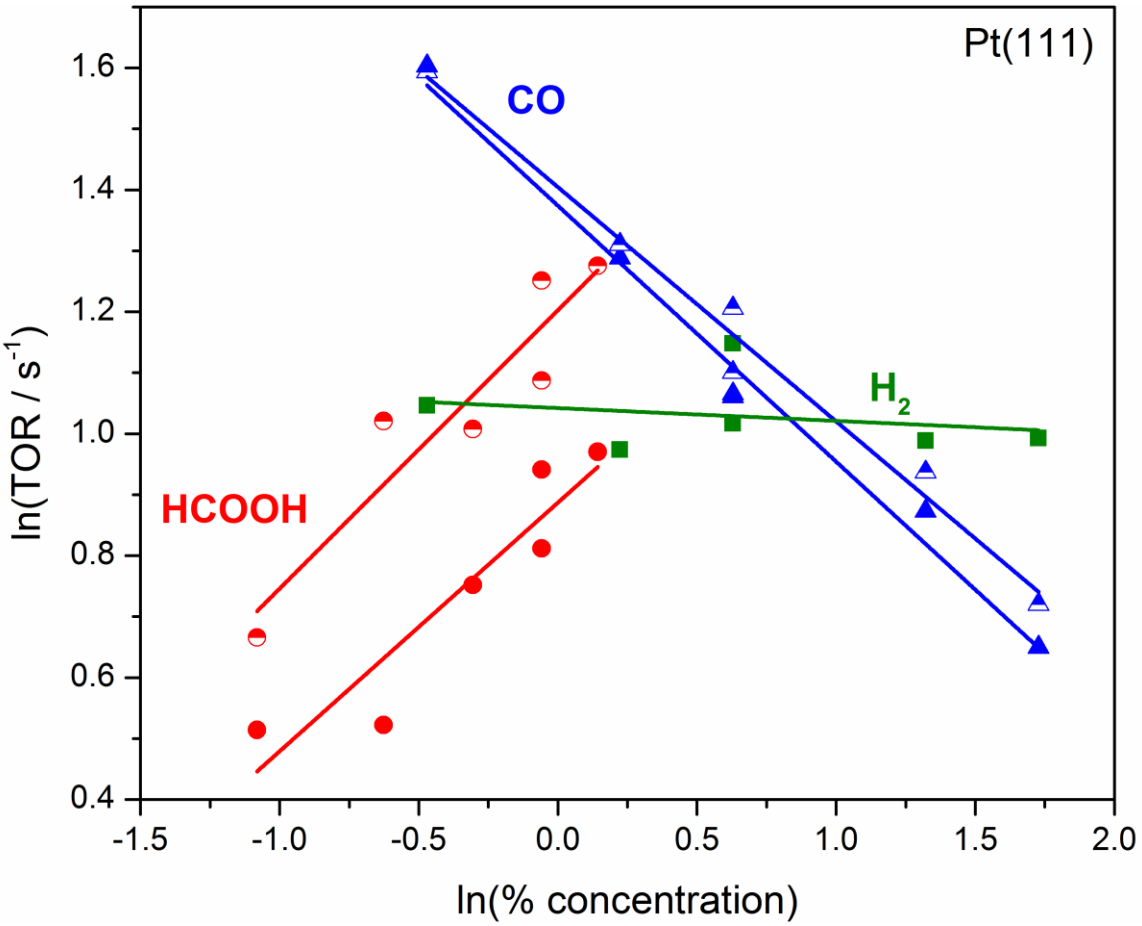

Figure 3.4 Top: Arrhenius plots for formic acid decomposition on Pt(111). Conditions: 5 Torr HCOOH, 15 Torr H2, 15 Torr CO, 800 Torr total (balance N2). Bottom: HCOOH, CO, and H2 reaction order plots on Pt(111) at T = 493 K.

Figure 3.4 continued

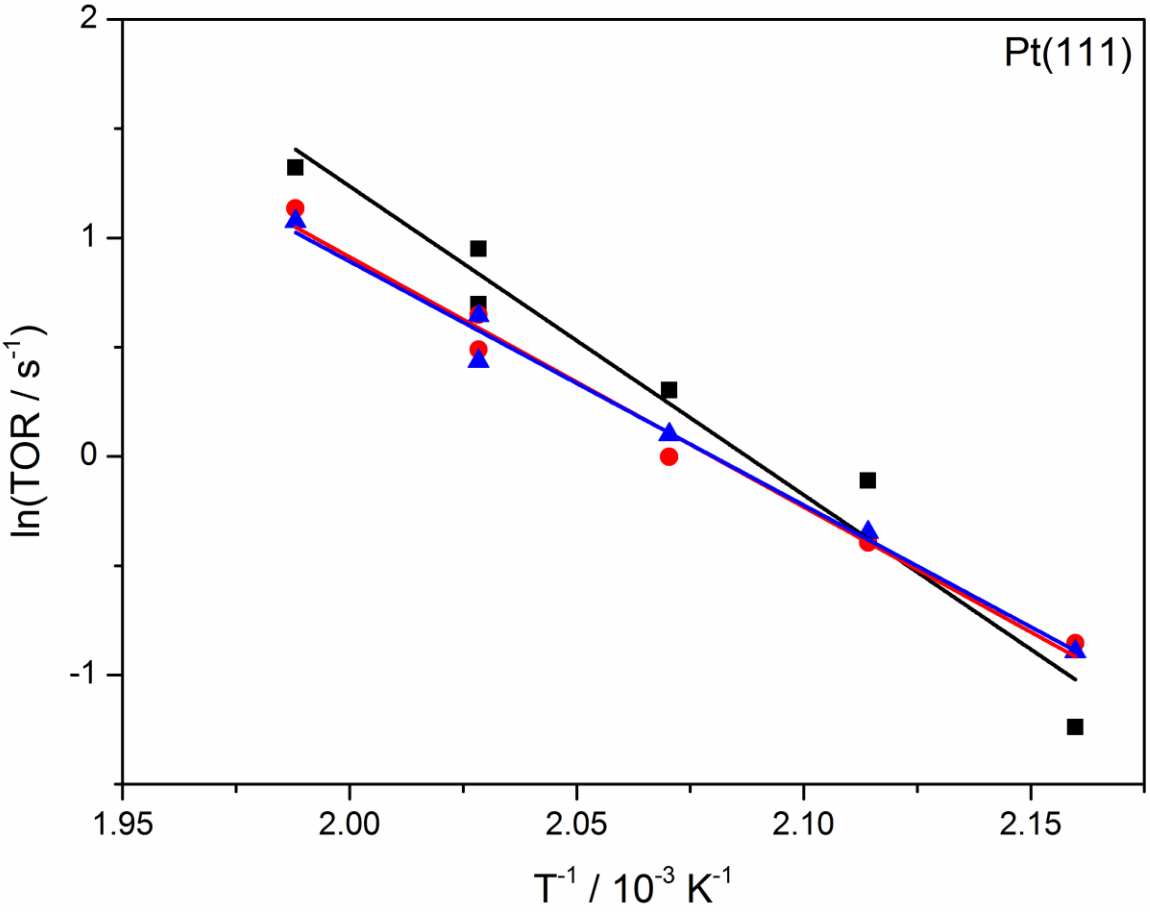

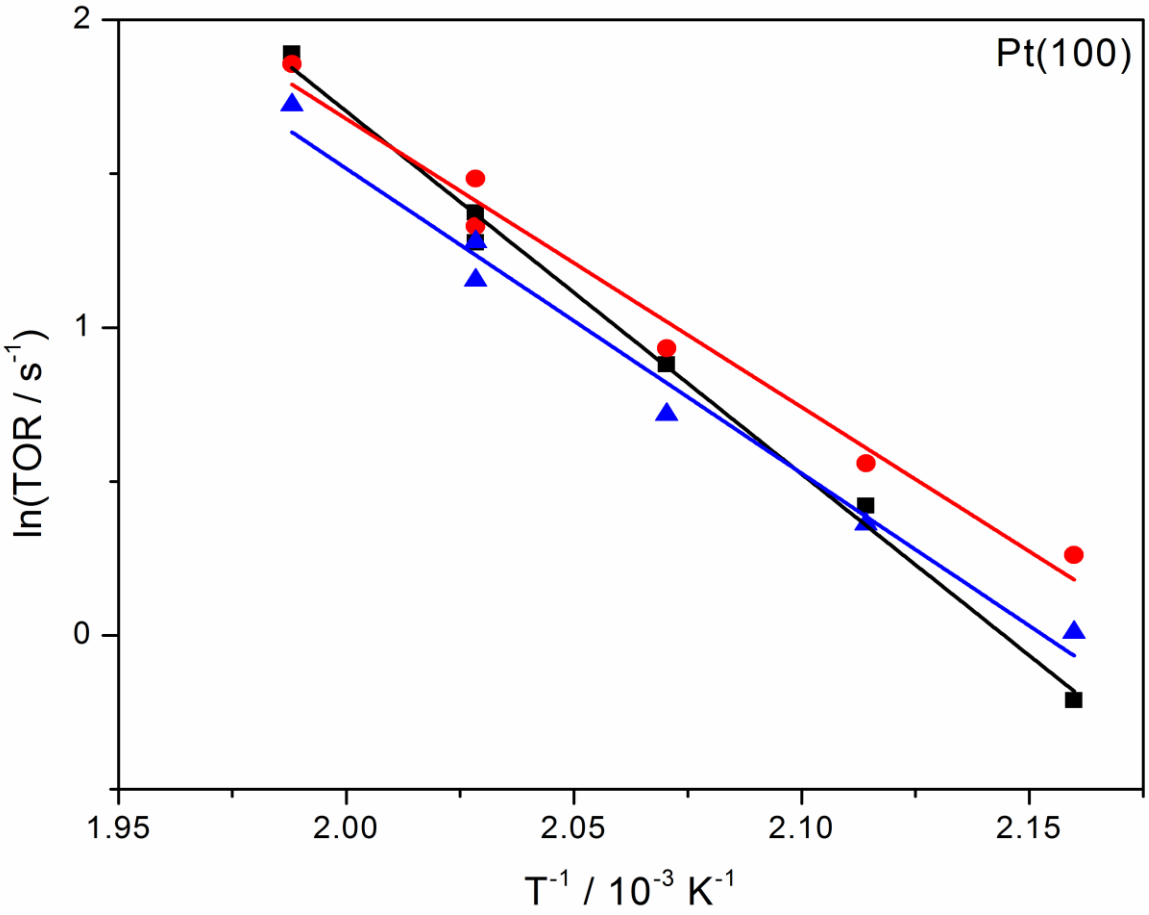

Figure 3.5 Top: Arrhenius plots for formic acid decomposition on Pt(100). Conditions: 5 Torr HCOOH, 15 Torr H2, 15 Torr CO, 800 Torr total (balance N2). Bottom: HCOOH, CO, and H2 reaction order plots on Pt(100) at T = 493 K.

Figure 3.5 continued

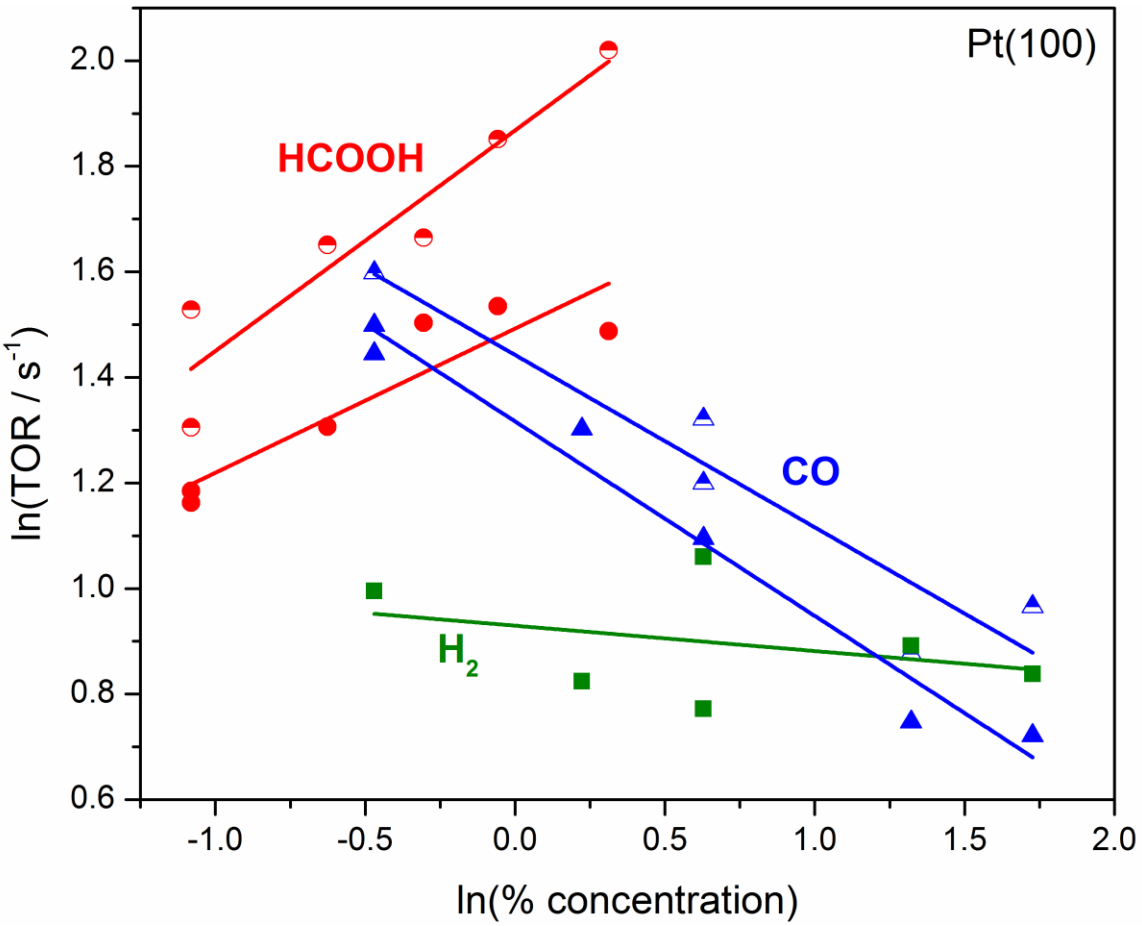

Average apparent activation energies, E_{app}, at standard conditions were 86 ± 11, 102 ± 14, and 94 ± 12 kJ mol^{-1} for Pt(100), (111), and foil, respectively, where the error is one standard deviation of E_{app} values calculated between runs. Runs used to calculate the average values of E_{app} at standard conditions are shown in Figure 3.4 and Figure 3.5 for Pt(111) and Pt(100), respectively.

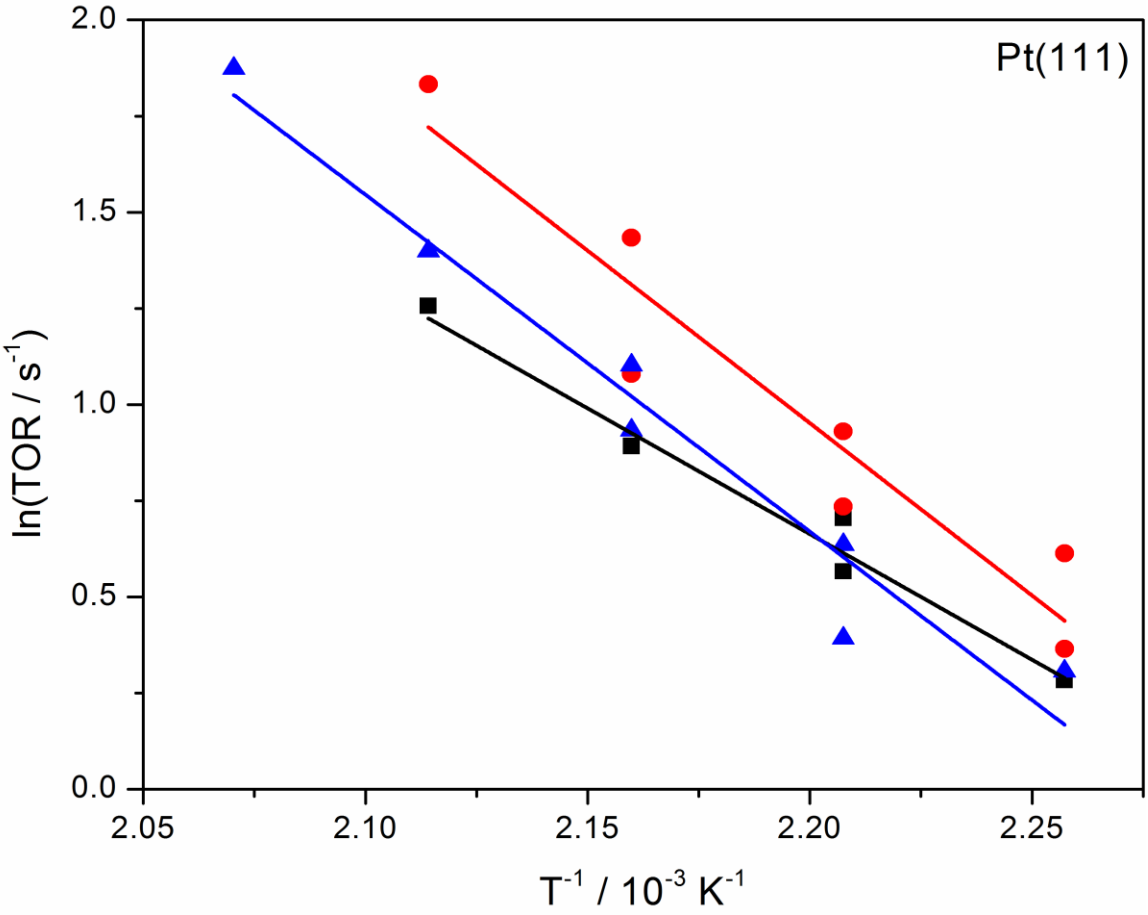

Figure 3.6 Apparent activation energies and CO reaction orders collected on Pt(111) and Pt(100) for low initial CO concentrations. Top: Arrhenius plots for formic acid decomposition on Pt(111). Conditions: 5 Torr HCOOH, 2 Torr H2, 2 Torr CO, 800 Torr total (balance N_2). Center: Arrhenius plots for formic acid decomposition on Pt(100). Conditions: 5 Torr HCOOH, 2-15 Torr H_2, 2 Torr CO, 800 Torr total (balance N_2). Bottom: CO Orders collected on both Pt(111) and Pt(100). Conditions were 5 Torr HCOOH, 2 Torr H_2, 800 Torr total, T = 463 K unless otherwise noted.

Figure 3.6 continued

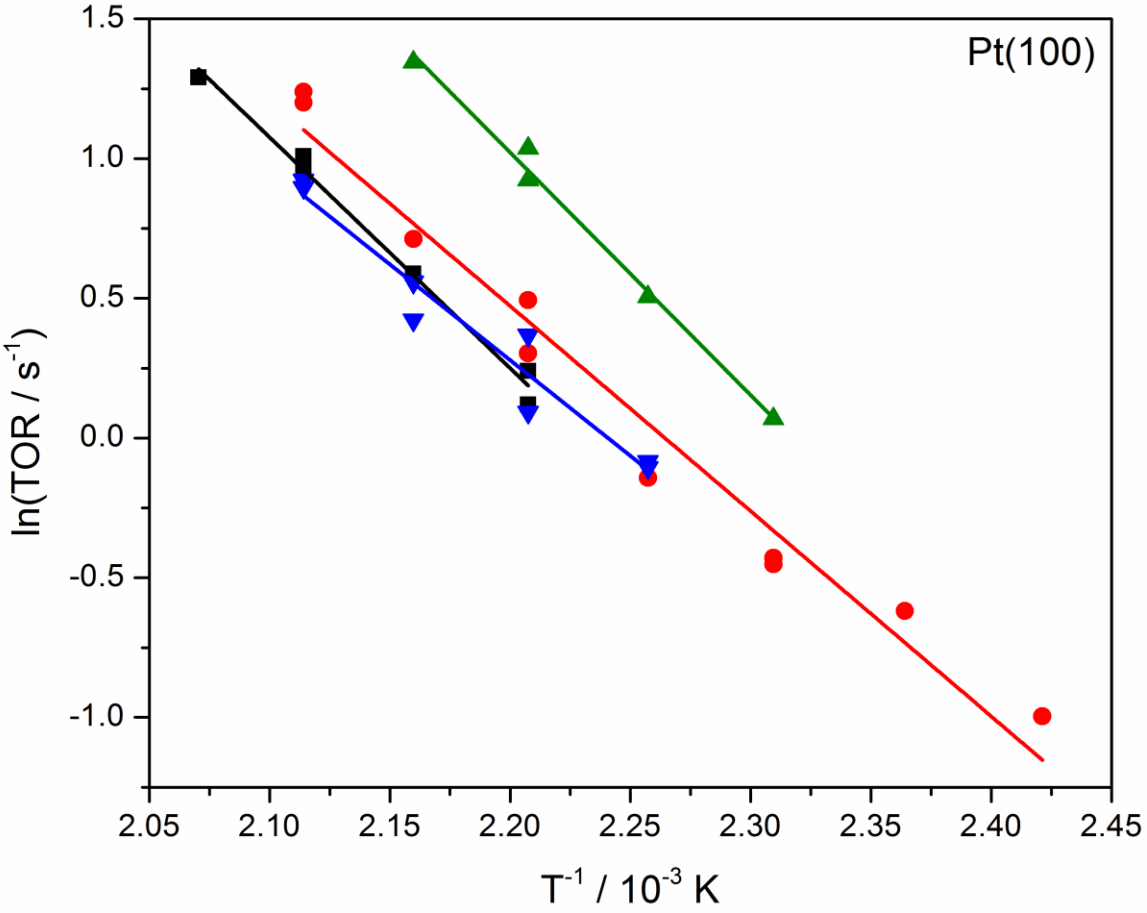

Figure 3.6 continued

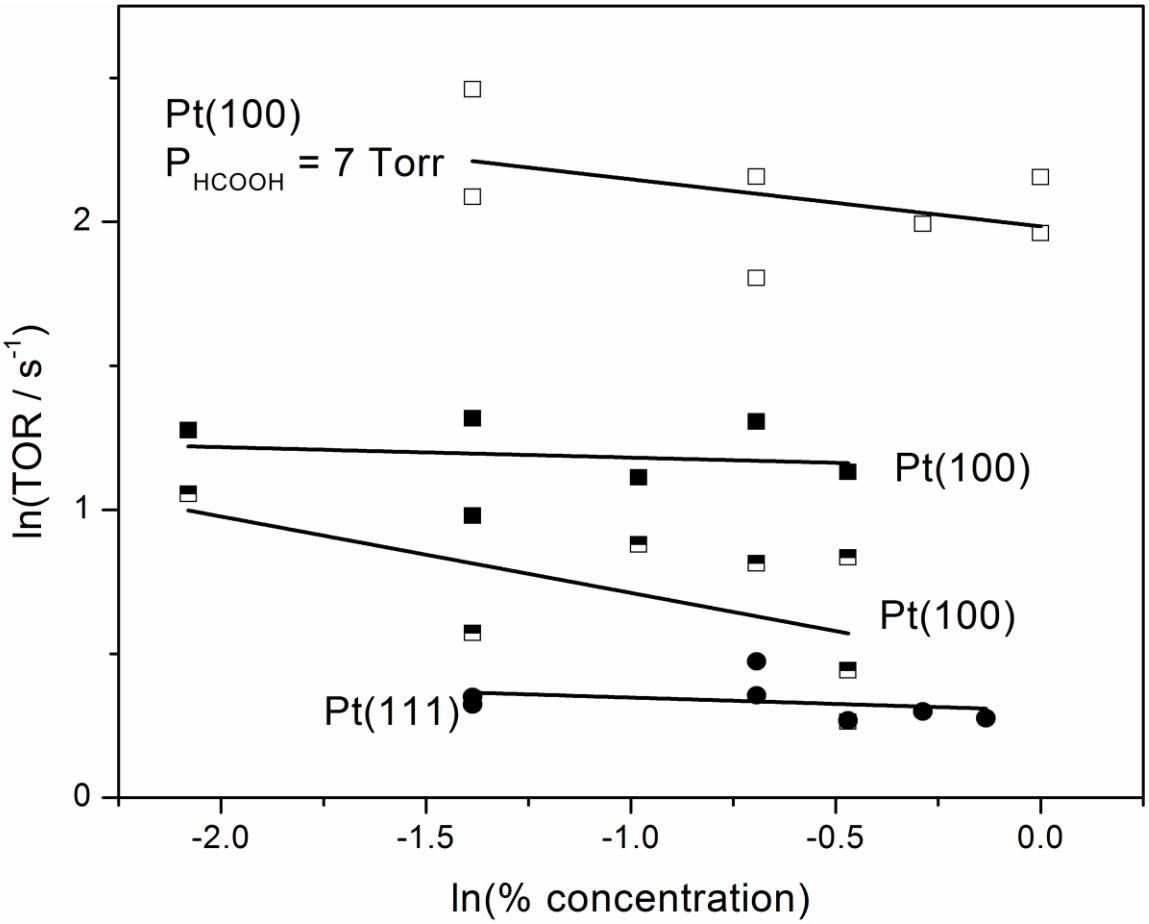

The average formic acid reaction orders were 0.35 ± 0.10, 0.43 ± 0.03, and 0.35 ± 0.15 for Pt(100), Pt(111), and Pt foil, respectively. These orders are reported with respect to the effective formic acid monomer concentration, which, as discussed earlier, is calculated by addition of the monomer concentration predicted by Equation 1 to two times the dimer concentration predicted by Equation 1. Errors reported for reaction orders represent one standard deviation between runs. Measured CO orders were -0.35 ± 0.03, -0.40 ± 0.03, and -0.43 ± 0.05 on the same surfaces, and H_2 was approximately zero order on all surfaces. H_2O was found to be zero order on Pt(100) and Pt(111), and CO_2 was zero order on Pt(100) using initial CO_2 concentrations less than 200 ppm. Typical reaction order plots for HCOOH, CO, and H_2 on Pt(111) and Pt(100) are given in Figure 3.4 and Figure 3.5, respectively.

3.4.5 Characterization with XPS

UHV-XPS was used in an attempt to identify surface species left after a reaction and to check the oxidation state of the Pt substrate. The spectra showed that only C and O species were left after a reaction, in addition to the Cu and S contaminants described above. The Pt $4f_{7/2}$ line had a BE of 70.9 eV before and after reaction and was assigned to metallic Pt [42], indicating that the Pt oxidation state was unchanged during reaction. In the C 1s region, it was not possible to differentiate C from formic acid contamination in the background and C left from the reaction. On all surfaces, a peak at about 284.3 eV was observed before and after reaction, assigned to isolated C, chain carbon, or graphitic carbon, which have been reported to produce C 1s BEs of 283.8, 284.1, and 284.8 eV, respectively [43]. After some runs, another peak at around 286 eV was observed, but it was unclear if this peak, assigned to CO-containing species, was left from a true reaction intermediate or re-adsorption of residual gases during transfer of the single crystal. Other than observing accumulation of C and O during the first reaction after cleaning, XPS did not provide additional clues regarding the formic acid decomposition pathway.

3.5 Discussion

Measured apparent activation energies for FA:CO concentration ratios < 1 (CO partial pressure = 15 Torr) on the Pt surfaces tested range from 86 ± 11 kJ mol^{-1} for Pt(100) to 102 ± 14 kJ mol^{-1} on Pt(111), with Pt foil having an intermediate activation energy of 94 ± 12 kJ mol^{-1} under the standard conditions used in this study. In all cases, these activation energies are higher than those reported in the literature for other kinetic studies on Pt-containing catalysts for formic acid decomposition. Reported values range between 41-72 kJ mol^{-1} [6, 7, 44, 45]. However, when the initial CO partial pressure was decreased to 2 Torr from 15 Torr, the measured apparent activation energies on Pt(111) and Pt(100) dropped to 67 ± 11 and 65 ± 7 kJ mol^{-1}, respectively, which fall within the range of reported literature values. Furthermore, fractional positive formic acid order values measured in this study are in agreement with a fractional positive order reported for formic acid partial pressures of less than ~15 Torr on Pt/Al_2O_3 [6].

Direct comparison of TORs measured in this study to those published for supported Pt catalysts is not possible due to differences in reaction conditions. Nevertheless, some comparisons can be made. Ojeda et al. found that for Pt/Al_2O_3, the TOR decreases with

increasing particle size. The turnover rate at their largest particle size, 8 nm, is approximately 1.2 x 10^{-2} molecules HCOOH decomposed per surface metal atom per second at 353 K (30 Torr HCOOH). Extrapolating to 463 K using their measured E_{app} of 72 kJ mol^{-1} measured over the range ~343--383 K yields a TOR of 4.1 s^{-1}. Extrapolating the TOR measured by Solymosi at 423 K on Pt/C to 463 K yields a TOR of 2.1 s^{-1} using their reported E_{app} of 70.7 kJ mol^{-1}, measured in the range 380—425 K in ~38—46 Torr formic acid. For comparison, the average TORs on Pt(111) and Pt(100) for 2 Torr initial CO partial pressure in 800 Torr total pressure at 463 K are 2.3 ± 0.8 and 2.4 ± 1.0 s^{-1}, respectively, but these TORs were collected in the fractional formic acid order regime whereas the studies above measured kinetics in the zero order regime. Extrapolation to the zero-order regime was not performed.

The goal of this work is not to present a comprehensive review of possible mechanistic routes for formic acid decomposition on Pt. Nevertheless, simple mechanisms were examined to determine the consistency of our data and that in the literature with reasonable assumptions regarding the kinetics of the reaction. Elementary steps include dissociative adsorption of formic acid as formate (HCOO·S; S = site) and a hydrogen atom (H·S), as observed in UHV experiments on Pt(111) [46, 47] and Pt(110) [48], formate dissociation to gaseous CO_2 and another bound hydrogen atom, and finally hydrogen recombination. The literature supports this mechanism by showing that C-H cleavage of the formate hydrogen is kinetically relevant and hydrogen recombination is semi-equilibrated on Pt/Al_2O_3 [6]. A CO adsorption-desorption step was also added. The elementary steps for a single-site formate dissociation step are shown in Equations 3-6:

$$HCOOH + 2 \cdot S \overset{K_1}{\leftrightarrow} HCOO \cdot S + H \cdot S \tag{3}$$

$$HCOO \cdot S \overset{k_2}{\rightarrow} CO_2 + H \cdot S \tag{4}$$

$$2H \cdot S \overset{K_3}{\leftrightarrow} H_2 + 2S \tag{5}$$

$$CO + S \overset{K_4}{\leftrightarrow} CO \cdot S \tag{6}$$

This mechanism yields the rate equation found in Equation 7, and its derivation can be found in the supporting information:

$$rate = \frac{LK_1k_2K_3^{1/2}[HCOOH]}{[H_2]^{1/2}\left(1 + \frac{K_1K_3^{1/2}[HCOOH]}{[H_2]^{1/2}} + \frac{[H_2]^{1/2}}{K_3^{1/2}} + K_4[CO]\right)} \quad (7)$$

Where L is the total number of sites.

This mechanism explains the various reaction order regimes. First, the fractional to zero-order regime transition for formic acid is satisfied, as this mechanism predicts that the formic acid order, n_{HCOOH}, is a function of formate coverage ($n_{HCOOH} = 1 - \theta_{HCOO}$), assuming that higher formate coverages are present at higher formic acid gas phase concentrations. Second, it requires CO order, n_{CO}, to be negative and that $\theta_{CO} = |n_{CO}|$. Finally, the H_2 order (n_{H2}) must be fractional negative. While the hydrogen coverage was not conclusively observed in our experiments, it was found to be close to zero, with the slope of the hydrogen order plots being generally negative but with large standard errors (error = approximately ± 100-200% of the slope). Given that the greatest possible value of n_{H2} is -0.2 at $\theta_{H2} = 0$, we cannot rule out a fractional negative H_2 order from our experiments. Based on the measured formic acid and CO orders, this mechanism predicts steady state coverages of the two species equal to 0.6 and 0.4 ML, respectively.

A similar mechanism includes an extra site in the second elementary step for formate dissocation, with all other steps the same:

$$HCOO \cdot S + S \xrightarrow{k_2} CO_2 + H \cdot S + S \quad (8)$$

This mechanism yields the rate equation in Equation 9. Its derivation can be found in the supporting information.

$$rate = \frac{zLK_1k_2K_3^{1/2}[HCOOH]}{[H_2]^{1/2}\left(1 + \frac{K_1K_3^{1/2}[HCOOH]}{[H_2]^{1/2}} + \frac{[H_2]^{1/2}}{K_3^{1/2}} + K_4[CO]\right)^2} \quad (9)$$

Where z is the coordination number.

This mechanism also explains the phenomena described above for the single site decomposition mechanism including $n_{H2} = -0.2$ at $\theta_{H2} = 0$. Predicted θ_{HCOO} and θ_{CO} coverages are 0.3 and 0.2 ML, respectively. Since the total coverage of surface adsorbates ≥ 0.5 ML in this case, and this range is much less than for the single site mechanism, for which $\theta_{Total} = 1$ (assuming $\theta_{H2} = 0$), the dual site mechanism seems more likely, since the dehydrogenation TOR did not become zero-order in formic acid as the formic acid concentration was increased.

CO was the only possible reaction product observed to affect the rate of reaction and kinetic parameters. A drop in apparent activation energy with lower CO concentrations was observed alongside an increase in the CO order from fractional negative to zero. This behavior is explained at least qualitatively by the Temkin equation [49], which relates the apparent and real activation energies to surface species' reaction orders and enthalpies of adsorption in cases where adsorption equilibrium is reached quickly relative to the rate of surface reaction:

$$E_a = E_{app} - \sum n_i \Delta H_i \quad (10)$$

Where E_a is the true activation energy, E_{app} is the apparent activation energy, n_i is the reaction order in species i, ΔH_i is the enthalpy of adsorption of species i (negative for exothermic reactions). The enthalpy of adsorption of CO on Pt(111) with a $\theta_{CO} = 0.4$ ML, the calculated CO coverage for HCOOH:CO < 1, is approximately -113 kJ mol^{-1} [50]. In this case, the Temkin equation predicts a real activation energy of about 57 kJ mol^{-1} given the measured apparent value of 102 kJ mol^{-1} and CO order of -0.4. This is within the error of the measured E_{app} in the FA:CO > 1 regime of 67 ± 11 kJ mol^{-1}. On Pt(100)-(1 x 1), using a similar approach and assuming an enthalpy of adsorption of -140 kJ mol^{-1} (measured at 0.5 ML) [51], the Temkin equation predicts

a real activation energy of 37 kJ mol^{-1}, lower than the measured value of 65 ± 7 kJ mol^{-1}. In both cases, the calculated activation energy in the fractional negative CO order regime is lower than the measured value in the zero-order CO regime, but this may be the result of the other species present on each surface, which could the CO adsorption energy less exothermic. While the change in order of reaction in formic acid, $n_{HCOOH,}$ from the measured 0.4 here to zero order should also produce a change in apparent activation energy as stated above, the measured value is close to those reported in literature for the zero-order regime. There is no simple, reversible formic acid adsorption step in our proposed mechanisms (i. e., HCOOH + S = HCOOH · S). If, instead, the enthalpy of reaction of the first elementary step is used in place of the enthalpy of adsorption of formic acid on Pt(111), calculated to be -38.8 kJ mol^{-1} for a formate coverage of 0.375 and H_2 coverage of 0 ML, respectively [52], then the change in apparent activation energy between the two regimes is expected to be 15.5 kJ mol^{-1}. Given that the absolute value of hydrogen adsorption enthalpy decreases with increasing coverage, this value could be reduced further to about 12.7 kJ mol^{-1} at a hydrogen coverage of 0.4-0.5 ML [53]. Given the error of our experiments and activation energies reported in literature of ~70 kJ mol^{-1}, this is reasonable.

Comparison of the kinetic parameters measured on metal single crystals to those measured on highly dispersed nanoparticles on porous supports is critical, as differences in the parameters may reveal the effect of the catalyst support and/or the effect of small metal particle size. For the case of a catalyst support effect, the reaction may proceed directly on the support or at the interface between the support and active metal. In this study, measured apparent activation energies and reaction orders for runs with low initial CO concentrations are in good agreement with literature values from studies on supported catalysts where CO was not co-fed, supporting the conclusion that the previous supports used with Pt for formic acid decomposition (Al_2O_3 [6], C (Norit) [7]) did not substantially alter the reaction mechanism. In the case of small metal nanoparticles, under-coordinated corner or perimeter atoms on nanoparticles could be responsible for the majority of catalytic activity [13], as has been shown for formic acid decomposition on Au through first principles calculations [54, 55]. Ojeda et al. demonstrated that smaller Pt nanoparticles have a higher TOR than larger nanoparticles [6]. Abbas and Madix, on the other hand, have previously attributed defect sites on Pt(111) to dehydration activity using temperature programmed experiments [56]. Given that selectivity toward dehydrogenation is > 98% [6, 7] (> 99% in this work when CO was not co-fed), consistency with the work of Abbas

and Madix would suggest that the smaller Pt nanoparticles used by Ojeda et al. demonstrate superior TORs due to intrinsic electronic effects of smaller nanoparticles, not necessarily because of their most under-coordinated sites (corners, edges). The most under-coordinated sites are likely blocked by CO, either co-fed or produced in the reaction at defect sites but slow to desorb since CO adsorbs more strongly on under-coordinated Pt atoms [57]. At high CO concentrations, CO can also block terrace sites, resulting in the reduction of the dehydrogenation TOR, but at low CO concentrations the effect is negligible, hence the near-zero CO order at CO partial pressures of 2 Torr. In this work, defect sites are also likely to be covered by other contaminants discussed above.

3.6 Conclusions

Formic acid dehydrogenation is not sensitive to the structure of Pt single crystal or foil catalysts tested within the precision of the measurements based on the TORs on Pt(111), Pt(100), and Pt foil at the reaction conditions used. Apparent activation energies for formic acid dehydrogenation measured on Pt(111) and Pt(100) in an initial CO partial pressure of 2 Torr at 800 Torr total pressure around 493 K are in agreement with those obtained from the literature on other Pt catalysts. CO, when included at partial pressures > 2 Torr in the initial reaction gas mixture, was shown to decrease the formic acid TOR on all surfaces, behavior explained qualitatively by the Temkin equation. The results suggest that supports used previously for Pt catalysts (Al_2O_3 [6] and C Norit [7]) do not affect the reaction mechanism, and that under-coordinated sites could be poisoned by CO, which binds strongly to such sites.

CHAPTER 4. PROMOTION OF METHANE AND METHANOL REFORMING ON PD SURFACES BY CVD-PREPARED SUB-NANOMETER ZR CLUSTERS

4.1 Abstract

An inverse Pd-Zr model catalyst was prepared by chemical vapor deposition (CVD) using zirconium-t-butoxide (ZTB) as an organometallic precursor. Pd-Zr interaction was then investigated with focus on the correlation of reforming performance with the oxidation state of Zr. As test reactions, dry reforming of methane (DRM) and methanol steam reforming (MSR) were chosen. Depending on treatments, either ZrO_xH_y or ZrO_2 overlayers or Zr as sub-nanometer cluster could be obtained. Following the adsorption of ZTB on Pd(111), a partially hydroxylated Zr^{4+}-containing layer was formed, which can be reduced to metallic Zr by thermal annealing in ultrahigh vacuum, leading to redox-active Zr^0 sub-nanometer clusters. Complementary density functional theoretical (DFT) calculations showed that a single layer of ZrO_2 on Pd(111) can be more easily reduced toward the metallic state than a double- and triple layer. Also, the initial and resulting layer compositions greatly depend on gas environment. The better the background pressure, the faster and more complete the reduction of Zr on Pd takes place. Dry reforming of methane is effectively promoted if these initially metallic Zr species are present in the pre-catalyst, leading to a Pd/ZrO_xH_y phase boundary by oxidative activation under reaction conditions. These reaction-induced active sites for DRM are stable with respect to carbon blocking or coking. Under methanol steam reforming conditions, water activation by hydroxylation of Zr occurs. In excess of methanol, strong coking is induced by the Pd/ZrO_xH_y interface.

4.2 Introduction

ZrO_2 is commonly regarded as a highly stable, “irreducible” refractory oxide. Nevertheless, it is currently under investigation to expand its applicability as a catalyst for selective aldehyde oxidation [58]. Regarding CO hydrogenation, the roles of different zirconia polymorphs in the synthesis of higher alcohols were studied both over pure and Pd- or Li-modified ZrO_2 [59]. It has also been shown to promote catalysts for methanol reforming

processes[60]. In this context, it has been successfully applied as a stabilizing support to prevent CuO_x nanoparticles from sintering, and therefore enhances the stability of methanol steam reforming catalysts[61]. Zr^{4+} ions have also been reported to play an important role as dopants in an Au/CeO_2 catalyst for CO oxidation[62] and in sol-gel-synthesized photocatalysts[63]. Interest in the chemical properties of ZrO_2 polymorphs also arises from its application as YSZ (yttrium-stabilized zirconium oxide), the standard electrolyte for solid oxide fuel cells, due to its electric insulation properties and permeability for O^{2-} ions [64].

Atomic layer deposition (ALD), or in its general form chemical vapor deposition (CVD), has been already successfully applied for ZrO_2. There are many precursor/oxidative agent pairs known to generate ZrO_2 layers[65], with the main application as protection/coating layers. Applications beyond catalysis can also be found in microelectronics, where ALD-prepared ZrO_2 was used on SiO_2 as an additional insulation layer[66]. The synthesis of metallic Zr via the ALD/CVD pathway from metal-organic precursors to form, by sophisticated activation, nanoparticles for catalysis, has - to our knowledge - not been documented sufficiently. Due to the very high formation enthalpy of ZrO_2, special preparation techniques for metallic Zr have been developed[67], with the aim to control problems of partial oxidation induced by the strong "getter" effect of Zr^0. Therefore, CVD from zirconium-tert-butoxide (ZTB) was chosen in the present study as an easily applicable, reliable and effective way to prepare ZrO_xH_y-overlayers on Pd. The as-prepared CVD layers are not metallic, but contain partially oxidized and partially hydroxylated Zr^{+4} species, which nevertheless, can be easily reduced on Pd to Zr^0 by means of an UHV-based post-treatment. Our own interest in Zr^0-based pre-catalysts arises from the fact that oxidative segregation on initially bimetallic surfaces under reaction conditions was recently shown to induce active and selective inverse model catalysts[68]. As they form their active/selective state under realistic reaction conditions, bimetallic pre-catalysts represent a promising approach to attain (with respect to surface area) strongly enhanced activities as compared to the related supported powder catalytic systems (prepared e.g. by conventional impregnation techniques). Enhancement of surface-specific rates can be assigned to the extremely high number of metal-oxide phase boundary sites induced by localized oxidative segregation starting from an atomically dispersed alloy or intermetallic initial state. One of these examples is the initially bimetallic Cu-Zn system[69]. Starting from a dilute Zn-in-Cu alloy, finely dispersed zinc-(hydr)oxide islands are formed *in situ*, leading to a maximum of

Cu/ZnO_xH_y phase boundary sites. Thus, an extremely active and selective "inverse" MSR catalyst is obtained. The same effect was shown for Cu-Zr[68]. Metallic Zr was sputter-prepared on a Cu substrate and was oxidized/hydroxylated under MSR conditions. The resulting phase boundary sites were found to improve CO_2-selectivity and activity in MSR significantly.

Two distinct test reactions, methanol steam reforming and dry reforming of methane were chosen to verify or disprove a co-catalytic and/or promotional function of surface-near Zr^0-dopants on Pd. MSR is an efficient way to generate CO-depleted H_2, however, issues in catalyst stability and minimized CO content of the reformate gas make it a still intensely investigated reaction[60]. Cu-based catalysts are known to be excellent to obtain high CO_2-selectivity and high reaction rates[69], but also Pd-based intermetallic systems are promising due to the methanol-activating function of Pd[70]. As a test reaction, MSR is useful to substantiate and quantify the low-temperature water activation activity of the investigated catalyst systems, because of the fact that CO_2 can only be formed via the reaction of activated methanol to formaldehyde, which further reacts with weakly bound –OH species from activated water toward CO_2.

Dry reforming of methane (DRM) is a relevant reaction for the one-step conversion of two climate-relevant greenhouse gases, CO_2 and CH_4, to useful syngas. It is performed at higher temperatures (~970 K) than MSR and does not so much rely on initial water- but rather on CO_2-activation. It is usually initiated by methane decomposition toward different carbon species. If the latter are sufficiently reactive, they can be further converted by the subsequent Boudouard reaction to CO, or else, they remain deposited as unreactive coke. However, also the inverse water-gas-shift reactivity of the catalyst may play a role[71], either as an additional intermediate process to generate water, which may be important for efficient gasification of carbon deposits, or as an unwanted side reaction reducing the H_2 yield. Transition metals such as Co, Ni, Ru, Rh, Ir and Pt on alumina and silica supports[72] have been reported as efficient DRM catalysts. Ceria as a support for Ni and Co was also applied[73], but also mixed ceria and zirconia supports[74]. Clean Pd is known for its pronounced methane- but simultaneously quite poor CO_2-activation ability. Therefore, DRM was chosen as a reference reaction to investigate the promotion of CO_2 activation on a Pd/Zr inverse model catalyst, in order to highlight the role of the initial Zr^0 nanoclusters for enhanced CO_2 activation.

The main goal of this inverse model catalyst study is therefore to highlight the co-catalytic/promotional role of redox-active Zr surface species on Pd beyond the simple function of zirconia as a structurally stabilizing catalyst support. As will be shown in the following, single Zr^0 atom clusters of 2-6 atoms adsorbed on Pd can be oxidized, reduced or hydroxylated reversibly at comparably low temperatures around 723 K. Beyond the redox properties, electronic structure nano-effects of small particles and surface islands have also been described for other elements, i.e. gold on TiO_2[75, 76] which may alter the catalytic properties dramatically. Zr, in its nanostructured highly redox-active surface-adsorbed state, is therefore investigated to be part of the redox active cycle and to open new reaction pathways.

4.3 Experimental and Computational Methods

Depending on the experiment requirements, the research was performed using mainly three experimental set-ups: An Omicron Surface Analysis Cluster (Birck Nanotechnology Center at Purdue University), an UHV-chamber with attached high-pressure recirculating batch reactor, and the Innovative Station for in situ Spectroscopy (Beamline ISISS at BESSY II synchrotron in Berlin).

4.3.1 Omicron Setup

The Omicron Surface Analysis Cluster consisted of a UHV preparation chamber and an analysis chamber with base pressures of 1×10^{-9} mbar and 5×10^{-11} mbar, respectively. A sample can be transferred between these chambers under UHV. The preparation chamber was equipped with a mass spectrometer, an Ar^+ sputtering gun, a gas manifold system, and resistive sample heating. The analysis chamber was equipped with X-ray Photoelectron Spectroscopy (XPS) (the electron energy analyzer - Omicron EAC 125 and the analyzer controller - Omicron EAC 2000), Low Energy Electron Diffraction (LEED) (Omicron), High Resolution Electron Energy Loss Spectroscopy (HREELS) (ELS5000, LK Technologies), Scanning Tunneling Microscopy (STM) (Omicron ambient temperature UHV STM/AFM), and resistive sample heating. XPS data were acquired using a non-monochromatic Mg Kα X-ray source ($h\nu$ = 1253.6 eV) at 150 W. High resolution spectra were recorded at the constant pass energy of 20 eV. Photoelectrons were ejected at a 45° angle with respect to the surface normal.

The Pd(111) single crystal (orientation accuracy <0.1°, Princeton Scientific) was cleaned by several cycles of Ar^+-sputtering (1 kV , 2µA sample ground current) and annealing to 900 - 1000 K until no contaminations could be detected by XPS, STM and LEED. Well-ordered monoatomic steps were seen in STM.

Zirconium (IV) tert-butoxide $Zr(O\text{-}t\text{-}C_4H_9)_4$ (Strem, purity: 99%) was used as ALD/CVD precursor and filled into an cylinder under Ar. Prior to dosing ZTB, several cycles of freeze-pump-thaw were performed for purification (cooling temperature: 223 K, freezing point ZTB: 269 K). ZTB has a sufficient vapor pressure at room temperature to dose it through a leak-valve. Before sample exposure, the preparation chamber was exposed to the precursor at 5×10^{-7} mbar for 5 minutes to passivate the chamber walls against precursor decomposition. The exposure was calculated from uncorrected ion gauge measurements in Langmuir, (1 L = 1 × 10^{-6} Torr s) and exposure pressure was in the range of 5×10^{-8} to 5×10^{-6} mbar. The adsorbate coverage was determined from XPS data; the details can be found in the XPS experimental section or additionally in refs.[77-80]. Due to the potential impact of radiation of the X-ray source to the sample topography/chemistry, STM studies were always done before XPS characterization. Sample heating was performed in the analysis chamber.

4.3.2 UHV-chamber with attached high pressure reactor

Sample preparation and characterization was performed in a combined preparation/analysis chamber with attached reaction cell, described in more detail elsewhere (base pressure in the low 10^{-9} mbar range)[81]. The sample is heated via a home-built e-bombardment setup. Electrons are ejected from a triple-filament emitter (operated with 30 W heating power) set to -500 V, while the sample is set to +300 V. The electron impact heating power is then controlled via the filament emission current. For spectroscopic analysis, the chamber is equipped with a hemispherical electron and ion analyzer (Thermo Fisher Electron Alpha 110), a double anode X-ray gun (Mg/Al, XR 50, Specs) for XPS, an ion gun (Omicron 100) sufficient to produce 1 kV He^+ Ions for ISS and an electron beam gun (KPI EGPS-2017B) for Auger electron spectroscopy. Additionally, a mass spectrometer (Balzers) for residual gas analysis and an Ar^+ ion sputter gun for sample cleaning is attached. A three way gas inlet allows to dose O_2 (Messer, 5.0), H_2 (Messer 5.0) or O_2 cleaned Ar (Messer 5.0) via leak valves into the chamber. All XPS spectra in this chamber where recorded with a non-monochromatic Mg Kα X-

ray source (hν = 1253.6 eV) at 250 W and the magic angle to the analyzer. For XPS the analyzer was operated using a constant pass energy of 20 eV.

All catalytic experiments were performed using a 20 x 18 mm ultra-clean polycrystalline Pd foil (Goodfellow, 99.95%) with a thickness of 0.125 mm. For reference experiments on pure ZrO_2, a pre-oxidized 0.127 mm Zr foil with the same size (Alfa Aesar, purity: 99.95 %) was used. The foils were cleaned before loading to the UHV chamber in a water and an ethanol ultrasonic bath for 20 min, respectively. ZTB (Sigma Aldrich, purity. 99.999 %) was filled and mounted as described for the Omicron instrument and attached to the combined preparation/analysis chamber. ZTB exposition was performed as described in the context of the individual experiments discussed below. However, the sample was heated with electron impact heating instead of resistive heating in this setup.

In order to validate the CVD-based catalytic results and to obtain a broader experimental basis of the Pd-Zr^0 system with respect to reforming performance, also an intermetallic bulk phase of Pd and Zr^0 was prepared. The preparation was performed under HV conditions (base pressure $1x10^{-7}$ mbar) by heating small pieces of the above-specified pure Pd and Zr foil samples resistively in a Ta crucible in the nominal atomic ratio 2:1. At a temperature slightly above the melting point of Pd (1828 K), spontaneous reaction between Pd and Zr leads to an intermetallic Pd-Zr melt, which then recrystallizes toward Pd-Zr bulk phases during cooling in vacuum. Thereafter, this sample was transferred to the UHV system with attached batch reactor for analysis and catalytic testing. Note, that this sample, in comparison to the CVD-prepared ones, was exposed to air at room temperature between preparation and characterization. The nominal 2:1 Pd:Zr stoichiometry (i.e. with Pd excess) was chosen with the idea to maintain at least some active Pd metal surface coexisting with oxidatively segregated Zr species under reaction conditions. Moreover, an excess of Pd is necessary because the melting point of Zr is very high and complete intermetallic formation reaction of Pd with Zr is necessary in order to distribute the Zr^0 homogeneously in the melt. The corresponding X-ray diffraction patterns of the initial Pd-Zr sample is made up by a complex superposition of at least two different Pd-Zr intermetallic phases, including Pd_3Zr and Pd_4Zr_3, alongside a small amount of oxidized monoclinic ZrO_2. Note that this is in striking contrast to the similarly prepared Cu-Zr case[81], indicating a much less initial homogeneous melt. In due course, as will be discussed below, after the DRM reaction,

the patterns are even more complicated, indicating phase transformations and partial (oxidative) decomposition of the intermetallic Pd-Zr compounds.

For catalytic testing in the ambient pressure recirculating batch reaction cell, a long z-transfer rod allows fast and reliable transfer without exposure to air. The all-quartz-glass high-pressure (up to 1 bar) batch reactor is equipped with a gas chromatograph with either intermediate or continuous EID-MS detection to determine the exact gas composition at any point of reaction. Continuous partial pressure detection is performed via a capillary leak to the GC-MS. The quartz-glass reactor with a total circulation volume of 296 ml was designed to measure small reaction rates and selectivity patterns within a temperature range between room temperature and 1300 K. A circulation pump ensures a constant flow and gas intermixing and an attached gas-premixing unit allows to set arbitrary compositions of the attached reactant vapors or introduced gases (methanol, methane (5.0), deionized and degassed water, CO_2 (5.0), O_2 (5.0), H_2 (5.0), Ar (5.0) and He (5.0). The sample holder itself is entirely made of quartz glass to avoid background reactivity from hot metal parts and is designed for 20 mm x 18 mm metal foils.

A partial pressure of 8-30 mbar argon added to all gas mixtures allows correcting the thermal expansion due to the temperature increase and the simultaneous gas loss through the capillary leak for continuous EID-MS detection. For partial pressure calculations, all base-line-corrected MS signals were calibrated using pure substances with quantitative consideration of fragmentation. For all MSR catalytic experiments shown in this work, the following initial conditions were applied: 12 mbar methanol, 24 mbar water, 8 mbar argon, followed by adding He to a total pressure of 1 bar. After an equilibration/premixing time of 10 min, a temperature ramp of 10 K min^{-1} up to 623 K was performed, followed by an isothermal period at 623 K. For all DRM catalytic experiments shown in this work, the following initial conditions were applied: 50 mbar methane, 50 mbar CO_2, 30 mbar Ar, followed by adding He to a total pressure of 1 bar. After an equilibration/premixing time of 10 min, a temperature ramp up to 1073 K within 30 min was performed, followed by an isothermal period at 1073 K. As for a discussion about mass and heat transport limitations, we refer to a thorough discussion of the catalytic setup in ref.[82].

4.3.3 In-situ XPS setup

Synchrotron-based *in situ* XPS experiments were performed at the ISISS (Innovative Station for *in situ* Spectroscopy) beamline at the BESSY II synchrotron in Berlin, Germany. The

experimental apparatus consists of a load lock and an *in situ* cell connected to the XPS spectrometer via differential pumping stages. The experimental apparatus has been described in the literature extensively.[83] Samples were heated in the *in situ* cell via a near-infrared semiconductor laser (λ = 808 nm) from the rear. The temperature was measured by a K-type (chromel−alumel) thermocouple positioned between sample holder back plate and Pd foil. All *in situ* experiments were performed on the same Pd foil sample that was used for the model catalyst preparation in the UHV instrument with attached batch reactor.

The same ZTB cylinder/leak valve setup described above was transferred to ISISS beamline. Due to the fact that ZTB only interacts with surfaces hotter than 500 K, it was safe to dose the organometallic precursor into the analysis chamber without any Zr deposition on the components of the vacuum system or on the X-ray window. The growth of ZTB could then be followed directly via XPS.

Photon energies were chosen (via the monochromator control) to obtain a kinetic energy of the ejected photoelectrons of ~120 eV for all monitored core-level photoemission peaks in order to extract information from a constant information depth and to have the same attenuation of the photoelectrons through the gas phase. Due to the fact that 95% of the signal arises from a sample depth up to ~1 nm, this operation mode is considered to be maximum "surface sensitive".

Photoelectrons were collected in the direction normal to the surface at constant pass energy of 10 eV. Binding energies were referenced to the Fermi edge, which was measured each time the monochromator moved to a new position (i.e. whenever the incident photon energy was changed). Photoemission peak intensities were corrected for the respective photon flux at a given photon energy. Since the BESSY II synchrotron operates in top-up mode (constant ring current), no additional correction for the ring current was required. Since all photoemission peaks were collected at the same kinetic energy of photoelectrons (120 eV), the attenuation through the gas phase was the same for all-core levels and thus cancels out in coverage calculations.

4.3.4 Analysis of the XPS Data

All spectra were analyzed using the CasaXPS software program, version 2.3.16 Pre-rel 1.4 (Casa Software Ltd.)[84]. A Shirley background was applied to all spectra and the associated Scofield relative sensitivity factors were considered for quantification. For peak fitting of the Zr 3d peaks a weighted sum of Gaussian and Lorenzian peak shapes (CasaXPS line shape SGL(30))

was used. A doublet separation (Zr $3d_{5/2}$ vs. Zr $3d_{3/2}$) of 2.4 eV for both metallic Zr[85] and zirconia[86] was used for fitting. The doublet area was kept constant at 3:2 as arising from spin-orbit d-electron coupling. Electron attenuation lengths were taken from the NIST database SR 82[87] and the orbital asymmetric parameter from the ELETTRA online database of ref.[40]. The quantification of the XPS data was done in terms of atomic percentages or coverage/thickness. The atomic percentage was estimated assuming homogeneously mixed elements. Since an adlayer on the substrate surface is not a homogeneous system, the coverage/thickness should give a better representation. The ZrO_xH_y surface coverage was calculated assuming a non-attenuating adlayer on a semi-infinite substrate.[77-80] As the maximum ZrO_xH_y layer thicknesses remained in the sub-monolayer regime in this study, the influence of a potential attenuation effect of the photoelectrons by the overlayer remained negligible even for the highest exposures. This was tested by comparing the results on a ~1 ML ZrO_xH_y covered sample, using both an attenuating and non-attenuating overlayer model, which eventually showed negligible differences. Details of these calculations are given in refs. [77-80] and in the Supporting Information, Section A.

4.3.5 Density Functional Theory (DFT)

All calculations were performed with plane-wave DFT using the Vienna *ab initio* simulation package (VASP) using the projector augmented wave (PAW) method[88, 89]. To elucidate the role of the van der Waals interaction in this system, we performed VdW-DF calculations, using the optB88 functional[90, 91]. The cutoff energy for the plane wave basis set was fixed at 400 eV. Geometry optimization was performed with a conjugate-gradient algorithm and considered to be converged when the forces on each unconstrained atom was <0.01 eV/Å. A Monkhorst-Pack grid of 2 × 2 × 1 was employed due to the large unit cell. We used a $\sqrt{7} \times \sqrt{7}$ surface unit cell for Pd(111) with five layers thickness. The bottom two layers are fixed at their bulk position. On top of the Pd surface, 1 to 3 layers of a (2 × 2) cubic ZrO_2 film were adsorbed and fully optimized. The calculated lattice mismatch between each other is 1.3%. The reaction energy ΔE of deposited ZrO_2 films on the Pd surface is calculated by

$$\Delta E = [E_{total}(ZrO_2\text{-}Pd) - E_{total}(Pd^{surf}) - n_{ZrO2}E_{total}(ZrO_2{}^{bulk})]/A_{cell} \quad (1)$$

which is defined by the difference between the total energy of the compound system $[E_{total}(ZrO_2\text{-}Pd)]$ and the sum of the total energy of the clean Pd surface $[E_{total}(Pd^{surf})]$ and the

total bulk energy [E_{total} (ZrO_2^{bulk})] of as many ZrO_2 formula units as are adsorbed within a unit cell on top of the metal surface (n_{ZrO2}) divided by the area of the unit cell A_{cell}. The smaller the ΔE value, the more stable structure becomes.

The formation energy of ZrO_2 films with a different number of layers is defined by

$$\Delta E_{film} = E_{total}(ZrO_2) - n_{ZrO2}E_{total}(ZrO_2^{bulk}) \qquad (2)$$

where $E_{total}(ZrO_2)$ is the total energy of the relaxed ZrO_2 film. Here the lattice (a=b) of ZrO_2 film and the ion positions are all allowed to change. The adsorption energy of the ZrO_2 film at the Pd(111) surface is calculated by

$$\Delta E_{ads} = E_{total}(ZrO_2\text{-}Pd) - E_{total}(Pd^{surf}) - E_{total}(ZrO_2). \qquad (3)$$

From Eqs. (1)-(3), it can be seen that $\Delta E = (\Delta E_{film} + \Delta E_{ads})/A$.

The temperature- and pressure-dependent terms of condensed phases are small and tend to be neglected in the free energy calculation. The differences between the chemical potentials can be approximated by the difference between their calculated DFT electronic energies (E_{total}). For the gas phase, we have to add the thermal contributions from the translational, rotational and vibrational enthalpies and entropies.[87] By this definition, the reaction energy ΔG_{diss} for oxygen dissolution into Pd sub-layer and ΔG_{diff} for oxygen diffusion to the available bare Pd(111) surface are not affected by the reaction temperature and pressure, and will be equal to the reaction energy at 0 K.

The reaction energy ΔG_{diss} for oxygen dissolution into Pd sub-layer is calculated by

$$\Delta G_{diss} = E_{total}(ZrO_2\text{-}O\text{-}Pd) - E_{total}(ZrO_2\text{-}Pd). \qquad (4)$$

$E_{total}(ZrO_2\text{-}O\text{-}Pd)$ is the total energy of ZrO_2-Pd system with one oxygen dissolving into the Pd sub-layer. The reaction energy ΔG_{diff} for oxygen diffusion to the available neighboring bare Pd(111) surface is then calculated by

$$\Delta G_{diff} = E_{total}[(ZrO_2)_{Ovacany}\text{-}Pd] + E_{total}(O\text{-}Pd) - E_{total}(ZrO_2\text{-}Pd) - E_{total}(Pd^{surf}). \qquad (5)$$

$E_{total}[(ZrO_2)_{Ovacany}\text{-}Pd]$ is the total energy of the compound ZrO_2-Pd system with one oxygen vacancy at the ZrO_2 film. $E_{total}(O\text{-}Pd)$ is the total energy of the Pd(111) surface with one adsorbed oxygen atom. All the Pd surfaces here have the same surface area. While for the production of O_2 in the gas phase, the reaction Gibbs free energy ΔG_{O2} is calculated by

$$\Delta G_{O2} = \Delta E_0 + 0.5G(T) \qquad (6)$$

where

$$\Delta E_0 = E_{total}[(ZrO_2)_{Ovacany}\text{-}Pd] + 0.5\, E_{total}(O_2) - E_{total}(ZrO_2\text{-}Pd). \quad (7)$$

Here, ΔE_0 is the reaction energy at 0 K including the zero-point energy evaluating from the difference of the electronic energies between the products and the reactants and $G(T)$ is the free energy of O_2 in the gas phase under the experimental reaction temperature and pressure. $E_{total}[(ZrO_2)_{Ovacany}\text{-}Pd]$ is the total energy of the compound ZrO_2-Pd system with one oxygen vacancy at the ZrO_2 film.

4.4 Results

4.4.1 ZTB adsorption on palladium surfaces and ALD/CVD window

Following ZTB exposure of Pd(111) at room temperature, only a small amount of zirconium was detected by XPS and only when Pd(111) was pre-treated with oxygen prior to ZTB exposure. The coverage of the as-deposited ZrO_xH_y was estimated to be in the range of 10^{-2} ML following high exposures of ~2000 L. In order to increase the ZrO_xH_y coverage, we explored an ALD-like approach: multi-cycles of ZTB exposure followed by annealing in UHV. ZTB exposure was performed at room temperature (the first half of ALD cycle) and annealing in UHV was done at 673 K (the second half of ALD cycle, no co-reactant). As shown in Figure 4.1 (panel A), this approach did not help to grow more Zr: no increase of the Zr amount was observed with number of cycles. Carbon coverage was in the range of ~1.5 ML, increasing after ZTB exposure and decreasing after UHV annealing, which also resulted in removing Zr.

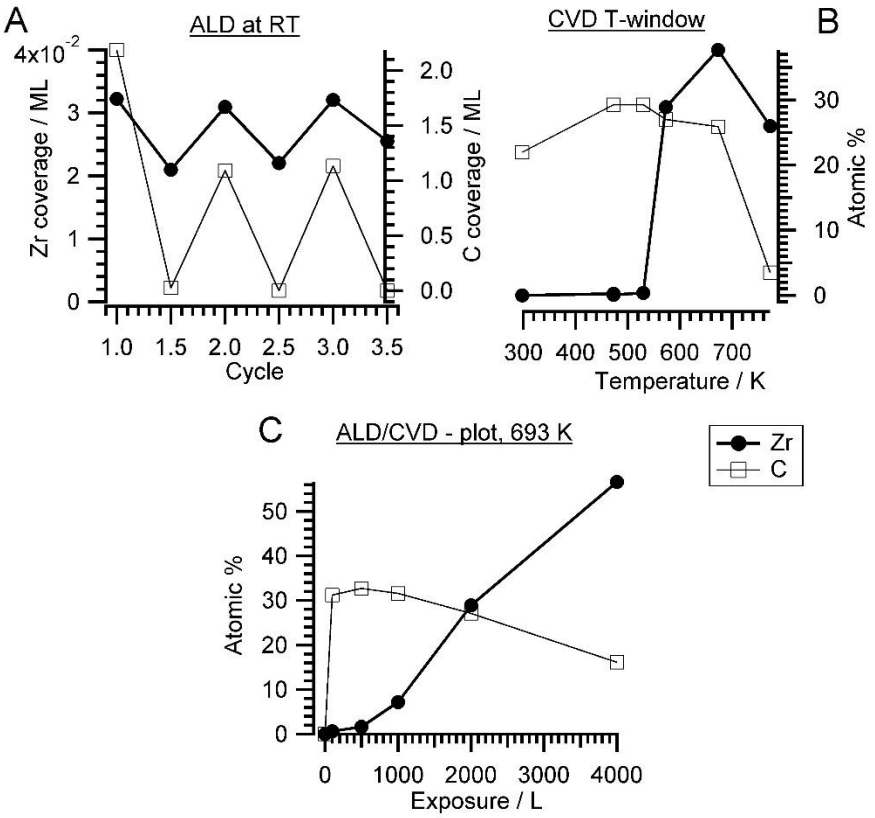

Figure 4.1 A) Zr and C coverage as a function of number of ALD-like cycles: 1st half cycle – 2000 L ZTB adsorption at RT and 2nd half cycle – annealing at 673 K in vacuum. Prior to the first ALD cycle, the clean Pd(111) surface was exposed to 2000 L O2. B) constant exposure of 2000 Langmuir at various temperatures, indicating the CVD window. C) Langmuir plot of Zr and C atomic % derived from Zr 3d, C 1s and Pd 3d versus ZTB exposure at 693 K (isothermal conditions).

Typically, an ALD/CVD process is characterized by a specific temperature window. For instance, the exposure temperature is recommended to be around 650 K for Si.[66] The ALD window for the decomposition of ZTB on a SiO_2 wafer was between 573 K and 673 K.[66, 92] The activation barrier was explained by a hydride elimination step, which was considered as a rate limiting step, and the formation of isobutene.[66] A pure ALD mechanism was supposed to occur below 573 K. We have investigated the dependence of the zirconium amount from the ZTB exposure temperature. Panel B of Figure 4.1 shows the amount of zirconium and carbon (in atomic percent for a rough quantitative estimation) calculated from the Zr 3d and C 1s XPS peaks as a function of ZTB exposure temperature. Carbon can be mainly found on the surface following exposure at temperatures below a sharp threshold of ~ 573 K. Above 573 K, the Zr/Pd

ratio increases rapidly and the amount of carbon decreases. A remarkably similar behavior was observed during ZrO_2 growth from ZTB on Si(100) by Cameron and George,[92] where the CVD rate of ZrO_2 increased sharply above 573 K and then started to drop above 773 K. At high temperatures, ZrO_2 deposition was supposed to be partially poisoned by carbon. Fourier transform infrared spectroscopy (FTIR) demonstrated hydroxyl (ZrOH*) and butoxide ($ZrOC(CH_3)_3$*) species on ZrO_2, whose concentration decreased roughly linearly with temperature from 300-800 K.[89] In our case, we did not detect much carbon deposition at high temperatures. On the other hand, a much lower ZTB pressure was used in our study (~10^{-5} torr vs. 0.05 torr in Ref. [92]) and Pd has a high capability to dissolve carbon.[93] Therefore, on Pd the amount of deposited Zr decreases above 673 K most likely due to kinetic limitations: fast desorption of ZTB effectively competes with dissociation. The temperatures between 550-773 K were most efficient for zirconium deposition, more effective than multiple ALD-like cycles at room temperature. The temperature of 693 K was usually used for the CVD experiments described in this study because of the empirically determined trade-off between reducing the unwanted carbon deposition and optimizing the Zr amount.

A Langmuir-type plot (deposited amount of Zr and C versus ZTB exposure in Langmuir) obtained at 673 K is shown in Figure 4.1, panel C. No zirconium saturation was observed even at 4000 L, while the carbon amount was declining with exposure. Growing with exposure, the Zr amount is more typical for CVD than for ALD. The CVD was also reported for ZTB adsorption on Si(100).[92] Interestingly, carbon is displaced by zirconium compounds, which might reflect a competition for adsorption/dissociation sites between ZTB and its decomposition products (i.e. hydrocarbons). ZTB dissociation products could hinder ZTB adsorption and block further ZTB dissociation. A similar situation was observed during trimethylaluminum and ferrocene adsorption on Pd(111) and Pt(111).[79, 94] The CVD growth of ZrO_xH_y on Cu was also monitored *in situ*. The XP spectra are shown in the Supporting Information in Figure A.1.

In order to identify adsorption species and to understand the low zirconium uptake below 550 K, ZTB adsorption was investigated by HREELS as shown in Figure 4.2. The molecularly adsorbed ZTB was prepared by 2000 L exposure on Pd(111) at 180 K and followed by warming up to 293 K (spectrum (a) in Figure 4.2). Despite the rather complex spectrum, all detected vibrations are very similar to those detected from FTIR in gas phase for the tert-butyl group and ZTB.[95, 96] From XPS (Supporting Information, Figure A.2), two separate C 1s peaks can be

seen at 286.9 and 284.9 eV following ZTB exposure, which can be attributed to carbon bound to oxygen or carbon, respectively. By comparison with the Zr $3d_{5/2}$ peak area, the C/Zr ratios for the oxygenated and non-oxygenated species are 4.9 and 17.4, respectively. This allows us to conclude that adsorption of ZTB is mostly molecular under these conditions. The characteristic frequencies of ZTB on Pd(111) are summarized in the Supporting Information in Table A.3 and compared with literature values. The HREELS spectrum obtained following ZTB adsorption on Pd(111) at 293 K (spectrum (a) in Figure 4.2) is slightly different. The main difference is a new peak at 1685 cm^{-1} (marked dark-green). This peak can be assigned to the stretching of the double C=C bond,[97-99] which most likely is due to adsorbed isobutylene species. Indeed, thermal desorption of isobutylene correlated with the ZrO_2 growth rate,[92] and this observation along with FT-IR-detected butoxide species ($ZrOC(CH_3)_{3,ads}$) allowed Cameron and George[92] to conclude that the butoxide species decomposition via β-hydride elimination is the rate-limiting step for ZrO_2 film growth. This conclusion is consistent with our HREELS data showing dissociation of ZTB and the appearance of the adsorbed isobutylene species. The intensity enhancement of a skeletal vibration of tert. butyl group, ν(C-C), at 780 cm^{-1} infers that the surface is covered with ZTB dissociation products. The C/Zr ratio increased compared to the molecular adsorption as well. The ratio for the room temperature-exposure roughly is 30:1 atomic-% C:Zr. Thus, hydrocarbon products of ZTB dissociation “passivate” the Pd(111) surface against further ZTB adsorption.

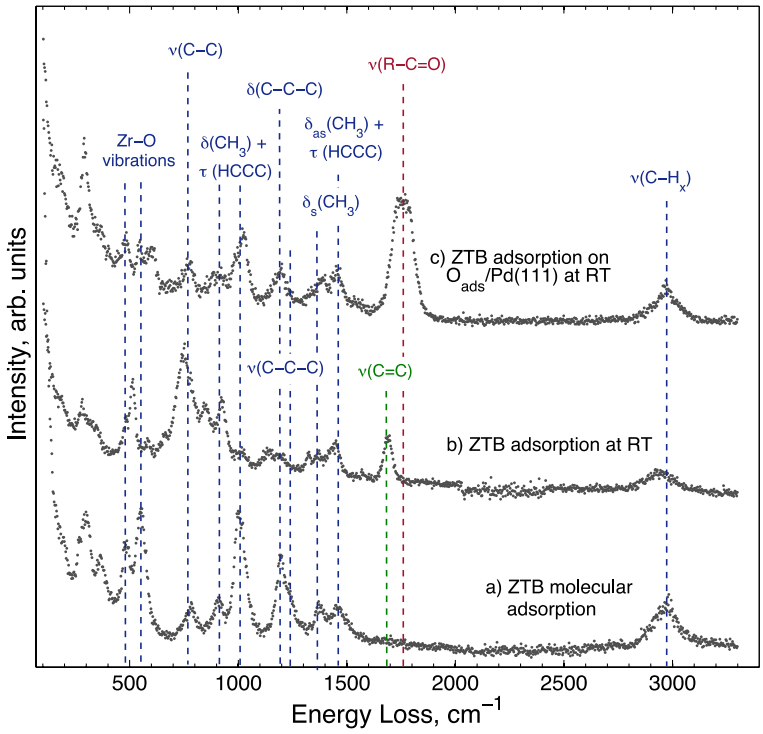

Figure 4.2 HREEL spectra obtained following 2000 L ZTB exposure of the Pd(111) surface (a) at 180 K and heated to 293 K in UHV, (b) and (c) at 293 K; for (c), Pd(111) was pre-exposed to 2000 L O2 at 673 K. HREELS spectra were collected at 293 K. The energy losses, which are characteristic of ZTB, are marked in blue.

Spectrum (c) in Figure 4.2 was obtained following 2000 L ZTB exposure of Pd(111) covered by O_{ads}. Interestingly, the spectrum is close to the one for the molecular adsorption of ZTB (spectrum (a), Figure 4.2): it is likely that the surface contains less ZTB dissociation products, as no adsorbed isobutylene species are found on the surface. On the other hand, a new peak appeared at 1745-1775 cm^{-1} (dark-red), which can be due to a C-O stretching vibration in aldehyde or ketones.[97-99] Likely, an isobutyl fragment splitting off ZTB could attach to a surface oxygen center without β-hydride elimination. It should be noted that we did not observe any OH vibration following ZTB adsorption in all three cases.

According to the HREELS data, even slight heating of ZTB adlayers in UHV resulted in decomposition of hydrocarbon species (Supporting Information, Figure A.5). Structure-wise, following adsorption of 100 L ZTB at 673 K, the surface is covered with a layer of rather disordered ZrO_x mixed with carbon (Figure 4.3, panel A). This layer is not uniform and contains holes and cracks (Figure 4.3, panel B). The surface carbon species seen in this stage are most

likely C_xH_y fragments and/or graphitic deposits, as deduced from the main C 1s components around 284 eV (not shown). A relatively broad height distribution within the terraces (not shown) indicates the limited uniformity of the overlayer.

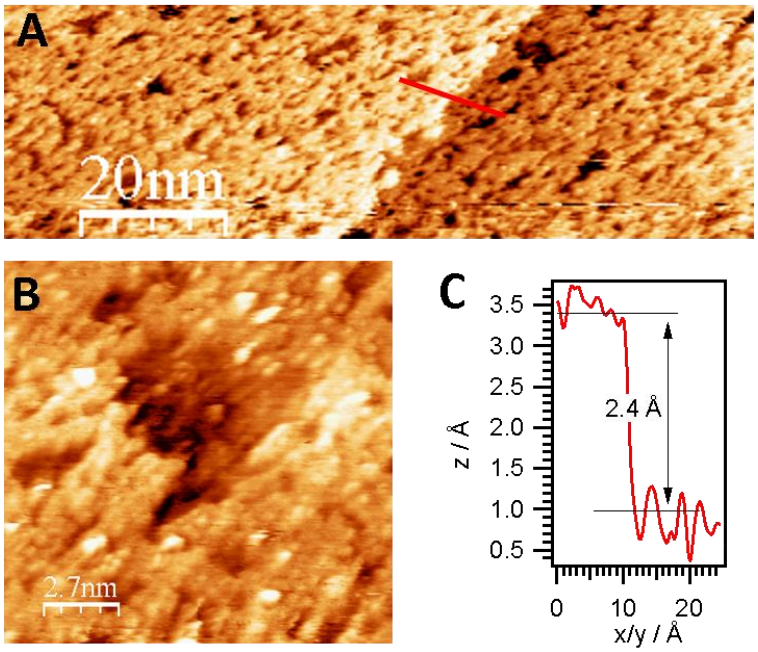

Figure 4.3 STM images of the CVD-grown ZrOx overlayer on Pd(111) (100 L ZTB at 673 K, ZrOxHy-Carbon layer coverage estimated to ~1 ML, bias voltage: -0.8 V, tunneling current: 0.4 nA). Panel A: monoatomic step edge in the Pd(111) surface, Panel B: crack in the non-uniform mixed ZrO_xH_y + carbon overlayer, Panel C: height profile of step edge.

Based on the data discussed above, we propose the following mechanism of ZTB – Pd surface interaction.

On clean Pd(111), ZTB dissociates via β-hydride elimination resulting in adsorbed isobutylene and butoxide ($ZrOC(CH_3)_{3,ads}$) species. Isobutylene species either desorb as isobutylene or decompose and hydrogenate leaving carbon on the surface. The adsorbed butoxide species dissociates further, resulting in ZrO_x deposition:

$$Zr(OC_4H_9)_4 + n * \rightarrow Zr(OC(CH_3)_3)_{x,ads} + (4-x)\ CH_2{=}CH\text{-}(CH_3)_{2,ads} + (4-x)\ O_{ads}$$

$$(x = 1, 2 \text{ and } n = 7, 5) \qquad (1)$$

$$Zr(OC(CH_3)_3)_{x,ads} + x * \rightarrow ZrO_x + x\ CH_2{=}CH\text{-}(CH_3)_{2,ads} \qquad (2)$$

$$CH_2{=}CH\text{-}(CH_3)_{2,ads} \rightarrow CH_2{=}CH\text{-}(CH_3)_2\uparrow + * \qquad (3)$$

$$CH_2{=}CH\text{-}(CH_3)_{2,ads} + 3\ * \rightarrow 4\ H_2\uparrow + 4\ C \quad (4)$$

$$ZrO + O_{ads} \rightarrow ZrO_2 + *. \quad (5)$$

As dissolution of carbon atoms in Pd is fast above 573 K on Pd,[93] we assume this process to dominate the ALD vacuum annealing step. Some oxygen could be consumed for hydrogen and carbon oxidation. The further fate of ZrO_2 is discussed separately. We can conclude that at temperatures below the threshold of ~550 K, the surface is poisoned by carbon compounds and above 773 K, the deposition rate starts to decline due to kinetic limitations (too fast desorption of ZTB).

On O_{ads}/Pd(111), the main difference is the appearance of alkoxide-like species showing C=O stretching vibrations. The exact configuration of this species is out of this work's scope and would require further investigation.

4.4.2 Reduction and oxidation of Zr-containing species on Pd surfaces

Annealing in vacuum at 673 K removed carbon efficiently (structure Figure 4.4, XP spectra shown in Figure 4.5). Surprisingly, annealing for 10 min results in zirconium reduction to Zr^0: the Zr $3d_{5/2}$ peak shifted from 183.15 eV for the precursor (Zr^{4+}) to 179.6 eV, which is formally Zr^0 _ENREF_45. This is a remarkable finding, since bulk zirconia is a very stable oxide and the reduction of bulk phases of this oxide without intimate contact to a noble metal is only possible under extremely harsh conditions. The oxide formation enthalpy is -1100 $kJmol^{-1}$ [100]. In fact, it is usually very hard to even keep Zr in its metallic state. Figure 4.4 shows the STM images obtained following 100 L ZTB exposure of Pd(111) at 673 K and annealing in UHV at 723 K. According to XPS, carbon is largely removed, and STM detects evenly-distributed sub-nanometer clusters with the height of ~0.4 nm, corresponding to a monoatomic height step of zirconium. These 2-6 atom clusters were assigned to metallic Zr. The Zr atoms can form a centered Zr hexagon. The atom-atom distance in the centered hexagonal plane of elemental Zr^0 (hcp lattice) amounts to 0.32 nm, and does, thus, fit to a certain degree to the dimensions of the centered hexagonal Pd arrangement of the Pd(111) surface, exhibiting a Pd-Pd distance of 0.28 nm between nearest neighboring atoms. The large misfit of the interatomic distances for Pd(111) and Zr(0001) likely prevents epitaxial growth of Zr on Pd(111).

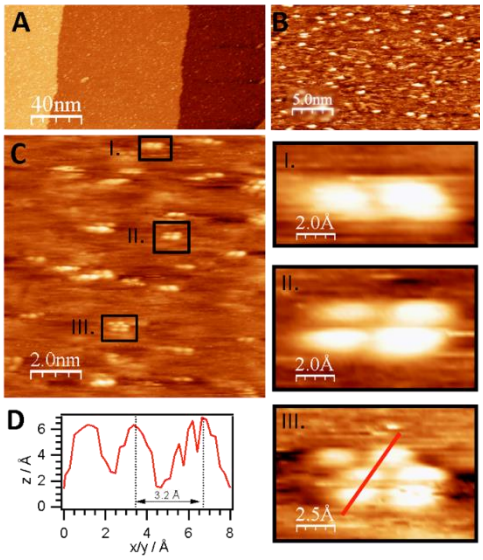

Figure 4.4 STM images obtained after CVD growth of the ZrOxHy + C overlayer (100 L ZTB at 673 K) on Pd(111) followed by UHV-annealing to 723 K in 5x10-11 mbar. The resulting Zr0 coverage was ~0.1 ML, and no more carbon was detected after annealing. The formed Zr-nanoclusters of 2-6 atoms are shown in panels C and I.-III. (gap voltage: 0.2 V, constant current mode, feedback setting: 0.2 nA). A-C: varying scale images, D: height profile of a Zr3 atom row within a Zr6 cluster.

The unusual behavior on Pd under vacuum conditions, leading to the formation of nanostructured Zr^0 islands, is explained by efficient removal of oxygen atoms and an extremely low re-oxidation rate. As deduced from STM images and DFT calculations shown later, metal support interaction effects are also highly beneficial. Even though a number of Pd-Zr intermetallic bulk phases and/or compounds in varying stoichiometry are known[100, 101], no such Pd-Zr phases can be formed at temperatures as low as 673 K. The Zr^0 metallic surface state was confirmed on the Pd(111) surface by (i) almost no shift of the Pd $3d_{5/2}$ peak (peak position: 335.2 eV) and (ii) the fact that the Zr 3d intensity did not change following annealing (neither dissolution nor evaporation) and (iii) the shift of the Zr 3d binding energy toward 179.4 eV typical for metallic Zr species[102, 103]. On the other hand, the interface between ZrO_x and the noble metal (Pd or Pt) likely plays an important role since this reduction is only working on Pd and Pt but e.g. not on Cu, which is a less active material.

In order to extend our understanding of ZTB CVD under UHV conditions to more realistic conditions, we compared the UHV results to the *in-situ* XPS data obtained at the synchrotron radiation facility BESSY-II. Figure 4.5 shows the Zr 3d spectra obtained during the

in vacuo heating of the CVD grown ZrO_x film (~2000 L ZTB at 673 K, deposited amount ~0.6 ML) on Pd(111) and on polycrystalline Pd foil by the UHV-XPS (Omicron) and in-situ by the NAP-XPS at BESSY II, respectively. The better vacuum conditions in the UHV-XPS set-up (5×10^{-11} mbar, water free) compared with the 5×10^{-8} mbar water-containing background in the NAP-XPS chamber allowed to obtain completely reduced zirconium. In *in situ* NAP-XPS, the highly reactive ZTB precursor was converted to mainly ZrO_2 right after preparation (Zr $3d_{5/2}$ at 182.4 eV). Also the amount of carbon is significantly lower in UHV-XPS, and we assign this enhanced precursor decomposition to the intense synchrotron beam of the *in situ* experiment and partally to the high base pressure. In both experiments, heating in vacuum resulted in reduction: only metallic Zr (179.4 eV) was detected in UHV-XPS, whereas a larger fraction of "partially reduced" zirconium (interfacial species) was additionally observed in the *in situ* NAP-XPS experiment, as a Zr $3d_{5/2}$ component is found at ca. 181.0 eV. This state was assigned to an ultrathin layer of ZrO_2[49]. We tentatively assign this peak to oxygen-deficient and not fully metallic interfacial ZrO_xH_y, e.g. with metal-metal bonds to the Pd substrate and still remaining Zr-O-Zr entities to the outermost ZrO_2 layer(s). This may explain the suggested oxidation state between Zr^{+4} and Zr^0, but rather if e.g. a bi- or multilayered precursor would be affected by loss of interfacial oxygen between Zr and Pd.

The reduction of Zr^{+4} is more difficult in the NAP-XPS-System, as not all Zr can be fully reduced to the metallic state (Figure 4.5). In the *ex situ* UHV experiment, where the reduction is fast and complete, and no such partially reduced intermediates could be detected. This difference most likely arises from the much poorer vacuum conditions of the *in situ* NAP-XPS chamber as discussed above. The background pressure of any oxygen containing molecules was, thus, found to be crucial for the eventual efficiency of Zr reduction. Also, the growth mode of the Zr^{4+} precursor species (i.e. layer thickness or island formation) may be already pre-determined by the residual gas conditions during deposition and/or annealing.

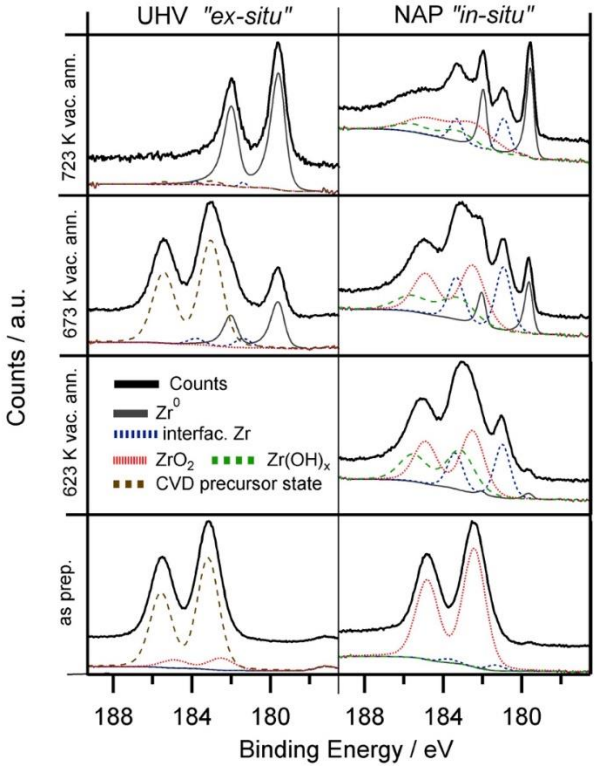

Figure 4.5 Zr 3d spectra of the CVD-grown ZrOxHy overlayer (673 K, 2000 L ZTB) at room temperature ("as prepared") and after annealing in vacuum to 623 K, 673 K and 723 K. Left side: experiments on Pd(111), base pressure of the UHV XPS chamber 5×10-11 mbar. Right side: experiments on a Pd foil at the NAP-XPS setup of ISISS beamline at HZB/BESSY II, base pressure 5×10-8 mbar. The initial Zr coverage for both experiments was approximately 0.6 ML.

Upon further annealing (T>780 K), dissolution of Zr into the Pd bulk occurs, leading to a significant loss of the Zr 3d intensity and the formation of a near-surface Pd-Zr alloy, as indicated by a slightly higher BE shift of the Pd 3d peaks (not shown herein). The BE of the dissolving Zr was found to be 179.6 eV, which is shifted about 0.2-0.4 eV towards higher BE from the position for bulk Zr^0.[103] The most likely reason is the enhanced Pd-Zr coordination in the subsurface regions, but charge-transfer processes and final state effects might also play a role.

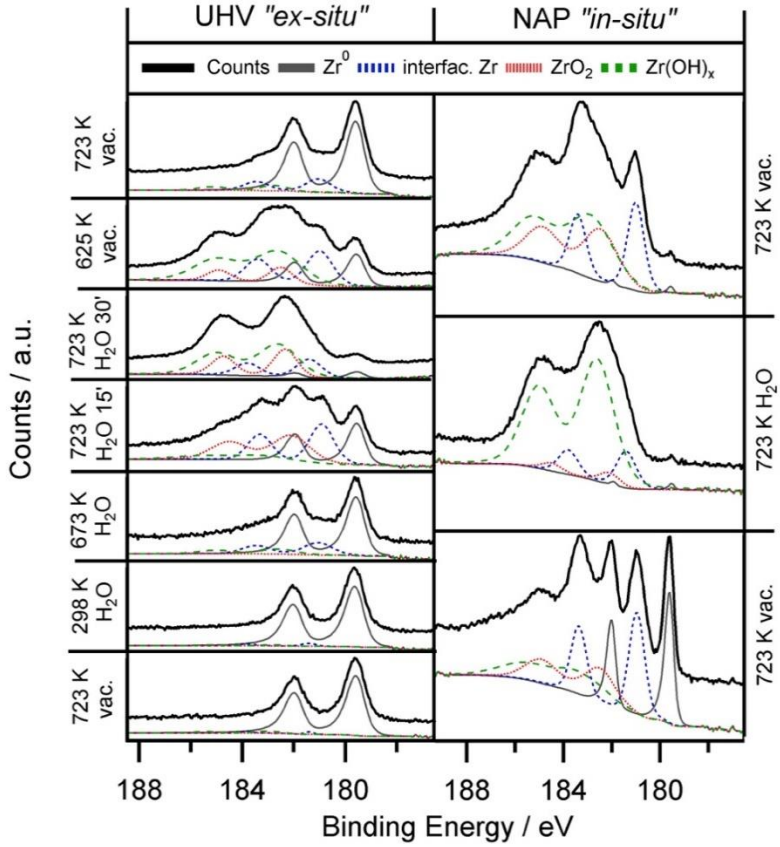

Figure 4.6 Zr 3d spectra obtained *ex situ* and *in situ* during heating of 0.2 ML Zr^0/ZrO_xH_y in water. Zr^0/ZrO_xH_y was prepared by annealing of CVD-grown ZrO_xH_y (at 673 K, 2000 L ZTB) in $5x10^{-11}/5x10^{-8}$ mbar for the *ex situ* and *in situ* experiment, respectively. Left panel: *ex situ* UHV XPS experiments on Pd(111), water pressure $5x10^{-7}$ mbar. Right panel: *in situ* NAP-XPS experiments on a Pd foil, water pressure 0.3 mbar for 20 min.

The reduced state of Zr was heated to 723 K in 5×10^{-6} and 0.3 mbar H_2O in the *ex situ* experiments and the *in situ* experiments, respectively. Hydroxylated zirconia, ZrO_xH_y, (Figure 4.6, binding energy Zr $3d_{5/2}$ ~183.0 eV) and also a minor ZrO_2 component were detected in both experiments. In 5×10^{-6} mbar H_2O, the hydroxylation is obviously slower because of a much lower H_2O pressure. At 723 K, hydroxylation mostly occurs within 15 min: the state assigned to interfacial Zr could be detected. Almost complete loss of Zr^0 and the highest degree of hydroxylation is reached after 30 min. Hydroxylation is faster and more complete in the *in situ* experiment (0.3 mbar) due to the higher H_2O pressure. The Zr $3d_{5/2}$ peak of hydroxylated Zr^{4+} differs from the fully oxidized state and is found at around 183.0 eV, which complies well with literature values.[104]

Only in the UHV *ex situ* experiment the hydroxylation process is fully reversible: annealing at 723 K fully re-establishes the metallic state of Zr. Most likely, the degree of reversibility of the reduction process is highly dependent on the background pressure of oxygen containing molecules such as H_2O and O_2 in the residual gas.

Even though a catalytic reforming cycle should rather involve reversibly formed hydroxyl groups at Zr sites, an analogous experiment can also be performed with O_2 instead of H_2O. Oxidative treatments in O_2 (*ex situ*) and 0.3 mbar O_2 (*in situ*) leads in both cases to fully oxidized ZrO_2. Oxidation in 5×10^{-7} mbar O_2 for the *ex situ* experiments is fast, after 10 min no more metallic Zr was found. Again, full reversibility to the Zr metal state was only achieved in the UHV chamber. Water-analogous results were also obtained for the *in situ* experiments with 0.3 mbar O_2 pressure. Here, again only partially reversible reduction is possible, highlighting the aforementioned limitations by the poorer background pressure.

4.4.3 DFT calculations of the initial stages of ZrO_2 reduction

To better understand the energetic pre-conditions leading to the pronounced reducibility of ultrathin ZrO_2 films on Pd surfaces, DFT calculations with variable ZrO_2 film thickness were performed. The reaction energy for deposition of a ZrO_2 film on the Pd(111) surface, as cut from the ZrO_2 bulk structure, is calculated by eq.(1) (see section 2, "computational methods"). The corresponding reaction energies ΔE for 1 ML, 2 ML, and 3 ML thick ZrO_2 are 1.20, 1.14 and 1.20 Jm^{-2}, indicating that the 2 ML ZrO_2 film is more stable than its 1 ML and 3 ML counterparts. The positive value of the reaction energy indicates that the process of cutting layers from the cubic ZrO_2 bulk structure and depositing them as an ultrathin ZrO_2 film on the Pd substrate is endothermic. To better understand the deposition of the ZrO_2 films, the reaction energy ΔE is separated into two parts, the formation energy ΔE_{film} of the respective ZrO_2 film from the bulk ZrO_2 structure, and the adsorption energy ΔE_{ads} of this film on the Pd substrate. Our calculations show that the formation of a freestanding ZrO_2 monolayer from the bulk structure would require an energy of 3.59 eV and an equilibrium lattice compressed by ~9%. The corresponding adsorption energy ΔE_{ads} for the 1 ML ZrO_2 film on the Pd substrate is -0.11 eV. Formation of a freestanding 2 ML ZrO_2 film from the bulk structure would require an energy of 5.09 eV and an equilibrium lattice compression of ~4%. The corresponding adsorption energy ΔE_{ads} for the 2 ML ZrO_2 film at the Pd(111) surface is -1.81 eV. To form a freestanding 3 ML ZrO_2 film from

the bulk structure would require an energy of 5.66 eV and an equilibrium lattice compression of ~3 %. The corresponding adsorption energy ΔE_{ads} for the 3 ML ZrO_2 film and Pd substrate is -2.18 eV. The lattice compression of ZrO_2 film with respect to the ideal bulk structure was observed in previous theoretical calculations[52]. With increasing thickness, the film lattice slowly approached the bulk lattice dimensions. It is noted that the 1 ML ZrO_2 film exhibits the smallest adsorption energy, which is partially due to the strongest film reconstruction among the discussed 1 - 3 ML scenarios. In summary, the 3 ML ZrO_2 film is less stable than the 2 ML one due to the required larger film formation energy from the ZrO_2 bulk, and the 1 ML ZrO_2 film is less stable than the 2 ML one due to the smaller adsorption energy at the Pd substrate.

We then investigated three possible competing reactions for oxygen atom removal: to release 0.5 O_2 into the gas phase directly, to dissolve an O atom into the Pd sub-layer and to diffuse the O atom to the available neighboring bare Pd(111) surface. The free reaction energy at 725 K, calculated for an equilibrium pressure above the surface of $P_{O2} = 10^{-12}$ mbar, is summarized in Table 4.1. Among the three possible competing reactions the interface oxygen diffusion to the neighboring bare Pd(111) surface is in any case the most favorable, followed by direct desorption into the gas phase as 0.5 O_2 and dissolution into the Pd sub-layer, which is the least favorable. The corresponding reaction energies for the interface-to-Pd oxygen diffusion are 0.74, 1.43, and 0.94 eV for the 1 ML, 2 ML and 3 ML thick ZrO_2 films, respectively, while the direct desorption of 0.5 O_2 into the gas phase is ~0.20 eV higher than the diffusion. The corresponding reaction energies for oxygen dissolution in the Pd sub-layer amount to 2.00, 3.09 and 2.48 eV, which is in all cases much higher than the diffusion to the neighboring Pd(111) surface. We also found that the surface oxygen of the topmost layer and the interface oxygen of the lowest layer show the same reactivity for the direct O_2 desorption for the 1 ML and 2 ML ZrO_2 films. However, for the 3 ML ZrO_2 film, the interface oxygen is more active than the surface oxygen, indicating that the oxygen vacancy is more stable at the interface than at the outer surface. The corresponding structures for oxygen diffusion to the neighboring Pd(111) surface and dissolution into the sub-layer of the Pd substrate are shown in Figure 4.7. As shown therein, the surface Pd atom moves up significantly by ~ 0.40-0.50 Å in order to adapt the dissolved oxygen atom. In Table 4.1, we also included the movement of an interface Zr atom. As expected, atomic Zr dissolution from the interface to the Pd sub-layer is less favorable than atomic oxygen dissolution due to the large size of atomic Zr. The corresponding reaction

energies are 2.78, 3.45 and 3.29 eV for the 1 ML, 2 ML, and 3 ML ZrO_2 films. Comparing all the reaction energies, it is noted that to move either O or Zr from the 2 ML ZrO_2 film is more difficult than that from the 1 ML and 3 ML films, suggesting that the 2 ML arrangement is the most stable one.

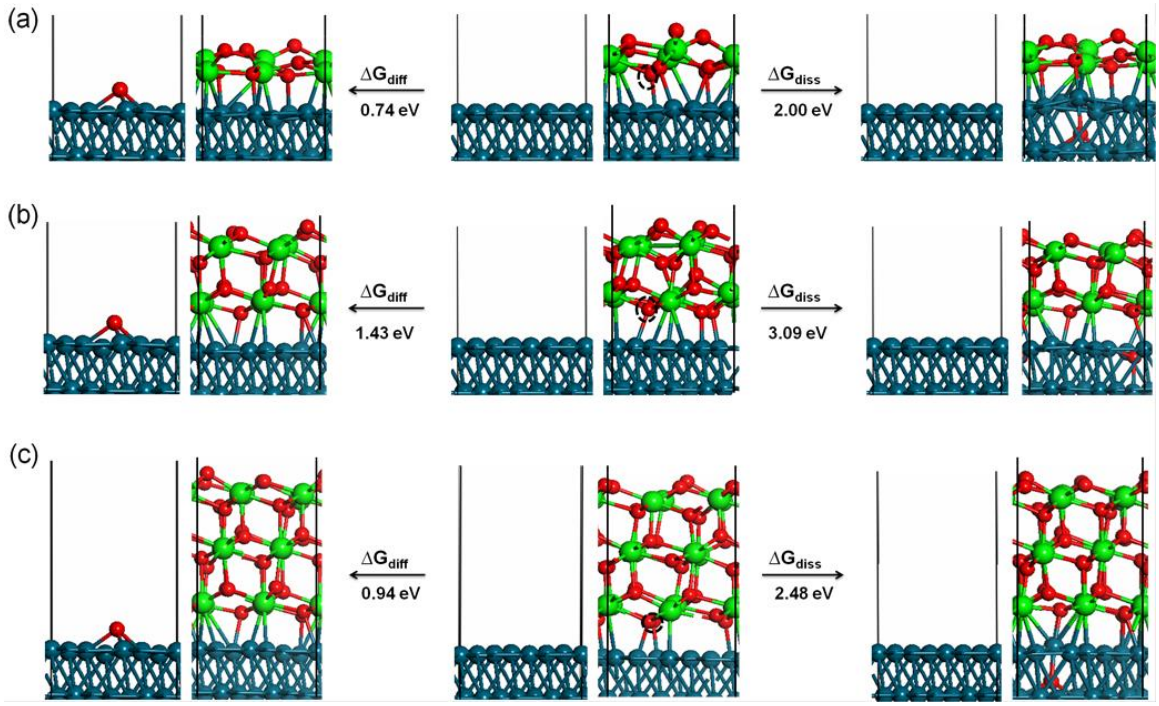

Figure 4.7 Structural models of interface oxygen dissolution to the sub-layer of Pd(111) and diffusion to the available neighboring bare Pd(111) surface. The reaction energies are labeled. Left: the Pd-O diffusion scenario; right: dissolution scenario; middle: 1 (a), 2 (b), and 3 (c) ML ZrO2 on the Pd(111) substrate. The moving O atom is marked by a dashed black circle. Small red spheres: O; large green spheres: Zr; blue spheres: Pd. The boxes indicate the computational supercell.

Table 4.1 Calculated reaction energy □Gdiss (eV) of O/Zr dissolution into the Pd sub-layer, reaction Gibbs free energy □GO2 (eV) of O2 production in the gas phase, reaction energy □Gdiff (eV) of O diffusion to the available neighboring bare Pd(111) surface at 725 K with PO2 = 10-12 mbar.

ZrO_2	1 layer	2 layer	3 layer
$\Delta G_{diss}(O_{interface} \rightarrow O_{sub\text{-}layer/Pd})$	2.00	3.09	2.48
$\Delta G_{O2}(O_{interface} \rightarrow 0.5O_2)$	0.94	1.63	1.14
$\Delta G_{O2}(O_{surface} \rightarrow 0.5O_2)$	0.94	1.68	1.46
$\Delta G_{diff}(O_{interface} \rightarrow O_{pd})$	0.74	1.43	0.94
$\Delta G_{diss}(Zr_{interface} \rightarrow Zr_{sub\text{-}layer/Pd})$	2.78	3.45	3.29

As discussed above, among the three possible competing reactions the interface oxygen rather prefers to diffuse to the available neighboring bare Pd(111) surface. Following this process, atomic oxygen may recombine to desorb as O_2 from the Pd surface. A number of previous experimental and theoretical studies have investigated O_2 adsorption/desorption on the Pd(111) surface.[105-109] Using thermal desorption spectrometry, one of our previous studies showed that the O_2 desorption rate from a chemisorbed O(ads) layer on Pd(111) reached its maximum at ~750 K, which implies that associative O_2 desorption from bare Pd is both possible and irreversible under the UHV-reduction conditions chosen in the present study.[110]

The conclusions from this section regarding the optimum growth conditions for subsequent full reducibility are: (i) preferential single layer growth of ZrO_2 and (ii) a large phase boundary of the sub-monolayer ZrO_2 islands toward the surrounding bare Pd surface should be realized already during the deposition process.

4.4.4 Catalytic Results

4.4.4.1 Methanol steam reforming (MSR)

Both the CVD “as-prepared” (1000 L ZTB at 693 K, ~0.5 ML ZrO_xH_y) and the partially reduced samples (annealed to 700 K in $5x10^{-9}$ mbar vacuum after CVD) were tested in the batch reactor setup for MSR. In our standard temperature-programmed experiment up to 623 K, in both cases no positive synergistic effects toward enhanced CO_2 selectivity were observed. The well-known methanol dehydrogenation activity of clean Pd toward almost 100 % CO and H_2 was

found to scale linearly with the fraction of ZrO_xH_y-free Pd surface. This is remarkable, since water-activating- and, thus, CO_2-promoting phase boundary effects could be verified under otherwise identical MSR conditions for the related inverse Cu/ZrO_2 and Cu/ZrO_xH_y model catalysts[70]. Even the "hydroxylative" activation of Zr^0 on the vacuum-pre-reduced $Pd/Zr^0/Zr^{+4}O_xH_y$ catalyst surface under MSR conditions does not promote low-temperature (T < 623 K) water activation and, thus, direct CO_2-formation, which so far could be verified for the related initially bimetallic PdZn[69, 111], CuZn[112] and CuZr[113] surfaces (compare also Figure 4.9). Even for the later discussed intermetallic Pd-Zr bulk phase, no increase in the CO_2 formation rate could be found in MSR.

The reason for the complete absence of any CO_2-beneficial Pd-Zr interaction was identified by *in situ* XPS measurements. In Figure 4.8, the evolution of the Pd 3d, Zr 3d, C 1s and O 1s regions after sequential treatment under MSR conditions, in clean methanol, water atmosphere and in O_2 are shown, starting from the CVD as-grown Pd/ZrO_xH_y pre-catalyst state. In excess of water (water:methanol = 2:1), only very little carbon formation was observed at ~700 K (compare Figure 4.8, lowest panel vs. Figure 4.9 (different scale for C 1s)). As soon as water is switched off (giving rise to a clean methanol atmosphere), a carbon layer starts to grow. This carbon is mostly assigned to graphitic species, according to the dominant C 1s BE component at 284.2 eV and the quite low FWHM of the C 1s peak of ~0.5 eV. If the temperature is then increased in a stepwise manner, the C 1s signal gains more and more intensity. Even though graphitic carbon is known for its rather less pronounced inelastic photoelectron attenuation effect (as it can be used as an electron transparent layer in the form of graphene), the observed large amount of carbon (well above 1 ML) must in principle cause a certain shielding effect both for the Pd 3d and Zr 3d signals if it was homogeneously covering the entire surface, especially upon consideration of the highly surface-sensitive operation mode (photoelectron kinetic energy ~120 eV). Surprisingly, this expectable attenuation strongly affects the Pd 3d region, but the Zr 3d signal remains almost unchanged. This effect can in principle be explained in two ways: (1) graphite only grows on Pd, but not on ZrO_xH_y, creating a thick carbon overlayer with holes at the ZrO_2 islands. Pd-Zr interface sites do not get lost but are blocked by graphitic carbon, resulting in the loss of any beneficial catalytic effect of these special sites. This hypothesis would also imply that the ZrO_2 islands are thick enough to be fully Pd 3d "attenuating", otherwise a carbon coverage independent Pd 3d signal passing through the ZrO_xH_y

islands should remain detectable. With the used photon energy of 410 eV the island height would have to exceed at least 3 ML. Considering the STM images of section 3.1. (Figure 4.3 and Figure 4.4), which show ZrO_xH_y-carbon overlayer on Pd(111) with a coverage close to 1 ML after CVD, and evenly distributed clusters of Zr atoms with 1 ML height after the subsequent UHV annealing step, this scenario appears rather doubtful. Therefore, a second explanation might be more reasonable: (2) carbon grows in a "sandwich-like" fashion between Pd and ZrO_xH_y and "lifts" the ZrO_xH_y islands up. As a consequence, the Pd-Zr interfacial sites would also get lost, resulting in the discussed catalytic inactivity. Note that such tremendous amounts of carbon were found neither on clean Pd nor on clean ZrO_2 under otherwise identical conditions. Therefore, a strong enhancement of coking caused by the Pd/ZrO_xH_y interface is strongly suggested. In such a way, the inactivity of the phase boundary in the water-containing MSR atmosphere might also be rationalized: The lift off effect might already play a role, even though the carbon formation propensity is lower due to the simultaneous water co-feed. Smaller amounts of graphitic carbon (C 1s BE = 284.3 eV) were always observed *ex situ* after MSR in the batch reactor setup. Moreover, MSR *in situ* XPS experiments at temperatures lower than 700 K are shown in Figure 4.9 and clearly indicate the formation of graphitic carbon also under MSR conditions. Quantification indicates a carbon coverage of 0.5-1 ML at 700 K under MSR condition (Figure 4.9) and around 1.5 ML at 700 K under pure methanol (Figure 4.8).

As the formed very thick carbon "interlayer" caused by pure methanol between 700 K and 750 K cannot be removed with H_2O and not even with O_2 at 750 K, as shown in the uppermost panels of Figure 4.8, its permanent poisoning effect and ineffective removal by water under MSR conditions is obvious.

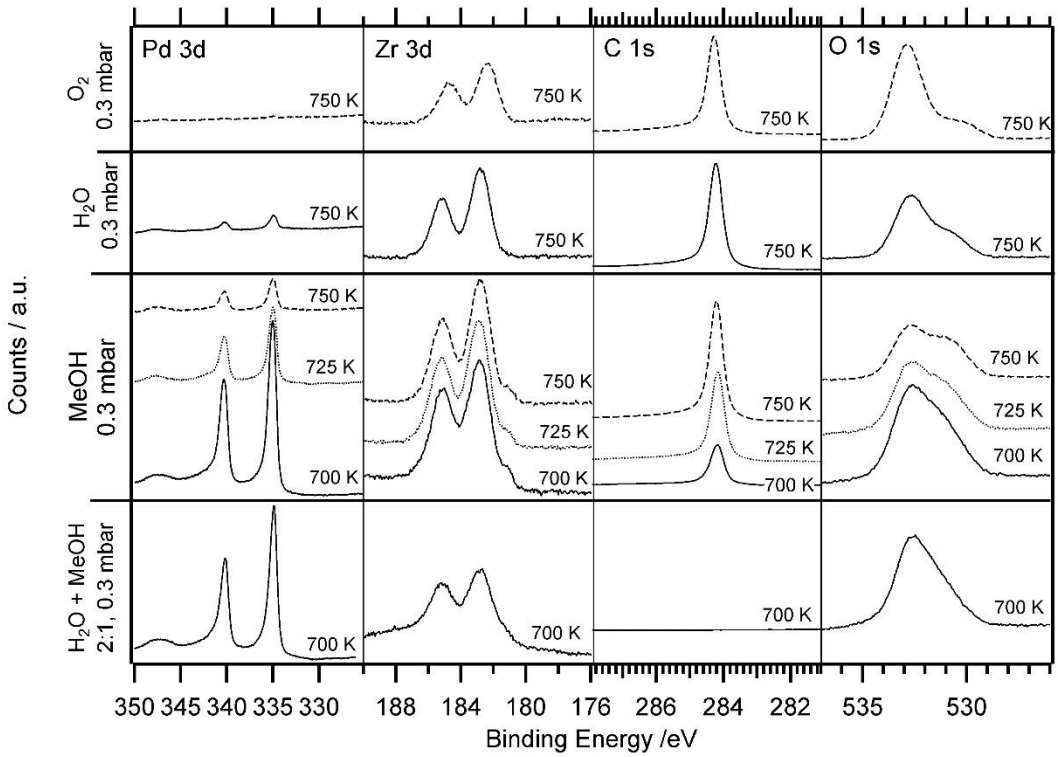

Figure 4.8 In situ NAP-XPS spectra (Pd 3d, Zr 3d, C 1s and O 1s (overlapping with Pd 3p) regions) of CVD grown 0.5 ML ZrOxHy model catalyst (1000 L ZTB at 723 K) under water-rich MSR conditions, clean methanol, water and oxygen (details see Y-axis). No vacuum annealing treatment after CVD was performed.

Starting from a partially reduced initial state (CVD followed by vacuum annealing), Figure 4.9 shows the temperature-dependent evolution of the *in situ* XPS spectra under MSR conditions. Up to 423 K carbon oxygenate species can be seen at binding energies around 286-288 eV. They arise from partial oxidation of methanol and prove the potential of the surface for methanol activation. Up to 548 K no hydroxylation is found. With increasing temperature, hydroxylation takes place under reaction conditions, along with a shift of the Zr 3d peak from 182.3 up to 183.0 eV due to reaction with H_2O in the gas feed. This indicates water activation and suggests the opening of water activation-dependent reaction channels. Moreover, graphitic carbon species (BE of 284.2 eV) are increasing between 298 and 648 K under MSR conditions. These carbon species disappear at higher temperatures. Both Pd bulk dissolution of carbon and the water gas reaction $C + H_2O \rightarrow CO + H_2$, which can cause the onset of CO formation above 650 K (see Figure 4.10), may be considered to explain this observation. In the O 1s region,

special care has to been taken when interpreting the peak shift to higher BE as Zr hydroxylation, since also carbon oxygenates may contribute to this trend and O 1s overlaps with Pd 3p.

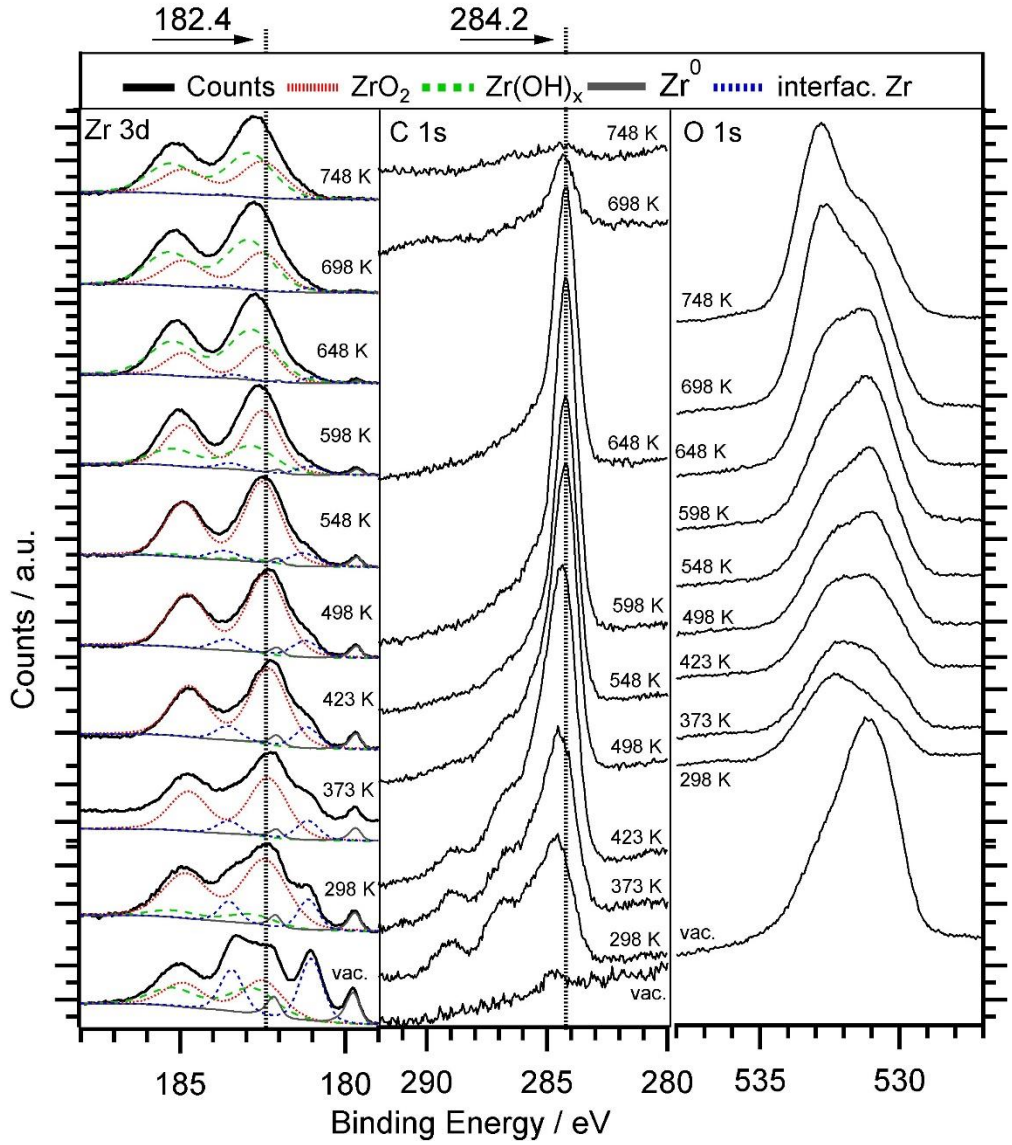

Figure 4.9 In situ NAP-XPS spectra (Zr 3d, C 1s and O 1s (overlapping with Pd 3p) regions) of 0.5 ML Zr0/ZrOxHy, prepared by annealing of CVD grown ZrOxHy (2000 L at 723 K) in 5x10-8 vacuum at 700 K under water-rich MSR conditions (H2O:MeOH = 2:1, ptotal = 0.3 mbar).

As mentioned above, neither the CVD-as-grown $Pd/Zr^{+4}O_xH_y$ nor the mixed valence $Pd/Zr^0/ZrO_xH_y$ model catalyst (prepared by vacuum annealing of the former) showed synergistic MSR effects in the standard temperature range up to 623 K. This range represents also the accumulation- and stability region of surface carbon species, as verified by the *in situ* XPS experiments of Figure 4.9. As the spectra at T > 648 K in Figure 4.9 both indicate additional

surface hydroxylation by water and pronounced carbon clean-off, high-temperature MSR experiments up to 873 K were additionally performed and are shown in Figure 4.10. Formation of CO starts around 623 K and is assigned to the methanol dehydrogenation activity of the residual clean Pd surface. On the initially clean Pd foil (without Zr), this reaction starts also slightly above 600 K. At ~700 K the CO formation rate passes through a maximum, then drops steeply and even becomes negative, i.e. already formed CO is consumed, which is clearly linked to simultaneous CO_2 formation. It is rather conclusive that the CO_2 formation arises from the onset of water gas shift (WGSR) activity, which is again coupled with the pronounced carbon clean-off effect starting above 650 K and shown in Figure 4.9. Thus, we suggest a water activation - carbon clean off - WGSR scenario mediated by "de-coked" and hence, activated Pd/ZrO_xH_y sites above ~650 K. The catalytic results of Figure 4.10 are therefore consistent with the *in situ* XPS spectra of Figure 4.9. In the isothermal reaction part, CO is still formed on Pd but partially re-consumed by the water gas shift reaction to form CO_2. Consequently, both formation rates, CO and CO_2, are positive. On this basis, we have to conclude that the low-temperature coking tendency, the high water-activation temperature and the CO_2-selectivity spoiling WGS reaction on the "re-activated" catalyst limit the relevance of Pd/ZrO_xH_y for selective MSR applications.

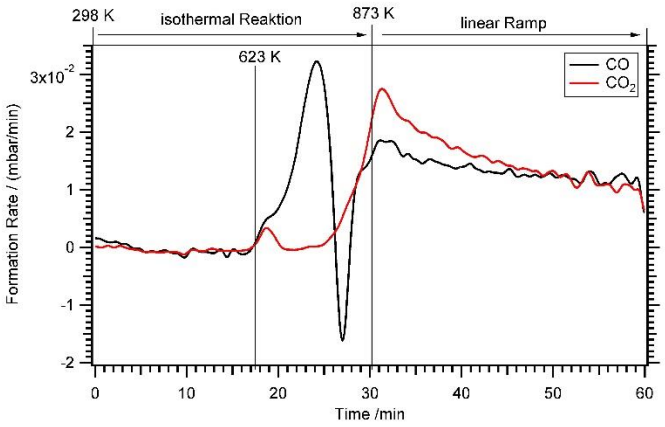

Figure 4.10 MSR on the CVD grown ZrOxHy model catalyst under water-rich MSR conditions (water:methanol = 2:1, p_{total} = 36 mbar). The exposure was about 1000 L ZTB at 700 K and the initial coverage with Zr estimated to ~0.4 ML. The temperature range of the MSR experiment was extended to 873 K.

4.4.4.2 Dry Reforming of Methane (DRM)

As an alternative reaction to MSR, the mixed valence $Pd/Zr^0/ZrO_xH_y$ model catalyst (again prepared by annealing of CVD grown ZrO_xH_y in vacuum), as well as the Pd:Zr=2:1 intermetallic "IM" reference catalyst described in the experimental section, were tested for methane dry reforming (DRM, $CH_4 + CO_2 \rightarrow 2\ CO + 2\ H_2$). For this reaction, no initial water activation is required, but active sites both for CO_2 and CH_4 activation are mandatory. Water can in principle play a "co-catalytic" role as an intermediate or spoil the reaction as a side product, if CH_4 is not stoichiometrically converted and the inverse WGS reaction is active:

Water-free:	Water-mediated:
$CH_4 \rightarrow C + 2\ H_2$	$CH_4 \rightarrow C + 2\ H_2$
$C + CO_2 \rightarrow 2\ CO$	$CO_2 + H_2 \rightarrow CO + H_2O$
	$C + H_2O \rightarrow CO + H_2$

The results of the DRM experiments are shown in Figure 4.11. In none of the catalytic experiments shown therein, H_2O was detected, thus, at least the side reaction to water associated with the inverse WGS reaction is of minor importance. Carbon was detected with XPS on the surface after the reaction, but in too low amounts (relative to the gaseous reactant/product amounts) to affect the overall stoichiometry. Figure 4.11 displays the DRM selectivity/activity pattern for a choice of "monofunctional" (pure Pd or Zr) and "bifunctional" (Pd-Zr) model catalysts. Clean Pd is completely inactive, as well as clean ZrO_2. Figure 4.12 shows the corresponding XPS spectra before and after selected DRM experiments of Figure 4.11. A pure Zr metal foil was oxidized in 1 bar O_2 at 673 K to form a ZrO_2 layer that is thicker than the XPS analysis depth (95% of signal from topmost 5 nm for ZrO_2 with Mg Kα radiation). After the DRM reaction, the ZrO_2 film is reduced within the accessible information depth and a single state of Zr is detected in the XPS 3d region at a binding energy of 179.4 eV, which agrees well both with literature BE values of Zr^0 [103] and zirconium carbide ZrC[114]. Destructive (sputter) depth profiling of this surface after catalysis is shown in the Supporting Information in Figure A.6, revealing a thickness of the carburized ZrC layer on top of Zr of at least 20 nm.

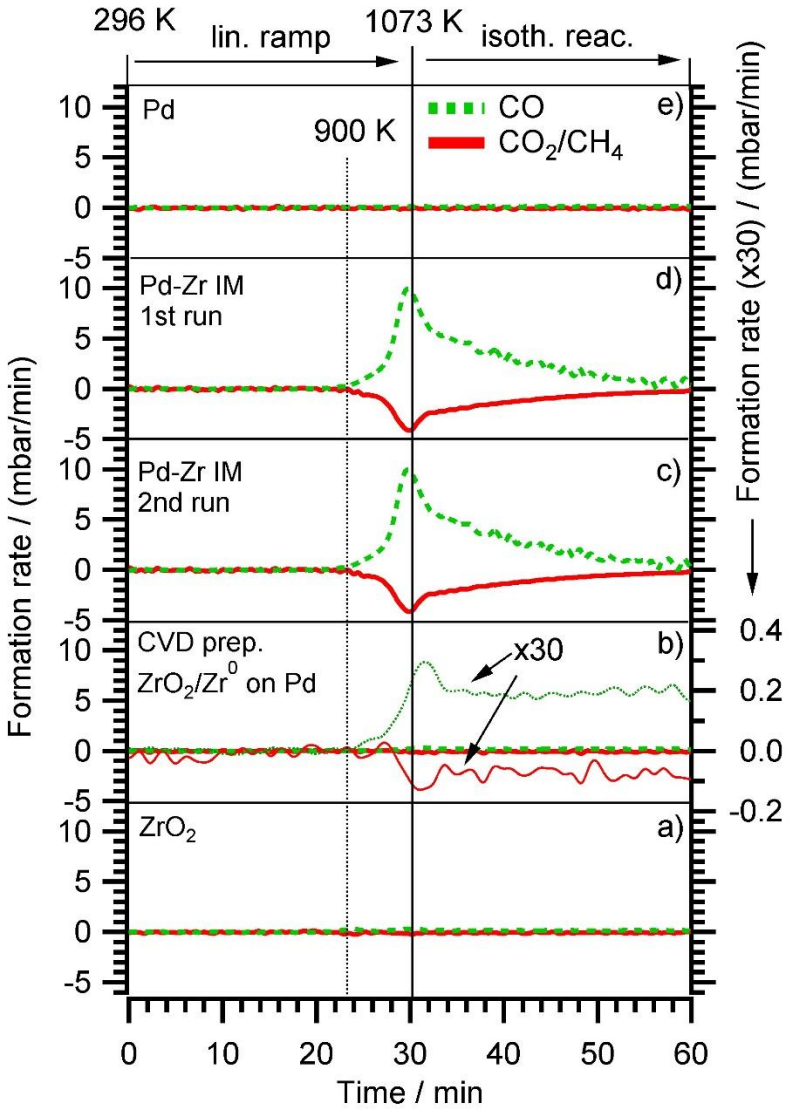

Figure 4.11 Methane dry reforming (DRM) on a) Clean oxidized Zr foil (identical with pattern for 0.3 ML ZrO2 on Pd, prepared by post annealing of CVD grown ZrOxHy in 5x10-7 mbar O2 at 700 K). b) 0.3 ML Zr0/ZrOxHy, prepared by annealing of CVD grown ZrOxHy in 5x10-9 mbar vacuum (the reactant consumption- and CO product formation rates were multiplied by a factor of 30 and plotted in the Y-scale range of the "IM" experiments c-d) two consequent DRM runs of an intermetallic Pd:Zr=2:1 "IM" bulk phase, e) pure Pd. Initial DRM conditions: CO2:CH4=1:1, total reactant pressure 100 mbar).

For the CVD-prepared and then vacuum- or oxygen-annealed $Pd/Zr^0/ZrO_xH_y$ or Pd/ZrO_2 samples, the activity in DRM depends on the initial oxidation state of Zr. As soon as there is a small fraction of Zr^0 available in the pre-catalyst (see arrow in Figure 4.12), a measurable CO formation rate could be detected. In Figure 4.11, the reaction rate is multiplied by a factor of 30

to show that there is some CO_2 consumed and CO formed at the stoichiometric ratio 1:2, but at a 30x lower rate as compared to the bulk-intermetallic "IM" catalyst described below. Again, no water side product formation could be detected. The temperature-programmed reaction profile for fully oxidized ZrO_2 on Pd (generated by annealing of the "as-grown" CVD layer in O_2 at 750 K) is not shown since no reactivity at all was detected, but the XP spectra for both ZrO_2 and ZrO_xH_y/Zr^0 on Pd are shown in Figure 4.12 before and after DRM. On this basis the fundamental activating function of Zr^0, which becomes in situ oxidized during DRM, could be shown qualitatively in spite of the very small initial Zr^0 amount. In order to substantiate this result, we decided to test an all-intermetallic bulk phase of Pd and Zr in the stoichiometry of 2:1 under otherwise identical DRM conditions ("IM" sample prepared by strongly exothermic co-melting, see chapter 2. The sample gets (surface) oxidized at room temperature over time, leading to a loss of Zr^0 in XPS (analysis depth ~2-3 nm). This oxidation was not found to be crucial for the catalyst performance. It does not matter whether Pd-Zr intermetallic is surface pre-oxidized in air at room temperature almost within the XPS analysis depth (Figure 4.12). The "before DRM" - IM spectra in Figure 4.12 shows the most air-oxidized state right before the catalytic experiment. Nevertheless, it shows residual Zr^0.

On this sample, the formation rate of CO is ~30 times higher than on the vacuum annealed CVD $Pd/Zr^0/ZrO_xH_y$ sample. This substantiates our interpretation that the (*in situ*) oxidative segregation from an initially intermetallic phase and/or surface leads to an enhanced number of reforming-active interfacial Pd/ZrO_xH_y sites. Again, we suggest the idea that the (*in situ*) oxidation of an atomically homogeneous intermetallic phase leads to the most disperse $Zr^{+4}O_xH_y$ surface-near distribution possible and therefore, to a maximum number of Pd/ $Zr^{+4}O_xH_y$ interface sites, i.e. to a quasi "atomically dispersed" phase boundary. The validity of this concept has previously been proven for Cu/Zn[69], Pd/Zn[70] and Cu/Zr[115] and is now also confirmed for Pd/Zr. The enhanced DRM reactivity on the $Pd/Zr_0/ZrO_xH_y$ pre-catalyst is therefore mainly assigned to the synergistic action of very small Zr^0 clusters, which become partially oxidized and/or hydroxylated under reaction conditions and exhibit a high number of direct Pd neighbours. Obviously, the number of these desirable interfacial sites is even higher on the *in situ* oxidized IM bulk phase pre-catalyst, eventually leading to a 30 times higher reaction rate.

Note that no deactivation of the IM catalyst was found on the time scale of our experiments (2x60 min each, 1st and 2nd run). In both cases, the decrease of the reaction rate in the isothermal reaction section is due to complete consumption of CO_2 and CH_4, as the reactor is operated in re-circulating batch mode. This reproducibility and stability with respect to catalytic performance holds despite a huge amount of carbon deposition (or, possibly, surface segregation) after cooling in the reaction mixture (see C 1s region of uppermost panel in Figure 4.12). The binding energy of ~284.5 eV and the rather large peak width (as compared to pure graphite) suggest a mix of sp3- or sp2-hybridized carbon species. The carbon layer is thick enough for complete shielding of both the Pd and Zr signals. This renders the absent deactivation of the catalyst after the first run even more surprising. Apparently, the catalytically active sites become again accessible during heating, e.g. if the carbon layer is reacted off by CO_2 and/or becomes re-dissolved in the bulk. Since the reaction sets in at ~900 K, the onset of the Boudouard reaction might explain this phenomenon. A final note on the bulk structure of the DRM-tested intermetallic Pd-Zr sample should be provided at this point. As already outlined in section 2 and further elaborated upon in the discussion of Figure A.7, highlighting the X-ray diffractograms before and after the DRM reaction. Despite the nominal 2:1 composition, the initial patterns reveal the presence of at least two intermetallic compounds with Pd excess, namely Pd_3Zr and Pd_4Zr_3. Upon performing the DRM reaction, the patterns get even more complex, including the complete removal of the Pd_3Zr phase and the formation of a new Pd_9Zr phase. Elementary, graphite-like carbon and partially oxidized ZrO_2 in the monoclinic and tetragonal modifications, formed by partial (oxidative) decomposition of the Pd-Zr intermetallic compounds, are equally observed. This is in striking contrast to Cu-Zr, where only one $Cu_{51}Zr_{14}$ compound was observed[81]. A common behavior (despite the different reactions) are the massive *operando* observed bulk structural changes accompanying the surface chemical alterations. However, due to the initially less homogeneous melt in the Pd-Zr case, the structural complexity is significantly more pronounced.

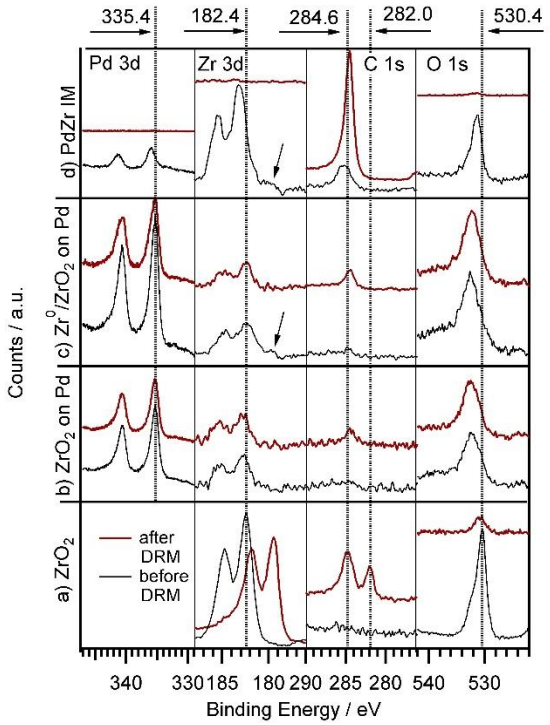

Figure 4.12 XPS (Pd 3d, Zr 3d, C 1s and O 1s (overlapping with Pd 3p) region) before and after DRM experiments for: a) clean Zr foil, pre-oxidized in 5x10-7 mbar O2 at 750 K for 15 min; b) 0.3 ML ZrO2 on Pd, prepared by thermal annealing of CVD grown ZrOxHy in 5x10-7 mbar O2 at 700 K; c) 0.3 ML Zr0/ZrOxHy, prepared by annealing of a CVD grown ZrOxHy in 5x10-9 mbar vacuum at 700 K; d) intermetallic Pd/Zr (2:1) "IM" bulk phase before first and after second DRM run. The arrow indicates the Zr0 component.

4.5 Conclusions

The CVD process of zirconium-t-butoxide ZTB was studied on a Pd(111) single crystal and on a polycrystalline Pd foil sample. A substrate temperature of ~700 K was found to be ideal to create a partially hydroxylated, carbon-depleted and vacuum-reducible ZrO_xH_y overlayer. Depending on the quality of the vacuum conditions, partial or full reduction to surface Zr^0 nanoclusters could then be accomplished. This very dynamic redox behaviour of ZrO_xH_y overlayers on Pd manifests itself in repeated oxidation (in water or oxygen) and vacuum-reduction cycles to the adsorbed Zr^0 metallic state without alloying up to 770 K. Nanoclusters of 2-6 Zr^0 atoms were found by STM if Pd/ZrO_xH_y was UHV-reduced at 723 K. DFT calculations show that the interfacial oxygen, especially that of a single-layer cubic ZrO_2 film, energetically prefers to diffuse to the available neighboring bare Pd(111) surface, rather than to desorb as O_2 or to become dissolved in the Pd subsurface region.

CVD prepared and vacuum-reduced $Pd/Zr^0/ZrO_xH_y$ model catalysts are not MSR active up to 623 K, due to the formation of an interlayer of graphitic carbon between Zr and Pd, resulting in the loss of active Zr/Pd phase boundary sites. In contrast to the related Cu/ZrO_xH_y system, MSR on $Pd/Zr^0/ZrO_xH_y$ does therefore not proceed via the low (<623 K) temperature/partial dehydrogenation route with intermediate formaldehyde, which is thereafter totally oxidized by activated water to CO_2. On Zr-"activated" Pd, rather the expected full dehydrogenation of methanol toward CO takes place on the bare Pd surface patches, followed by the (also water-activation dependent) water gas shift route toward CO_2 at higher temperatures above ~650 K. The latter process is only possible in the presence of an active Pd/ZrO_xH_y phase boundary, which is re-established above ~650 K by reactive removal of carbon deposits.

Dry reforming activity with almost 100 % CO-selectivity is only observed if Zr^0 species either in a CVD-prepared/vacuum-reduced or melt-prepared intermetallic Pd-Zr "pre-catalyst" are initially present. With an intermetallic pre-catalyst bulk phase with a nominal 2:1 composition consisting of Pd^0 and Zr^0, the highest CO formation rates were obtained. At the surface of both systems, Zr^0 is not stable under DRM conditions, and $Zr^{+4}O_xH_y$ species are formed by *in situ* reactive oxidation/hydroxylation. This process is likely to lead to a particularly high number of active phase boundary sites. As discussed above, further studies will most likely are focused on identifying sophisticated synthesis routines, allowing to prepare single-phase Pd-Zr intermetallic compounds, whose intrinsic (catalytic) properties can thus be studied.

DFT calculations to describe the Pd/ZrO_xH_y induced CO_2 activation and the reaction mechanism to CO and H_2 are planned. Besides enhanced CO_2 activation, also formation of surface adsorbed carbon from CH_4 may be positively influenced by Pd/ZrO_xH_y. The present study provides phenomenological evidence for an enhanced phase boundary synergism, including a beneficial carbon chemistry Thus, theoretical studies of the microscopic reaction mechanism at the active sites are imperative.

CHAPTER 5. A DISCOVERS OF STRONG METAL-SUPPORT BONDING IN NANOENGINEERED AU-Fe_3O_4 DUMBBELL-LIKE NANOPARTICLES BY IN SITU TRANSMISSION ELECTRON MICROSCOPY

5.1 Abstract

The strength of metal-support bonding in heterogeneous catalysts determines their thermal stability, therefore, a tremendous amount of effort has been expended to understand metal-support interactions. Herein, we report the discovery of an anomalous "strong metal-support bonding" between gold nanoparticles and "nano-engineered" Fe_3O_4 substrates by *in-situ* microscopy. During *in-situ* vacuum annealing of Au-Fe_3O_4 dumbbell-like nanoparticles, synthesized by the epitaxial growth of nano-Fe_3O_4 on Au nanoparticles, the gold nanoparticles transform into the gold thinfilms and wet the surface of nano-Fe_3O_4, as the surface reduction of nano-Fe_3O_4 proceeds. This phenomenon results from a unique coupling of the size-and shape-dependent high surface reducibility of nano-Fe_3O_4 and the extremely strong adhesion between Au and the reduced Fe_3O_4. This strong-metal support bonding reveals the significance of controlling the metal oxide support size and morphology for optimizing metal-support bonding and, ultimately, for the development of improved catalysts and functional nanostructures.

5.2 Introduction

Metal nanoparticles (NPs) supported on an oxide substrate are among the most important types of heterogeneous catalysts for producing chemical products and for exhaust gas clean-up. It has long been known that, in many cases, the catalytic performances, including the activity, selectivity, and stability, is strongly dependent both on the supported metal NPs themselves and on the metal support interactions. Since the metal support interaction can dramatically change the catalytic properties, many efforts have been made to understand and utilize the interaction for the real catalytic applications.

Among the parameters determining the catalytic properties, the strength of the metal-support bonding (MSB) is of the utmost importance for the industrial heterogeneous catalysts because the MSB directly determines the stability (lifetime) of the supported catalytic metal NPs.[116] This is especially critical for the supported gold catalysts owing to their low sintering

resistance. Since the discovery of the high catalytic activity of gold NP catalysts for low temperature CO oxidation,[117, 118] gold catalysts have been extensively studied for various chemical processes for which they showed excellent catalytic activities.[119] Despite the high potential of the gold catalysts for greener chemical processes, however, rapid deactivation of them by sintering of the gold NPs limits the realization of a wide range of industrial applications of the supported gold catalysts.[120, 121]

Over the past two decades, although, there have been various studies on the MSB between gold and metal oxide supports showing not only high catalytic activities[16, 122, 123] but also high stability[124] against sintering, no attempts to understand the observed catalytic improvements[125, 126]—whether activity or selectivity—at the molecular level, to elucidate the fundamental physicochemical factors that govern the metal/oxide interaction, or to generalize the fundamental understanding to various metal/oxide systems, have been reported, and such information is required to ultimately design the next generation of functional nanocatalysts.

Here, we report *in-situ* transmission electron microscopy (TEM), electron and X-ray spectroscopies, and Density Functional Theory (DFT) results showing a direct experimental evidence of the SMSB between gold and iron oxide in the Au-Fe_3O_4 dumbbell nanoparticles (DNPs), where the average diameters of the Au NPs and the Fe_3O_4 NPs are 5.0 nm and 10.4 nm, respectively. Drastic morphological changes of Au NP from a spherical NP to Au thin film (i.e., complete wetting) on Fe_3O_4 during the vacuum annealing directly indicates the presence of SMSB between Au and Fe_3O_4 during the *in-situ* annealing experiment. This result also emphasizes the importance of the precise control of the metal oxide supports in rational design of a stable gold catalyst. To the best of our knowledge, this is the first discovery of the SMSB in gold-iron oxide system and it generalizes the results and provides molecular-level explanations that could be applicable to many different systems.

5.3 Experimental

Au-Fe_3O_4 DNPs were prepared by initiating the epitaxial growth of Fe on Au NP seeds followed by Fe oxidation in an organometallic solution synthesis[127-129]. Organic methods of synthesis were employed to tightly regulate the size distribution of the nanoparticles and to direct the controlled growth of Fe_3O_4 on the exposed (111) facets of the Au seeds.

In-situ TEM and STEM videos and images were collected both at 300 kV and 60 kV using a probe aberration-corrected FEI Titan-S 80-300 equipped with a Gatan OneView CMOS camera and a Protochips Aduro heating stage at Oak Ridge National Laboratory. *In-situ* STEM-EELS were performed at 300 kV on an FEI Titan ETEM 80-300 equipped with a Gatan Tridiem GIF and Gatan single tilt 752 heating stage. XPS spectra were obtained by a Kratos Axis Ultra DLD spectrometer with monochromatic Al Kα radiation (1486.6 eV) at pass energy of 20 and 160 eV for high-resolution and survey spectra, respectively.

Periodic Density Functional Theory (DFT) calculations were performed with VASP[88, 130, 131] using the Projector Augmented Wave Method (PAW)[89, 132, 133] for Fe_2O_3 (0001), Fe_3O_4 (111), FeO (111) and Fe (110) surfaces. Au nanoparticles are modeled as Au (111) films with pseudomorphic registry on the iron oxides and a moiré pattern on Fe (110). Geometries of the models are shown in Figure 5.4 (b) (see SI for more details). Self-consistent electronic energies are calculated using the PBE functional[134, 135] within the Generalized Gradient Approximation (GGA). The PBE+U[136, 137] approach is employed to partially correct the self-interaction error prevalent in standard GGA functionals like PBE. The specific implementation of DFT+U used in this work follows Dudarev *et al*.[138, 139] Electronic cores of Fe, O and Au are represented by PAW PBE pseudopotentials. Further details, including kinetic energy cutoffs, k-points based on the Monkhorst Pack scheme,[140] magnetization and the numerical tolerances employed for iterative solutions of the Kohn Sham equations, are provided in the SI. An *ab initio* phase diagram analysis indicating the thermodynamic stability of iron oxide surfaces with and without Au films, based on the method proposed by Reuter and Scheffler,[141] is also reported in the Supplementary Information.

5.4 Results

Figure 5.1 shows snapshots of the *in-situ* TEM movie summarizing the thermal behaviors and morphological changes (i.e., wetting) of the Au-Fe_3O_4 DNPs and Au NPs with increasing temperature. Au NPs were intentionally mixed with the DNPs with the aim of comparing the thermal behaviors of the DNPs and Au NPs (marked with dotted line in Figure 5.1a). The Au-Fe_3O_4 DNPs were gradually heated up from room temperature up to 550 °C under high vacuum

(1.88×10^{-7} Torr) with the heating profile (time vs. temperature) of the *in-situ* TEM experiment presented in Figure 5.1g.

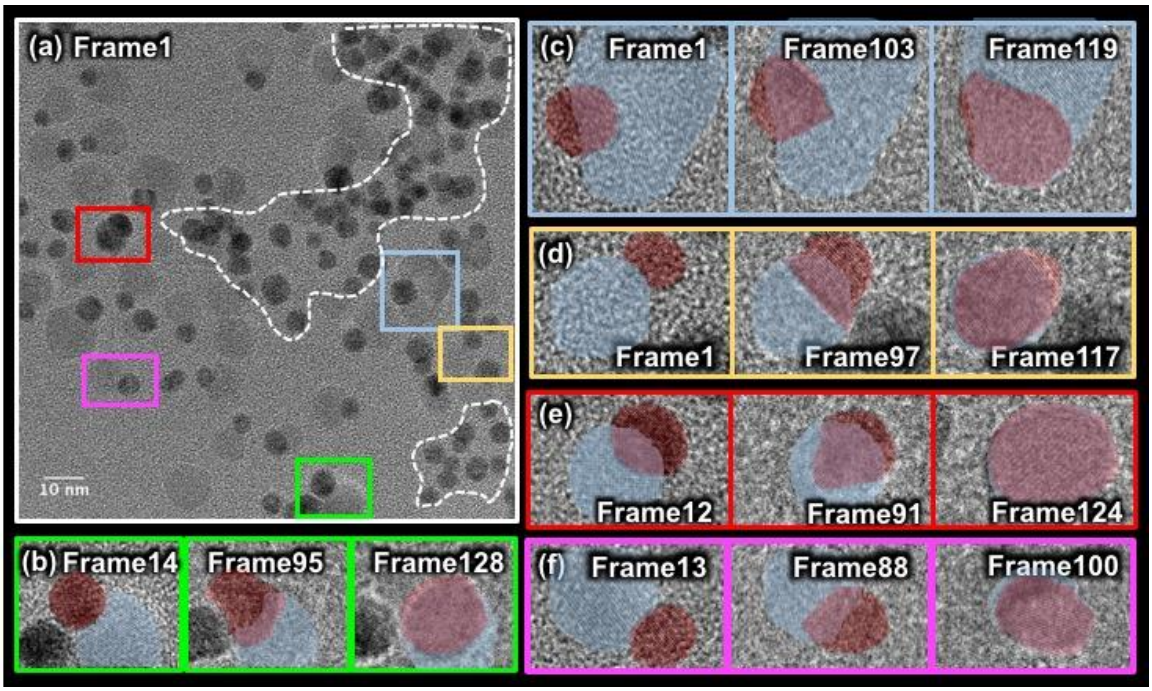

Figure 5.1 Snapshots of an in-situ heating TEM movie summarizing the thermal behavior of Au-Fe3O4 DNPs. (a) The initial frame taken at ~ 100 degree ^{o}C (b)-(f) Sequential snapshots showing the wetting behaviors of Au NPs on iron oxide domains. For better visibility, Au and Fe3O4 are false colored as transparent red and blue, respectively. (g) Temperature vs. time profile of the annealing experiment.

With increasing annealing temperature from room temperature to ~ 350 °C, a neck formation between regular Au NPs (without Fe_3O_4), which is the first step of sintering process, was observed. As the temperature was further increased, the regular Au NPs coalesced and formed several bigger Au particles. However, the gold domain of the DNPs started to flatten and partially covered the surface of the iron oxide domains at ~ 350 °C (Figure 5.1 b-f). As the wetting process proceeded, the iron oxide domain was totally covered by the gold thinfilm at ~ 500 °C. The thickness of the flattened Au on iron oxide was calculated as 1.9 Å, which corresponds to one monolayer of Au film on an iron oxide NP, assuming the shape of Au and Fe_3O_4 are spherical and their volumes are conserved during the entire heating experiment (Figure A.8).

The observed structures of gold thin film on a Fe_3O_4 domain indicate that strong bonds (SMSB) were formed at the interface between Au and Fe_3O_4 during the *in-situ* annealing. This

result implies that the metal-substrate (Au-Fe_3O_4) interfacial adhesion is stronger than the metal-metal (Au-Au) bonds, which is related to the surface tension of the Au NP. This is surprising, because it is contradictory to the well-known fact that a gold film grown on an extended surface of a single-crystalline Fe_3O_4 substrate at high temperatures (400°C and 750°C) has a 3D island shape rather than a 2D film structure,[142, 143] which corresponds to a Volmer-Weber growth mode, wherein the strength of the interfacial adhesion is weaker than gold-gold bonds. The change in strength of the MSB between the Au-Fe_3O_4 DNPs during annealing can be estimated by calculating the adhesion energy using Young-Dupré equation (Eq. 1).

$$E_{adh} = g_{np}(1 - \cos q) \quad (1)$$

where γ_{np} and θ are the surface tension of the supported nanoparticle and the contact angle, respectively.

In our case of a gold thin film on an iron oxide nanoparticle where theta equals 180°, the surface tension is estimated as 2.56 J/m^2 ($2\times\gamma_{Au(111)}$) and this value is 0.26 J/m^2 higher than the previously reported value of Au(111)/Fe_3O_4(111) (2.3 J/m^2) reported elsewhere.[144]

The major structural difference between the Au-Fe_3O_4 DNPs and Au/single-crystalline Fe_3O_4 with an extended surface, which might be the reason for the directly-opposed wetting behavior, is the size and morphology of the nano-Fe_3O_4. In the case of the DNPs, the nano-Fe_3O_4 domain has an average diameter of only ~10 nm. Moreover, due to the large curvature of the nano-Fe_3O_4 domain, the chemical potential of the surface atoms on the spherical Fe_3O_4 with ~ 5 nm radius is much higher compared to the extended flat Fe_3O_4, as predicted from the Gibbs-Thomson equation. This higher surface chemical potential possibly causes the surface to be more reactive and form a stronger adhesion with gold than the flat Fe_3O_4 surfaces.

Another remarkable difference between the nano-Fe_3O_4 of the DNPs and regular Fe_3O_4 is the facets enclosing the Fe_3O_4 crystal. In contrast to the regular Fe_3O_4, the nano-Fe_3O_4 domain in the DNPs are epitaxially grown on the Au NP seeds during the synthesis of the DNPs (see SI for the details of the sample preparation). Therefore, thermodynamically less favorable Fe_3O_4 (011) and (131) facets[145, 146] can be formed along with Fe_3O_4 (111) due to the epitaxial relationship of Au and Fe_3O_4 (Au(220)[112]//Fe_3O_4(440)[112] and Au(111)[112]//Fe_3O_4(222)[112] with a ~2.7 % and ~3 % lattice mismatch, respectively) (Figure A.9a, b). The epitaxial facet development of Fe_3O_4 in the DNPs were also observed from the annular-dark field (ADF)

electron tomography investigation (Figure A.9, c. d). In this regard, we believe the energetically reactive facets of the DNPs might also contribute to the SMSB.

To investigate the changes in the local chemical nature of the DNPs during the vacuum annealing, we performed *in-situ* scanning TEM (STEM) electron energy loss spectroscopy (EELS) during annealing of the Au-Fe_3O_4 DNPs at 500 °C. Several different DNPs, which correspond to the "*initial*", "*intermediate*", and "*final*" state of the gold wetting/flattening process, were characterized. Figure 5.3 shows annular dark-field (ADF) STEM images of the DNP representing one of the aforementioned states along with the locally collected EEL spectra from the DNPs shown in the STEM images. The locations where EEL spectrum collections were performed, and the corresponding spectra, are color-coded accordingly.

The DNP before the flattening maintained its dumbbell shape and a noticeable phase transformation, such as an intermixing between gold and iron oxide, was not observed (Figure 5.2a). However, as can be seen in Figure 5.2b where the hemisphere of iron oxide domain was partially covered by flattened gold, we found that the surface of the "gold covered" iron oxide hemisphere was heavily reduced. Consequently, the O K edge intensity was negligible. On the contrary, as it is evident from the EEL spectrum collected from DNPs, representative of the "intermediate" stage of the wetting process (green spectra in Figure 5.2b), the portion of the iron oxide with no Au coverage (darker region of the DNP in Figure 5.2b) remained as an oxide. The "final" state shown in Figure 5.2c illustrates that the iron oxide is fully covered by the Au film while the core remained an oxide and the iron oxide surface was highly reduced. By considering these *in-situ* STEM-EELS results as well as *in-situ* electron diffraction results (Figure A.10), it can be concluded that the core part of the final state still has a form of unreduced Fe_3O_4 and this suggests that the drastic morphology change of the DNPs is not due to the Au-Fe binary alloy particle formation but is due to the interaction between the Au thin film and the iron oxides.

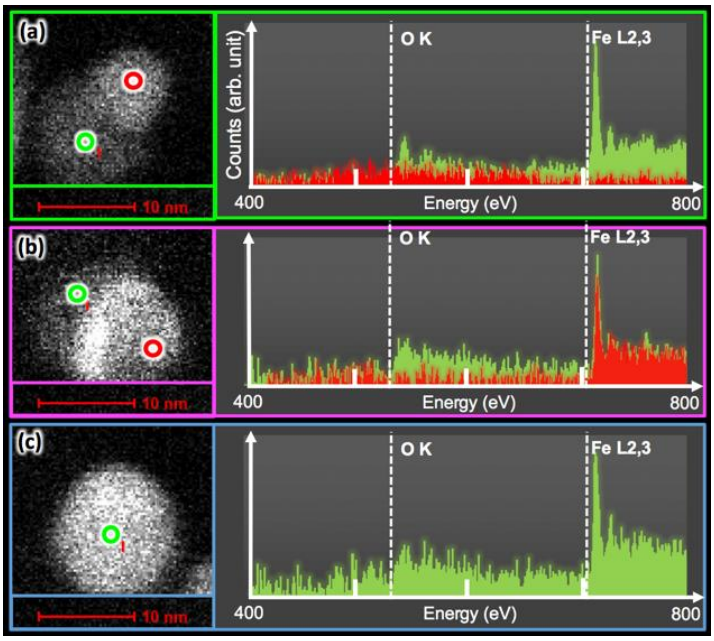

Figure 5.2 Results of in-situ STEM-EELS showing ADF-STEM images and EEL spectrum collected from the DNPs at (a) "initial", (b) "intermediate", and (c) "final" state of the wetting/flattening process.

Furthermore, these results suggest that the SMSB in the Au-Fe_3O_4 DNPs is correlated with the surface reduction of the iron oxide domain. The role of surface oxygen vacancies of the metal oxides on MSB has been investigated by several researchers and it has been reported that the surface oxygen vacancies of CeO_2 and TiO_2 strongly stabilize metal NPs.[147, 148] Moreover, it has also been pointed out that the amount of surface oxygen vacancies contributing to the strength of the MSB for oxide-enclosed metal nanoparticles is strongly dependent on the facets enclosing the support particles because the redox capability of a metal oxide is dependent upon the type of facets.[124, 125, 149] Therefore, we may conclude that the unique SMSB of the DNPs is due to the higher reducibility (or higher surface oxygen vacancy concentration) of nano-Fe_3O_4, having high surface chemical potentials and reactive facets, as discussed above. The SMSB with reduction of Fe_3O_4 is further investigated below through XPS and DFT based atomistic simulations.

In order to determine the oxidation states during the iron oxide reduction process, we performed X-ray photoelectron spectroscopy (XPS) analysis of the DNPs before and during vacuum annealing at 500 °C. The heating was performed *in-situ* in UHV allowing spectra to be obtained while the sample was held at 500 °C and one hour was given to equilibrate the system

before beginning the acquisition. Before heating the sample, the Fe $2p_{3/2}$ main peak is located at 710.5 eV with no distinct shake up feature, which is characteristic of the convolution of the Fe^{3+} and Fe^{2+} features present in Fe_3O_4.[150] During the vacuum annealing, the centroid of the Fe $2p_{3/2}$ peak shifts to 709.3 eV and a distinct shake-up feature appears at 715.6 eV, as shown in Figure 5.3a. Both the peak position and the distance between the main peak and the shake-up indicate Fe^{2+} formation.[151] Along with the reduction of Fe^{3+} to Fe^{2+}, a prominent feature representing approximately 30% of the total Fe 2p area appears at 706.8 eV, indicating the reduction to metallic iron. Accompanying the reduction of Fe, a shift in the Au $4f_{7/2}$ peak from 83.8 eV to 84.2 eV is seen, as shown in Figure 5.3b. This +0.4 eV chemical shift can be explained either by a size effect [152] (in our case, morphological changes observed in TEM) or by gold coordinating with iron forming an intermetallic phase, a similar shift as observed in the Au_xIn_y alloy system.[153]

This XPS result indicating the surface reduction of the nano-Fe_3O_4 hints at a fundamentally new phenomenon in metal/oxide nanoscience, involving a cooperative size- and metal-induced reduction of oxide nanoparticle surfaces. According to Syed *et al*.,[152] a100 nm thick Fe_3O_4 thin film deposited on Si substrate was completely stable against the reduction in the vacuum annealing (from 573 K to 973 K at 9.75×10^{-7} Torr) and therefore, the Fe 2p3/2 peak in the XPS spectra remained on the same binding energy. Also, a characteristic peak indicating a metallic Fe has never appeared.[40] This suggests that the spherical nano-Fe_3O_4 has a higher reducibility and a higher capability of containing oxygen vacancies on its surface compared to flat extended Fe_3O_4. As already observed from *in-situ* STEM-EELS, the SMSB and the gold wetting behavior are closely related to the surface reduction of Fe_3O_4. In order to further verify that this reduction is likely due to nanosize effect, we also conducted XPS on 5 μm Fe_3O_4 (bulk) treated using the same conditions as the DNPs. As shown in Figure 5.3a, the XPS spectra collected after vacuum annealing were consistent with bulk Fe_3O_4, containing both Fe^{3+} and Fe^{2+} peaks of appropriate intensity with no distinct shake-up or metallic iron features. This compelling result strongly suggests that nanosize effects contribute to the reducibility of the iron oxide particles.

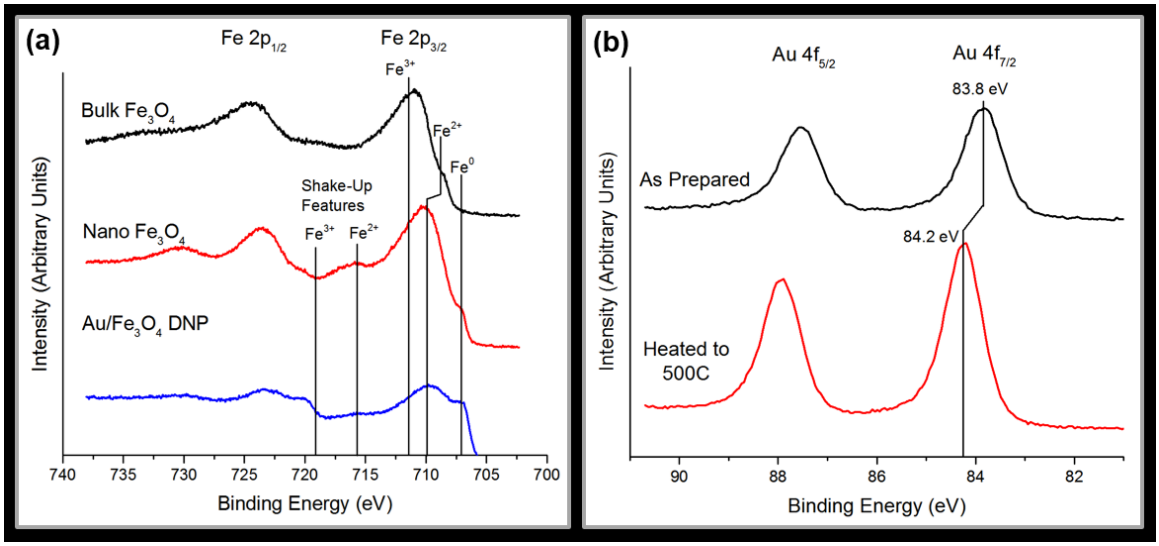

Figure 5.3 XPS measurement. (a) Fe 2p spectra collected at 500 °C for bulk Fe3O4, nano-Fe3O4, and Au/Fe3O4 DNPs. Reference lines for the features are shown to help guide the eyes and are taken from Ref. 39. (b) Au 4f spectra from the Au/Fe3O4 DNPs taken as prepared and after annealing to 500 °C.

A similar XPS experiment was performed on the nano-Fe_3O_4 NPs synthesized without gold to determine if the reduction behavior is exclusively due to the size effect of the nano-Fe_3O_4 or if gold plays an important role in the observed reduction phenomena. The spectra of the nano-Fe_3O_4, shown in Figure 5.3a, obtained from before heating and *in situ* are qualitatively similar to the Au-Fe_3O_4 DNPs, in terms of the peak positions and the shake-up features. Both show a reduction of Fe_3O_4 to FeO and Fe, but the difference arises in the relative concentration of the metallic iron formed. As shown in Figure 5.3a (red line), without the presence of gold, only 7.5% of the total iron signal appears as metallic iron compared to the 30% when gold is present (Figure 5.3a, blue line). These results prove that the nano-Fe_3O_4 is reducible even without gold, however, gold substantially accelerates the reduction phenomena. This effect is further analyzed below with DFT calculations on FeO, which represents a partially reduced iron oxide support. These results strongly imply that a novel, concerted nanosize- and metal-dependent reduction phenomena must exist to produce the observed difference in the reducibility between the nano-Fe_3O_4 and the extended Fe_3O_4.

TEM and XPS studies highlight the SMSB between Au and Fe_3O_4 in DNPs, as evidenced by wetting of Au nanoparticles during in situ annealing experiments. Furthermore, experimental results demonstrate that the SMSB is observed with a concomitant reduction of the iron oxide

surface. To provide an atomic-level description and interpretation of this phenomenon, we performed first principles Density Functional Theory (DFT) calculations of the gold/iron oxide interface. The interaction between progressively reduced iron oxide supports and Au nanoparticles was studied through a trend based analysis of the stability of Au (111) films on a range of extended iron oxide surfaces, with a variety of oxidation states, including Fe_2O_3 (0001), Fe_3O_4 (111), FeO (111), and Fe (110) surfaces, in order of decreasing iron oxidation state. The Au (111) films possess a pseudomorphic registry on Fe_2O_3 (0001), Fe_3O_4 (111) and FeO (111), while the film is modeled as a moiré pattern on Fe (110) to minimize strain effects (further details regarding lattice registries between films and substrates are presented in the SI). As DFT calculations of Au/Fe_3O_4 nanoparticles are computationally intractable, extended surface models are employed to provide approximate treatments of the gold/iron oxide interface, and thereby describe trends in how gold facilitates the reduction of the DNPs as nanoparticle.

Binding energies ($E^{binding}$) of Au films on the oxygen- and iron-terminated surfaces of iron oxide models (Equation 2), reflecting heats of adsorption of Au films on iron oxide substrates, are shown in Figure 5.4 a. The binding energies are referenced to bulk FCC Au.

$$E^{binding} = \frac{E_{Au\ on\ FexOy} - E_{FexOy} - N_{Au}E_{Au\ atom\ in\ bulk}}{N_{Au\ on\ surface}} \quad \ldots \text{ Equation 2.}$$

where E_i is the DFT calculated ground state energy of system i, and N_{Au} is number of Au atoms. A more negative value of the binding energy indicates stronger binding.

The total energy of bulk Au is corrected for nanoparticle size effects using the Gibbs–Thompson relation (see Supporting Information). The binding energy of Au (111) on the iron terminated (oxygen terminated) surfaces is represented on the right (left) for each iron oxide substrate in Figure 5.4a. Adsorption energies of surfaces terminated by mixtures of iron and oxygen atoms, which are between the two limiting cases discussed in Fig. 4 (a), are reported in SI. Au (111) interacts very weakly with the O terminated surface, as evidenced by the positive binding energies. In contrast, the adsorption energy of Au (111) on iron-terminated surfaces is quite exothermic, being -0.37 eV for Fe_2O_3 (0001), -0.20 eV for Fe_3O_4 (111), -0.80 eV for FeO (111) and -0.64 eV for Fe (110), where the energies have been normalized per gold atom at the interface. Moreover, the monotonic decrease in the binding energy of Au (111) with supports containing progressively lower iron oxidation states shows increased interaction between Au and the iron oxide surface upon reduction. Such a trend is fully consistent with the electron

microscopy and XPS observations which report a flattening of Au nanoparticles and concomitant reduction of the Au/iron oxide interface with increasing temperature.

DFT calculations were further combined with thermodynamic relations to construct *ab initio* phase diagrams of Au films supported on Fe_2O_3 (0001), Fe_3O_4 (111), and FeO (111) (see Supporting Information). The phase diagrams show that, at low oxygen chemical potentials (representing high temperatures and low oxygen partial pressures), Au (111) films on reduced iron oxide are the thermodynamically most stable phase, while at higher oxygen chemical potentials, the bare iron oxide supports show the highest stability. This result is also in line with the experimental observations that flattening of Au nanoparticles occurs at higher temperatures. Finally, the calculations show that the oxygen vacancy formation energy for FeO (111), which is the phase present immediately prior to metallic iron formation and full gold wetting, is lowered by 0.74 eV in the presence of an Au film, indicating that the formation of oxygen vacancy in FeO (111) becomes significantly more favorable in presence of Au. This evidence, concurrent with XPS results, demonstrate that Au NPs accelerate the latter stages of the reduction of iron oxide.

Overall, DFT calculations show progressively stronger binding of Au films with the reduction of the iron oxide support. The phase diagrams further confirm stability of Au films under a reducing environment with increasing temperature. Thus, stronger adhesion of thin films on reduced iron oxide and more favorable oxygen vacancy formation in the presence of Au lead to the increased stability of Au thin films on reduced iron oxide surfaces at high temperatures. DFT-based atomistic calculations therefore strongly support the SMSB between Au and Fe_3O_4 DNPs, as evidenced by the flattening of Au NPs through the *in-situ* TEM experiment.

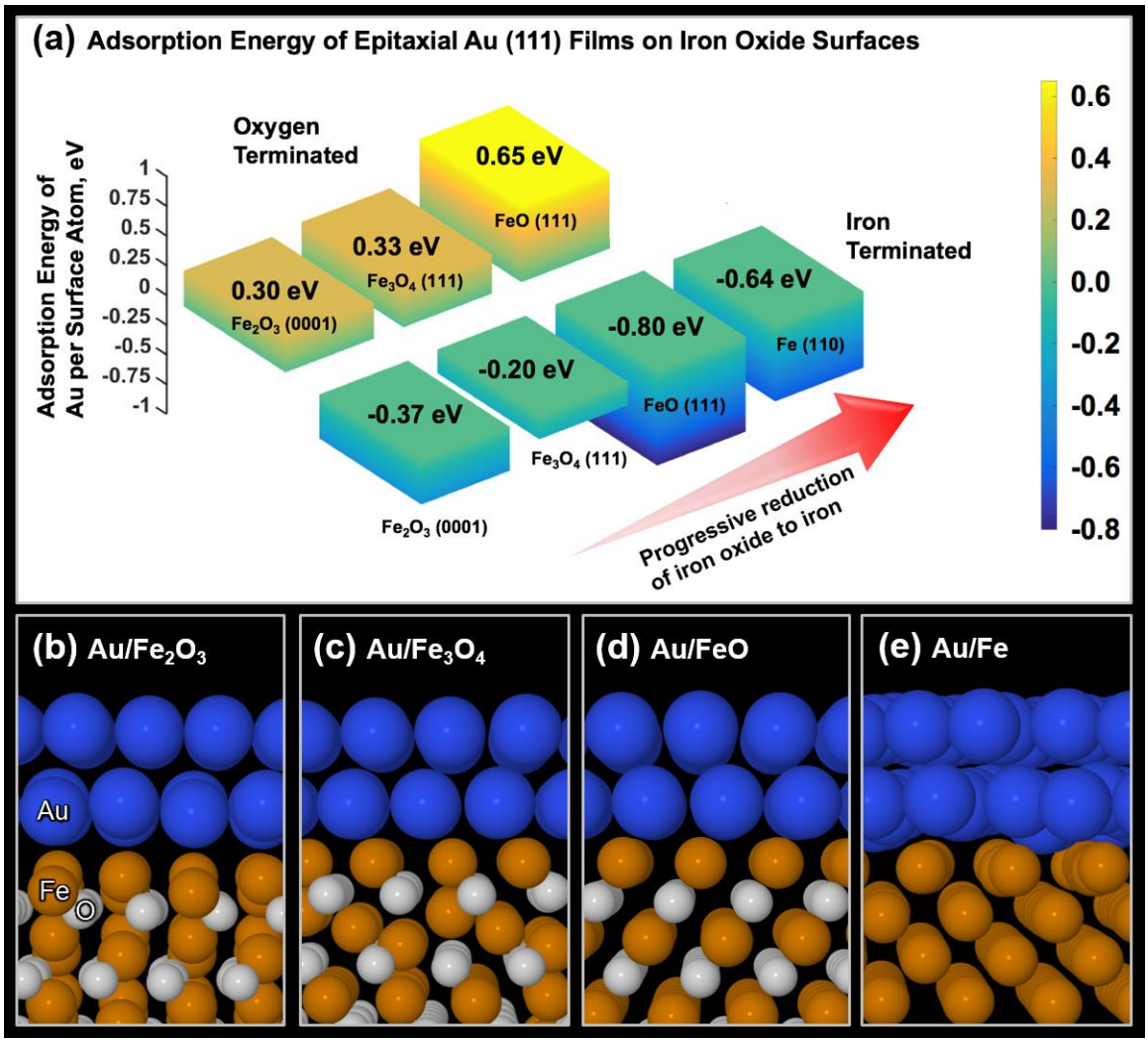

Figure 5.4 DFT calculation results. (a) Trends in adsorption energies of epitaxial Au (111) films as iron oxide is progressively reduced from Fe2O3 to Fe. Binding on the iron terminated surfaces (bars in the right) is significantly more favorable in comparison with oxygen terminated surfaces (bars in the left). The monotonic reduction in binding energy with reduction of iron oxide confirms experimental observations regarding an increase in wetting/SMSB between Au and iron oxide during in situ annealing. Binding energies are normalized by the number of gold atoms present at the interface. (b) 2 monolayered (ML) Au film supported on the 2-Fe termination of Fe2O3 (0001). (c) 2 ML Au film supported on the oct-1 Fe3O4 (111) termination. (d) 2 ML Au film adsorbed on Fe-terminated FeO (111) surface. (e) 2 ML Au (111) film adsorbed on the metallic Fe (110) surface (see SI for more information about adsorption configurations). Au, Fe, and O atoms are depicted in yellow, brown, and red, respectively.

5.5 Conclusions

In summary, we have employed a combination of in-situ TEM, XPS, and DFT calculations to obtain a mechanistic understanding of the wetting behavior of the gold

nanoparticles in dumbbell-like nanoparticle (DNP) assemblies with completely gold covered iron oxide domains during high temperature annealing. This drastic morphological change of Au is a direct evidence of the strong metal-support bonding (SMSB) between gold and iron oxide, which occurred during the vacuum annealing. The origin of the SMSB is attributed to a combination of the higher reducibility and higher concentration of the surface oxygen vacancies of the spherical nano-Fe3O4 (i.e., iron oxide domains of the DNPs) and to the direct interaction of the Au NP's with the iron oxide surface. In-situ STEM-EELS showed that the Au covered part of the nano-Fe3O4 was highly reduced. XPS experiments showed that the nano-Fe3O4 NPs were readily reduced during the vacuum annealing, while extended Fe3O4 thin films were highly stable against surface reduction. A series of our experimental results suggests a strong correlation between the wetting/SMSB and the surface reduction. DFT calculations further revealed that (1) thin Au films possess a stronger bonding to the iron oxide support with increasing reduction and (2) Au accelerates the vacancy formation in DNPs, thereby strongly supporting the experimentally observed wetting of Au nanoparticles on reduced iron oxide supports.

The SMSB observed in the Au-Fe3O4 DNPs is not only physically interesting but also practically important because it emphasizes the significance of the size and morphology control of a metal oxide support for tuning the metal-support bonding. Moreover, it opens up a novel way for preparing highly stable Au catalysts by optimizing the support size. In this regard, we believe that it is imperative to revisit the commonly utilized metal oxide supports and carefully investigate their size dependent properties owing to the fact that the metal-support interaction can potentially be very different with respect to the morphology and the size of materials, as we here observed. More importantly, this work demonstrates the prominence of nano-engineering to develop novel material systems ultimately for the development of improved catalysts and tunable and highly stable functional nanostructures for other applications, such as energy storage and conversion devices.

CHAPTER 6. REACTIVE METAL-SUPPORT INTERACTION AT MODERATE TEMPERATURE IN TWO-DIMENSIONAL NIOBIUM-CARBIDE-SUPPORTED PLATINUM CATALYSTS

6.1 Abstract

The reactive metal–support interaction (RMSI) offers electronic, geometric and compositional effects that can be used to tune catalytic active sites. Generally, supports other than oxides are disregarded as candidates for RMSI. Here, we report an example of non-oxide-based RMSI between platinum and Nb_2CT_xMXene—a recently developed, two-dimensional metal carbide. The surface functional groups of the two-dimensional carbide can be reduced, and a Pt–Nb surface alloy is formed at a moderate temperature (350 °C). Such an alloy exhibits weaker CO adsorption than monometallic platinum. Water-gas shift reaction kinetics reveals that the RMSI stabilizes the nanoparticles and creates alloy–MXene interfaces with higher H_2O activation ability compared with a non-reducible support or a bulk niobium carbide. This RMSI between platinum and the niobium MXene support can be extended to other members of the MXene family and opens new avenues for the facile design and manipulation of functional bimetallic catalysts.

6.2 Introduction

Supported bimetallic nanoparticles represent a wide range of catalysts with tunable compositions and electronic properties [154, 155]. Common strategies for preparing bimetallic catalysts include impregnation, reductive deposition precipitation and atomic layer deposition [154, 156]. Recently, a so-called reactive metal–support interaction (RMSI) has been shown to provide a facile route for preparing bimetallic alloys. RMSI refers to a chemical reaction between a metal and the support that induces the formation of bimetallic structures that may not be easy to obtain by other synthetic methods. The reducibility of the support plays a crucial role in its RMSI activity. For instance, materials with RMSIs involving reducible oxides, such as TiO_2 and CeO_2, can be prepared at lower temperatures than those involving hard-to-reduce oxides (such as SiO_2 and Al_2O_3)[20]. Until now, only oxide supports have been considered as candidates for RMSI, but high-temperature reductions (>550 °C) are often needed, which limits

the compositional variety of catalysts available, and may lead to particle agglomeration and difficulty in controlling the size of the nanoparticles [157, 158]. More reactive or reducible supports, such as carbides, represent an alternative that could be involved in RMSIs at lower temperatures and be prepared with well-dispersed active sites. Nonetheless, interactions between metals and supports other than oxides are not well understood even though they are key to establishing general rules for rational catalyst design via RMSI.

MXenes—a new family of two-dimensional (2D) metal carbides, nitrides or carbonitrides—are usually produced by selective extraction of the 'A' layers from layered ternary transition metal carbides called MAX phases[159]. This synthetic procedure generates surface termination groups within MXenes, including –OH, –O and –F groups. Thus, MXenes have the general formula $M_{n+1}X_nT_x$, where M represents an early transition metal, X is C or N, *n* varies from 1 to 3, T represents for the surface functional groups and *x* represents the uncertainty of the surface terminations[160]. To date, MXenes have been extensively developed as electrodes for batteries and supercapacitors due to their good electrical conductivities[161]. Recently, MXenes have started to gain attention in photo- and electrochemical applications due to their unique surface functional groups[162, 163]. Functional groups on the surface of supports have been known to facilitate the adsorption of metal precursors by electrostatic interactions and thus serve as anchors for active sites[164-166]. Atomic concentrations of O and F on the surface of Ti_2CT_xMXene decreased after hydrogen annealing at low temperature (227 °C)[167]. Removal of the terminal groups on the surface of the MXenes also exposes new terminal metal sites (for example, Nb, Ti and V) that are redox active[163]. For MXene-supported catalysts, these sites can also form admetal–support interfaces that are catalytically active. Moreover, highly reducible and reactive surfaces make MXenes promising candidates for involvement in RMSIs with metal nanoparticles. Considering the reducibility of the 2D carbides, RMSIs may occur at lower temperatures (<550 °C) for MXene-supported catalysts.

Here, we report a platinum nanoparticle catalyst supported on Nb_2CT_xMXene exhibiting an RMSI after reduction in H_2 at moderate temperature (350 °C). Quasi in situ X-ray photoelectron spectroscopy (XPS) indicate that the surface of the Nb_2CT_xMXene is reducible based on the removal of the surface –O and –OH terminations, and enrichment of Nb_2O_5 on the reduced MXene surface upon subsequent air exposure. Electron energy-loss spectroscopy (EELS) and in situ X-ray absorption spectroscopy (XAS) show that a Pt–Nb surface alloy is formed as a

result of the H_2 reduction. The water-gas shift (WGS) reaction was selected as a model reaction to understand the effects of RMSI on adsorbates and metal–support interfaces. WGS kinetics at 300 °C suggest that CO has a lower relative surface coverage on the Pt/Nb_2CT_x, and the alloy nanoparticles form active interfaces for H_2O activation with the reduced Nb_2CT_x MXene surface, which exhibits enhanced H_2O dissociation activity compared with Pt/Al_2O_3. In contrast with Pt/Nb_2CT_x, platinum supported by conventional bulk NbC was inert in the WGS reaction. The catalyst underwent significant particle agglomeration, and no alloy formation was observed. This work demonstrates that RMSI can be achieved on supports other than oxides, and 2D Nb_2CT_x MXene allows the catalyst to become involved in RMSIs at 350 °C while retaining control of the particle size.

6.3 Experimental

6.3.1 Synthesis of the Nb2AlC Phase

The Nb_2AlC powder was synthesized by spark plasma sintering of niobium, aluminium and graphite mixtures. Commercial powders of niobium (99.8%, 325-mesh), graphite (99%, 7–11 μm) and aluminium (99.5%, 325-mesh) were mixed in a molar ratio of Nb:Al:C = 2:1.4:0.9 in a graphite die coated with boron nitride. Excess aluminium and less than a full equivalent of graphite were added because aluminium is lost during high-temperature processing, and carbon deficiencies exist in most aluminium-containing MAX phases[101, 168]. Then, the material was loaded in a Fuji-211lx spark plasma sintering system and sintered at 1,500 °C under 30 MPa for 1 h. The resulting Nb_2AlC was then pulverized and sieved through a 325-mesh screen.

6.3.2 Preparation of Nb2CTx Mxene

Approximately 1 g of the prepared Nb_2AlC powder was immersed in 10 ml of 50% aqueous hydrofluoric acid solution for approximately 3 days at 55 °C. The resulting MXene suspension was repeatedly washed with deionized water and centrifuged at 8,900 r.p.m. until the pH reached ~5. The final MXene was dried under vacuum at room temperature and stored in a glove box until usage.

6.3.3 Preparation of the Pt/Nb2CTx Catalysts

Tetraamine platinum nitrate (99.995%; Sigma–Aldrich) was loaded on the Nb_2CT_x MXene and bulk NbC (99%; Sigma–Aldrich) supports by incipient-wetness impregnation. Specifically, a certain amount of platinum precursor was dissolved in deionized water to generate a solution with a concentration of $0.02\ g\ Pt\ ml^{-1}$. The solution was then added dropwise to the support until incipient-wetness impregnation (approximately $0.5\ ml\ g^{-1}$ of support). The mixture was then dried under vacuum at ambient temperature. The procedure was repeated once so the final catalyst (referred to as Pt/Nb_2CT_x fresh) had an empirical platinum loading of approximately 1–2%.

6.3.4 Determination of the WGS reaction kinetics

The WGS reaction was monitored in a parallel plug flow reactor, which has been described previously[21]. The WGS reaction rates were measured under differential conditions; namely, the conversion was maintained below 10% and the products of the WGS reaction (CO_2 and H_2) were also co-fed into the reaction system. The WGS rate can be expressed by the power rate law given below:

$$r=Aexp(-E_{app}RT)[CO]^a[CO^2]^b[H^2]^c[H^2O]^d(1-\beta)r=Aexp(-EappRT)[CO]a[CO2]b[H2]c[H2O]d(1-\beta) \quad (1)$$

where r is the overall rate, A and E_{app} are the apparent pre-exponential factor and activation energy for the forward rate, $R$is gas constant, and T is reaction temperature, respectively, a, b, c and d are the forward reaction orders, $\beta=([CO_2][H_2])/(K_{eq}[CO][H_2O])\beta=([CO2][H2])/(Keq[CO][H2O])$ is the approach to equilibrium, which measures the deviance from the equilibrium conditions, and K_{eq} is the equilibrium constant for the WGS reaction. Under the WGS conditions tested here, $\beta \ll 1\beta \ll 1$, implying the reaction is far from equilibrium.

For each measurement, approximately 300 mg of the as-prepared Pt/Nb_2CT_x catalyst was loaded into the reactor. The catalyst was pre-treated by reduction in 25% H_2/Ar at 350 °C for 2 h (the total flow rate was $50\ ml\ min^{-1}$ and the temperature ramping rate was $5\ °C\ min^{-1}$). After pre-treatment, the temperature was decreased to 300 °C and the catalysts were exposed to the WGS reaction mixture (standard conditions: 6.8% CO, 21.9% H_2O, 8.5% CO_2 and 37.4% H_2 balanced

by argon) at a flow rate of 75.4 ml min^{-1}. The catalyst was stabilized at 300 °C for a period of approximately 20 h to reach initial stabilization. The apparent reaction orders were measured over the stabilized catalyst by varying the partial pressures of one component at a time over the range of 4–21% for CO, 5–25% for CO_2, 11–34% for H_2O and 14–55% for H_2. The WGS reaction rate under standard conditions was determined after evaluation of each apparent reaction order to measure the deactivation, if there was any. For this catalyst, after the initial stabilization period, no significant deactivation was observed during the full test period (approximately 50 h). The apparent activation energy was measured under standard conditions by varying the temperature between 290 and 320 °C. The WGS rate was normalized by the total platinum loading or by the number of surface platinum atoms as determined by CO chemisorption. After all measurements had been taken, the catalysts were passivated at room temperature in 30 ml min^{-1} 2% O_2/Ar gas flow for 4 h before they were removed from the reactors.

6.4 Results

6.4.1 Preparation and Characterizations of the Nb2CTx support

The preparation of few-layer niobium MXene (Nb_2CT_x) via hydrofluoric acid treatment is summarized in the Methods. The X-ray diffraction pattern of the prepared Nb_2CT_x support (Supplementary Figure A.23) shows that the (002) peak of the hydrofluoric acid-treated Nb_2AlC powder shifted to 2θ of 9.3°, which corresponds to a c-lattice parameter of 19 Å compared with that observed in the initial MAX (Nb_2AlC) phase (13.9 Å). XAS was performed to confirm the structure of the niobium carbide MXene. The results of niobium K-edge X-ray absorption near-edge structure (XANES) analysis are presented in Figure 6.1a and show that the shape of the XANES spectrum of Nb_2CT_x is similar to that of commercial NbC (Sigma–Aldrich) but different from those of Nb_2AlC and Nb_2O_5 (Sigma–Aldrich). The edge energy of the MXene (19,000.7 eV) is close to that of NbC (19,000.2 eV) but distinct from those of Nb_2AlC (18,998.7 eV) and Nb_2O_5 (19,003.3 eV), which confirms the removal of aluminium from the parent MAX phase. The edge energy of Nb_2CT_x is slightly higher than that of NbC, suggesting that the Nb_2CT_x is partially oxidized due to the terminal groups or Nb_2O_5 on its surface[17]. X-ray absorption fine-structure (EXAFS) spectra (Figure 6.1b) were also used to confirm the 2D structure of the material since Nb_2CT_x showed first-shell (Nb–C) scattering similar to that of NbC but second-

shell (Nb–C–Nb) scattering much lower than that of NbC due to the reduced dimensionality. Moreover, the typical lamellar structure of Nb_2AlC (Supplementary Figure A.24a) was converted to an accordion-like structure (Figure 6.1c), confirming the exposure of individual grains along the basal planes. After mildly sonicating the Nb_2CT_x MXene multilayers in deaerated ethanol, few-layered electron transparent nanosheets could be obtained, as shown in the transmission electron microscopy (TEM) image (Figure 6.1d).

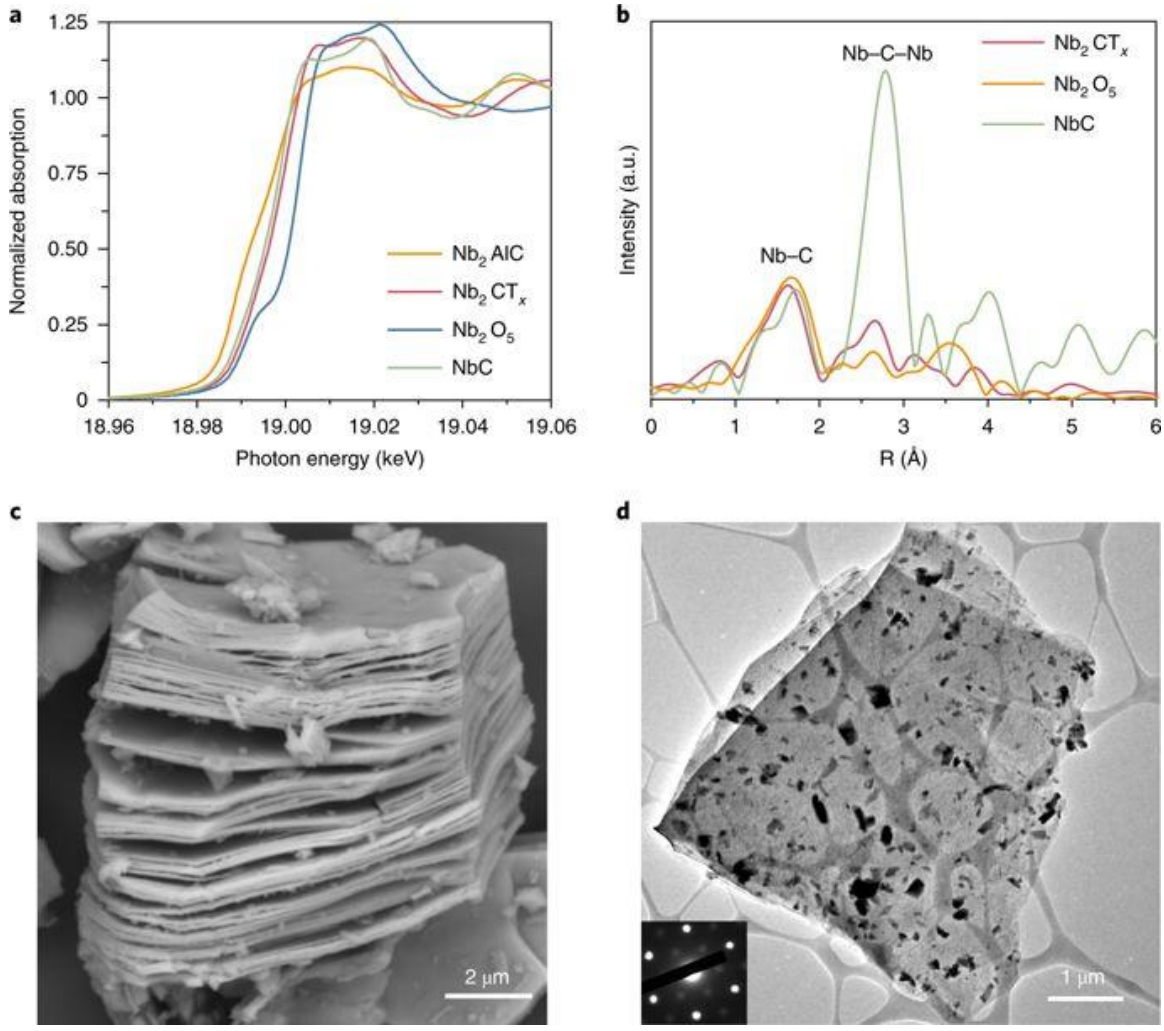

Figure 6.1 a, Niobium K-edge XANES of Nb2AlC, Nb2CT x MXene, NbC and Nb2O5. b, Fourier transforms of the k2 EXAFS of Nb2CT x compared with the references (NbC and Nb2O5). c, Scanning electron microscopy micrograph of Nb2CT x MXene. d, TEM image of Nb2CT x nanosheets. Inset: selected-area electron diffraction pattern showing hexagonal basal plane symmetry of the Nb2CT x nanosheets.

6.4.2 Kinetics of the WGS Reaction

Platinum was loaded onto the Nb_2CT_x support via incipient-wetness impregnation, as reported in ref. [169]. The platinum loading was estimated to be 1% by atomic absorption spectroscopy. The 1% Pt/Nb2CT x catalyst was then tested for activity in the WGS reaction under standard conditions (see Methods). As shown in Figure 6.2a, the catalyst was stable under the conditions used for the WGS reaction kinetics tests. The WGS reaction rate per mole of platinum in 1% Pt/Nb2CT x measured at 300 °C was 0.016 mol H2 (mol Pt)−1 s−1, and the apparent activation energy was 71 ± 3 kJ mol−1 (Supplementary Figure A.25). The spent 1% Pt/Nb2CT x catalyst had an average particle size of approximately 2.6 ± 0.6 nm based on high-angle annular dark field scanning transmission electron microscopy (HAADF-STEM) (Supplementary Figure A.26), which showed that the MXene support stabilized small platinum nanoparticles. We selected the 1.5% Pt/Al2O3 catalyst (Table 6.1) from our previous work19 as the reference catalyst because the particle size (estimated by platinum dispersion) is comparable to that of the 1% Pt/Nb2CT xcatalyst. Moreover, Al2O3 is considered a non-reducible oxide at the moderate reduction temperature (350 °C) in contrast with the reducible Nb2CT x support. Although, according to CO chemisorption, 35% of the platinum was exposed on the surface of the 1.5% Pt/Al2O3 catalyst, we did not observe any measurable CO uptake at ambient temperature or at −30 °C for the fresh 1% Pt/Nb2CT x catalyst after it was reduced in situ at 350 °C (Supplementary Methods). The suppressed CO chemisorption was not due to particle agglomeration, and the average particle size of 1% Pt/Nb2CT x should have corresponded to an estimated dispersion of 38%. This large discrepancy can be attributed to surface alloy formation due to the reducible surface of the niobium MXene-supported catalyst, which will be discussed later. No measurable WGS conversion was observed for platinum supported by commercial NbC (bulk) under the same WGS test conditions. We found that the platinum particles had sintered significantly (average particle size: ~13.8 ± 9.6 nm) in the Pt/NbC (bulk) catalyst (Supplementary Figure A.26). The agglomeration of nanoparticles substantially reduced the number of metal–support interface sites, which presumably led to the observed loss in WGS activity.

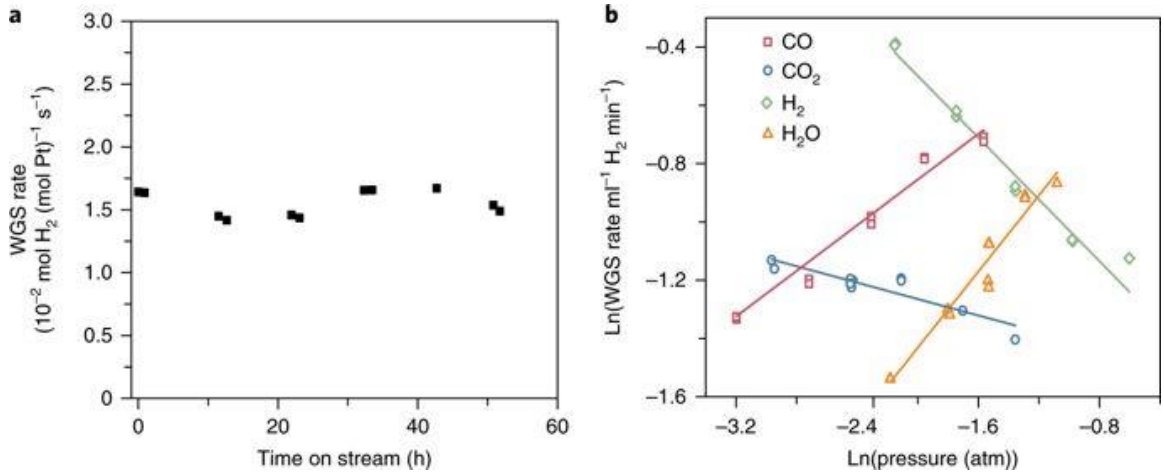

Figure 6.2 a, WGS rates normalized by the amount of platinum in the 1% Pt/Nb2CT x catalyst. The rates were measured at 300 °C with a feed composition of 6.8% CO, 21.9% H2O, 8.5% CO2 and 37.4% H2 balanced by argon (standard conditions). b, Apparent reaction orders for CO, CO2, H2 and H2O for 1% Pt/Nb2CT x . Reaction orders were determined under standard conditions, with each component varying in the following range: 4–21% for CO, 5–25% for CO2, 11–34% for H2O and 14–55% for H2.

Table 6.1 WGS kinetics of Pt/Nb2CT x and Pt/Al2O3

Catalysts	WGSs rates at 300 °C (10^{-2} mol H_2 (mol Pt)$^{-1}$ s^{-1})	TOR at 300 °C (10^{-2} mol H_2(mol surface metal)$^{-1}$ s^{-1}	E_a (kJ mol^{-1}) (±3)	Reaction orders (±0.03)				Percentage of exposed Pt (%)
				H_2O	CO_2	CO	H_2	
1% Pt/Nb_2CT_xMXene	1.6	−	71	0.65	−0.09	0.39	−0.47	−
1.5% Pt/Al_2O_3(ref. 19)	1.4	4	96	0.9	−0.1	0.1	−0.5	35

1. E_a, activation energy; TOR, turnover rate

The apparent reaction orders are shown in Figure 6.2b and Table 6.1. As the log derivative analysis of the Langmuir–Hinshelwood mechanism (Supplementary Methods) shows, the apparent reaction order may be related to the relative surface coverage of the corresponding adsorbates. Lower apparent reaction orders with respect to certain reactants imply higher relative coverage of the adsorbed species[169]. Compared with the Pt/Al_2O_3 catalyst, Pt/Nb_2CT_x showed a higher apparent reaction order with respect to CO, which suggests that CO adsorption is weaker on the MXene-supported catalyst. At the same time, Pt/Nb_2CT_x had a lower apparent reaction order with respect to H_2O, indicating that the MXene support has a stronger H_2O adsorption affinity than that of Al_2O_3. Previous studies have also reported that the support surface plays a significant role in the activation of H_2O during the WGS reaction, and that the most active site of WGS is at the metal–support interface[170]. Here, Nb_2CT_x outperforms Al_2O_3 as a support for WGS catalysis due to its stronger interactions with H_2O or hydroxyl groups. The apparent reaction order for CO_2 was slightly negative and approached zero for both catalysts, which can be attributed to the weak interaction between the surface of the platinum and CO_2. The apparent reaction order with respect to H_2 was −0.47 for Pt/Nb_2CT_x, which is indicative of H_2 inhibition of the forward WGS reaction. The inhibition indicates that H_2 competes with CO for the limited number of active sites.

6.4.3 Reducibility of the Pt/Nb2CTx Catalysts

To understand the change in the Nb_2CT_x MXene support after H_2 reduction, a series of quasi in situ XPS measurements were carried out (Supplementary Methods). In the niobium 3*d* spectrum of a fresh Pt/Nb_2CT_x sample (top spectrum in Figure 6.3a), three pairs of peaks at 204.1/206.8 eV, 205.5/208.3 eV and 207.4/210.1 eV were identified as the $3d_{5/2}/3d_{3/2}$ doublets of Nb–C, $NbC_xO_yF_z$ and Nb_2O_5, respectively[171]. The presence of surface terminations (–OH, –O and –F associated with the $NbC_xO_yF_z$ species) on the fresh Pt/Nb_2CT_x catalyst was also confirmed by high-resolution spectra in the O 1*s* and F 1*s* regions (bottom spectra in Figure 6.3b,c). The fresh Pt/Nb_2CT_x catalyst was then reduced at 350 or 550 °C (designated as R350 °C and R550 °C, respectively) and the samples were analysed by XPS under ultrahigh vacuum conditions without exposure to air. Figure 6.3a shows the XPS spectra of the niobium 3*d* regions of the samples reduced at 350 and 550 °C, and the sample reduced at 350 °C and then exposed to air. The negligible change in the peaks corresponding to Nb–C (204.1 eV) indicates that the

structure of Nb_2CT_x MXene was preserved after reduction at both 350 and 550 °C. However, after exposing the reduced sample to air, the intensity of the carbide peak decreased dramatically, and the Nb(V) oxide peak became better resolved (Figure 6.3a), which implies that the oxide species (Nb_2O_5) is enriched on the surface of the material, and the surface Nb–C partly decomposes. Moreover, after reduction at 350 °C (Figure 6.3b,c), the peaks for the adsorbed O and terminal OH/O groups that were present on the fresh Pt/Nb_2CT_x surface disappeared, indicating that these surface OH/O terminations can be effectively removed. Following H_2 temperature-programmed reduction of Nb_2CT_x MXene, a peak indicative of H_2O at 340 °C appeared (Supplementary Figure A.28), which was probably due to the removal of the O and OH functional groups. The atomic concentration of F terminations, as estimated by XPS analysis, decreased from 4 to 1.8% after reduction at 350 °C, but these were completely removed in the higher-temperature reduction (550 °C) (Figure 6.3c). The higher temperature required to remove the F moieties indicates that F groups bind more strongly than OH/O groups to the surface of the MXene. The results of the quasi in situ XPS analysis suggest that the surface of the catalyst is reduced under moderate temperature (350 °C). It is plausible that with the removal of surface functional groups from MXene, its coordinatively unsaturated surface is prone to oxidation in air, which suggests that the reduced surface is highly redox active.

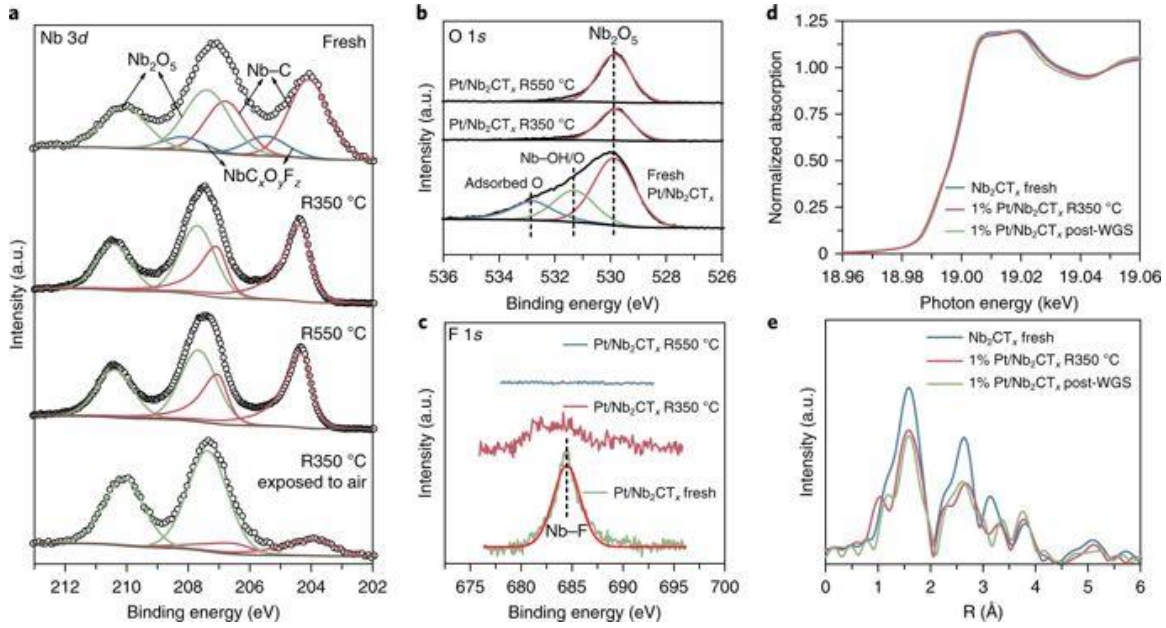

Figure 6.3 a, Niobium 3d region of ex situ XPS of a fresh 1% Pt/Nb2CT x sample, quasi in situ XPS of 1% Pt/Nb2CT x reduced at 350 and 550 °C, and ex situ XPS of 1% Pt/Nb2CT x reduced at 350 °C and exposed to air before analysis. b, Quasi in situ XPS of the O 1s region of 1% Pt/Nb2CT x reduced at 350 and 550 °C. c, Quasi in situ XPS of the F 1s region of 1% Pt/Nb2CT x reduced at 350 and 550 °C. d, XANES spectra of the niobium K-edge of fresh Nb2CT x scanned in air, fresh 1% Pt/Nb2CT x treated with 3% H2/He at 350 °C (in situ) and post-WGS reaction 1% Pt/Nb2CT x catalyst scanned in air. e, Fourier transform magnitude of the k2 EXAFS of fresh Nb2CT x , reduced fresh 1% Pt/Nb2CT x and post-WGS reaction 1% Pt/Nb2CT x catalyst. All treatments were the same as those used to collect the XANES spectra.

Pt/Nb_2CT_x samples with different treatments (fresh, 350 °C reduced and post-WGS) were also investigated by niobium K-edge XAS analysis (Figure 6.3d,e). In the spent Pt/Nb_2CT_x catalyst and fresh Pt/Nb_2CT_x sample reduced by H_2 at 350 °C, the supports maintained the same carbide structure matrix as was present in the fresh Pt/Nb_2CT_x, based on the minimal changes observed in the XANES spectra. The scattering intensity in the EXAFS decreased slightly, which probably corresponded to the decrease in the number of ligands on the surface of Nb_2CT_x. The spent catalyst still showed the typical accordion-like structure of MXene (Supplementary Figure A.24) and the characteristic diffraction features of carbide (Supplementary Figure A.30), suggesting that the MXene support did not collapse during the WGS reaction. Therefore, our results indicate that the main structure of Nb_2CT_x remains intact during the reduction and WGS reaction, but the surface of Nb_2CT_x can be reduced at the

moderate temperature (350 °C). The reducibility of the Nb_2CT_x support suggests that it can be used to introduce significant metal–support interactions to the catalyst.

6.4.4 RMSI

The interaction between platinum and the Nb_2CT_x support and the corresponding changes in the nanoparticles were further investigated by in situ platinum L_{III} edge XAS as well as platinum region XPS. For the platinum L_{III} edge XANES (Figure 6.4a), the whiteline of the 1% Pt/Nb_2CT_x catalyst reduced at 350 °C was more intense and narrower in shape than that of 2% Pt/Al_2O_3, which indicates the presence of non-platinum neighbours surrounding the platinum atoms. The change in the nanoparticle structure was also reflected by the altered EXAFS (Figure 6.4b) of the Pt/Nb_2CT_x catalyst compared with that of monometallic platinum on Al_2O_3. The relative intensities of the peaks were different in the metal–metal distance region, suggesting that Pt–Nb interferes with Pt–Pt scattering; that is, through the formation of a bimetallic structure. Our fitting results of Pt/Nb_2CT_x reduced at 350 °C (7.4 Pt–Pt bond at 2.75 Å and 0.9 Pt–Nb bond at 2.76 Å) imply that a Pt-rich bimetallic surface alloy is formed at this moderate temperature, which indicates that RMSI occurs between the platinum nanoparticles and the Nb_2CT_x support.

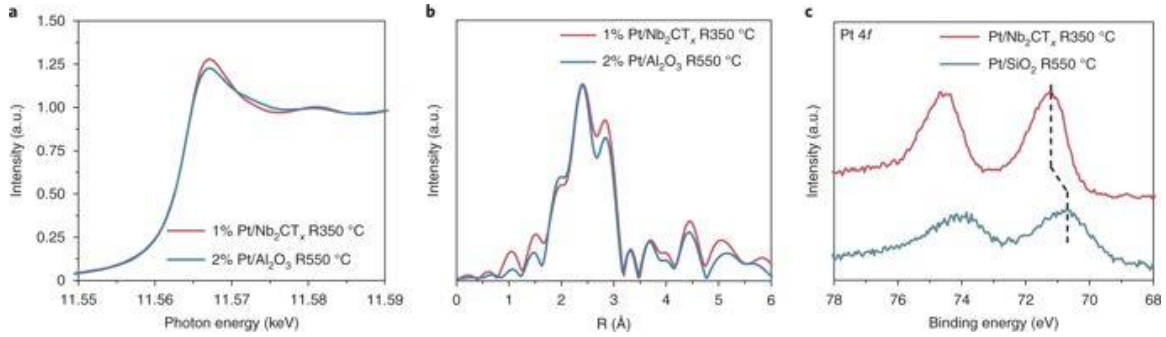

Figure 6.4 **a**, In situ XANES spectra of the platinum L_{III} edge of the 2% Pt/Al_2O_3 sample treated at 550 °C and fresh 1% Pt/Nb_2CT_x treated at 350 °C in 3% H_2/He. **b**, Fourier transform magnitude of the k^2 EXAFS of the 2% Pt/Al_2O_3 sample treated at 550 °C and fresh 1% Pt/Nb_2CT_x treated at 350 °C in 3% H_2/He. **c**, Quasi in situ XPS spectra of platinum 4*f* of Pt/SiO_2 reduced at 550 °C and 1% Pt/Nb_2CT_x reduced at 350 °C.

Quasi in situ XPS analysis was also conducted to investigate the potential electronic effect of the formation of the bimetallic surface alloy. We used Pt/SiO_2 as a reference instead of Pt/Al_2O_3 because the aluminium 2*p* region overlaps with the platinum 4*f* region, and SiO_2 is a non-reducible oxide similar to Al_2O_3. In previous works on Pt–M alloy systems (M = Sn, Co, Ru

or Ti), the binding energies of platinum were reported to shift to higher values with respect to pure Pt[172-174]. In our XPS spectra (Figure 6.4c), the platinum $4f_{7/2}$ binding energy exhibited a positive shift (~0.5 eV) for Pt/Nb_2CT_x compared with Pt/SiO_2, which is consistent with the literature and is indicative of the formation of a Pt–Nb bimetallic structure. When the reduction temperature was increased to 550 °C, similar changes of a greater magnitude were observed in the XPS and XAS analyses, and corresponded to a higher-degree alloy formation. We discuss this in more detail in Supplementary Figure A.31. Previous DFT studies suggest that the formation of alloys with transition metals modifies the electronic structure of platinum atoms and leads to shifts in the d-band centres, which could weaken CO adsorption[173, 175, 176]. This electronic effect resulting from the formation of the Pt–Nb surface alloy explains the suppressed CO chemisorption, as well as the altered relative coverage of CO on the Pt/Nb_2CT_x catalyst.

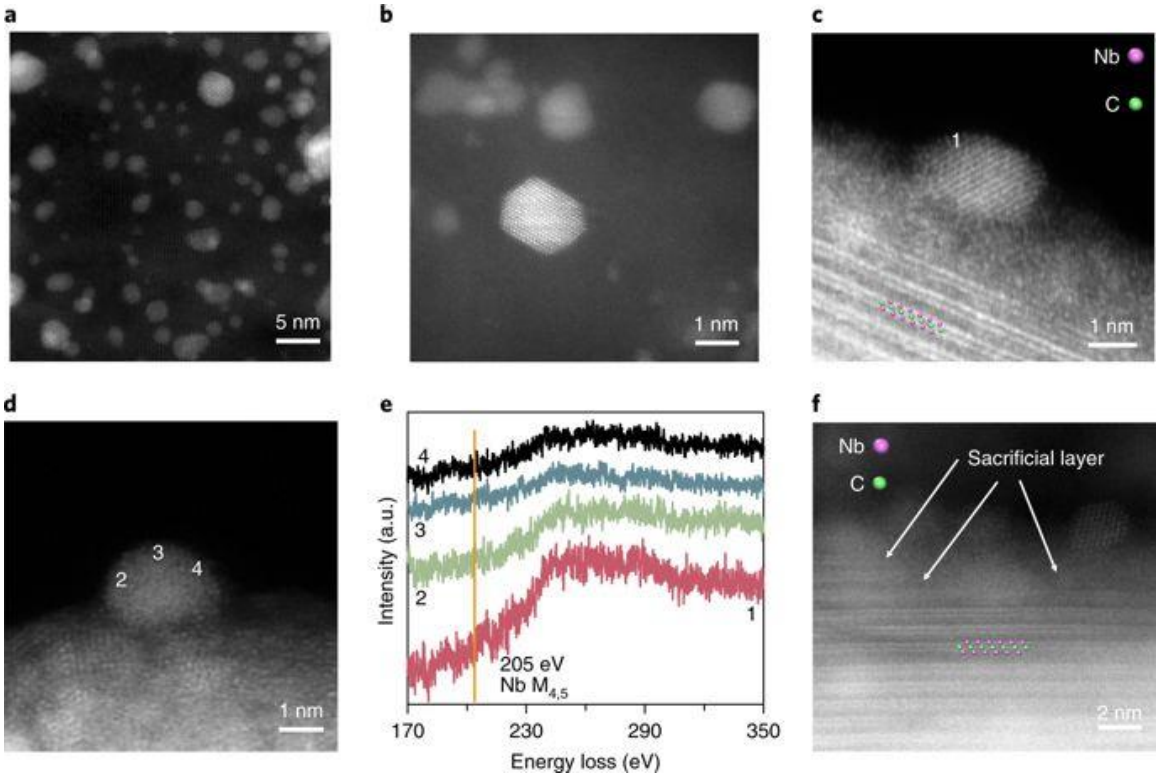

Figure 6.5 a,b, High-angle annular dark-field scanning TEM (HAADF-STEM) images of the post-WGS 1% Pt/Nb2CT x catalyst. c,d, HAADF-STEM images of typical nanoparticles supported by Nb2CT x MXene. The majority of each particle is hanging over the vacuum to avoid niobium interference from the support. e, EELS images acquired at several points on the particle surface, the locations of which are shown by corresponding numbers in c and d. f, HAADF-STEM image showing discontinuous Nb2CT x MXene layers.

Although the in situ XAS and energy-dispersive spectroscopy (EDS) results (Supplementary Figure A.32) suggest that a uniform bulk alloy was not formed after reduction at the moderate temperature (350 °C), EELS in an aberration-corrected STEM was employed to provide a more direct characterization of the near-surface region of the Pt–Nb nanoparticles. Figure 6.5a shows typical Nb_2CT_x MXene-supported nanoparticles with an average particle size of approximately 2.6 nm. The two-dimensionality of the MXene facilitates the STEM characterization of supported nanoparticles relative to conventional bulk carbide, so a twinned nanoparticle 3 nm in diameter can be atomically resolved (Figure 6.5b). Figure 6.5c,d shows Z-contrast STEM images of typical Pt–Nb alloy nanoparticles approximately 3 nm in diameter. The particles are only partially attached to the Nb_2CT_x MXene to avoid signals from the support. Energy-loss spectra were taken with the electron beam scattering through several different points around the surface edge of the particles. The spectra from the edge of the nanoparticles provided electronic information primarily on near-surface atoms and exhibited a distinct 205 eV onset absorption band for niobium $M_{4,5}$ (Figure 6.5e), which indicates that niobium atoms are present on the surface of the particles. In comparison, we did not observe Pt–Nb alloy formation in the Pt/NbC (bulk) catalysts that were tested under the same conditions (Supplementary Figure A.33). This finding is consistent with previous work showing that platinum did not form an alloy with bulk carbide at moderate temperature, including Mo_2C that had been reduced at 450 °C[177], and these findings emphasize the significant role that the reducibility of MXenes plays in the RMSI.

Figure 6.5f shows nanoparticles supported by three-atom-thick Nb_2CT_x MXene layers. The MXene layers that were close to the nanoparticles decomposed (discontinued) and sacrificial layers were formed directly beneath the Pt–Nb particles. Taking the in situ XAS results in conjunction with the XPS results, this sacrificial layer may be the result of RMSI occurring at the interface between MXene and the nanoparticles. In addition, with the removal of surface terminations such as –OH, –O and –F, exposed terminal niobium sites are generated on the surface of the Nb_2CT_x MXene support. These exposed niobium metal terminals are in contact with the Pt–Nb surface alloy and form interfaces that have strong affinities for H_2O or OH, as indicated by the WGS kinetics. The RMSI stabilizes and disperses the nanoparticles (~2.6 nm), which creates more interfaces than Pt/NbC (bulk) catalysts. Since the active sites of the WGS reaction are often thought to be the metal–support interfaces that are responsible for H_2O dissociation[178], the newly generated interfaces (with higher H_2O coverage than the Pt/Al_2O_3)

are presumed to make Pt/Nb_2CT_x an active WGS catalyst. Thus, the Pt/Nb_2CT_x catalyst becomes involved in RMSIs after reduction at the moderate temperature (350 °C), which probably tunes the catalytic properties through alloy formation, as well as modifying the admetal–support interface. Neither of these effects can be achieved using the conventional bulk niobium carbide.

Previous studies have shown that surface functional groups are not unique to Nb2CT x [160]. Considering the shared characteristics of the MXene family (prepared by etching)[161], such as reducible surface terminations and 2D structures, it is anticipated that RMSIs similar to the one between platinum and Nb2CT x MXene also apply to other MXene materials. We further investigated Ti3C2T x —another important member of the MXene family—as the support for platinum at 1% loading. EDS elemental mapping (Supplementary Figure A.34) was acquired in an area where nanoparticles were partially attached to the Ti3C2T x support to avoid the titanium signals from the MXene. The distribution of platinum and titanium overlapped through the nanoparticles, indicating the formation of Pt–Ti bimetallic structures. This result suggests that RMSIs can be extended to members of the MXenes family other than Nb2CT x , which showcases the generality of using MXenes as supports for preparing bimetallic catalysts.

6.5 Conclusions

In summary, we have demonstrated that 2D Nb_2CT_x MXene can be used as support for platinum and become involved in RMSIs after reduction at a moderate temperature (350 °C). The RMSI induces the formation of a bimetallic surface alloy and admetal–Nb_2CT_x interfaces that impact CO adsorption, H_2O activation and, ultimately, the kinetics of the WGS reaction. The highly reducible surface of Nb_2CT_x is vital to the introduction of the RMSI. The RMSI can be further extended to the $Pt/Ti_3C_2T_x$ system with the formation of Pt–Ti bimetallic nanoparticles. Taken together, our results indicate that the RMSI between platinum and 2D carbides is probably a general phenomenon for members of the MXene family, which will open new avenues for designing bimetallic catalysts.

APPENDIX A. SUPPLEMENTAL INFORMATION

SI – CHAPTER 3

Gas Phase FTIR Peak Assignments.

Table A.1 Observed FTIR peaks, references, and vibrational mode assignments for batch reactor charged with 1 Torr HCOOH, 800 Torr total pressure (balance N_2) and held at room temperature.

	Frequency / cm^{-1}	Reference(s)	Assignment*
HCOOH	1033	1033,[179] 1033.4[180]	δ(CH)
	1106	1103.8,[181] 1105,[179] 1105.4[180]	ν(C-O),[179, 181] COH-CO def.[180]
	1393	1380.6,[181] 1387,[179] 1387.0[180]	δ(CH),[179, 180] δ(H-C=O)[181]
	1774	1776.6,[181] 1770,[179] 1776.2[180]	ν(C=O)
	2945	2942.0,[181] 2943,[179] 2943.8[180]	ν(CH)
	3568	3568.9,[181] 3570,[179] 3570.0[180]	ν(OH)
$(HCOOH)_2$	925	917[182]	δ(OH)
	1218	1214.0,[181] 1218[182]	ν(C-O)
	1308	1283[182]	n.a.
	1363	1365[182]	δ(CH)
	1918	1923[182]	n.a.
	2200	2222[182]	n.a.

2416	2427,[182] 2415[183]	ν(C=O)+ δ(OCO) or 2ν(C-O)[183]
2570	2582,[182] 2570[183]	δ(OH) + ν(C-O)[183]
2613	2623,[182] 2610[183]	δ(OH) + ν(C-O)[183]
2723	2735,[182] 2722[183]	2δ(OH)[183]
2813	2815,[182] 2810[183]	ν(C=O)+ ν(C-O)[183]
2875	2856[183]	ν(C=O)+ ν(C-O)
2887	2886[182]	n/a
3015	3028[182], 2990[183]	ν(C=O)+ δ(OH)[183]
3055	3040[183]	ν(C=O)+ δ(OH)
3104	3110[182, 183]	ν(C=O)+ δ(OH),[183] ν(OH)[182]
3136	3150[182]	n.a.
3389	3385,[182] 3362[183]	ν(C=O)+ ν(C=O)[183]

*Assignments without references are unanimous for references for that mode in the "Reference(s)" column.

n.a. = Not Available.

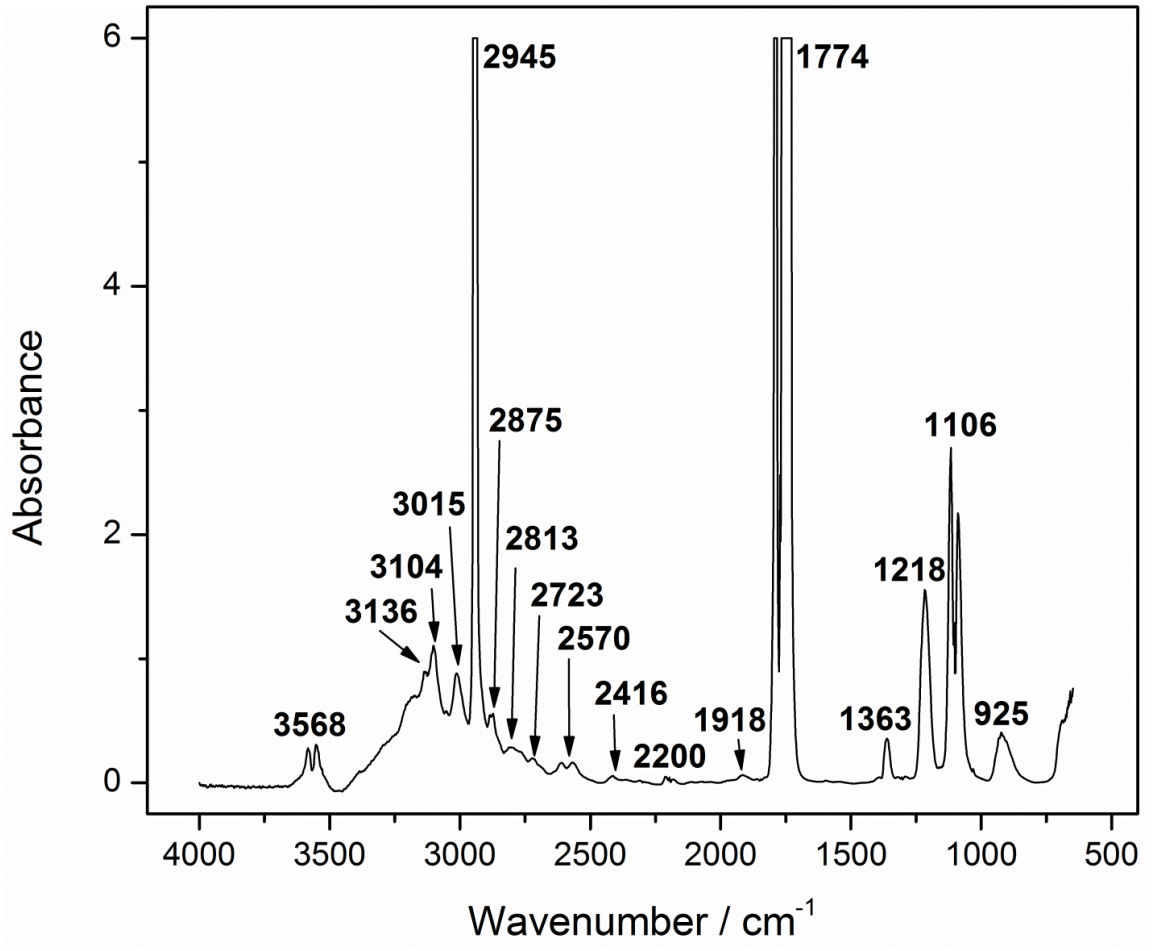

Figure A.1 FTIR spectrum of reactor gas cell charged with 1 Torr HCOOH, 800 Torr total pressure (balance N_2).

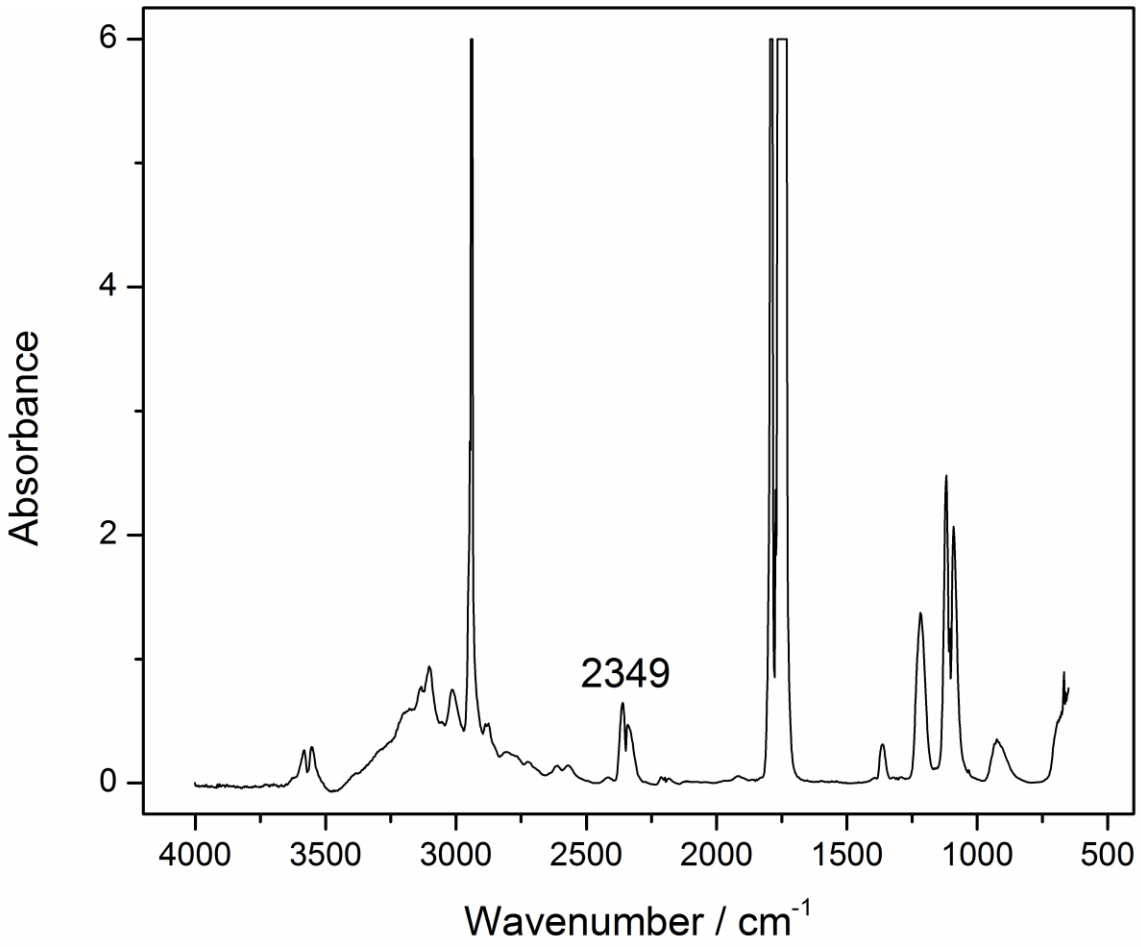

Figure A.2 FTIR spectrum of reactor gas cell charged with 1 Torr HCOOH, 800 Torr total pressure (balance N_2) after reaction at 200°C for 52 minutes.

SI – CHAPTER 4

A. XPS Overlayer model

- **Coverage estimation by an non-attenuated overlayer model:**

$$Coverage \equiv \frac{s_l}{s_s} = \frac{N_l(\theta) \times \Omega_s(E_s) \times A_S(E_s) \times \frac{d\sigma_s}{d\Omega} \times \Lambda_e^{subst}(E_s) \times cos\theta}{N_s(\theta) \times \Omega_l(E_l) \times A_l(E_l) \times \frac{d\sigma_l}{d\Omega} \times d_s}$$

- **Overlayer thickness estimation by an attenuated model:**

$$\frac{N_l(\theta)}{N_s(\theta)} = \frac{I_l \times \rho_l \times \frac{d\sigma_l}{d\Omega} \times \Lambda_l(E_l) \times cos\theta}{I_s \times \rho_s \times \frac{d\sigma_s}{d\Omega} \times \Lambda_s(E_s) \times cos\theta} \times \frac{\left(1 - exp\left(\frac{-t}{\Lambda_l(E_l) \times cos\theta}\right)\right)}{\left(exp\left(\frac{-t}{\Lambda_l(E_s) \times cos\theta}\right)\right)}$$

ρ … Atom density / cm^{-3}
I … X-ray flux (constant)
$\frac{d\sigma}{d\Omega}$… differential cross section
θ … analysis angle
t … overlayer thickness
N … normalized XPS Intensity (peak area)
$\Lambda(E)$ … electron attenuation length (from SRD 82 data base [184])
d_s … average separation of layers in substrate
$\Omega(E)$ … acceptance solid angle of the analyzer (constant)
$A(E)$ … effective substrate area (constant)
s… mean 2D surface atom density

Indices:
$_s$….. substrate
$_l$…… overlayer/adlayer

The Coverage is unitless and defined by the ratio of mean 2D surface atom density of substrate to mean 2D surface atom density of overlayer. It gives the (fractional) monolayer coverage of the atomic species.

The parameters used for calculation are summarized in the following Table A.2:

Table A.2 Parameters for coverage and film thickness estimation via XPS

	E_{kin} /eV	EAL / Å		
Zr 3d $_{5/2}$ in ZrO_2	195	4.77	d (Pd)	2.25 Å
	1074	16.97		
Pd 3d in Pd	125	3.70	Atom density in	2.98×10^{22} cm^{-3}
	919	13.07	ZrO_2	
Pd 3d in ZrO_2	125	3.86	Atom density in Pd	6.78×10^{22} cm^{-3}
	919	14.92		
EAL for 11 Å Pd	125	3.3		
EAL for 33 Å Pd	919	11.5		

B *In situ* XPS of ALD

The similar increasing of Zr coverage was confirmed by *in situ* XPS as shown Figure A.3. The ZTB pressure in the NAP-apparatus was 6×10^{-6} mbar and the base pressure around 5×10^{-8} mbar; each spectrum was collected for 30 min. In the inset of the figure, the Zr 3d integrated peak area is plotted versus the exposure time. It is worth noting, that a smooth start of the Zr deposition is followed by a linear growth after about 100 s.

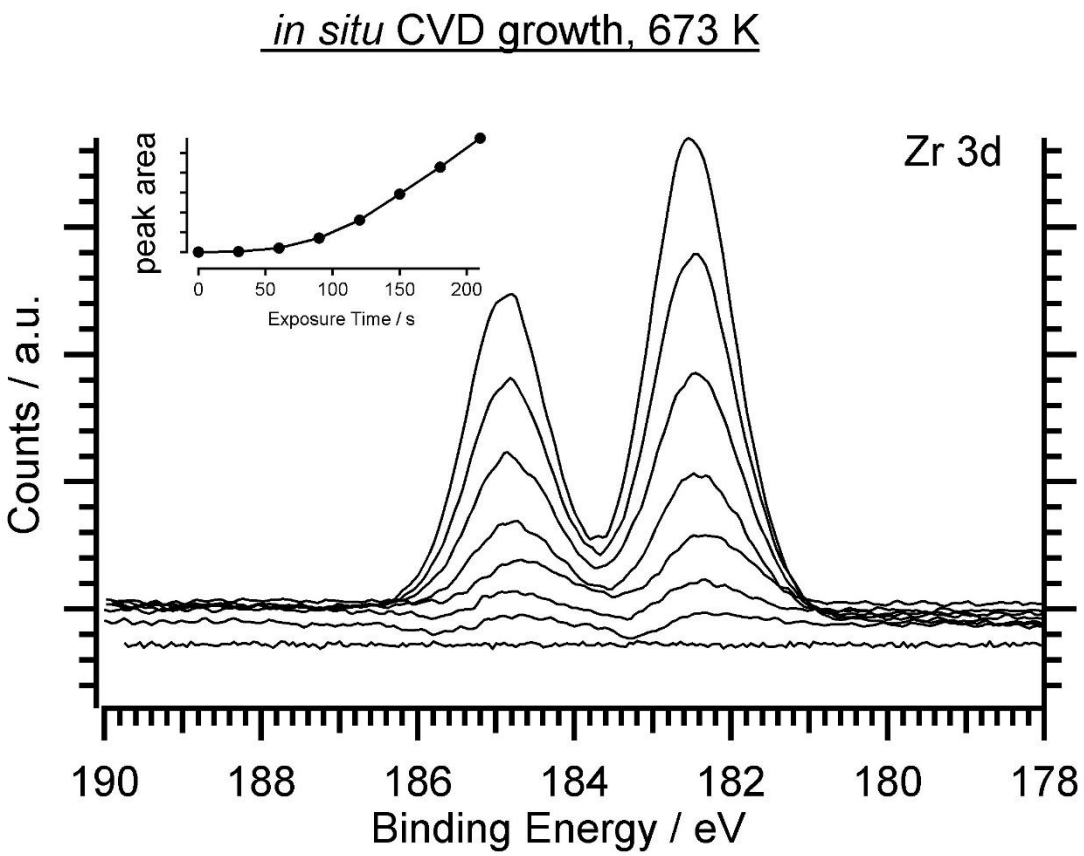

Figure A.3 *In situ* CVD growth monitored at 673 K in 5x10-6 mbar ZTB (one spectrum each 30 sec). The inset shows the peak area evolution with exposure time.

C XPS Following Molecular Adsorption of ZTB

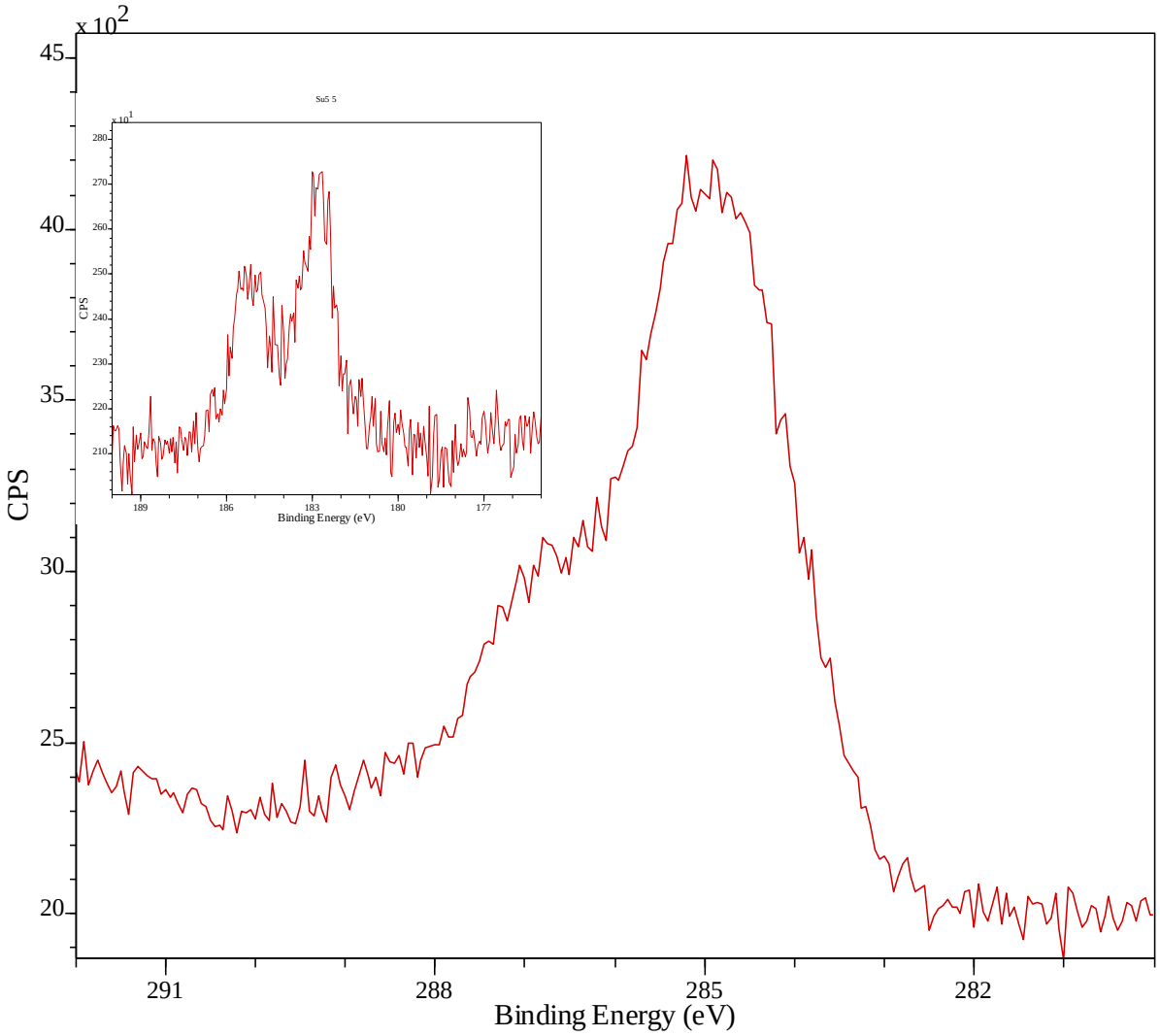

Figure A.4 C 1s spectra following 2000L of ZTB exposure at 140K and subsequent heating to 273K. The inset shows the Zr 3d peak under the same conditions.

D Summary of ZTB HREELS Peak Assignments

Table A.3 Major HREELS Peaks Observed from Pd(111) After Various Deposition Procedures[1]

	Energy Loss (cm^{-1}) (This work)	Vibrational Frequency (cm^{-1}) (Literature)	Assignment
ZTB Molecular Adsorption	297^{w}	300[95]	NA
	370^{vw}	357[95]	NA
	483^{w}	481[185]	Zr-O vibrations
	552^{s}	550[185]	Zr-O vibrations
	780^{vw}	765[96]	ν(C-C)
	906^{vw}	924[96]	$\delta(CH_3)$
	1006^{s}	1027[96]	τ(HCCC)
	1192^{w}	1151[96]	δ(C-C-C)
	1238^{sh}	1221 & 1242[96]	ν(C-C-C)
	1372^{vw}	1348 & 1366[96]	$\delta_s(CH_3)$
	1463^{vw}	1449[96]	$\delta_{as}(CH_3)+ \tau$(HCCC)
	2967^{br}	2930-3009[96]	$\nu(C-H_x)$
ZTB adsorption at RT	281^{w}	300[95]	NA
	333^{sh}	357[95]	NA
	480^{w}	481[185]	Zr-O vibrations
	513^{s}	522[185]	Zr-O vibrations
	579^{vw}	550[185]	Zr-O vibrations
	752^{s}	765[96]	ν(C-C)
	854^{s}	844[96]	ν(C-C)
	925^{s}	924[96]	$\delta(CH_3)$
	1008^{vw}	1027[96]	τ(HCCC)
	1137^{vw}	1151[96]	τ(HCCC)

[1] Abbreviations: w, weak; s, strong; sh, shoulder; br, broad. NA: not assigned.

	1194^{vw}	1151[96]	δ(C-C-C)
	1322^{vw}	1348 & 1366[96]	$\delta_s(CH_3)$
	1368^{vw}	1348 & 1366[96]	$\delta_s(CH_3)$
	1443^{w}	1449[96]	$\delta_{as}(CH_3)$+ τ(HCCC)
	1690^{w}	1649[98]	ν(C=C)
	2949^{br}	2930-3009[96]	$\nu(C\text{-}H_x)$
ZTB adsorption on O_{ads}/Pd(111) at RT	293^{s}	300[95]	NA
	345^{sh}	357[95]	NA
	482^{w}	481[185]	Zr-O vibrations
	546^{w}	522[185]	Zr-O vibrations
	599^{w}	550[185]	Zr-O vibrations
	771^{w}	765[96]	ν(C-C)
	914^{vw}	924[96]	$\delta(CH_3)$
	1018^{s}	1027[96]	τ(HCCC)
	1194^{w}	1151[96]	δ(C-C-C)
	1378^{w}	1348 & 1366[96]	$\delta_s(CH_3)$
	1459^{w}	1449[96]	$\delta_{as}(CH_3)$+ τ(HCCC)
	1730^{s}	1720[98]	ν(R-C=O)
	1786^{s}	1720[98]	ν(R-C=O)
	2972^{br}	2930-3009[96]	$\nu(C\text{-}H_x)$

E Decomposition of ZTB After Slight Annealing

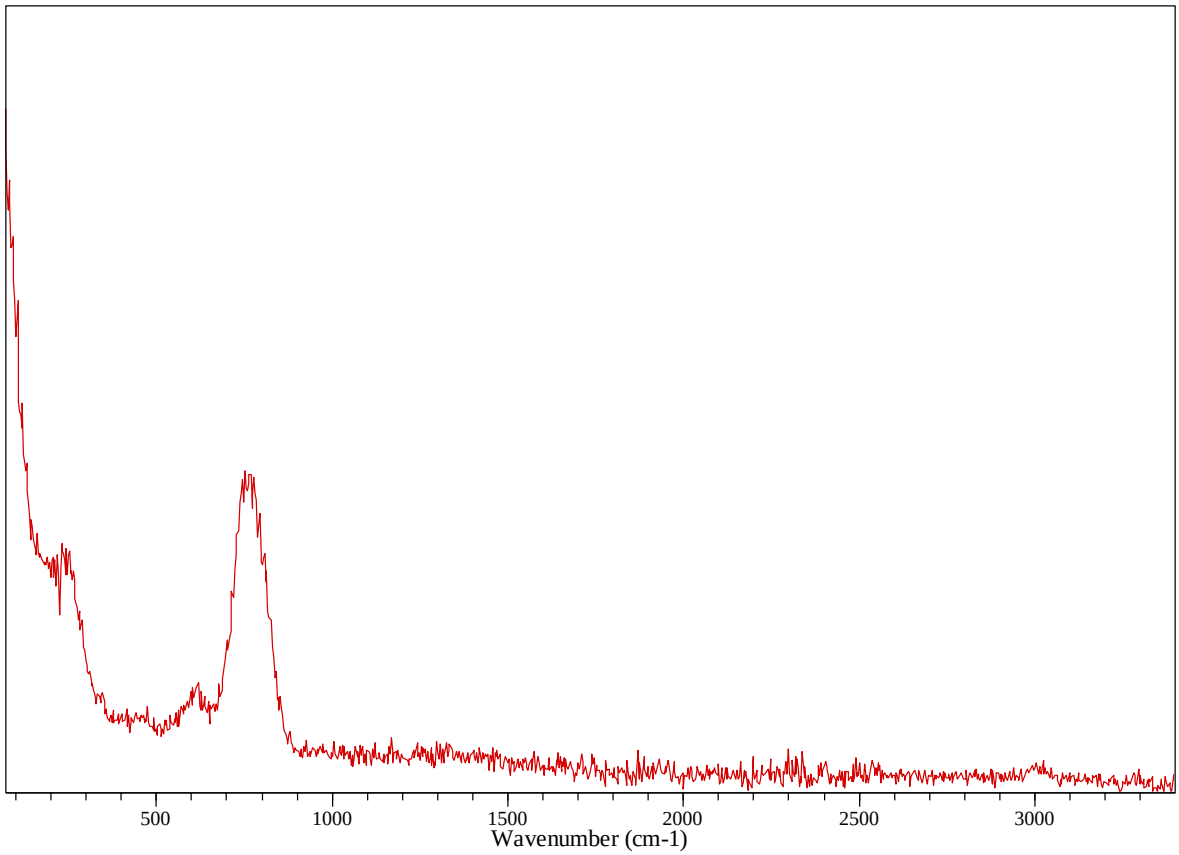

Figure A.5 HREELS spectra of 2000L ZTB exposed to Pd(111) at 293K and annealed to 373K for 5 minutes.

F Depth Profiling XPS of a pre-oxidized Zr foil after DRM

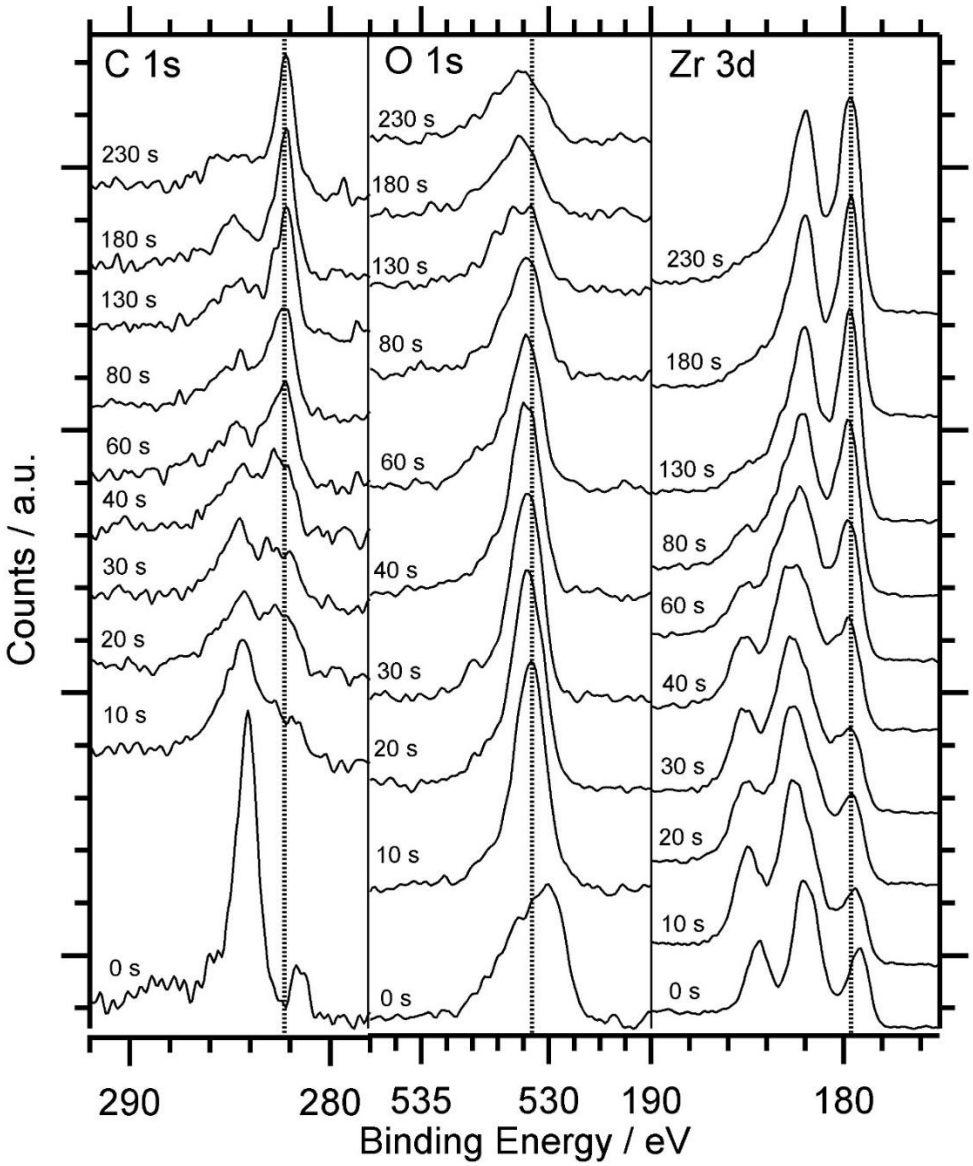

Figure A.6 Destructive depth profiling of pre-oxidized Zr foil after DRM with Ar^+ sputtering. The sputter time is labeled in the figure. 10 s of sputter time correspond to approximately 1 nm.

In the DRM experiment, ZrO_2 gets fully reduced (see Figure 12 main paper). With this reduction, the formation of a zirconium carbide comes along, indicated by a binding energy of C 1s at 282.0 eV beside a hydrocarbon peak at 284.5 eV. Zr 3d Binding Energy was found at 179.4 eV for the surface zirconium carbide and 182.4 eV for the surface oxidation due to the transport via air. Destructive depth profiling of the sample after methane dry reforming (spectra shown in

Figure 12) clearly indicates that the hydrocarbon overlayer is very thin (~5 nm) and the Zr carbide reaches much deeper (>20 nm). Due to the transport over air a thin (< 5nm) passivating ZrO_2 overlayer (Zr 3d BE 182.4 eV) is formed and cannot be seen after DRM when sample was not exposed to air (compare Figure 13). With removal of this oxide layer and the carbon species at 284.0 eV that are formed under DRM and increase in quantity due to air exposure by Ar^+ sputtering, metallic Zr and a carbon peak at 282.0-282.1 eV arises. This near-surface carbon species is also seen in XPS right after DRM (Figure 13) and assigned to the formation of Zirconium carbide[6]. Summing up, the sample can be described as a layered system consisting of Zr (substrate), ZrC(>20 nm) and on top ZrO_2/C_xH_y (~5 nm).

G XRD Analysis of the nominal 2:1 Pd-Zr intermetallic compound before and after DRM

For the DRM-active intermetallic Pd-Zr bulk phase catalyst, XRD patterns before and after the reaction were collected in analogy to the highly MSR-active Cu-Zr catalyst. For Cu-Zr, a straightforward assignment of the pattern to a single intermetallic Cu-Zr phase in contact to metallic Cu was possible. In contrast, for the Pd-Zr intermetallic phase, this was not an easy task, because the melt-prepared sample is much less homogeneous. A number of possible intermetallic compounds in varying stoichiometries (in accordance with the overall 2:1 stoichiometry of Pd:Zr in the initial melt) potentially match the pattern recorded prior to DRM, including Pd_3Zr and Pd_4Zr_3.[7] The presence of Pd_2Zr can be ruled out due to mismatch with reference diffractograms. A small amount of oxidized monoclinic ZrO_2 can also be found. After DRM, tremendous changes in the diffraction pattern indicate massive structural changes, alongside a further increase in sample inhomogeneity. Pd_3Zr is not present anymore, but a number of new intermetallic/oxo-intermetallic compounds have been formed, including Pd_9Zr and Pd_4Zr_3. A small amount of monoclinic and tetragonal ZrO_2 is also present, most probably stemming from partial oxidative decomposition of the Pd-Zr intermetallic compounds. Generally, it seems plausible, that the Pd-Zr phases are not as much affected by selective oxidative decomposition under DRM conditions as it was the case for Cu-Zr under MSR conditions, because the DRM reaction conditions are far more reducing. For pure ZrO_2 on Zr, complete reduction of ZrO_2 and the formation of ZrC was found after DRM at 1073 K. In the post-DRM XRD pattern, metallic

Zr could be found.[8] Note that due the fact the Pd-Zr intermetallic phase has been prepared on a Ta crucible, the not assigned peaks in Figure A.7 arise from metallic Ta or Ta_2O_5. However, no Ta-Pd or Ta-Zr phases could be identified, indicating that metal intermixing during the preparation process is absent.

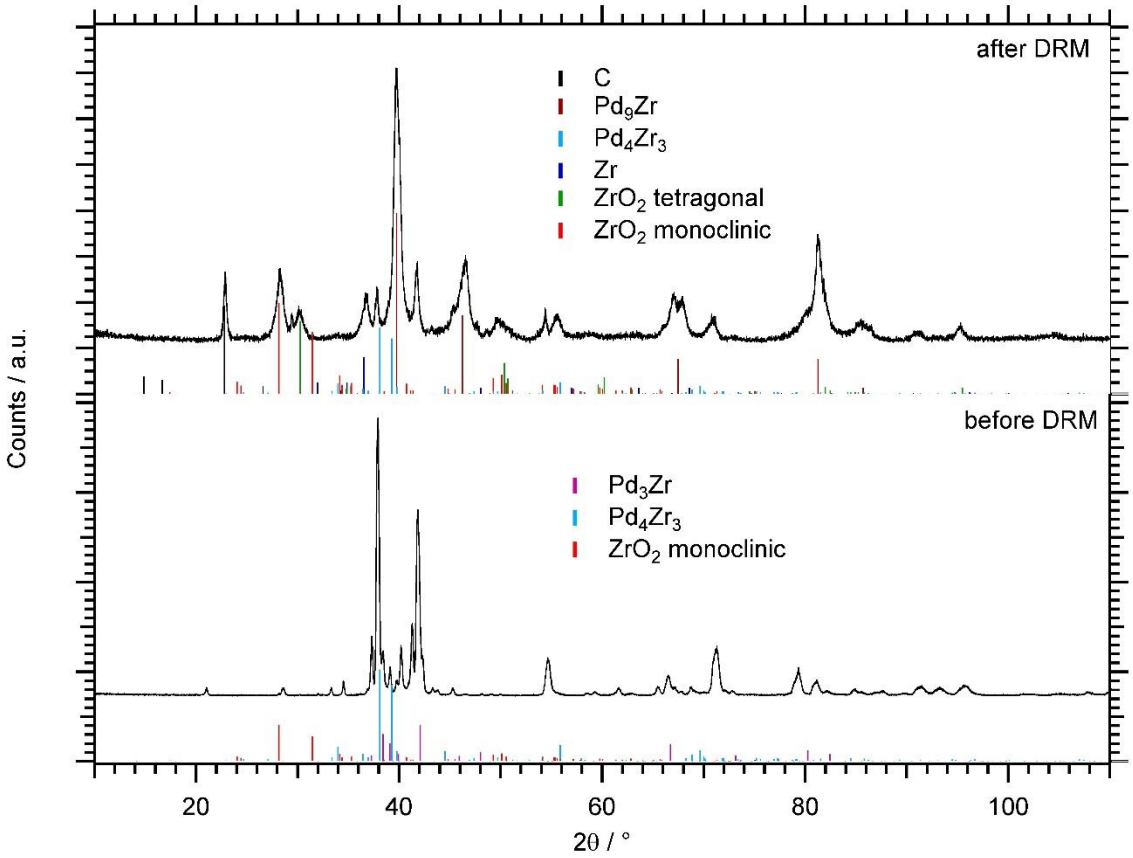

Figure A.7 X-ray diffraction patterns of the Pd-Zr bulk sample (nominal composition 2:1 = Pd-Zr). The bars indicate the reference peaks of the present phases.

SI – CHAPTER 5

1. Methods – Transmission Electron Microscopy

1.1. In-situ high temperature TEM imaging

In-situ TEM videos (2024*2024 resolution) were collected at 300 kV using a probe aberration-corrected FEI Titan-S 80-300 equipped with a Gatan OneView CMOS camera and a Protochips Aduro MEMS heating stage at Oak Ridge National Laboratory. Thanks to a low thermal-drift rate of the MEMS heating stage during the annealing, morphological transformations of the DNPs could be investigated from room temperature to 550 °C at the same locations and same particles. The electron beam-current and the dose rate were 3.32 nA and 87300 e/nm^2-sec, respectively. The frame rate of collecting the videos were variably chosen from 10 fps to 25 fps. Due to the extremely large size of the videos (a few TB in total, ~ 6 MB/frame), only the first frame of each minute could be chosen and aligned using the StackReg code[186] implemented in the ImageJ[187] to make a drift corrected *in-situ* video shown in Figure 1. Therefore, although raw videos have a higher frame rate (i.e., 10 fps to 25 fps), the final corrected videos have a frame rate of 1 fpm. We repeated *in situ* TEM experiments at a lower acceleration voltage, 60 kV to make sure the wetting process was not induced by an energetic electron beam (300 kV). The beam-current and the dose rate for the 60 kV experiments were 3.26 nA and 57200 e/nm^2-sec.

1.2. HAADF-STEM Tomography

The 3D structures of the pristine DNPs were analyzed by ADF-STEM electron tomography. An ADF tilt series (1024*1024 resolution, 5 second frame time) was collected from -70 ° to 52 ° with 2 ° increment using an FEI Titan ETEM 80-300. The magnification during the tilt series collection was 450 kX and the probe current was 0.296 nA (spot size 6). The tilt series was aligned by the fiducial marker alignment using the IMOD software[188] and the aligned tilt series was reconstructed using a model based iterative algorithm implemented in the TEMBIR software.[189] 3D visualization (volume rendering) of the reconstructed tomogram was performed using the Tomviz software.[5]

1.3. In-situ STEM-EELS

In-situ STEM-EELS were performed at 500 °C on a 300 kV FEI Titan ETEM 80-300 equipped with a Gatan Tridiem GIF with an energy dispersion of 0.3 eV/ch and Gatan single tilt

752 heating stage. The STEM probe current (Spot size 4) was 0.078 nA (dose rate: 87.7 e/Å^2-sec) and the camera length was 100 mm to increase the collection efficiency, although the signal to noise ratio of ADF-STEM imaging was not the optimal. The GIF entrance aperture was 2 mm and the acquisition time per spectra was 2 seconds with a vertical binning of 8.

1.4. *In-situ* electron diffraction

In-situ electron diffraction experiment was performed using a Gatan 628 single tilt (inconel furnace) heating stage and an FEI Titan ETEM 80-300 microscope (operating voltage: 300 kV). Electron diffraction patterns were collected using a Gatan GIF Tridiem. Post-acquisition camera length calibration was done using Au NP samples and DiffTools software. Background subtraction and radial integration were done by PASAD Software. Diffraction intensity profiles were normalized with respect to Au (111) peak intensity.

2. Methods – X-ray Photoelectron Spectroscopy

XPS data were obtained using a Kratos Axis Ultra DLD spectrometer with monochromic Al Kα radiation (1486.6 eV) at pass energy of 20 and 160 eV for high-resolution and survey spectra, respectively. A commercial Kratos charge neutralizer was used to avoid non-homogeneous electric charge of non-conducting powder and to achieve better resolution. The resolution measured as full width at half maximum of the curve fitted C 1s peak was approximately 1 eV. Binding energy (BE) values refer to the Fermi edge and the energy scale was calibrated using Au 4f7/2 at 84.0 eV and Cu 2p3/2 at 932.67 eV. XPS data were analyzed with CasaXPS software version 2313 Dev64 (www.casaxps.com). Prior to data analysis, the C-C component of the C 1s peak was set to a binding energy of 284.8 eV to correct for charge on each sample. Curve-fitting was performed following a linear or Shirley background subtraction using Gaussian/Lorentzian peak shapes. The atomic concentrations of the elements in the near-surface region were estimated taking into account the corresponding Scofield atomic sensitivity factors and inelastic mean free path (IMFP) of photoelectrons using standard procedures in the CasaXPS software. Fe_3O_4 nanoparticles and Au/Fe_3O_4 heterodimers were drop cast on silicon wafers attached to a copper sample holder. Bulk Fe_3O_4 powder (<5 μm, 95%) was purchased

from Sigma-Aldrich and loaded directly onto a sample holder. In-situ heating was performed using a built in resistive heating block to anneal the samples to 500°C for at least one hour prior to collecting XPS data.

3. Methods – Electronic Structure Calculations

3.1 Computational Details

Spin polarized DFT calculations were performed using VASP (Vienna Ab-initio Simulation Package)[88, 130, 131] with the Projector Augmented Wave (PAW) implementation[89, 132, 133] for Au (111) films supported on Fe_2O_3 (0001), Fe_3O_4 (111), FeO (111) and (100), and Fe (110). The electronic cores are represented by PAW PBE pseudopotentials having electronic configurations [$Xe4f^{14}$] $5d^{10}6s^1$, [$Ne3s^2$] $3p^6 3d^6 4s^2$ and [He] $2s^2 2p^4$ for Au, Fe, and O respectively. Calculations were performed with a kinetic energy cutoff of 600 eV. The convergence limit of electronic energies for the Kohn Sham equations was set to be 10^{-4} eV. Geometries were optimized until the magnitude of forces were less than 0.02 eV/Å. The adsorption energies of Au (111) films on iron oxide substrates were converged to within a numerical error of less than 0.05 eV. All energies were computed with the PBE[134, 135] functional. We evaluate the effect of Hubbard U corrections for the Fe_3O_4 (111) surface, for which extensive benchmarks are available in the literature. PBE + U[136, 137] with U = 3.8 eV[190-192] was employed for Fe_3O_4 (111), and given the preponderance of results for this treatment in the literature, we have reported all energies for Fe_3O_4 (111) using the U correction. However, as is shown later in the Supporting Information, trends in surface thermodynamics are not substantially altered by inclusion of Hubbard U corrections, and no conclusions from the computational analysis are changed. Thus, to conserve computational effort, we report results for FeO and Fe_2O_3 without such corrections. The dipole correction is applied perpendicular to the surface to cancel spurious electrostatic interactions between images (along [010]). Partial occupancies were determined by a Gaussian smearing of 0.05 eV, ensuring rapid convergence of the Kohn - Sham equations. Gas phase calculations for oxygen are computed at a kinetic energy cutoff of 400 eV in 12x13x14 Å unit cells with (1x1x1) k-points. We note that the total energy of oxygen calculated with PBE is overestimated with standard GGA functionals. To account for this overbinding, the gas-phase energy of O_2(g) was fitted to the formation energy of H_2O (g) at

298.15 K[193]. Calculation details for the model systems are listed below. Graphics of molecular structures are created using the VESTA program[194].

Fe_2O_3 (0001)

Bulk calculations were done with anti-ferromagnetic spin of Fe atoms, using a (10x10x10) Monkhorst Pack[140] point grid. The calculated lattice constants of α-Fe_2O_3, a = 5.024 Å, c = 13.826 Å agree well with previous experimental[195] and theoretical studies[23]. Surface calculations were done using mirrored slabs of *p(1x1)* unit cell with typical slab thickness of 25 Å. Sufficient vacuum was provided between consecutive slab in z direction (>30 Å). Spin polarized calculations were performed considering the anti-ferromagnetism of Fe_2O_3. The Brillouin zone was sampled using the gamma point scheme with a k-point grid density of 6x6x1. Gaussian smearing with a width of 0.05 eV was applied. Various surface terminations – O terminated, single Fe terminated, ferryl terminated and bi-iron terminated surfaces were considered, as shown in Figure A.10. Au films of varying thicknesses between 1 to 3 layers were considered for adsorption energy calculations. The films were oriented in a pseudomorphic fashion on the Fe_2O_3 surfaces with the Au atoms positioned on top sites of Fe atoms. The resulting strain in the Au films is about 0.1%, as shown in Table A.4. Adsorption energy calculations were also performed using Au-Fe alloy film on Fe_2O_3, by replacing some of the Au atoms on the film with Fe atoms, the details of which are provided later. As mentioned above, since we are primarily interested in trends in adsorption energies for this system, we did not consider U calculations for Fe_2O_3.

Fe_3O_4 (111)

Bulk calculations of Fe_3O_4 involve a (1x1) primitive unit cell consisting of 6 Fe atoms and 8 O atoms. A (8x8x8) Monkhorst Pack[140] k-point mesh in reciprocal space is used to solve the Kohn Sham equations. The bulk lattice constant is estimated to be 8.25 Å and 8.54 Å with PBE and PBE + U (U = 3.8 eV), in good agreement with experiments[196, 197]. Symmetric p(1x1) slabs of Fe_3O_4 with the oct2, tet1, O, O-vacancy and oct1 terminations (see Figure A.12) were considered. This is because, to decrease internal polarity perpendicular to the surface, ionic relaxation is expected and a symmetric model, having a net zero dipole, will minimize these effects. The slab thickness varied from 25 layers for the oct1 surface to 31 layers for the oct2

termination. 9 central layers in the middle of the slab were fixed at the bulk crystal positions to simulate the bulk oxide. Slabs were separated from their periodic images with a vacuum spacing of at least 20 Å. All calculations are spin polarized. A Ferrimagnetic magnetic ordering of Fe_3O_4 is considered for all calculations where the sign of the octahedral Fe atoms is antiparallel to the tetrahedral Fe atoms. Calculations are conducted at a (4, 4, 1) Monkhorst Pack k-point mesh in reciprocal space[21]. As mentioned above, a Hubbard U parameter of 3.8 eV was applied following previous studies on Fe_3O_4 surfaces[190-192, 198]. With this value of U, the local magnetic moments of the octahedrally and tetrahedrally coordinated Fe atoms are computed to be 4.1 and -4.0 respectively, in good agreement with experimental values[192, 198]. Calculations with PBE + U include progressive ramping of the U value in increments of 1.0 eV, from 0.0 eV to 3.8 eV. Each calculation is started with converged charge densities and wave functions from the previous calculation. Two monolayered Au (111) films are adsorbed on various terminations of the Fe_3O_4 (111) surface (see Figure A.14). The most favorable adsorption configurations for Au atoms are hollow sites on Fe terminated surfaces and top sites on O terminated surfaces.

FeO (100) and (111)

Bulk calculations of FeO are carried out on cubic (1x1) unit cells consisting of 4 Fe and 4 O atoms. A (10x10x10) Monkhorst Pack k-point scheme is applied[140]. The bulk lattice parameter is estimated to be 4.31 Å. (1x1) slabs of (100) and (111) surfaces are cleaved from the bulk crystal structure and shown in Figure A.16. Symmetric slabs for the (111) surface are employed to cancel internal dipoles in the polar (111) surface termination. Slab thicknesses for the (111) slab vary from 11 to 13 layers for the Fe and O terminated surfaces, respectively. 3 central layers located in the middle of the slab are fixed to simulate the bulk. The (100) surface is modeled as a 7-layered slab. Symmetric models are not considered as each layer is non-polar and there are no internal dipoles within the system. The lowest three layers are fixed to simulate the bulk crystal. All calculations are spin polarized and the antiferromagnetic configuration is enforced for the (111) termination while a ferromagnetic structure is applied to the (100) surface. This assumption will not affect any trends in adsorption energies of Au (111) films. As mentioned above, no Hubbard U corrections are applied to the FeO results. DFT computations are conducted using a (8x8x1) and (5x5x1) Monkhorst Pack k-point mesh for the (100) and (111) slabs respectively. Two monolayered epitaxial Au (111) and Au (100) films are adsorbed on

various terminations of the (111) and (100) slabs respectively and depicted in Figure A.17. The most stable adsorption site for Au atoms are oxygen top sites on O terminated (111), Fe three-fold hollow sites on Fe terminated (111) and four-fold hollow sites on FeO (100).

Fe (110)

Bulk calculations for Fe in a BCC unit cell consisting of 2 Fe atoms with (12x12x12) Monkhorst Pack k-points in reciprocal space[140] yield a bulk lattice parameter of 2.84 Å, in good agreement with experiments. Bulk calculations of Au in a FCC unit cell consisting of 4 Au atoms with (12x12x12) Monkhorst Pack k-points[140] give a lattice constant of 4.17 Å. 5 layered (2x2) Fe (110) surfaces are constructed from the bulk crystal, with the lowest two layers kept fixed to simulate the bulk. Several two layered Au (111) films adsorbed on Fe (110) that form moiré patterns with strains less than 2% are considered with models provided in Figure A.20. Adsorption energies of pseudomorphic Au (110) films on FeO (110) are also computed. The most stable configuration for Au atoms is the four-coordinated bridge site on the (110) surface.

3.2 Adsorption energy and vacancy formation energy

Adsorption energies or binding energies of Au (111) films are reported on a per surface atom basis and referenced to bulk FCC Au, as shown in equation (1). The total energy of Au is corrected for nanoparticle size effects by using the Gibbs Thomson relation as shown in equation (2)[199]. The surface energy of Au[200], γ, volume per atom, Ω, and nanoparticle diameter, R, are estimated to be 1.5 J/m^2, 18.1 Å^3/atom and 2 nm respectively. Oxygen vacancy formation energies are reported based on equation (3).

$$E^{binding} = \frac{E_{Au\ on\ FexOy} - E_{FexOy} - N_{Au}E_{Au\ atom\ in\ bulk}}{N_{Au\ on\ surface}} \quad (1)$$

$$E(R) - E(\infty) = \frac{2\gamma\Omega}{R} \quad (2)$$

$$\Delta E^{vacancy} = E^{vacancy} - E^{clean} + \frac{1}{2}E_{O_2}^{gas} \quad (3)$$

Adsorption energies of Au films are reported for Fe, O and a mixture of Fe and O terminations, which are between the two limiting cases are discussed in Tables S2, S3 and S4. The adsorption energies for Au decreases monotonically (towards stronger adsorption) as the O terminated surface is reduced to an Fe terminated one. This is consistent for Fe_3O_4 (111), FeO (111) and (100). Au (111) films promote the reduction of in FeO, as the oxygen defect formation energy is more favorable in the presence of an Au film. Further details are provided in Table A.9.

3.3 Ab Initio phase diagram analysis

An ab initio phase diagram based approach is applied to calculate the surface free energy (γ), as a function of the oxygen chemical potential for bare iron oxide (equation 12) and Au covered iron oxide (equation 13) surfaces. The methodology followed is described in equations (4) to (13) and is based on the approach proposed by Reuter and Scheffler (2001)[141].

$$\Omega = \frac{1}{2}\left(\mu_{Fe_XO_Y} - X\mu_{Fe} - Y\mu_O\right) \tag{4}$$

$$\mu_{Fe_XO_Y} = E_{Fe_XO_Y} \tag{5}$$

$$\mu^{bulk}{}_{Fe_3O_4} = 3\mu_{Fe} + 4\mu_O \tag{6}$$

$$\mu^{bulk}{}_{Fe_3O_4} = E^{bulk}{}_{Fe_3O_4} \tag{7}$$

$$\mu_{Fe} = \frac{E^{bulk}{}_{Fe_3O_4} - 4\mu_O}{3} \tag{8}$$

$$\mu_O = \frac{1}{2}\mu_{O_2} = \frac{1}{2}\left(\mu^0_{O_2} + kTln\left(\frac{P}{P^0}\right)\right) \tag{9}$$

$$\mu^0_{O_2} = E_{O_2} - TS^0_{O_2} \tag{10}$$

$$\Omega = \frac{1}{2}\left(E_{Fe_XO_Y} - X\frac{E^{bulk}_{Fe_3O_4}}{3} + \left(\frac{4X}{3} - Y\right)\mu_O\right) \tag{11}$$

$$\gamma = \frac{1}{2A}\left(E_{Fe_XO_Y} - X\frac{E^{bulk}_{Fe_3O_4}}{3} + \left(\frac{4X}{3} - Y\right)\mu_O\right) \quad (12)$$

$$\gamma_{Au\ film} = \frac{1}{2A}\left(E_{AuFe_XO_Y} - X\frac{E^{bulk}_{Fe_3O_4}}{3} + \left(\frac{4X}{3} - Y\right)\mu_O - N_{Au}\mu^{Bulk}_{Au}\right) \quad (13)$$

Surface phase diagram of various Fe_2O_3 terminations are shown in Figure A.11. The most stable surface termination at high oxygen chemical potentials was the O-terminated surface, while lower chemical potentials of oxygen results in more Fe rich terminations. Single-Fe termination is the most stable at intermediate oxygen chemical potentials and bi-Fe terminated surface is stable only at very low oxygen chemical potentials. These results agree with previous studied on surface terminations of Fe_2O_3[201]. The phase diagram for Au and Fe films on Fe_2O_3 are shown in Figure A.14. At high oxygen chemical potentials the O-terminated surface is still the most stable, indicating there is no attractive interactions between Au and the O-terminated surface. The single Fe terminated surface is slightly stabilized by about 0.04 eV/ Au atom. The bi-Fe termination is, however, stabilized to a larger extent, by about 0.2 eV/Au atom. This occurs due to the attractive interactions between Au and a reduced Fe_2O_3 surface. The presence of the Au film, therefore, shifts the chemical potential of oxygen at which bi-Fe termination becomes stable, to larger values. The number of Au layers is seen to have little effect on the stabilization. At very low oxygen chemical potentials, the three-layered structure consisting of Au-Fe alloy sandwiched between metallic Fe at the bottom and Au at the top (red solid line) becomes most stable. Interestingly, this structure is more stable than the two layered structures with only alloy and Au at the top (green and magenta solid lines), indicating the strong preference of metallic Fe to be present on the oxide surface at such low oxygen chemical potentials. The red dotted line indicating segregated metallic Fe and Au layers is also seen to be among the most stable structures.

Phase diagrams for terminations of Fe_3O_4 (111) are given in Figure A.16. For Fe_3O_4, the tet1 termination is the most stable phase in the high and intermediate oxygen chemical potential range with the oct2 termination becoming more favorable in more negative oxygen chemical potentials. PBE and PBE+U show similar phase diagrams for Fe_3O_4. This is consistent with prior experimental and theoretical investigations [145, 198, 202, 203]. The stability of Au (111) epitaxial films on Fe_3O_4 (111) terminations with PBE (Figure A.15) and PBE+U (Figure A.16) is

discussed. The most favorable termination for Au adsorption is the iron terminated oct1 surface. With decreasing O_2 chemical potentials (signifying a higher temperature or a lower oxygen partial pressure), the thermodynamically most stable state shifts from the tet1 termination to the Au (111) covered oct1 phase. This is because of favorable interactions between Au and the reduced interface, as evidenced through the negative adsorption energy (Table A.6). The phase diagrams qualitatively support the experimentally determined enhanced wetting of Au nanoparticles on iron oxide supports with increasing temperature. Furthermore, trends in surface free energies are consistent with PBE and PBE + U (3.8 eV) approaches. The ab initio thermodynamic analysis is extended to Au films on FeO (100) and (111), shown in Figure A.18 and Figure A.19. As observed with Fe_3O_4, the thermodynamically most stable phase shifts from oxygen covered bare FeO terminations to iron terminated surfaces having adsorbed Au films as the oxygen chemical potential is reduced.

4. Methods – Materials Synthesis

4.1. Materials and Chemicals

The following chemicals were purchased and used as-received without further purification: anhydrous ethanol (C_2H_5OH, 200 proof, ACS/USP grade, Pharmco-Aaper), hexanes (C_6H_{14}, technical grade, naphtha solvent, Fisher), isopropanol (C_3H_8O, certified ACS plus, Fisher), gold(III) chloride trihydrate ($HAuCl_4$-$3H_2O$, $\geq$ 99.9% trace metals basis, Aldrich), iron(0) pentacarbonyl ($Fe(CO)_5$, Aldrich), borane tert-butylamine complex (BTB, $C_4H_{14}BN$, 97%, Aldrich), 1-octadecene ($C_{18}H_{36}$, technical grade, 90%, Alfa Aesar), oleic acid ($C_{18}H_{34}O_2$, technical grade, 90%, Aldrich), and oleylamine ($C_{18}H_{33}NH_2$, $\geq$ 98% primary amine, Aldrich).

4.2. Organometallic Synthesis.

Bifunctional composite Au-Fe_3O_4 dumbbell-like nanoparticles (DNPs) were prepared by initiating the epitaxial growth of Fe on Au nanoparticle seeds[204] followed by Fe oxidation in an organometallic solution synthesis.[127-129] Organic methods of synthesis were employed to tightly regulate the size distribution of the nanoparticles and to direct the controlled growth of Fe_3O_4 on the exposed (111) facets of the Au seeds.

4.3. Synthesis of Au Nanoparticles.

Au nanoparticle seeds were prepared by mixing 0.1 mmol of $HAuCl_4$-$3H_2O$ in 10 mL of oleylamine and 10 mL of hexanes. The solution was heated to 40°C and purged under inert Ar gas. After 10 min, 0.2 mmol of borane tert-butylamine complex (BTB) dissolved in 1 mL of oleylamine and 1 mL of hexanes was quickly injected and the solution was stirred for an additional 1 hr as the nucleation and growth of the nanoparticles proceeded. The Au nanoparticles were washed with ethanol and re-dispersed in hexanes for further use.

4.4. Synthesis of Au-Fe_3O_4 Nanoparticles.

To synthesize Au-Fe_3O_4 nanoparticles, 0.5 mL of oleic acid was added to 20 mL of 1-octadecene. The solution was stirred and purged with Ar gas at 120°C for 15 min. 0.02 mL of $Fe(CO)_5$ in 1 mL of 1-octadecene was injected into the solution. The solution was stirred at 120°C for 20 min. 0.5 mL of oleylamine added to 10 mg of Au seeds dispersed in 2 mL of hexanes. This seed solution was quickly injected into the reaction mixture. The resulting solution was rapidly heated to 300°C and held at refluxing conditions for 15 min. The resulting Au-Fe_3O_4 dumbbell-like heterodimers were cooled to room temperature and washed with isopropanol to remove excess surfactants.

5. **Supplementary Tables**

Table A.4 Strain in epitaxial Au films adsorbed on Fe_2O_3 (001), Fe_3O_4 (111), FeO (111), FeO (100) and Fe (110).

System	Strain (%)
Au (111)/Fe_2O_3 (0001)	0.1
Au (111)/Fe_3O_4 (111)	2.4
Au (111)/FeO (111)	3.6
Au (100)/FeO (100)	3.4
Au (111)/Fe (110)	1.8 along (100) and -1.8 along (010)
Au (110)/Fe (110)	3.7

Table A.5 Comparison between adsorption energies of Au (111) films on terminations of Fe_2O_3 (0001).

Au (111)/ Fe_2O_3 (111) Terminations	Adsorption energy per surface Au, eV, PBE
O-terminated	0.29
Ferryl	0.19
Single-Fe terminated	0.08
Bi-Fe terminated	-0.37

Table A.6 Comparison between adsorption energies of Au (111) films on terminations of Fe_3O_4 (111) with and without the Hubbard U correction (3.8 eV). The trend of exothermic adsorption of Au (111) on Fe terminated surface (Oct1) over O terminated films is obtained with and without the correction. Geometric configurations are shown in Figure A.14.

Au (111)/ Fe_3O_4 (111) Terminations	Adsorption energy per surface Au, eV, PBE	Adsorption energy per surface Au, eV, PBE + U
Tet1	0.46	0.48
O1	0.33	-0.10
O1Vac	0.47	0.26
Oct1	-0.20	-0.36

Table A.7 Adsorption energies of Au (111) and Au (100) films on iron and oxygen terminated surfaces of FeO (111) and FeO (100) respectively. Geometric configurations are shown in Figure A.17.

Au (111)/FeO (111) Terminations	Adsorption energy per surface Au, eV	Au (100)/FeO (100) Terminations	Adsorption energy per surface Au, eV
O	0.65	O	0.60
O-1Vacancy	0.47	O-Vacancy	0.11
O-2Vacancy	0.24	Fe	-0.92
Fe	-0.80		

Table A.8 Adsorption energies of Au (111) films on Fe (110) surfaces. The strain in the Au films is also reported. Adsorption geometries are provided in Figure A.18.

Au (111)/Fe (110) Surfaces	Adsorption energy per surface Au, eV	Strain (%) along (100), (010)
1	-0.54	0.5, 0.5
2	-0.65	1.8, -1.8
3	-0.56	0.9, -1.7
4	-0.52	-2.4, 0.5
5	-0.54	-1.1, -1.7

Table A.9 Vacancy formation energies for FeO (111) and FeO (100) in the presence and absence of an Au film.

System	Oxygen vacancy formation energy, bare FeO surface, eV	Oxygen vacancy formation energy, Au (111) covered surface, eV
Au (111)/ FeO (111)	2.62	1.88
Au (111)/ FeO (100)	2.97	2.01

6. **Supplementary Figures**

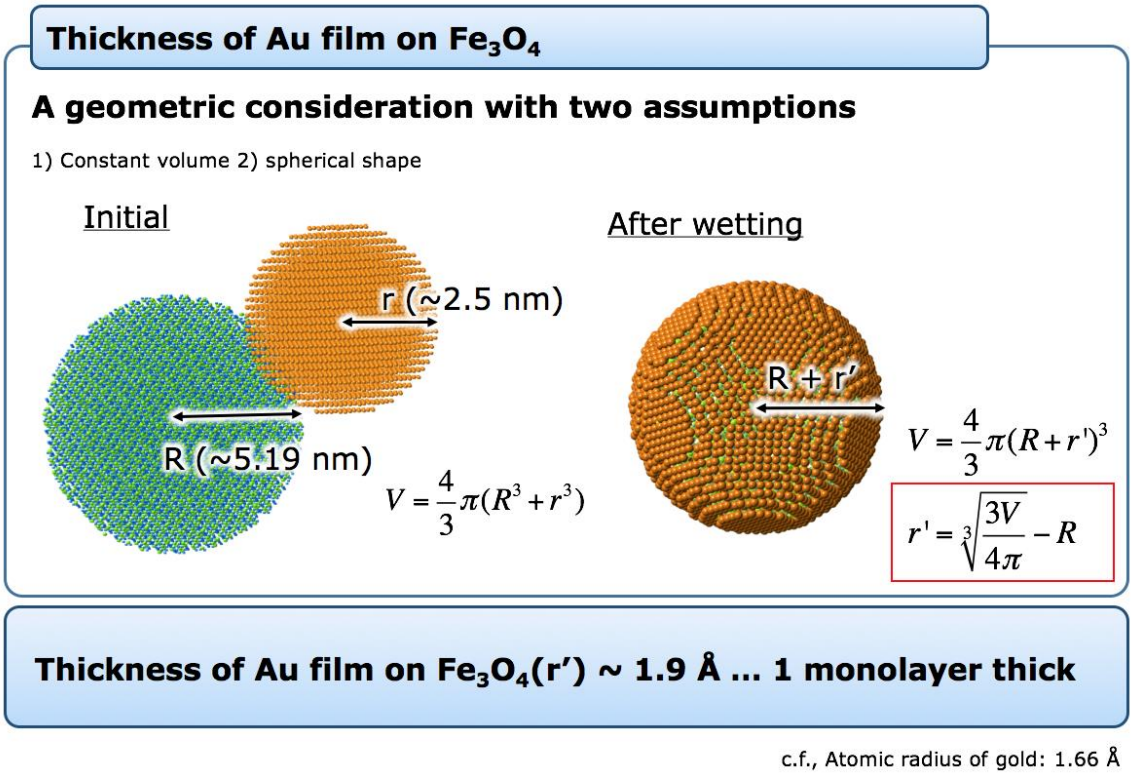

Figure A.8 Calculation of a thickness of Au film on Fe_3O_4 after the complete wetting

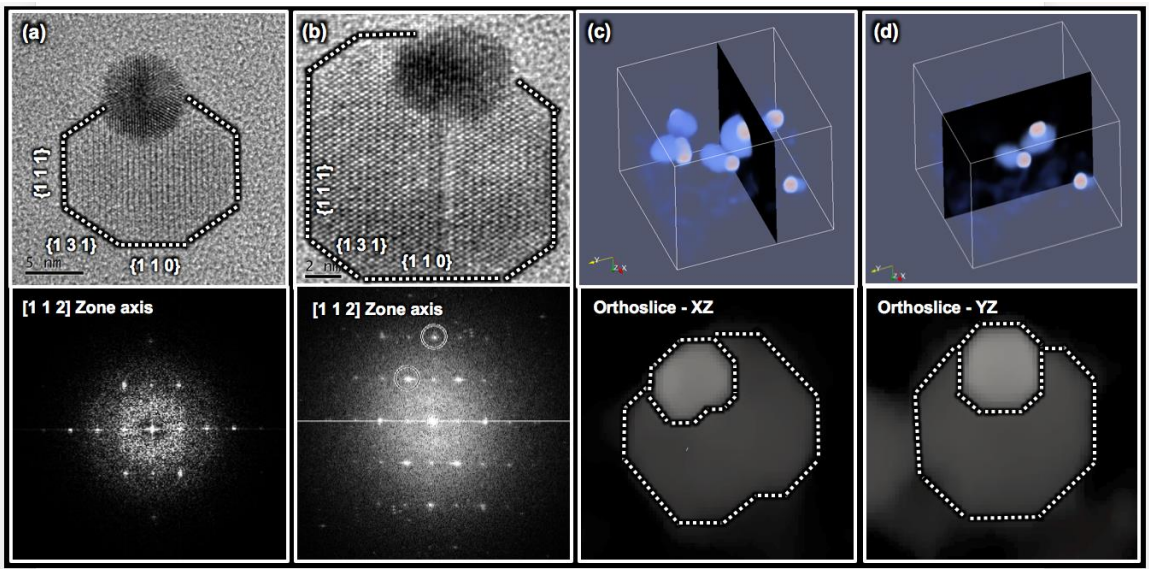

Figure A.9 HRTEM and 3D Tomogram of Au-Fe_3O_4 showing an epitaxial relationship between Au and Fe_3O_4 (a, b) High resolution TEM images (top) and fast-Fourier transformation (FFT) patterns (bottom) of Au-Fe_3O_4 DNPs showing the facets of Fe_3O_4. FFT patterns were collected from Fe_3O_4 to determine a zone axis. (c) Volume-rendered ADF-STEM Tomogram (top) and orthogonal slice (bottom) of Au-Fe_3O_4 DNPs showing the facet relationship (Contrast adjustment for the orthogonal slice was performed for a better visibility of Fe_3O_4).

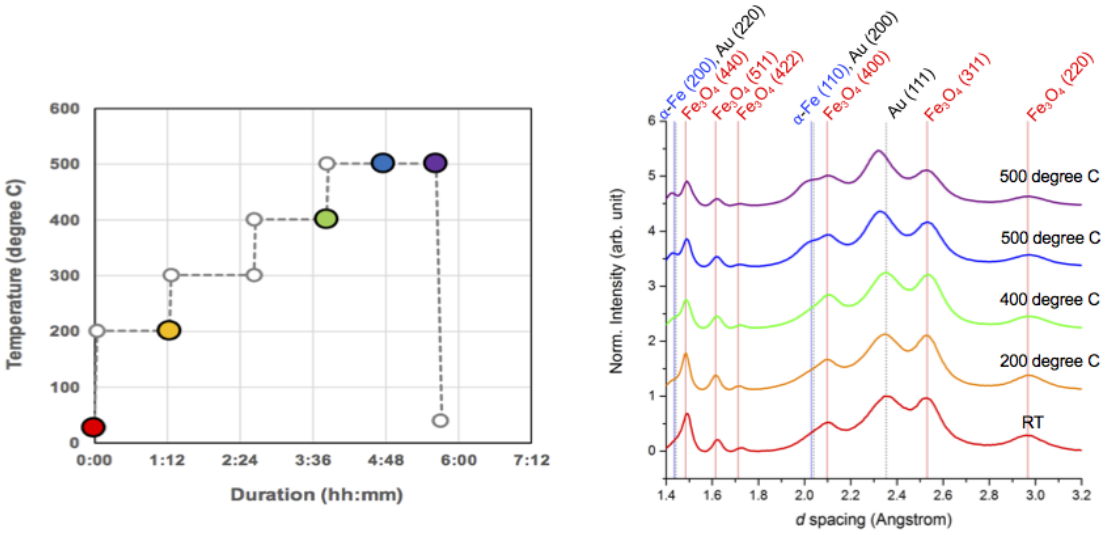

Figure A.10 Results of in-situ heating electron diffraction experiments. (Left) Temperature profile of in-situ heating electron diffraction experiment (Right) Time and temperature series of diffraction intensity profiles. Temperature and diffraction intensity profiles are color-coded, accordingly.

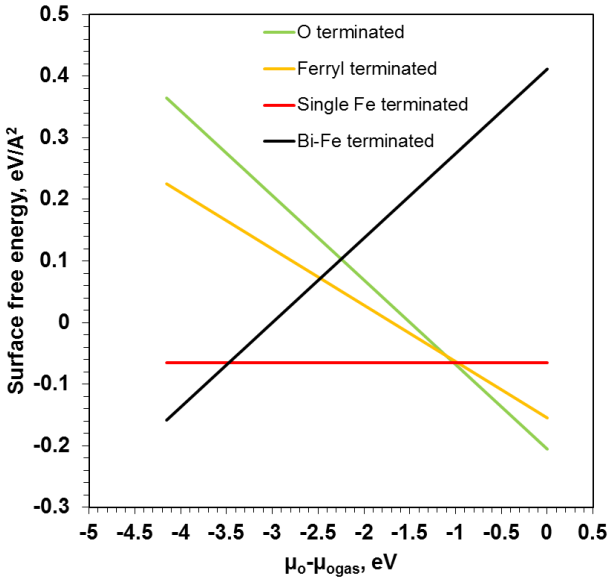

Figure A.11 Surface phase diagrams of Fe_2O_3 (0001)

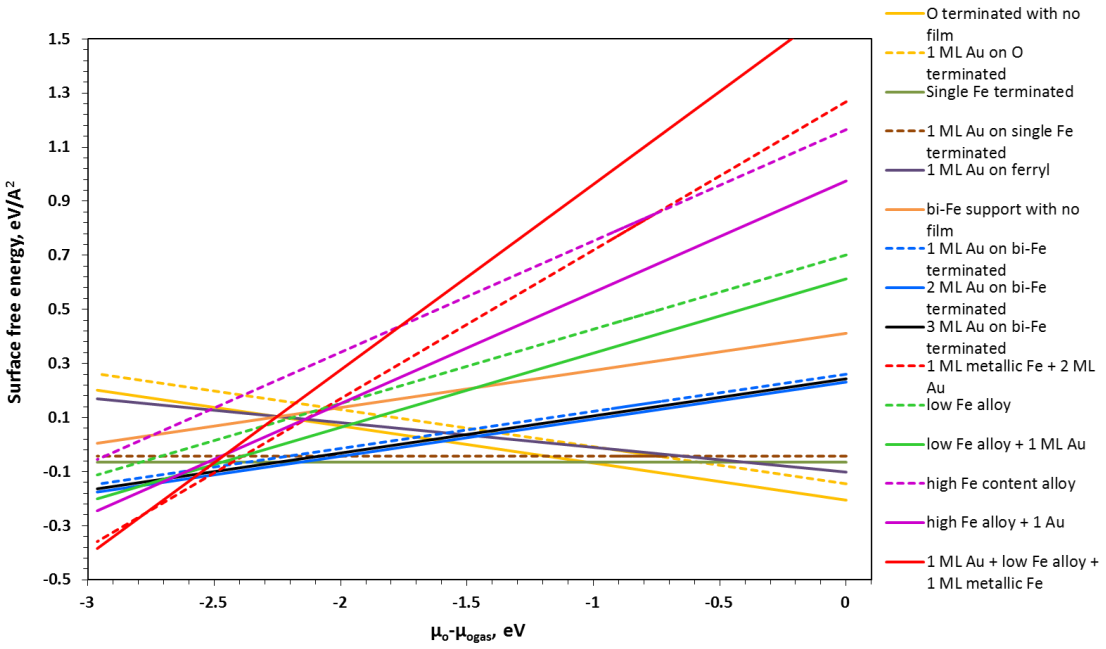

Figure A.12 Fe_2O_3 phase diagram with various film structures on the (0001) surface. The structures are denoted in the legend. Legends having + in them denote multiple layers of the film, for example – 1 ML Au + low Fe alloy + 1 ML metallic Fe denotes the structure in Figure A.11 and so on.

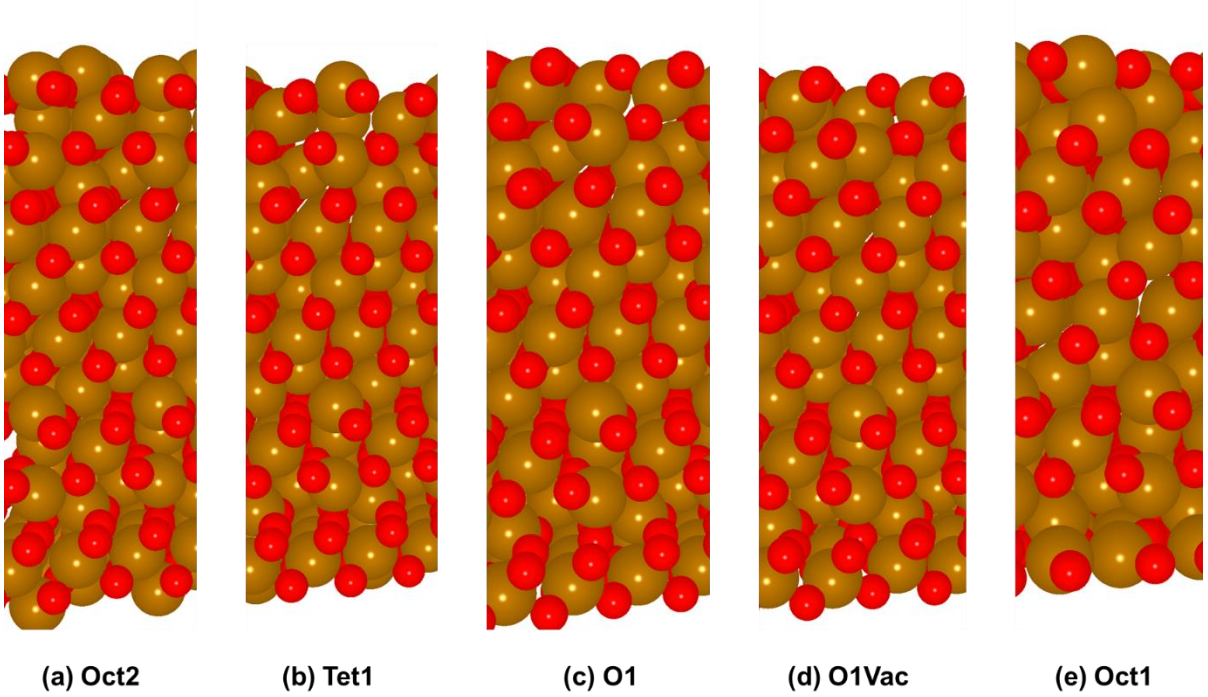

Figure A.13 (a) through (e), Five terminations of the Fe_3O_4 (111) surface considered in this study. Fe and O atoms are represented in brown and red respectively.

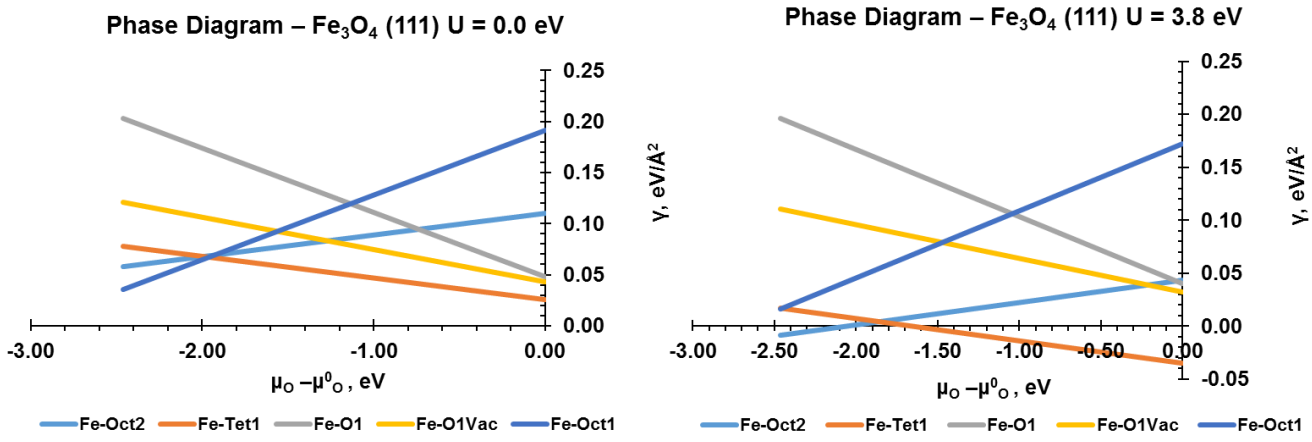

Figure A.14 Surface phase diagram for Fe_3O_4 (111) with PBE (left) and PBE + U (right). Surface free energy is presented as a function of the oxygen chemical potential. The most stable termination for a wide range of oxygen chemical potential is Fe – tet1 (Figure A.12(b)), in agreement with prior experimental and computational investigations. PBE + U and PBE approaches represent qualitatively similar phase diagrams, with similar trends in the stability of Fe_3O_4 (111) terminations.

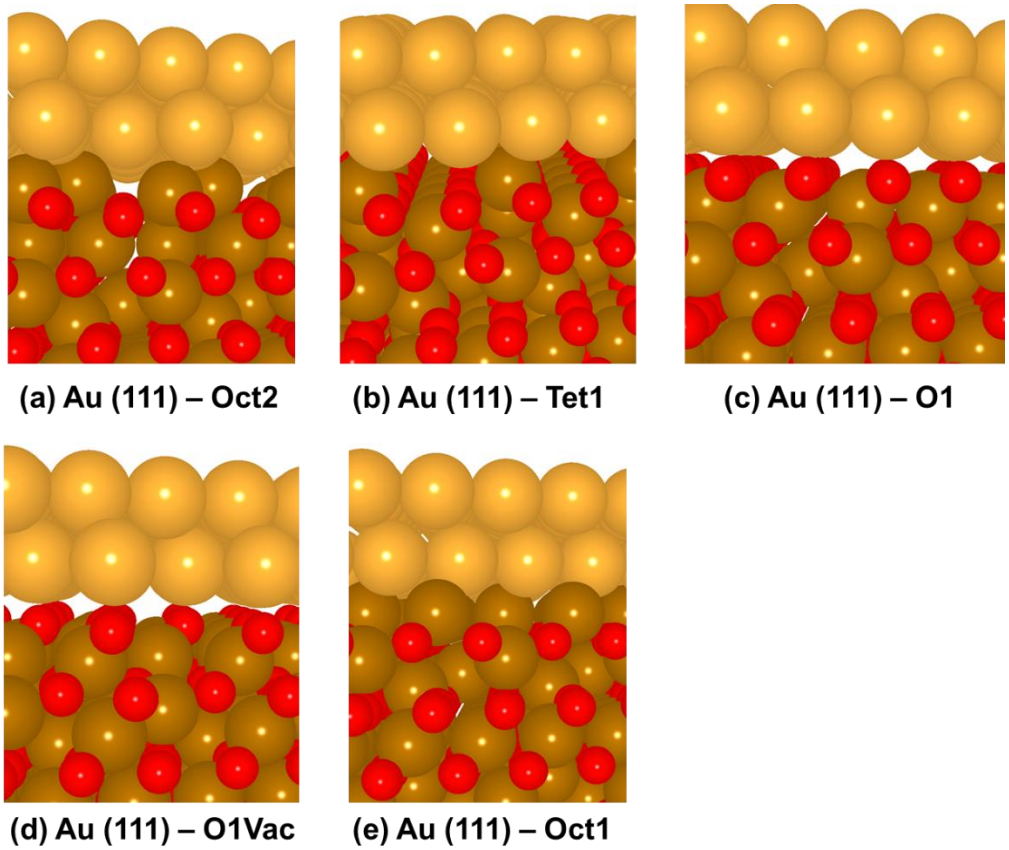

Figure A.15 Adsorption configurations of Au (111) epitaxial films on Fe and O terminations of Fe_3O_4 (111). Au atoms adsorb on the iron three-fold site for Fe terminated surfaces and top site of oxygen on O terminated surfaces. Au, Fe, and O atoms are depicted in yellow, brown and red respectively.

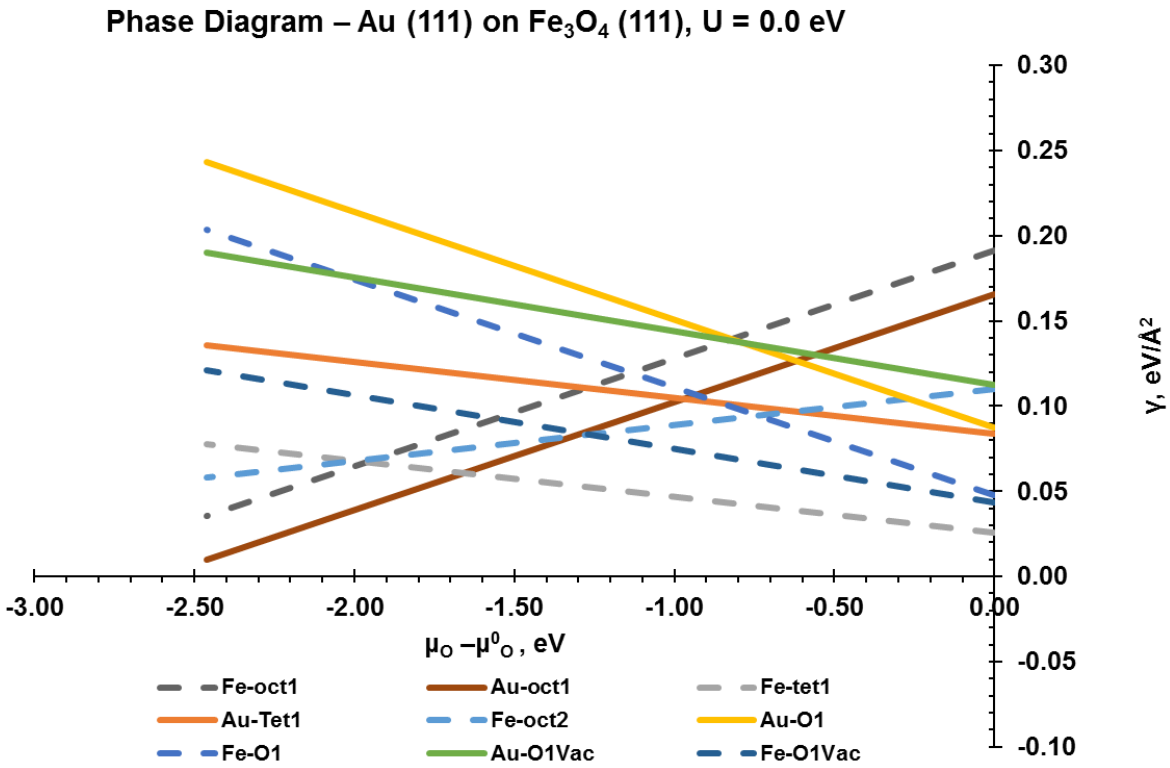

Figure A.16 Surface free energy for bare Fe_3O_4 (111) (shown as dashed lines) and 2 ML epitaxial Au (111) (shown as solid lines) covered Fe_3O_4 (111) surfaces having several terminations is plotted as a function of the oxygen chemical potential. All calculations are the PBE. Under negative oxygen chemical potential, Au (111) film adsorbed on the iron terminated oct-1 termination (solid brown line) is the most stable phase. This is consistent with experimentally observed wetting of Au nanoparticles on Fe_3O_4 DBNPs during in situ annealing.

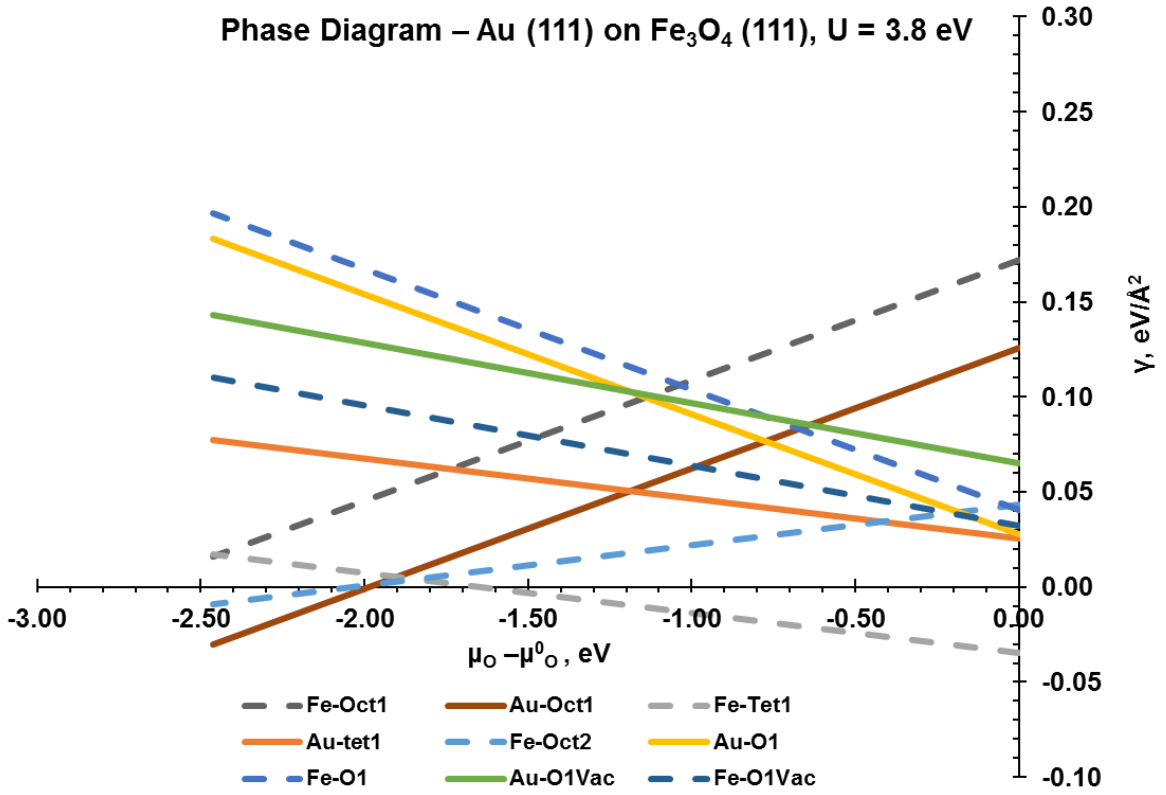

Figure A.17 Surface free energy for bare Fe_3O_4 (111) (shown as dashed lines) and 2 ML epitaxial Au (111) (shown as solid lines) covered Fe_3O_4 (111) surfaces having several terminations is plotted as a function of the oxygen chemical potential. All calculations are the PBE + U (3.8 eV). The trends in stability are like those obtained with PBE (Figure A.15), with the Au (111) covered iron terminated surface of Fe_3O_4 (solid brown line) being the thermodynamically stable phase under reducing conditions.

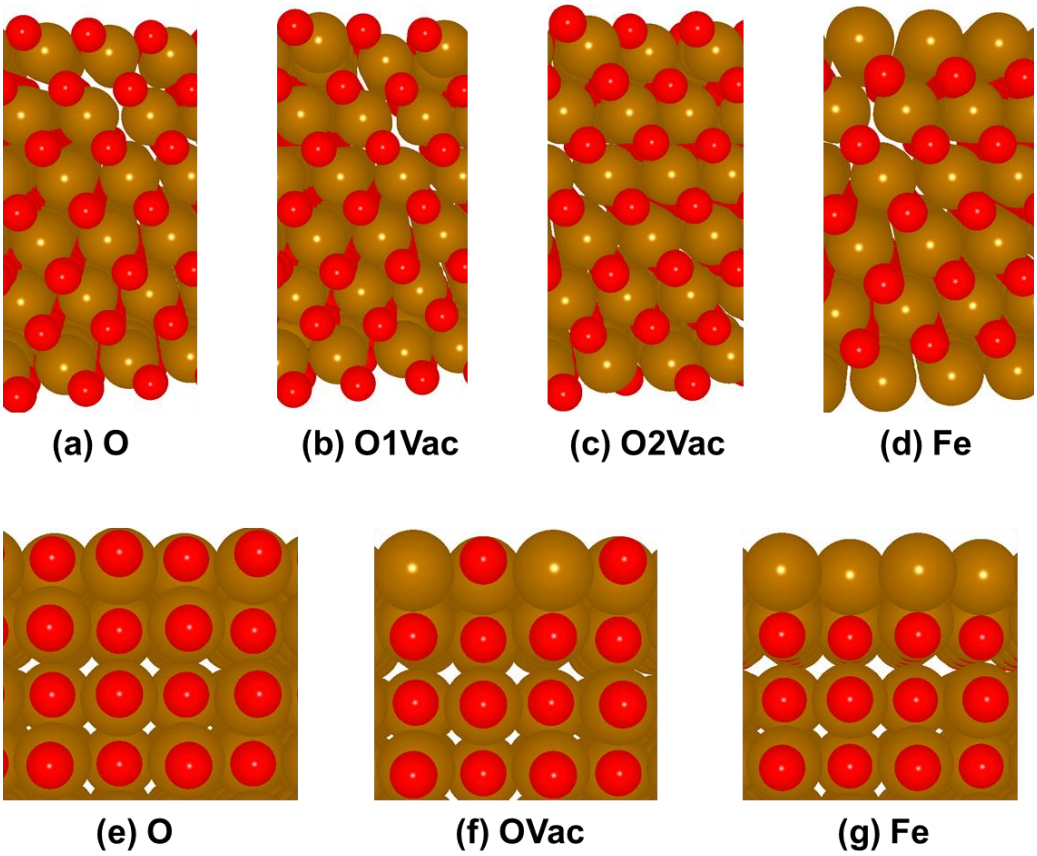

Figure A.18 (a) through (d), Oxygen and iron terminated surfaces of FeO (111). (e) through (g), Oxygen and iron terminated surfaces of FeO (100). Fe and O atoms are shown in brown and red respectively.

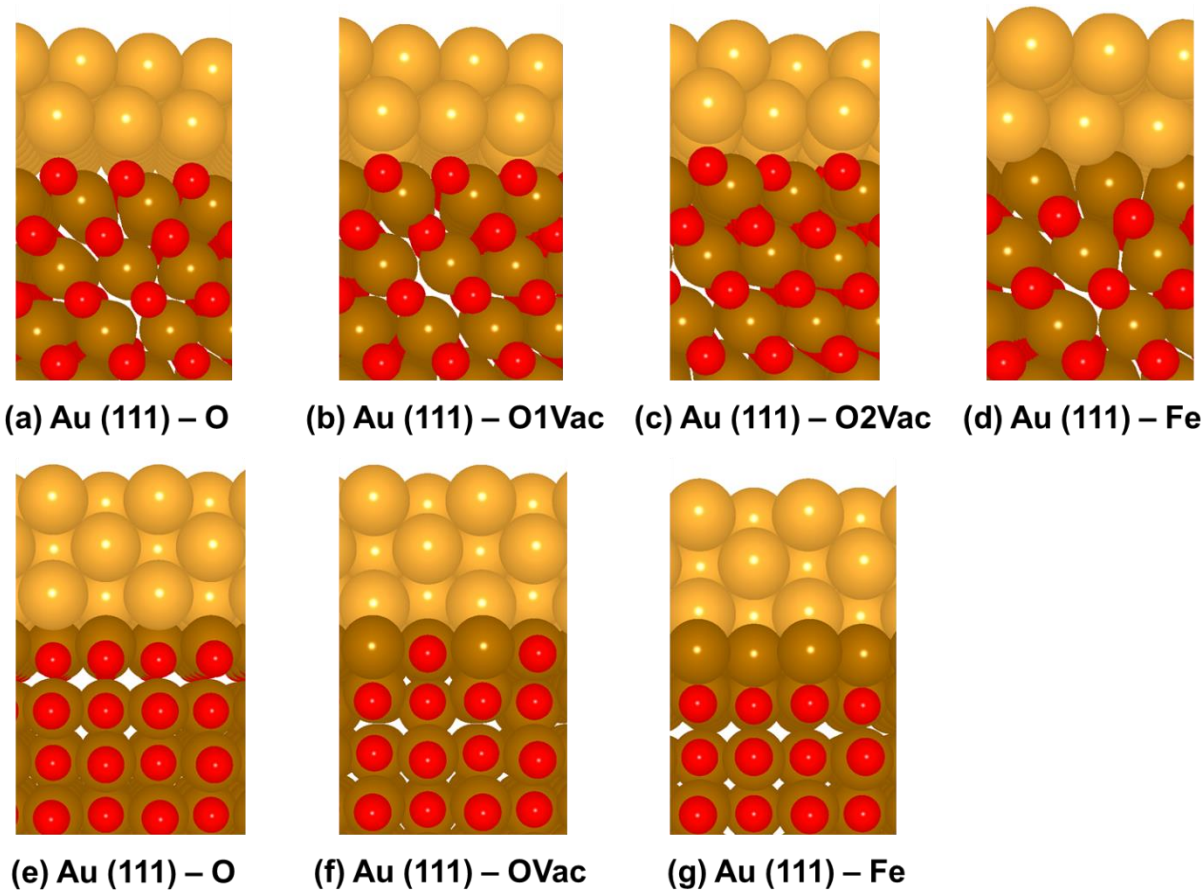

Figure A.19 (a) through (d), Adsorption geometries of epitaxial Au (111) films on FeO (111) surfaces. Au atoms adsorb on iron three-fold sites on the Fe terminated surfaces and oxygen top sites on the O terminated surfaces. (e) through (g), adsorption configurations of epitaxial Au (100) films on FeO (100) surfaces. Au atoms adsorb on iron four-fold sites on the Fe terminated surfaces and oxygen top sites on the O terminated surfaces. Au, Fe, and O atoms are depicted in yellow, brown and red respectively.

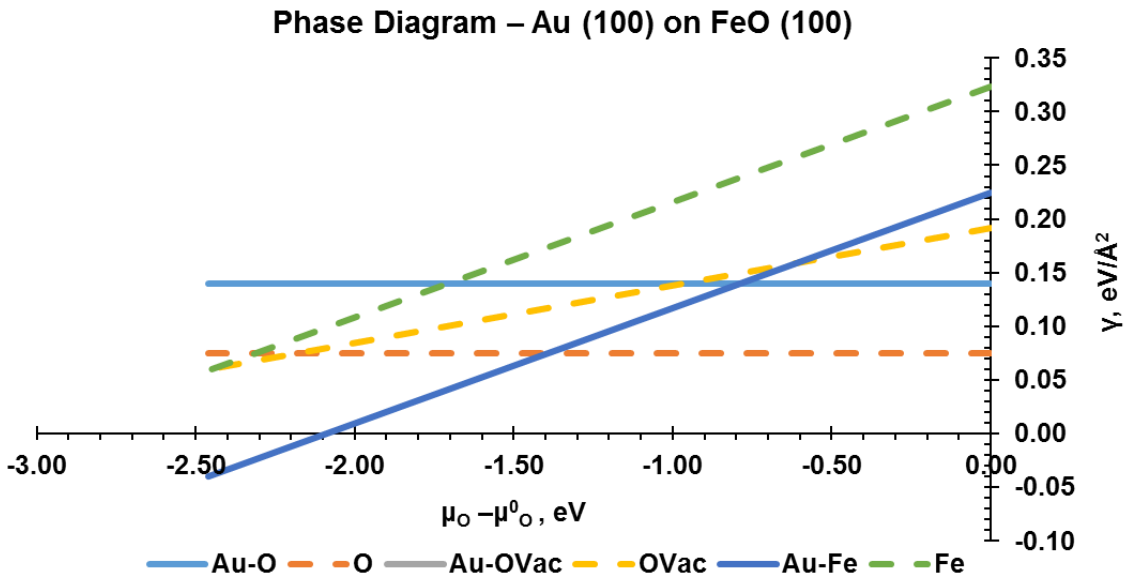

Figure A.20 Surface free energy of bare (dashed lines) and Au (100) (solid lines) covered FeO (100) terminations as a function of the oxygen chemical potential. At low oxygen, chemical potentials, the Fe terminated surface (solid dark blue line) is the thermodynamically most favorable phase due to the strong adsorption of Au atoms on Fe four-fold hollow sites.

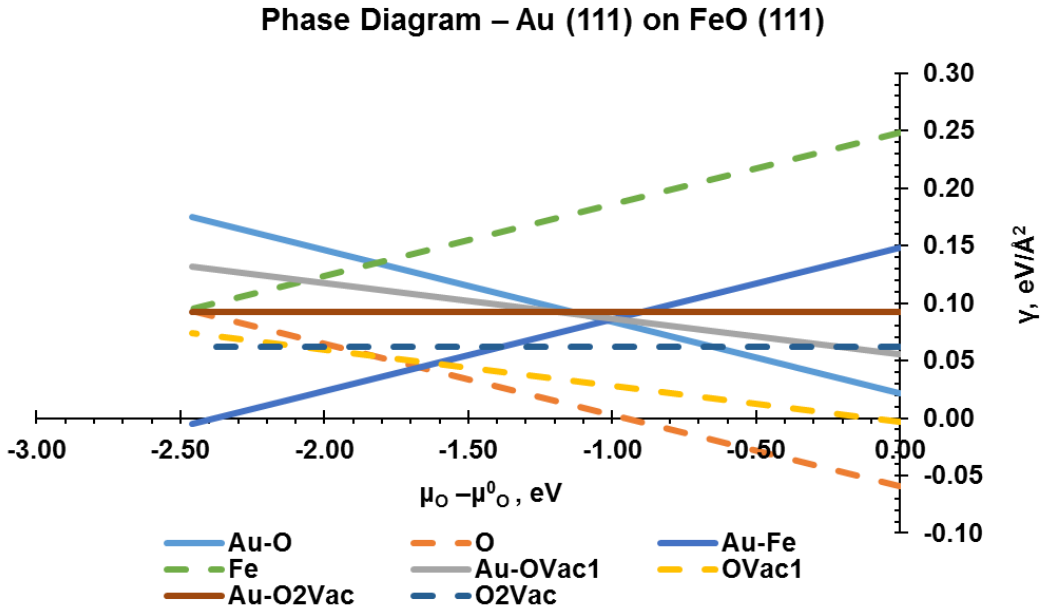

Figure A.21 Surface free energy of bare (dashed lines) and Au (111) (solid lines) covered FeO (111) terminations as a function of the oxygen chemical potential. At low oxygen, chemical potentials, the Fe terminated surface (solid dark blue line) is the thermodynamically most favorable phase due to the strong adsorption of Au atoms on Fe three-fold hollow sites.

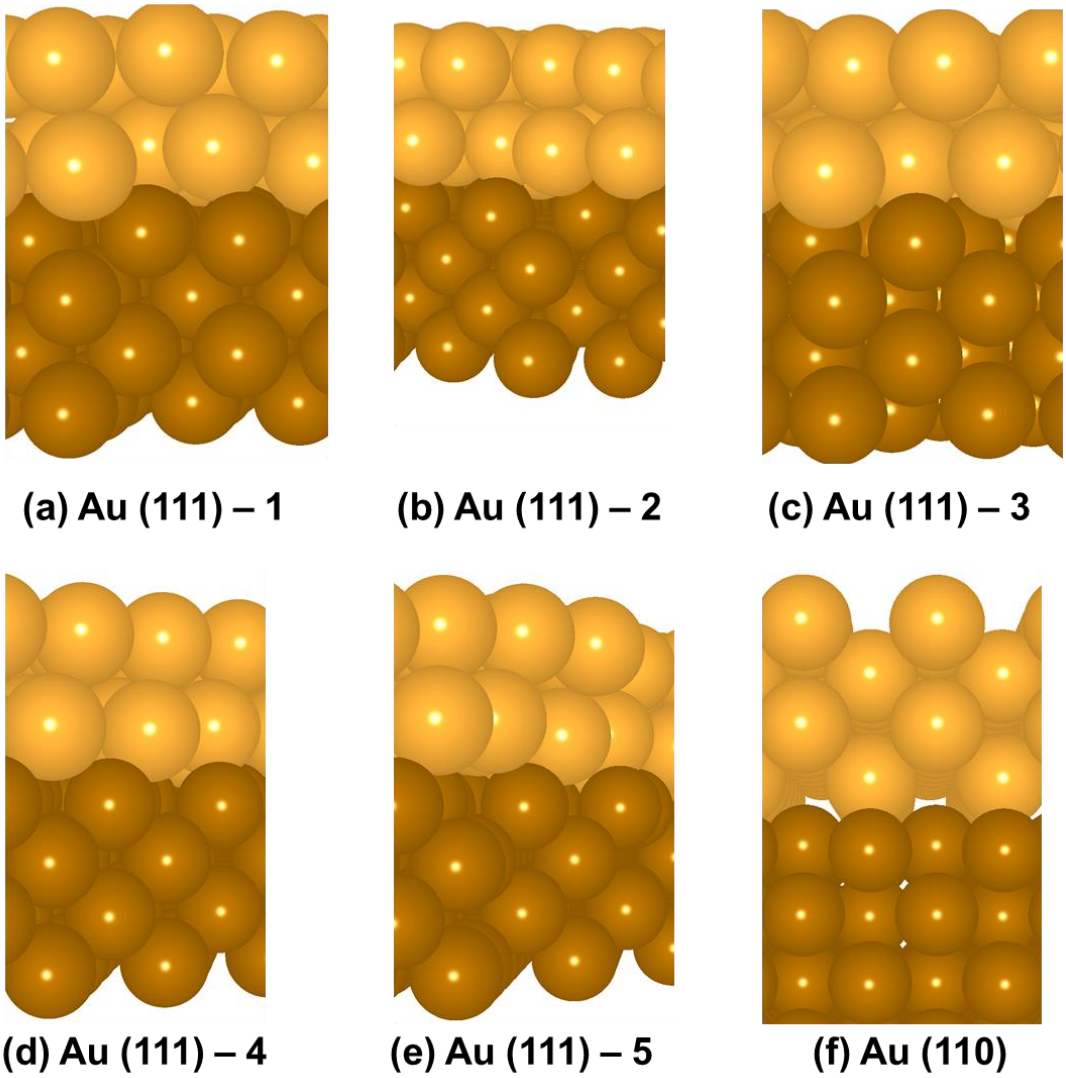

Figure A.22 (a) through (e), adsorption configurations of Au (111) films on Fe (110). These films are non-pseudomorphic, thus form moiré patterns. The strain in Au – Au bond distances parallel to the surface along (100) and (010) is provided in Table A.8. (f) adsorption geometry of Au (110) pseudomorphic film on Fe (110). Au atoms are shown in yellow, while Fe atoms are depicted in brown.

SI – CHAPTER 6

Powder X-ray diffraction (XRD) was carried out on a Rigaku Ultima U4 diffractometer, with Cu Kα radiation (λ = 1.5418 Å), at 40 kV and 44 mA. Scanning electron microscopy (SEM) was acquired on a FEI Quanta 250. Aberration-corrected high angle annular dark field scanning transmission electron microscopy (HAADF-STEM) images and electron energy loss spectroscopy (EELS) were acquired on a Titan Themis 300 probe corrected TEM equipped with a Super- X EDX detector at Sensitive Instrument Facility (SIF) of Ames Lab.

Pt loading of the Pt/Nb2CTx catalyst was determined by atomic absorption spectroscopy (AAS). Specifically, the catalyst was digested by aqua regia in a Nalgene® amber polyethylene bottle for 3 days and the solution was then diluted to desired concentration for the AAS measurement.

H2 temperature programmed reduction (TPR) experiment was performed with an Autochem 2000 unit. About 70 mg of the Nb2CTx support was loaded in the unit and dried in 50 sccm He at 200°C overnight. Then the catalyst was cooled to room temperature and purged with pure H2. The temperature was ramped from room temperature to 900°C under 50 sccm pure H2. The products were analyzed by a mass spectroscopy.

CO chemisorption was measured with an ASAP 2020 unit. About 100 mg of the fresh Pt/ Nb2CTx catalyst was loaded and reduced at 350 °C in pure H2 before measuring for CO chemisorption. CO/Pt stoichiometry factor of 1 was used to calculate the Pt dispersion.

Due to the low CO adsorption quantity on the catalyst, sub-ambient temperature CO pulse chemisorption was performed on a Micromeritics Autochem 2920 unit. Typically, about 100 mg of the fresh catalyst was loaded and reduced at 350 °C for 1 hour in 10% H2/Ar with a total flow of 30 mL/min. Then the system was flushed with He and the sample was cooled to – 30 °C. After reaching the stable temperature, CO pulse was introduced and the accumulated adsorption quantity was calculated.

XPS data were obtained using a Kratos Axis Ultra DLD spectrometer with monochromic Al Kα radiation (1486.6 eV) at pass energy of 20 and 160 eV for high-resolution and survey spectra, respectively. A commercial Kratos charge neutralizer was used to avoid non-homogeneous electric charge of non-conducting powder and to achieve better resolution. The resolution measured as full width at half maximum of the curve fitted C 1s peak was approximately 1 eV. Binding energy (BE) values refer to the Fermi edge and the energy scale

was calibrated using Au 4f7/2 at 84.0 eV and Cu 2p3/2 at 932.67 eV. XPS data were analyzed with CasaXPS. Curve-fitting was performed following a linear or Shirley background subtraction using Gaussian/Lorentzian peak shapes (GL and LF). The atomic concentrations of the elements in the near-surface region were estimated considering the corresponding Scofield atomic sensitivity factors and inelastic mean free path (IMFP) of photoelectrons using standard procedures in the CasaXPS software. For the quasi in situ XPS measurements, sample treatments were performed in a reaction cell (≈30 cm3) connected to the XPS spectrometer and all samples were reduced in 5% H2 at least for 30 minutes. Then the samples were moved between the reaction cell and the analysis chamber under ultrahigh vacuum (UHV) conditions without contact to air.

X-ray absorption measurements were acquired at the Nb K edge (18.9856 keV) and Pt LIII edge (11.5640 keV) on the bending magnet beam line of the Materials Research Collaborative Access Team (MRCAT) at the Sector 10 in the Advanced Photon Source, Argonne National Laboratory. 5 Measurements were made in transmission step-scan mode. The ionization chambers were optimized for the maximum current with linear response with 10% absorption in the incident ion chamber and 70% absorption in the transmission detector. A third detector in series simultaneously collected a Nb or Pt metal foil reference spectrum with each measurement for energy calibration. Solid samples were pressed into a cylindrical sample holder consisting of six wells, forming a selfsupporting wafer. The sample holder was placed in a quartz reactor tube sealed with Kapton windows by two ultra-torr fittings through which gas could be flowed. Nb2CTx materials, parent Nb2AlC and reference compounds Nb2O5, NbO2, NbC (Sigma-Aldrich) were scanned in air. Fresh Pt on Nb2CTx catalyst were reduced in 3% H2/He with a flow rate of 50 cm3 /min at 350 or 550o C for at least 30 min, then cooled to room temperature and flushed with He before they were scanned. The 1% Pt/Nb2CTx catalysts after water-gas-shift reaction were scanned in air.

The fits of the Extended X-ray Absorption Fine Structure (EXAFS) were evaluated using Artemis software[205]. The EXAFS coordination parameters were obtained by a least-squares fit in R-space of k2 -weighted Fourier transform data together. The data range is from 3.0 to 12.0 Å-1 in k space. For R space, the data was fitted from 1.0 to 3.0 Å in R space at the Nb edge and 1.6 to 3.2 Å at the Pt edge. The S0 2 value was obtained at Nb edge by fitting the NbC standard and at Pt edge by fitting Pt foil. The bond distances were adjusted based on initial inputs from

standard crystal structure information files of Nb2AlC and Pt3Nb for the fits of Nb edge and Pt edge, respectively[206, 207].

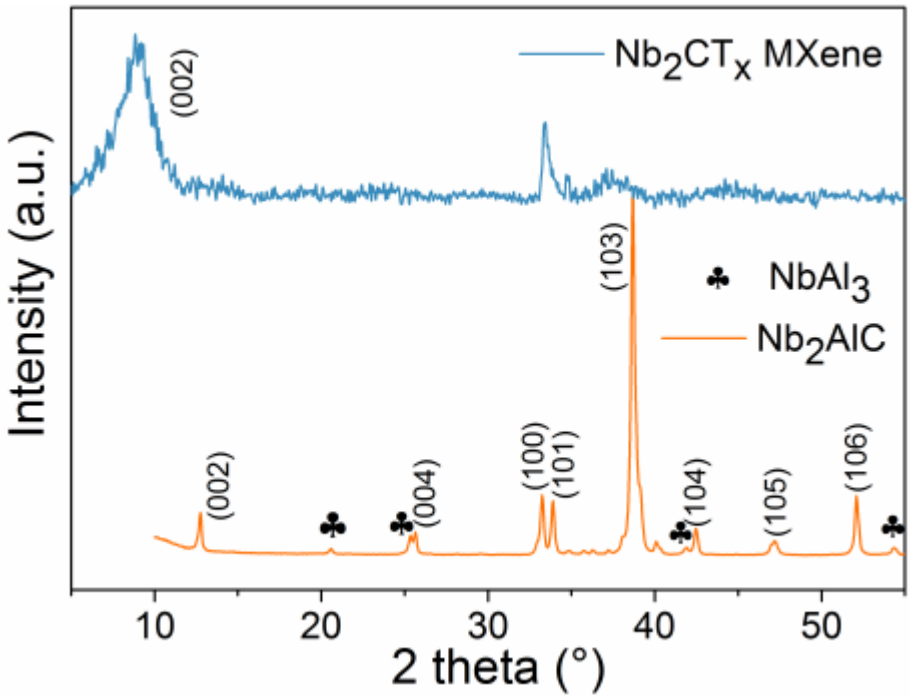

Figure A.23 XRD patterns of Nb2AlC MAX phase and Nb2CTx MXene

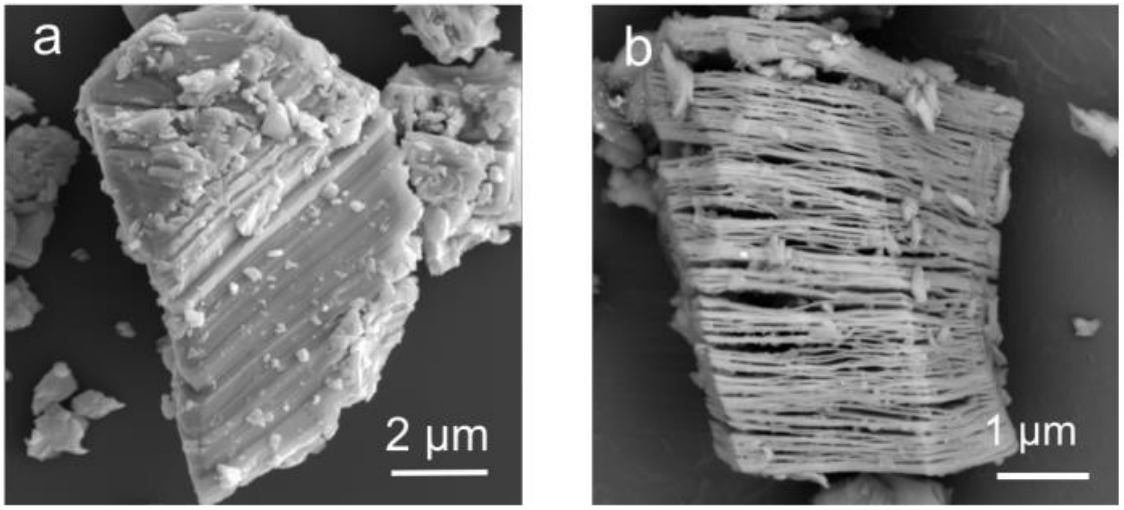

Figure A.24 (a) SEM image of Nb2AlC MAX. The as-synthesized Nb2AlC shows the typical lamellar structure. (b) SEM image of 1% Pt/Nb2CTx after WGS reaction showing the Pt/Nb2CTx maintains the typical layered structure of MXene.

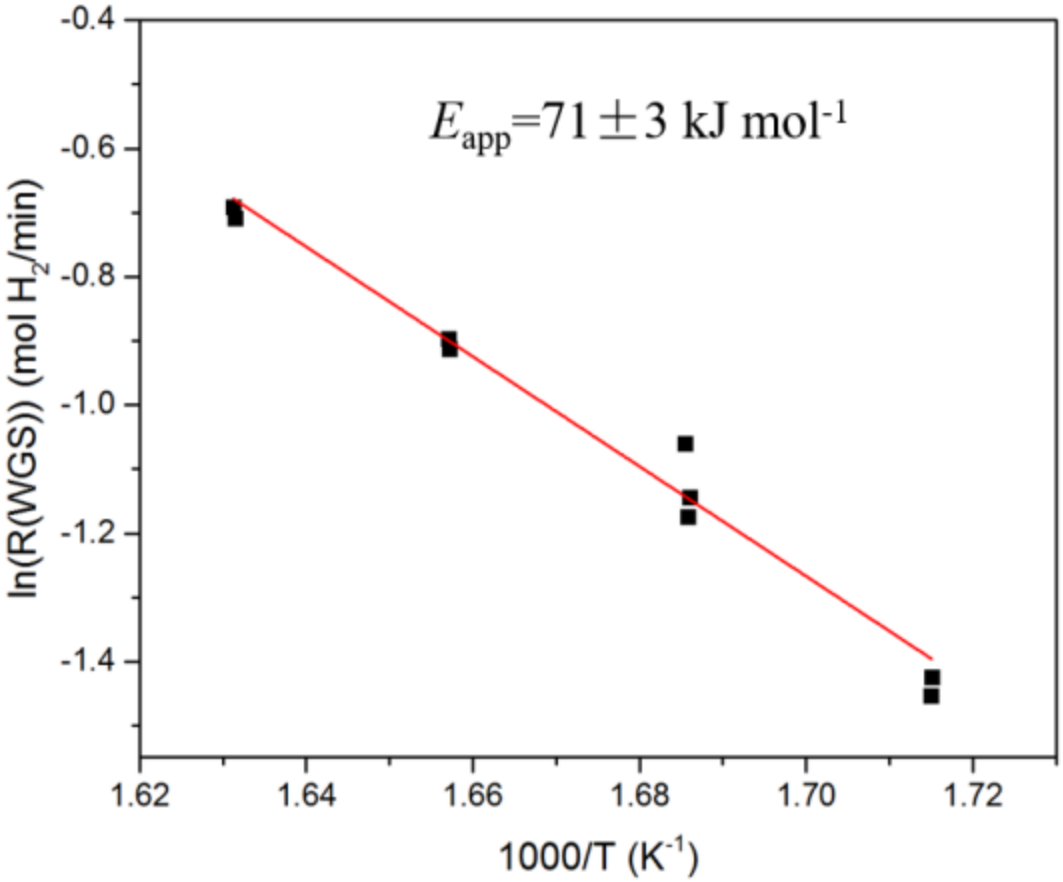

Figure A.25 Arrhenius plots for WGS over 1% Pt/Nb2CTx-MXene catalyst. The WGS rates were measured in presence of 7% CO, 22% H2O, 8.5% CO2, 37% H2, and balance Ar.

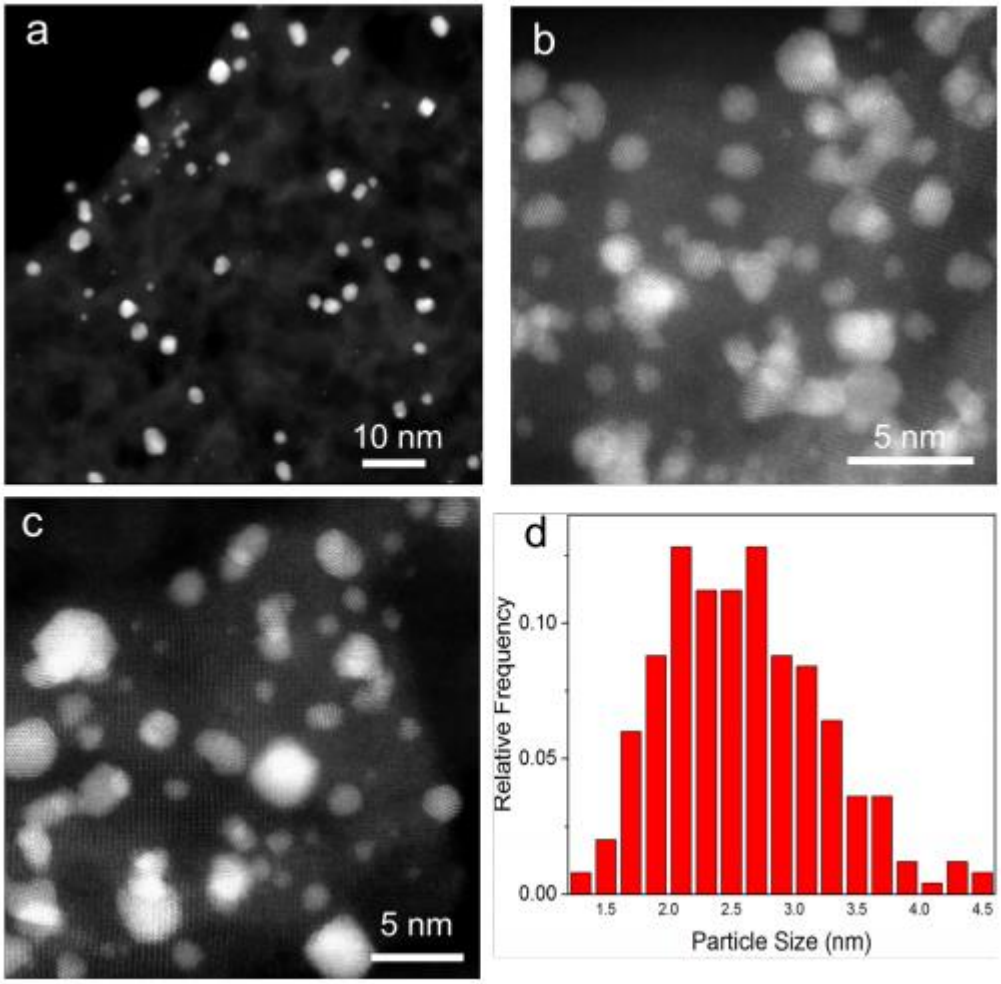

Figure A.26 HAADF-STEM images of 1% Pt/Nb2CTx after WGS reaction. (d) Particle size distribution statistics of used 1% Pt/Nb2CTx catalyst, and the average particle size is determined to be 2.6 ± 0.6 nm.

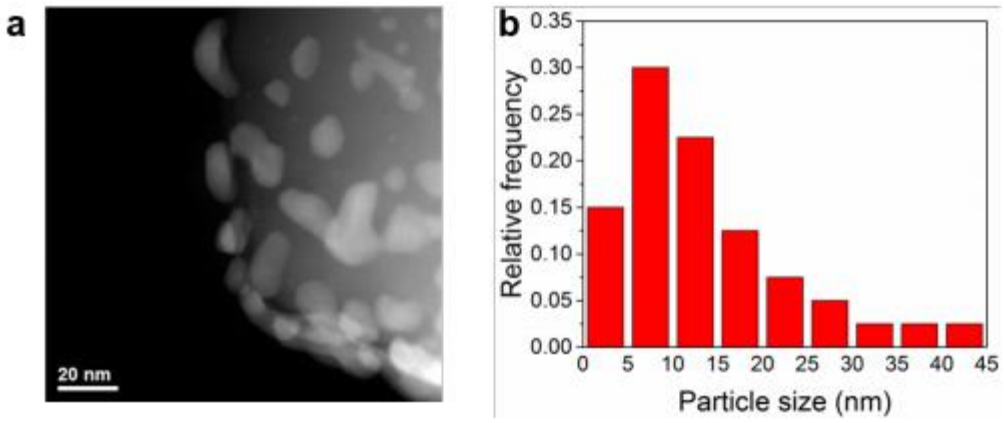

Figure A.27 (a) HAADF-STEM image of 1% Pt/NbC (bulk) after WGS reaction. (b) Particle size distribution statistics of used 1% Pt/NbC (bulk), and the average particle size is determined to be 13.8 ± 9.6 nm.

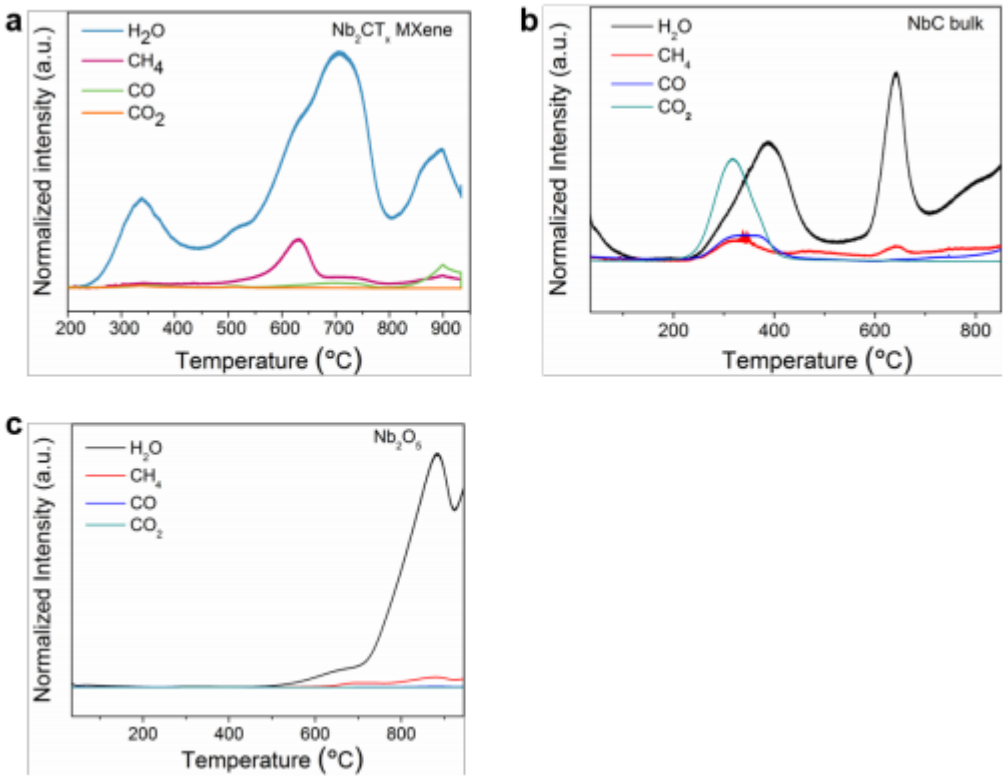

Figure A.28 (a) Temperature programmed reduction (TPR) profile of Nb2CTx MXene. The H2O peak around 340o C can be attributed to the reduction of O and OH terminations on the surface of Nb2CTx MXene, which is consistent with the results of the quasi in situ XPS. Comparing with the TPR profile of Nb2O5, the additional H2O peaks located above 600o C can be assigned to the reduction of residual Nb2O5 after HF etching[208]. The residue oxygen on the surface also desorbs as CO and CO2 [209] (b) TPR profile of commercial bulk NbC. The H2O peaks at around 400 °C and 650 °C are likely due to the removal of the surface residue oxygen [210]. (c)

TPR profile of commercial bulk Nb2O5. The peak between 800 °C and 900 °C is due to the reduction of Nb2O5 to NbO2 [211].

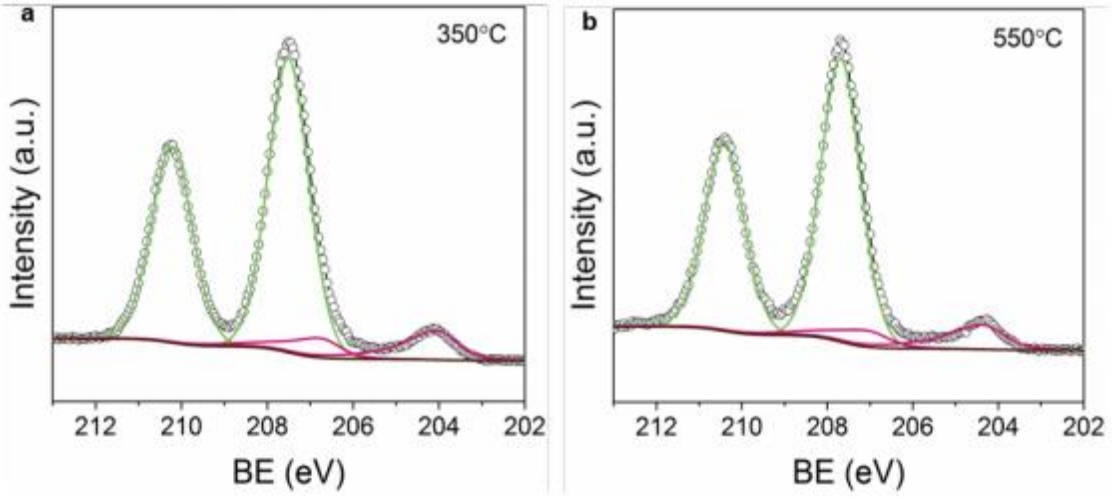

Figure A.29 Quasi in situ XPS spectra of Nb 3d of pre-reduced 1% Pt/Nb2CTx sample (the fresh sample was reduced at 350 °C by H2 and then exposed to air before the quasi in-situ XPS measurement) reduced at 350 °C and 550 °C again. These results indicate the enriched Nb2O5 induced by subsequent air exposure is not reducible by H2 at 550 °C.

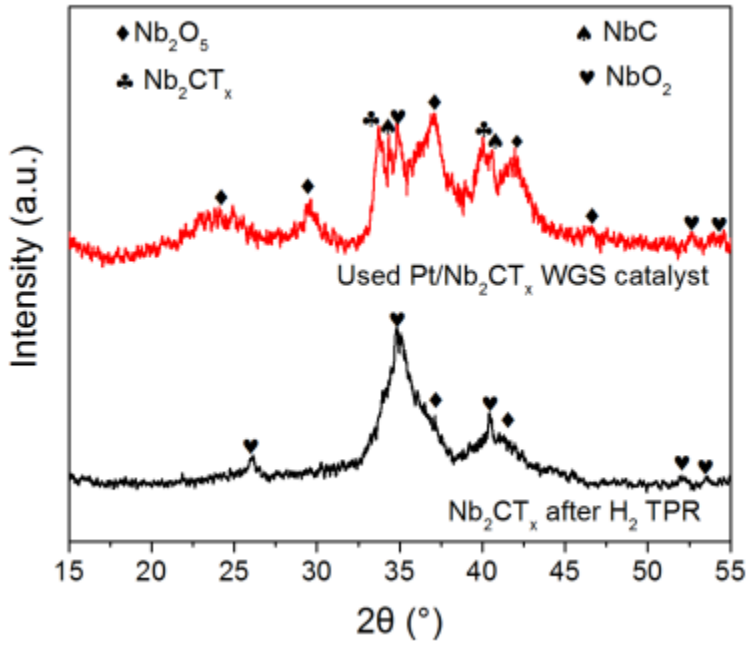

Figure A.30 XRD patterns of spent 1% Pt/Nb2CTx catalyst after WGS reaction (red line) and Nb2CTx MXene after TPR treatment (black line).

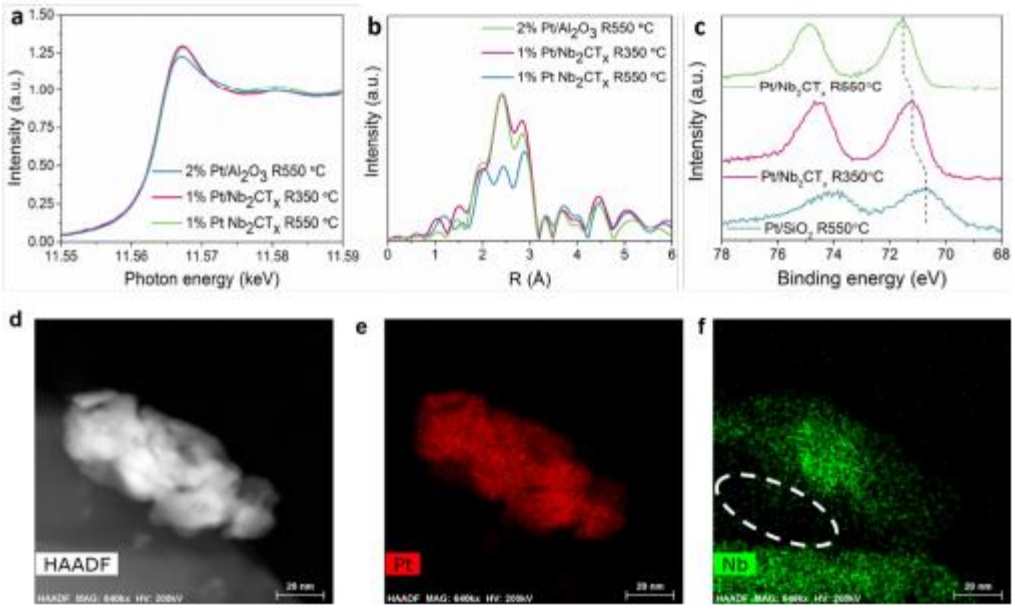

Figure A.31 (a) in situ XANES spectra of Pt LIII edge of 2% Pt/Al2O3 sample treated at 550 o C and fresh 1% Pt/Nb2CTx treated at 350 o C and 550 o C in 3 % H2/He. (b) Fourier transform magnitude of the k2 EXAFS of 2% Pt/Al2O3 sample treated at 550° C and fresh 1% Pt/Nb2CTx treated at 350 °C and 550 °C in 3 % H2/He. (c) Quasi in situ XPS spectra of Pt 4f7/2 of Pt/SiO2 reduced at 550 o C and Pt/Nb2CTx sample reduced at 350 o C and 550 o C. (d) HAADF-STEM image of fresh 1% Pt/Nb2CTx catalyst reduced in H2 at 550 °C. Particle agglomerates after the high temperature (550 °C) reduction. (e) Elemental mapping of Pt. (f) Elemental mapping of Nb. A Nb deficient area is circled by the white dash line.

To test our hypothesis that only Pt-Nb surface alloy is formed for 1% Pt/Nb2CTx reduced at 350^{o}C, we further increased reduction temperature to 550°C. Stronger evidence is observed from EXAFS of Pt/Nb2CTx sample reduced at higher temperature (550^{o}C), which is substantially different from that of Pt/Nb2CTx reduced at 350^{o}C because of the incorporation of larger amount of Nb in the nanoparticles. Fitting the spectra gives CN=6.7 for Pt-Pt bonds (2.77 Å) and CN=1.8 for Pt-Nb bonds (2.75 Å). Quasi in situ XPS spectra show Pt 4f7/2 components have binding energies equal to 70.7 eV, 71.2 eV and 71.6 eV for Pt/SiO2 sample reduced at 550 o C and 16 Pt/Nb2CTx sample reduced at 350^{o}C and 550^{o}C, respectively. Pt-Nb alloy with higher degree is presumably formed, as indicated by the further binding energy shift for Pt/Nb2CTx reduced at higher temperature (550^{o}C vs 350^{o}C). The alloy formation is further confirmed by HAADFSTEM with X-ray spectroscopy (EDS) elemental mapping. Interestingly, a

niobium deficient area is right beneath the alloy nanoparticle, which may imply diffusion of reduced Nb species.

Note the fitting results of XAS represent average numbers of the sample. The homogeneity and order of the alloys formed at 550 °C merit detailed study in the future.

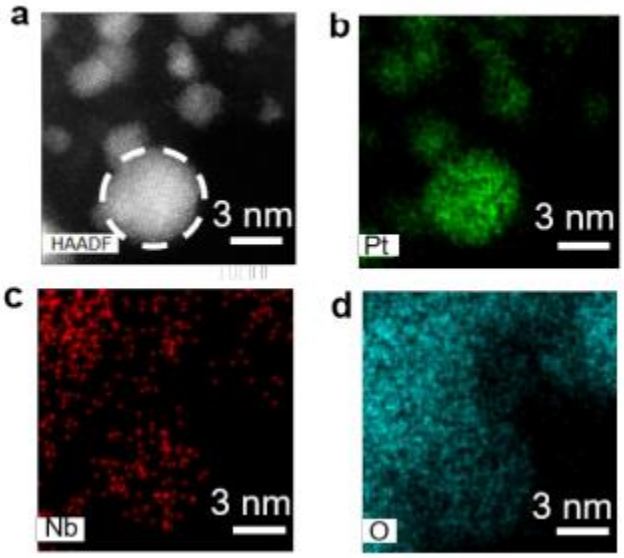

Figure A.32 (a) HAADF-STEM image of used 1% Pt/Nb2CTx WGS catalyst. (b) Elemental mapping of Pt (c) Elemental mapping of Nb, (d) Elemental mapping of O. The area of interest (circled using white dash line) is a nanoparticle which is hanging over vacuum to avoid Nb signal from the Nb2CTx support. The EDS result suggests that uniform bulk Pt-Nb alloy is not formed.

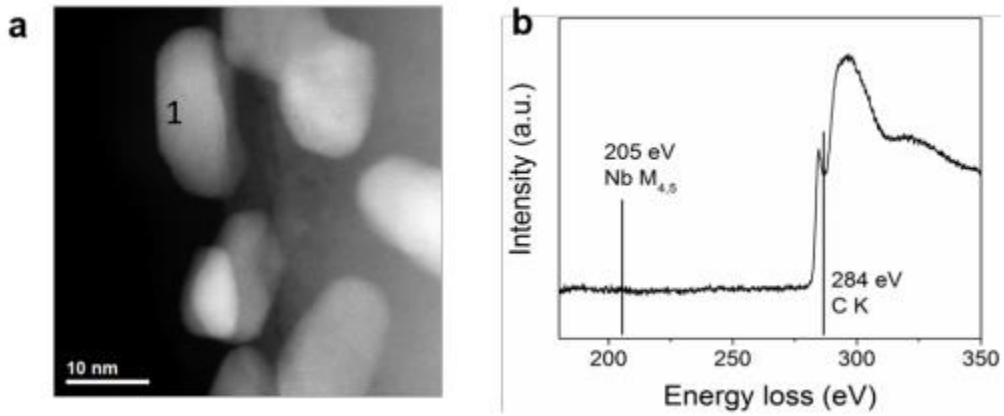

Figure A.33 (a) HAADF-STEM image of used 1% Pt/NbC bulk catalyst. (b) Spectrum of electron-energy loss acquired at a point (marked as ‘‘1’’) on the particle surface. The absence of Nb M4,5 absorption edge with onset at 205 eV indicates no Pt-Nb surface alloy is formed for Pt supported by bulk NbC. The signal of C can be caused by carbon lacey of the TEM grid or

carbon contamination of the catalysts. Note the catalyst was synthesized and treated using the same procedure with 1% Pt/Nb2CTx WGS catalyst.

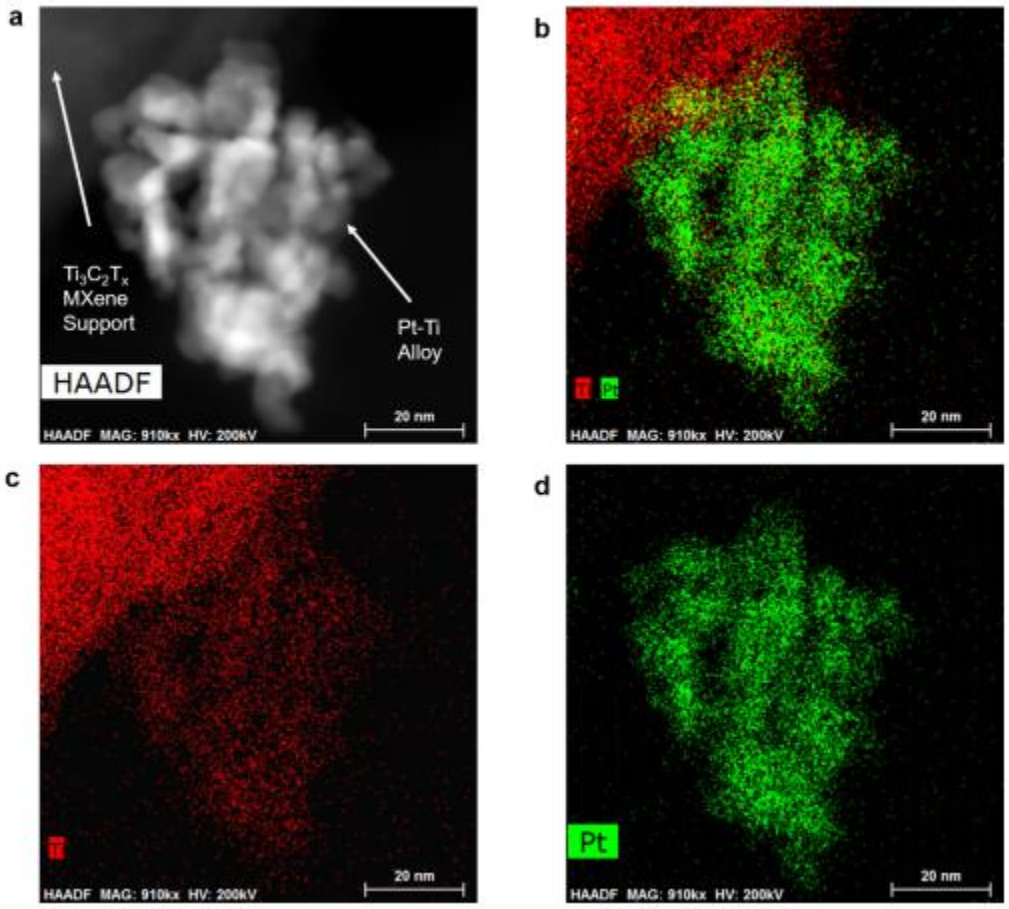

Figure A.34 (a) HAADF-STEM image of fresh 1% Pt/Ti3C2Tx catalyst reduced in H2 at 550 °C. Particles agglomerated after the high temperature (550 °C) reduction. (b) Elemental mapping of Pt and Ti. (c) Elemental mapping of Ti, (d) Elemental mapping of Pt.

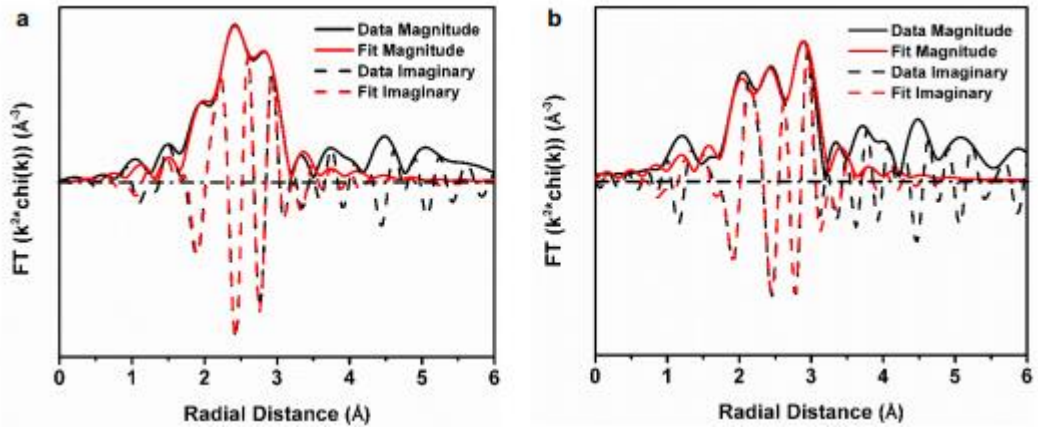

Figure A.35 The magnitude and imaginary part of the Fourier Transform of the k2 weighted EXAFS plot and corresponding first shell fit for Pt/Nb2CTx catalyst reduced at a) 350 °C and b) 550 °C. The fitting ranges are Δk = 2.7-11.7 Å-1 and ΔR = 1.6-3.2 Å. Corresponding fitting results are as below.

Table A.10 Quantitative evaluation of the EXAFS fit (Artemis Software)

Sample	Scattering Pair	S_0^2 *	CN *	Bond Length (Å) *	ΔE_0 (eV) *	σ^2 (Å ^{2}) *
Pt/Nb_2CT_x Reduced at 350 °C	Pt-Pt	0.8	7.4	2.75	4.2	0.005
	Pt-Nb		0.9	2.76		0.010
Pt/Nb_2CT_x Reduced at 550 °C	Pt-Pt	0.8	6.7	2.77	5.5	0.005
	Pt-Nb		1.8	2.75		0.008

REFERENCES

1. Cavani, F., N. Ballarini, and A. Cericola, *Oxidative dehydrogenation of ethane and propane: How far from commercial implementation?* Catalysis Today, 2007. **127**(1-4): p. 113-131.
2. Curtis, J.B., *Fractured shale-gas systems.* Aapg Bulletin, 2002. **86**(11): p. 1921-1938.
3. Mamedov, E.A. and V.C. Corberan, *Oxidative Dehydrogenation of Lower Alkanes on Vanadium Oxide-Based Catalysts - the Present State-of-the-Art and Outlooks.* Applied Catalysis a-General, 1995. **127**(1-2): p. 1-40.
4. Sattler, J.J.H.B., et al., *Catalytic Dehydrogenation of Light Alkanes on Metals and Metal Oxides.* Chemical Reviews, 2014. **114**(20): p. 10613-10653.
5. Childers, D.J., et al., *Modifying structure-sensitive reactions by addition of Zn to Pd.* Journal of Catalysis, 2014. **318**: p. 75-84.
6. Ojeda, M. and E. Iglesia, *Formic Acid Dehydrogenation on Au-Based Catalysts at Near-Ambient Temperatures.* Angewandte Chemie, 2009. **121**(26): p. 4894-4897.
7. Solymosi, F., et al., *Production of CO-free H< sub> 2</sub> from formic acid. A comparative study of the catalytic behavior of Pt metals on a carbon support.* Journal of Catalysis, 2011. **279**(1): p. 213-219.
8. Fan, M.S., A.Z. Abdullah, and S. Bhatia, *Catalytic Technology for Carbon Dioxide Reforming of Methane to Synthesis Gas.* Chemcatchem, 2009. **1**(2): p. 192-208.
9. Pakhare, D. and J. Spivey, *A review of dry (CO2) reforming of methane over noble metal catalysts.* Chemical Society Reviews, 2014. **43**(22): p. 7813-7837.
10. Farrauto, R.J., *Introduction to solid polymer membrane fuel cells and reforming natural gas for production of hydrogen.* Applied Catalysis B-Environmental, 2005. **56**(1-2): p. 3-7.
11. Farrauto, R., et al., *New material needs for hydrocarbon fuel processing: Generating hydrogen for the PEM fuel cell.* Annual Review of Materials Research, 2003. **33**: p. 1-27.
12. Newsome, D.S., *The Water-Gas Shift Reaction.* Catalysis Reviews-Science and Engineering, 1980. **21**(2): p. 275-318.
13. Williams, W.D., et al., *Metallic Corner Atoms in Gold Clusters Supported on Rutile Are the Dominant Active Site during Water− Gas Shift Catalysis.* Journal of the American Chemical Society, 2010. **132**(40): p. 14018-14020.
14. Sabnis, K.D., et al., *Determination of effect of the oxide support for the water-gas shift reaction over supported Au and Pt nanoparticles.* Abstracts of Papers of the American Chemical Society, 2013. **246**.
15. Cybulskis, V., et al., *Water activation by the supports for Pt catalysts during the water-gas shift reaction.* Abstracts of Papers of the American Chemical Society, 2016. **251**.
16. Fu, Q., H. Saltsburg, and M. Flytzani-Stephanopoulos, *Active nonmetallic Au and Pt species on ceria-based water-gas shift catalysts.* Science, 2003. **301**(5635): p. 935-938.
17. Gland, J.L. and E.B. Kollin, *Carbon-Monoxide Oxidation on the Pt(111) Surface - Temperature Programmed Reaction of Coadsorbed Atomic Oxygen and Carbon-Monoxide.* Journal of Chemical Physics, 1983. **78**(2): p. 963-974.
18. Goodman, A.L., E.T. Bernard, and V.H. Grassian, *Spectroscopic study of nitric acid and water adsorption on oxide particles: Enhanced nitric acid uptake kinetics in the presence of adsorbed water.* Journal of Physical Chemistry A, 2001. **105**(26): p. 6443-6457.

19. Shekhar, M., et al., *Size and Support Effects for the Water-Gas Shift Catalysis over Gold Nanoparticles Supported on Model Al2O3 and TiO2.* Journal of the American Chemical Society, 2012. **134**(10): p. 4700-4708.
20. Penner, S. and M. Armbruester, *Formation of Intermetallic Compounds by Reactive MetalSupport Interaction: A Frequently Encountered Phenomenon in Catalysis.* Chemcatchem, 2015. **7**(3): p. 374-392.
21. Bollmann, L., et al., *Effect of Zn addition on the water-gas shift reaction over supported palladium catalysts.* Journal of Catalysis, 2008. **257**(1): p. 43-54.
22. Iwasa, N., et al., *HIGHLY SELECTIVE SUPPORTED PD CATALYSTS FOR STEAM REFORMING OF METHANOL.* Catalysis Letters, 1993. **19**(2-3): p. 211-216.
23. Iwasa, N., et al., *STEAM REFORMING OF METHANOL OVER PD/ZNO - EFFECT OF THE FORMATION OF PDZN ALLOYS UPON THE REACTION.* Applied Catalysis a-General, 1995. **125**(1): p. 145-157.
24. gallagher, J., et al., *Structural evolution of an intermetallic Pd–Zn catalyst selective for propane dehydrogenation.* Phys. Chem. Chem. Phys, 2015.
25. Chen, Z.X., et al., *Surface structure and stability of PdZn and PtZn alloys: Density-functional slab model studies.* Physical Review B, 2003. **68**(7): p. 8.
26. Horcas, I., et al., *WSXM: A software for scanning probe microscopy and a tool for nanotechnology.* Review of Scientific Instruments, 2007. **78**(1): p. 013705.
27. Ley, L., et al., *X-RAY PHOTOEMISSION FROM ZINC - EVIDENCE FOR EXTRA-ATOMIC RELAXATION VIA SEMILOCALIZED EXCITONS.* Physical Review B, 1973. **8**(6): p. 2392-2402.
28. MacLeod, J.M., et al., *Surface structure of Pd(111) with less than half a monolayer of Zn.* Physical Chemistry Chemical Physics, 2013. **15**(30): p. 12488-12494.
29. Gabasch, H., et al., *Zn adsorption on pd(111): ZnO and PdZn alloy formation.* Journal of Physical Chemistry B, 2006. **110**(23): p. 11391-11398.
30. Weirum, G., et al., *Growth and Desorption Kinetics of Ultrathin Zn Layers on Pd(111).* Journal of Physical Chemistry C, 2009. **113**(22): p. 9788-9796.
31. Tamtogl, A., et al., *Adsorption/desorption of H-2 and CO on Zn-modified Pd(111).* Journal of Chemical Physics, 2008. **129**(22).
32. Guo, X.C. and R.J. Madix, *Origin of vinylic C-H bond activation in the combustion of alkenes on palladium: an HREELS study of propene on Pd(100)-p(2x2)-O.* Surface Science, 1997. **391**(1-3): p. L1165-L1171.
33. Monteiro, R., et al., *Turnover rate and reaction orders for the complete oxidation of methane on a palladium foil in excess dioxygen.* Journal of Catalysis, 2001. **199**(2): p. 291-301.
34. Smeltz, A., et al., *Coupled theoretical and experimental analysis of surface coverage effects in Pt-catalyzed NO and O< sub> 2</sub> reaction to NO< sub> 2</sub> on Pt (111).* Catalysis Today, 2008. **136**(1): p. 84-92.
35. Hagstrom, S., H.B. Lyon, and G.A. Somorjai, *Surface Structures on Clean Platinum (100) Surface.* Physical Review Letters, 1965. **15**(11): p. 491-&.
36. Schoofs, G.R. and J.B. Benziger, *Decomposition of acetic acid monomer, acetic acid dimer, and acetic anhydride on Ni (111).* Surface science, 1984. **143**(2): p. 359-368.
37. Coolidge, A.S., *The vapor density and some other properties of formic acid.* Journal of the American Chemical Society, 1928. **50**(8): p. 2166-2178.

38. Fadley, C.S., *Basic concepts of x-ray photoelectron spectroscopy.* Electron Spectrosc. Theory, Tech. Appl., 1978. **2**: p. 1-156.
39. Scofield, J.H., *Hartree-Slater subshell photoionization cross-sections at 1254 and 1487 eV.* Journal of Electron Spectroscopy and Related Phenomena, 1976. **8**(2): p. 129-137.
40. Yeh, J.J. and I. Lindau, *Atomic subshell photoionization cross sections and asymmetry parameters: 1 ⩽ Z ⩽ 103.* Atomic Data and Nuclear Data Tables, 1985. **32**(1): p. 1-155.
41. Powell, C.J. and A. Jablonski, *NIST Electron Effective-Attenuation-Length Database - Version 1.3, National Institute of Standards and Technology*. 2011, Gaithersburg, MD.
42. Moulder, J.F., J. Chastain, and R.C. King, *Handbook of X-ray photoelectron spectroscopy: a reference book of standard spectra for identification and interpretation of XPS data*. 1995, Eden Prairie, MN: Physical Electronics.
43. Rodriguez, N.M., et al., *XPS, EM, and catalytic studies of the accumulation of carbon on Pt black.* Journal of Catalysis, 2001. **197**(2): p. 365-377.
44. Chun, W.-J., et al., *Surface structure change of a [Pt4 (μ-CH3COO) 8]/SiO2 catalyst active for the decomposition of formic acid.* J. Chem. Soc., Faraday Trans., 1995. **91**(22): p. 4161-4170.
45. Block, J. and J. Vogl, *Scheinbare und wahre Aktivierungswärmen beim katalytischen Zerfall der Ameisensäure an Platin.* Zeitschrift für Elektrochemie, Berichte der Bunsengesellschaft für physikalische Chemie, 1959. **63**(1): p. 3-6.
46. Avery, N.R., *Adsorption of formic acid on clean and oxygen covered Pt (111).* Applications of Surface Science, 1982. **11**: p. 774-783.
47. Columbia, M., A. Crabtree, and P. Thiel, *Effect of CO on Pt-catalyzed decomposition of formic acid in ultrahigh vacuum.* Journal of Electroanalytical Chemistry, 1993. **345**(1): p. 93-105.
48. Hofmann, P., et al., *Orientation of chemisorbed species from electron impact and dipole selection rules: The formate on Pt {110}.* Surface Science Letters, 1983. **133**(1): p. L459-L464.
49. Temkin, M., *Relation between the apparent and the true activation energy of heterogeneous reactions.* Acta physicochim. URSS, 1935. **2**: p. 313-316.
50. Ertl, G., M. Neumann, and K.M. Streit, *Chemisorption of CO on Pt(111) Surface.* Surface Science, 1977. **64**(2): p. 393-410.
51. Thiel, P.A., et al., *The Interaction of CO and Pt(100) .2. Energetic and Kinetic-Parameters.* Journal of Chemical Physics, 1983. **78**(12): p. 7448-7458.
52. Silbaugh, T.L., E.M. Karp, and C.T. Campbell, *Energetics of Formic Acid Conversion to Adsorbed Formates on Pt(111) by Transient Calorimetry.* Journal of the American Chemical Society, 2014. **136**(10): p. 3964-3971.
53. Koeleman, B.J.J., et al., *Adsorption Study of Hydrogen on a Stepped Pt (997) Surface Using Low-Energy Recoil Scattering.* Nuclear Instruments & Methods in Physics Research, 1983. **218**(1-3): p. 225-229.
54. Singh, S., et al., *Formic acid decomposition on Au catalysts: DFT, microkinetic modeling, and reaction kinetics experiments.* AIChE Journal, 2014. **60**(4): p. 1303-1319.
55. Herron, J.A., et al., *Trends in Formic Acid Decomposition on Model Transition Metal Surfaces: A Density Functional Theory study.* ACS Catalysis, 2014. **4**: p. 4434-4445.
56. Abbas, N. and R. Madix, *Surface reaction modification: The effect of structured overlayers of sulfur on the kinetics and mechanism of the decomposition of formic acid on Pt (111).* Applications of Surface Science, 1983. **16**(3): p. 424-440.

57. Hammer, B., O.H. Nielsen, and J.K. Norskov, *Structure sensitivity in adsorption: CO interaction with stepped and reconstructed Pt surfaces.* Catalysis Letters, 1997. **46**(1-2): p. 31-35.
58. Fujimoto, K., et al., *Structure and reactivity of PdOx/ZrO2, catalysts for methane oxidation at low temperatures.* Journal of Catalysis, 1998. **179**(2): p. 431-442.
59. He, D., et al., *Effects of zirconia phase on the synthesis of higher alcohols over zirconia and modified zirconia.* Journal of Molecular Catalysis A: Chemical, 2004. **208**(1–2): p. 267-271.
60. Behrens, M. and M. Armbrüster, *Methanol Steam Reforming*, in *Catalysis for Alternative Energy Generation*, L. Guczi and A. Erdôhelyi, Editors. 2012, Springer New York. p. 175-235.
61. Purnama, H., et al., *Activity and selectivity of a nanostructured CuO/ZrO2 catalyst in the steam reforming of methanol.* Catalysis Letters, 2004. **94**(1-2): p. 61-68.
62. Sudarsanam, P., et al., *Nano-Au/CeO2 catalysts for CO oxidation: Influence of dopants (Fe, La and Zr) on the physicochemical properties and catalytic activity.* Applied Catalysis B: Environmental, 2014. **144**(0): p. 900-908.
63. Du, W., et al., *Photocatalytic studies of Ho–Zr–O nano-composite with controllable composition and defects.* Materials Characterization, 2013. **83**(0): p. 178-186.
64. Atkinson, A., et al., *Advanced anodes for high-temperature fuel cells.* Nat Mater, 2004. **3**(1): p. 17-27.
65. Puurunen, R.L., *Surface chemistry of atomic layer deposition: A case study for the trimethylaluminum/water process.* Journal of Applied Physics, 2005. **97**(12): p. -.
66. Chang, J.P., et al., *Ultrathin zirconium oxide films as alternative gate dielectrics.* Journal of Vacuum Science & Technology B, 2001. **19**(6): p. 2137-2143.
67. Mayr, L., et al., *An (ultra) high-vacuum compatible sputter source for oxide thin film growth.* Review of Scientific Instruments, 2013. **84**(9): p. 094103.
68. Mayr, L., et al., *Steering of methanol reforming selectivity by zirconia–copper interaction.* Journal of Catalysis, 2015. **321**(0): p. 123-132.
69. Rameshan, C., et al., *Hydrogen Production by Methanol Steam Reforming on Copper Boosted by Zinc-Assisted Water Activation.* Angewandte Chemie, 2012. **124**(12): p. 3057-3061.
70. Rameshan, C., et al., *Subsurface-Controlled CO2 Selectivity of PdZn Near-Surface Alloys in H-2 Generation by Methanol Steam Reforming.* Angewandte Chemie-International Edition, 2010. **49**(18): p. 3224-3227.
71. Wang, S.B., G.Q.M. Lu, and G.J. Millar, *Carbon dioxide reforming of methane to produce synthesis gas over metal-supported catalysts: State of the art.* Energy & Fuels, 1996. **10**(4): p. 896-904.
72. Ferreira-Aparicio, P., A. Guerrero-Ruiz, and I. Rodriguez-Ramos, *Comparative study at low and medium reaction temperatures of syngas production by methane reforming with carbon dioxide over silica and alumina supported catalysts.* Applied Catalysis a-General, 1998. **170**(1): p. 177-187.
73. Ay, H. and D. Üner, *Dry reforming of methane over CeO2 supported Ni, Co and Ni–Co catalysts.* Applied Catalysis B: Environmental, 2015. **179**: p. 128-138.
74. Elsayed, N.H., et al., *Low temperature dry reforming of methane over Pt-Ni-Mg/ceria-zirconia catalysts.* Applied Catalysis B-Environmental, 2015. **179**: p. 213-219.

75. Kertis, F., et al., *Structure/processing relationships in the fabrication of nanoporous gold.* JOM, 2010. **62**(6): p. 50-56.
76. Valden, M., X. Lai, and D.W. Goodman, *Onset of Catalytic Activity of Gold Clusters on Titania with the Appearance of Nonmetallic Properties.* Science, 1998. **281**(5383): p. 1647-1650.
77. Gharachorlou, A., et al., *Trimethylaluminum and Oxygen Atomic Layer Deposition on Hydroxyl-Free Cu(111).* Acs Applied Materials & Interfaces, 2015. **7**(30): p. 16428-16439.
78. Gharachorlou, A., et al., *Surface Chemistry of Trimethylaluminum on Pd(111) and Pt(111).* Journal of Physical Chemistry C, 2015. **119**(33): p. 19059-19072.
79. Gharachorlou, A., et al., *Palladium Nanoparticle Formation on TiO2(110) by Thermal Decomposition of Palladium(II) Hexafluoroacetylacetonate.* Acs Applied Materials & Interfaces, 2014. **6**(16): p. 14702-14711.
80. Paul, R., et al., *Atomic Layer Deposition of FeO on Pt(111) by Ferrocene Adsorption and Oxidation.* Chemistry of Materials, 2015. **27**(17): p. 5915-5924.
81. Mayr, L., et al., *Boosting Hydrogen Production from Methanol and Water by in situ Activation of Bimetallic Cu-Zr Species.* Chemcatchem, 2016. **8**(10): p. 1778-1781.
82. Mayr, L., et al., *Combined UHV/high-pressure catalysis setup for depth-resolved near-surface spectroscopic characterization and catalytic testing of model catalysts.* Review of Scientific Instruments, 2014. **85**(5).
83. Knop-Gericke, A., et al., *X-Ray Photoelectron Spectroscopy for Investigation of Heterogeneous Catalytic Processes*, in *Advances in Catalysis, Vol 52*, B.C. Gates and H. Knozinger, Editors. 2009. p. 213-272.
84. *CasaXPS Version 2.3.16 Pre-rel 1.4*. 2011, Casa Software Ltd.
85. Wagner, C.D.R., W. M.; Davis, L. E.; Moulder, J. F.; Muilenberg, G. E. , *Handbook of X-Ray Photoelectron Spectroscopy*. Vol. Vol. 55344. 1979, Eden Prairie, Minnesota: Perkin-Elmer Corporation, Physical Electronics Division.
86. Majumdar, D. and D. Chatterjee, *X-RAY PHOTOELECTRON SPECTROSCOPIC STUDIES ON YTTRIA, ZIRCONIA, AND YTTRIA-STABILIZED ZIRCONIA.* Journal of Applied Physics, 1991. **70**(2): p. 988-992.
87. Shi, X.-R., et al., *Theoretical studies on chemisorption of oxygen on beta-Mo2C catalyst and its surface oxidation.* Surface Science, 2012. **606**(15-16): p. 1187-1194.
88. Kresse, G. and J. Furthmuller, *Efficiency of ab-initio total energy calculations for metals and semiconductors using a plane-wave basis set.* Computational Materials Science, 1996. **6**(1): p. 15-50.
89. Kresse, G. and D. Joubert, *From ultrasoft pseudopotentials to the projector augmented-wave method.* Physical Review B, 1999. **59**(3): p. 1758-1775.
90. Klimes, J., D.R. Bowler, and A. Michaelides, *Chemical accuracy for the van der Waals density functional.* Journal of Physics-Condensed Matter, 2010. **22**(2).
91. Klimes, J., D.R. Bowler, and A. Michaelides, *Van der Waals density functionals applied to solids.* Physical Review B, 2011. **83**(19).
92. Cameron, M.A. and S.M. George, *ZrO2 film growth by chemical vapor deposition using zirconium tetra-tert-butoxide.* Thin Solid Films, 1999. **348**(1-2): p. 90-98.
93. Gabasch, H., et al., *Carbon incorporation during ethene oxidation on Pd(111) studied by in situ X-ray photoelectron spectroscopy at 2 x 10(-3) mbar.* Journal of Catalysis, 2006. **242**(2): p. 340-348.

94. Gharachorlou, A., et al., *The Surface Chemistry of Trimethylaluminum on Pd(111) and Pt(111).* Journal of Physical Chemistry C, 2015.
95. Lynch, C.T., et al., *INFRARED SPECTRA OF TRANSITION METAL ALKOXIDES.* Analytical Chemistry, 1964. **36**(12): p. 2332-&.
96. Sert, Y., et al., *Vibrational frequency analysis, FT-IR, DFT and M06-2X studies on tert-Butyl N-(thiophen-2yl)carbamate.* Spectrochimica Acta Part a-Molecular and Biomolecular Spectroscopy, 2014. **128**: p. 46-53.
97. Oelichmann, H.J., D. Bougeard, and B. Schrader, *COUPLED CALCULATION OF VIBRATIONAL FREQUENCIES AND INTENSITIES .5. IR AND RAMAN-SPECTRA OF GLYOXAL AND ACROLEIN.* Journal of Molecular Structure, 1981. **77**(1-2): p. 149-163.
98. Oelichmann, H.J., D. Bougeard, and B. Schrader, *COUPLED CALCULATION OF VIBRATIONAL FREQUENCIES AND INTENSITIES .4. IR AND RAMAN-SPECTRA OF CROTONALDEHYDE, METHACROLEIN AND METHYLVINYLKETONE.* Journal of Molecular Structure, 1981. **77**(3-4): p. 179-194.
99. Brown, N.F. and M.A. Barteau, *REACTIONS OF UNSATURATED OXYGENATES ON RHODIUM(111) AS PROBES OF MULTIPLE COORDINATION OF ADSORBATES.* Journal of the American Chemical Society, 1992. **114**(11): p. 4258-4265.
100. Chase, M.W., *NIST-JANAF Themochemical Tables, Fourth Edition.* J. Phys. Chem. Ref. Data 1998. **Monograph 9**: p. 1-1951.
101. Hu, C., et al., *In situ reaction synthesis, electrical and thermal, and mechanical properties of Nb(4)AlC(3).* Journal of the American Ceramic Society, 2008. **91**(7): p. 2258-2263.
102. Li, H., et al., *Growth of an Ultrathin Zirconia Film on Pt3Zr Examined by High-Resolution X-ray Photoelectron Spectroscopy, Temperature-Programmed Desorption, Scanning Tunneling Microscopy, and Density Functional Theory.* Journal of Physical Chemistry C, 2015. **119**(5): p. 2462-2470.
103. Sinha, S., S. Badrinarayanan, and A.P.B. Sinha, *AN XPS STUDY OF HYDROGEN IMPLANTED ZIRCONIUM.* Journal of the Less-Common Metals, 1987. **134**(2): p. 229-236.
104. Huang, C.Y., Z.L. Tang, and Z.T. Zhang, *Differences between zirconium hydroxide (Zr(OH)(4)center dot nH(2)O) and hydrous zirconia (ZrO2 center dot nH(2)O).* Journal of the American Ceramic Society, 2001. **84**(7): p. 1637-1638.
105. Leisenberger, F.P., et al., *Surface and subsurface oxygen on Pd(111).* Surface Science, 2000. **445**(2-3): p. 380-393.
106. Cao, Y. and Z.-X. Chen, *Slab model studies of water adsorption and decomposition on clean and X- (X = C, N and O) contaminated Pd(111) surfaces.* Physical Chemistry Chemical Physics, 2007. **9**(6): p. 739-746.
107. Ji, M., et al., *Theoretical Study of Oxygen Chemisorption on Pd (111), Au (111) and Pd-Au (111) Alloy Surfaces.* Journal of Computational and Theoretical Nanoscience, 2012. **9**(3): p. 394-400.
108. Klikovits, J., et al., *Surface oxides on Pd(111): STM and density functional calculations.* Physical Review B, 2007. **76**(4).
109. Gabasch, H., et al., *Growth and decay of the Pd(111)-Pd5O4 surface oxide: Pressure-dependent kinetics and structural aspects.* Surface Science, 2006. **600**(1): p. 205-218.
110. Klotzer, B., et al., *Oxygen-induced surface phase transformation of Pd(111): sticking, adsorption and desorption kinetics.* Surface Science, 2001. **482**: p. 237-242.

111. Rameshan, C., et al., *Subsurface-Controlled CO2 Selectivity of PdZn Near-Surface Alloys in H-2 Generation by Methanol Steam Reforming.* Angewandte Chemie-International Edition, 2010. **49**(18): p. 3224-3227.
112. Rameshan, C., et al., *Hydrogen Production by Methanol Steam Reforming on Copper Boosted by Zinc-Assisted Water Activation.* Angewandte Chemie-International Edition, 2012. **51**(12): p. 3002-3006.
113. Mayr, L., et al., *Steering of methanol reforming selectivity by zirconia-copper interaction.* Journal of Catalysis, 2015. **321**: p. 123-132.
114. Kaufmann, R., et al., *Xps Studies of the Thermal-Behavior of Passivated Zircaloy-4 Surfaces.* Surface and Interface Analysis, 1988. **11**(10): p. 502-509.
115. Mayr, L., et al., *Steering of methanol reforming selectivity by zirconia-copper interaction.* Journal of Catalysis, 2015. **321**: p. 123-132.
116. Farmer, J.A. and C.T. Campbell, *Ceria Maintains Smaller Metal Catalyst Particles by Strong Metal-Support Bonding.* Science, 2010. **329**(5994): p. 933-936.
117. Hutchings, G.J., *VAPOR-PHASE HYDROCHLORINATION OF ACETYLENE - CORRELATION OF CATALYTIC ACTIVITY OF SUPPORTED METAL CHLORIDE CATALYSTS.* Journal of Catalysis, 1985. **96**(1): p. 292-295.
118. Haruta, M., et al., *NOVEL GOLD CATALYSTS FOR THE OXIDATION OF CARBON-MONOXIDE AT A TEMPERATURE FAR BELOW 0-DEGREES-C.* Chemistry Letters, 1987(2): p. 405-408.
119. Hashmi, A.S.K. and G.J. Hutchings, *Gold catalysis.* Angewandte Chemie-International Edition, 2006. **45**(47): p. 7896-7936.
120. Choudhary, T.V. and D.W. Goodman, *Oxidation catalysis by supported gold nano-clusters.* Topics in Catalysis, 2002. **21**(1-3): p. 25-34.
121. Bokhimi, X., R. Zanella, and C. Angeles-Chavez, *Rutile-Supported Ir, Au, and Ir Au Catalysts for CO Oxidation.* Journal of Physical Chemistry C, 2010. **114**(33): p. 14101-14109.
122. Fu, Q., A. Weber, and M. Flytzani-Stephanopoulos, *Nanostructured Au-CeO2 catalysts for low-temperature water-gas shift.* Catalysis Letters, 2001. **77**(1-3): p. 87-95.
123. Rodriguez, J.A., et al., *Activity of CeOx and TiOx nanoparticles grown on Au(111) in the water-gas shift reaction.* Science, 2007. **318**(5857): p. 1757-1760.
124. Ta, N., et al., *Stabilized Gold Nanoparticles on Ceria Nanorods by Strong Interfacial Anchoring.* Journal of the American Chemical Society, 2012. **134**(51): p. 20585-20588.
125. Boucher, M.B., et al., *'Shape effects' in metal oxide supported nanoscale gold catalysts.* Physical Chemistry Chemical Physics, 2011. **13**(7): p. 2517-2527.
126. Carrettin, S., et al., *Nanocrystalline CeO2 increases the activity of an for CO oxidation by two orders of magnitude.* Angewandte Chemie-International Edition, 2004. **43**(19): p. 2538-2540.
127. Yu, H., et al., *Dumbbell-like bifunctional Au-Fe3O4 nanoparticles.* Nano Letters, 2005. **5**(2): p. 379-382.
128. Yin, H., et al., *Colloidal deposition synthesis of supported gold nanocatalysts based on Au-Fe3O4 dumbbell nanoparticles.* Chemical Communications, 2008(36): p. 4357-4359.
129. Lee, Y., et al., *Synthetic Tuning of the Catalytic Properties of Au-Fe3O4 Nanoparticles.* Angewandte Chemie-International Edition, 2010. **49**(7): p. 1271-1274.
130. Kresse, G. and J. Hafner, *Ab-Initio Molecular-Dynamics for Open-Shell Transition-Metals.* Physical Review B, 1993. **48**(17): p. 13115-13118.

131. Kresse, G. and J. Hafner, *AB-INITIO MOLECULAR-DYNAMICS SIMULATION OF THE LIQUID-METAL AMORPHOUS-SEMICONDUCTOR TRANSITION IN GERMANIUM.* Physical Review B, 1994. **49**(20): p. 14251-14269.
132. Blochl, P.E., *PROJECTOR AUGMENTED-WAVE METHOD.* Physical Review B, 1994. **50**(24): p. 17953-17979.
133. Marsman, M. and G. Kresse, *Relaxed core projector-augmented-wave method.* Journal of Chemical Physics, 2006. **125**(10).
134. Perdew, J.P., K. Burke, and M. Ernzerhof, *Generalized gradient approximation made simple (vol 77, pg 3865, 1996).* Physical Review Letters, 1997. **78**(7): p. 1396-1396.
135. Perdew, J.P., K. Burke, and M. Ernzerhof, *Generalized gradient approximation made simple.* Physical Review Letters, 1996. **77**(18): p. 3865-3868.
136. Anisimov, V.I., J. Zaanen, and O.K. Andersen, *BAND THEORY AND MOTT INSULATORS - HUBBARD-U INSTEAD OF STONER-I.* Physical Review B, 1991. **44**(3): p. 943-954.
137. Liechtenstein, A.I., V.I. Anisimov, and J. Zaanen, *DENSITY-FUNCTIONAL THEORY AND STRONG-INTERACTIONS - ORBITAL ORDERING IN MOTT-HUBBARD INSULATORS.* Physical Review B, 1995. **52**(8): p. R5467-R5470.
138. Dudarev, S.L., et al., *Electron-energy-loss spectra and the structural stability of nickel oxide: An LSDA+U study.* Physical Review B, 1998. **57**(3): p. 1505-1509.
139. Bengone, O., et al., *Implementation of the projector augmented-wave LDA+U method: Application to the electronic structure of NiO.* Physical Review B, 2000. **62**(24): p. 16392-16401.
140. Monkhorst, H.J. and J.D. Pack, *SPECIAL POINTS FOR BRILLOUIN-ZONE INTEGRATIONS.* Physical Review B, 1976. **13**(12): p. 5188-5192.
141. Reuter, K. and M. Scheffler, *Composition, structure, and stability of RuO2(110) as a function of oxygen pressure.* Physical Review B, 2002. **65**(3).
142. Gatel, C. and E. Snoeck, *Comparative study of Pt, Au and Ag growth on Fe3O4(001) surface.* Surface Science, 2006. **600**(13): p. 2650-2662.
143. Gatel, C. and E. Snoeck, *Epitaxial growth of Au and Pt on Fe3O4(111) surface.* Surface Science, 2007. **601**(4): p. 1031-1039.
144. Shaikhutdinov, S.K., et al., *Size and support effects for CO adsorption on gold model catalysts.* Catalysis Letters, 2003. **86**(4): p. 211-219.
145. Santos-Carballal, D., et al., *A DFT study of the structures, stabilities and redox behaviour of the major surfaces of magnetite Fe3O4.* Physical Chemistry Chemical Physics, 2014. **16**(39): p. 21082-21097.
146. Zhao, L., et al., *Morphology-controlled synthesis of magnetites with nanoporous structures and excellent magnetic properties.* Chemistry of Materials, 2008. **20**(1): p. 198-204.
147. Wahlstrom, E., et al., *Bonding of gold nanoclusters to oxygen vacancies on rutile TiO2(110).* Physical Review Letters, 2003. **90**(2).
148. Chen, M.S. and D.W. Goodman, *Interaction of Au with titania: the role of reduced Ti.* Topics in Catalysis, 2007. **44**(1-2): p. 41-47.
149. Lee, Y., et al., *Raman Analysis of Mode Softening in Nanoparticle CeO2-delta and Au-CeO2-delta during CO Oxidation.* Journal of the American Chemical Society, 2011. **133**(33): p. 12952-12955.

150. McIntyre, N.S. and D.G. Zetaruk, *X-RAY PHOTOELECTRON SPECTROSCOPIC STUDIES OF IRON-OXIDES.* Analytical Chemistry, 1977. **49**(11): p. 1521-1529.
151. Grosvenor, A.P., et al., *Investigation of multiplet splitting of Fe 2p XPS spectra and bonding in iron compounds.* Surface and Interface Analysis, 2004. **36**(12): p. 1564-1574.
152. Syed, S., et al., *Change of magnetic properties and structure in Fe3O4 films on Si substrates with annealing temperature.* Materials Transactions, 2008. **49**(1): p. 175-178.
153. Jayne, D.T., N.S. Fatemi, and V.G. Weizer, *AN X-RAY PHOTOELECTRON-SPECTROSCOPY STUDY OF AUXINY ALLOYS.* Journal of Vacuum Science & Technology a-Vacuum Surfaces and Films, 1991. **9**(3): p. 1410-1415.
154. Yu, W., M.D. Porosoff, and J.G. Chen, *Review of Pt-Based Bimetallic Catalysis: From Model Surfaces to Supported Catalysts.* Chemical Reviews, 2012. **112**(11): p. 5780-5817.
155. Sankar, M., et al., *Designing bimetallic catalysts for a green and sustainable future.* Chemical Society Reviews, 2012. **41**(24): p. 8099-8139.
156. Wang, H.W., et al., *Precisely-controlled synthesis of Au@Pd core-shell bimetallic catalyst via atomic layer deposition for selective oxidation of benzyl alcohol.* Journal of Catalysis, 2015. **324**: p. 59-68.
157. Wang, D., et al., *Silicide formation on a Pt /SiO2 model catalyst studied by TEM, EELS, and EDXS.* Journal of Catalysis, 2003. **219**(2): p. 434-441.
158. Penner, S., et al., *Platinum nanocrystals supported by silica, alumina and ceria: metal-support interaction due to high-temperature reduction in hydrogen.* Surface Science, 2003. **532**: p. 276-280.
159. Lukatskaya, M.R., et al., *Cation Intercalation and High Volumetric Capacitance of Two-Dimensional Titanium Carbide.* Science, 2013. **341**(6153): p. 1502-1505.
160. Naguib, M., et al., *25th Anniversary Article: MXenes: A New Family of Two-Dimensional Materials.* Advanced Materials, 2014. **26**(7): p. 992-1005.
161. Anasori, B., M.R. Lukatskaya, and Y. Gogotsi, *2D metal carbides and nitrides (MXenes) for energy storage.* Nature Reviews Materials, 2017. **2**(2).
162. Ma, T.Y., et al., *Interacting Carbon Nitride and Titanium Carbide Nanosheets for High-Performance Oxygen Evolution.* Angewandte Chemie-International Edition, 2016. **55**(3): p. 1138-1142.
163. Ran, J., et al., *Ti3C2 MXene co-catalyst on metal sulfide photo-absorbers for enhanced visible-light photocatalytic hydrogen production.* Nature Communications, 2017. **8**.
164. Schreier, M. and J.R. Regalbuto, *A fundamental study of Pt tetraammine impregnation of silica 1. The electrostatic nature of platinum adsorption.* Journal of Catalysis, 2004. **225**(1): p. 190-202.
165. Lambert, S., et al., *Synthesis of very highly dispersed platinum catalysts supported on carbon xerogels by the strong electrostatic adsorption method.* Journal of Catalysis, 2009. **261**(1): p. 23-33.
166. Lu, J., et al., *Effect of composition and promoters in Au/TS-1 catalysts for direct propylene epoxidation using H-2 and O-2.* Catalysis Today, 2009. **147**(3-4): p. 186-195.
167. Rakhi, R.B., et al., *Effect of Postetch Annealing Gas Composition on the Structural and Electrochemical Properties of Ti2CTx MXene Electrodes for Supercapacitor Applications.* Chemistry of Materials, 2015. **27**(15): p. 5314-5323.
168. Wang, X.H. and Y.C. Zhou, *Microstructure and properties of Ti3AlC2 prepared by the solid-liquid reaction synthesis and simultaneous in-situ hot pressing process.* Acta Materialia, 2002. **50**(12): p. 3141-3149.

169. Sabnis, K.D., et al., *Water-gas shift catalysis over transition metals supported on molybdenum carbide.* Journal of Catalysis, 2015. **331**: p. 162-171.
170. Sabnis, K.D., et al., *Probing the active sites for water-gas shift over Pt/molybdenum carbide using multi-walled carbon nanotubes.* Journal of Catalysis, 2015. **330**: p. 442-451.
171. Naguib, M., et al., *New Two-Dimensional Niobium and Vanadium Carbides as Promising Materials for Li-Ion Batteries.* Journal of the American Chemical Society, 2013. **135**(43): p. 15966-15969.
172. Balakrishnan, K. and J. Schwank, *A CHEMISORPTION AND XPS STUDY OF BIMETALLIC PT-SN/AL2O3 CATALYSTS.* Journal of Catalysis, 1991. **127**(1): p. 287-306.
173. Wakisaka, M., et al., *Electronic structures of Pt-Co and Pt-Ru alloys for Co-tolerant anode catalysts in polymer electrolyte fuel cells studied by EC-XPS.* Journal of Physical Chemistry B, 2006. **110**(46): p. 23489-23496.
174. Beard, B.C. and P.N. Ross, *PT-TI ALLOY FORMATION FROM HIGH-TEMPERATURE REDUCTION OF A TITANIA-IMPREGNATED PT CATALYST - IMPLICATIONS FOR STRONG METAL SUPPORT INTERACTION.* Journal of Physical Chemistry, 1986. **90**(26): p. 6811-6817.
175. Hammer, B., Y. Morikawa, and J.K. Norskov, *CO chemisorption at metal surfaces and overlayers.* Physical Review Letters, 1996. **76**(12): p. 2141-2144.
176. Gauthier, Y., et al., *Adsorption sites and ligand effect for CO on an alloy surface: a direct view.* Physical Review Letters, 2001. **87**(3).
177. Schaidle, J.A., et al., *On the preparation of molybdenum carbide-supported metal catalysts.* Journal of Catalysis, 2012. **289**: p. 210-217.
178. Cui, Y., et al., *Participation of interfacial hydroxyl groups in the water-gas shift reaction over Au/MgO catalysts.* Catalysis Science & Technology, 2017. **7**(22): p. 5257-5266.
179. Millikan, R.C. and K.S. Pitzer, *Infrared spectra and vibrational assignment of monomeric formic acid.* The Journal of Chemical Physics, 1957. **27**(6): p. 1305-1308.
180. Redington, R.L., *Vibrational-Spectra and Normal Coordinate Analysis of Isotopically Labeled Formic-Acid Monomers.* Journal of Molecular Spectroscopy, 1977. **65**(2): p. 171-189.
181. Bertie, J.E. and K.H. Michaelian, *The Raman spectra of gaseous formic acid-h2 and-d2.* The Journal of Chemical Physics, 1982. **76**(2): p. 886-894.
182. Millikan, R.C. and K.S. Pitzer, *The Infrared Spectra of Dimeric and Crystalline Formic Acid.* Journal of the American Chemical Society, 1958. **80**(14): p. 3515-3521.
183. Wolff, H., H. Müller, and E. Wolff, *Structure of the OH stretching vibrational band of formic acid.* The Journal of Chemical Physics, 2008. **64**(5): p. 2192-2196.
184. Powell, C.J. and A. Jablonski, *NIST Electron Effective-Attenuation-Length Database SRD 82*. Vol. Version 1.3. 2011, Gaithersburg: National Instititue of Standards and Technology.
185. Verhoef, R., et al. *Correlation between Zirconium Tetra tert-Butoxide plasma phase and deposited layers*. in *21nd International Symposium on Plasma Chemistry*. 2013.
186. Thevenaz, P., U.E. Ruttimann, and M. Unser, *A pyramid approach to subpixel registration based on intensity.* Ieee Transactions on Image Processing, 1998. **7**(1): p. 27-41.

187. Schneider, C.A., W.S. Rasband, and K.W. Eliceiri, *NIH Image to ImageJ: 25 years of image analysis.* Nature Methods, 2012. **9**(7): p. 671-675.
188. Kremer, J.R., D.N. Mastronarde, and J.R. McIntosh, *Computer visualization of three-dimensional image data using IMOD.* Journal of Structural Biology, 1996. **116**(1): p. 71-76.
189. Venkatakrishnan, S.V., et al., *A Model Based Iterative Reconstruction Algorithm For High Angle Annular Dark Field-Scanning Transmission Electron Microscope (HAADF-STEM) Tomography.* Ieee Transactions on Image Processing, 2013. **22**(11): p. 4532-4544.
190. Leonov, I., et al., *Charge and orbital order in Fe3O4.* Physical Review Letters, 2004. **93**(14).
191. Jeng, H.T., G.Y. Guo, and D.J. Huang, *Charge-orbital ordering and verwey transition in magnetite.* Physical Review Letters, 2004. **93**(15).
192. Yu, X.H., et al., *Fe3O4 surface electronic structures and stability from GGA plus U.* Surface Science, 2012. **606**(9-10): p. 872-879.
193. Zeng, Z.H., et al., *Towards First Principles-Based Prediction of Highly Accurate Electrochemical Pourbaix Diagrams.* Journal of Physical Chemistry C, 2015. **119**(32): p. 18177-18187.
194. Momma, K. and F. Izumi, *VESTA 3 for three-dimensional visualization of crystal, volumetric and morphology data.* Journal of Applied Crystallography, 2011. **44**: p. 1272-1276.
195. Wang, X.G., et al., *The hematite (alpha-Fe2O3) (0001) surface: Evidence for domains of distinct chemistry.* Physical Review Letters, 1998. **81**(5): p. 1038-1041.
196. Finger, L.W., R.M. Hazen, and A.M. Hofmeister, *High-Pressure Crystal-Chemistry of Spinel (Mgal2o4) and Magnetite (Fe3o4) - Comparisons with Silicate Spinels.* Physics and Chemistry of Minerals, 1986. **13**(4): p. 215-220.
197. Okudera, H., K. Kihara, and T. Matsumoto, *Temperature dependence of structure parameters in natural magnetite: Single crystal x-ray studies from 126 to 773 K.* Acta Crystallographica Section B-Structural Science, 1996. **52**: p. 450-457.
198. Li, X.K. and J. Paier, *Adsorption of Water on the Fe3O4(111) Surface: Structures, Stabilities, and Vibrational Properties Studied by Density Functional Theory.* Journal of Physical Chemistry C, 2016. **120**(2): p. 1056-1065.
199. Campbell, C.T., S.C. Parker, and D.E. Starr, *The effect of size-dependent nanoparticle energetics on catalyst sintering.* Science, 2002. **298**(5594): p. 811-814.
200. Skriver, H.L. and N.M. Rosengaard, *Surface-Energy and Work Function of Elemental Metals.* Physical Review B, 1992. **46**(11): p. 7157-7168.
201. Rohrbach, A., J. Hafner, and G. Kresse, *Ab initio study of the (0001) surfaces of hematite and chromia: Influence of strong electronic correlations.* Physical Review B, 2004. **70**(12).
202. Noh, J., et al., *Magnetite Fe3O4 (111) Surfaces: Impact of Defects on Structure, Stability, and Electronic Properties.* Chemistry of Materials, 2015. **27**(17): p. 5856-5867.
203. Parkinson, G.S., *Iron oxide surfaces.* Surface Science Reports, 2016. **71**(1): p. 272-365.
204. Peng, S., et al., *A Facile Synthesis of Monodisperse Au Nanoparticles and Their Catalysis of CO Oxidation.* Nano Research, 2008. **1**(3): p. 229-234.
205. Athena, A., *HEPHAESTUS: data analysis for X-ray absorption spectroscopy using IFEFFIT.* J. synchrotron rad., 2005(12): p. 537-541.

206. Jeitschko, W., Nowotny, H. & Benesovsky, F., *Kohlenstoffhaltige ternäre Verbindungen (H-phase).* Monatshefte für Chemie und verwandte Teile anderer Wissenschaften, 1963(94): p. 672-676.
207. Zhao, J.T., L. Gelato, and E. Parthe, *Structure Refinement of Monoclinic 12-Layer Tani3 with Beta-Nbpt3 Type - New Crystallographic Descriptions of This Type and of the Nb3rh5 Type Based on Smaller Unit Cells.* Acta Crystallographica Section C-Crystal Structure Communications, 1991. **47**: p. 479-483.
208. Nowak, I. and M. Jaroniec, *"Hard" vs. "Soft" Templating Synthesis of Mesoporous Nb(2)O(5) Catalysts for Oxidation Reactions.* Topics in Catalysis, 2008. **49**(3-4): p. 193-203.
209. Ribeiro, F.H., et al., *Preparation and Surface-Composition of Tungsten Carbide Powders with High Specific Surface-Area.* Chemistry of Materials, 1991. **3**(5): p. 805-812.
210. Oyama, S.T., et al., *Preparation and Characterization of Early Transition-Metal Carbides and Nitrides.* Industrial & Engineering Chemistry Research, 1988. **27**(9): p. 1639-1648.
211. daSilva, V.L.S.T., M. Schmal, and S.T. Oyama, *Niobium carbide synthesis from niobium oxide: Study of the synthesis conditions, kinetics, and solid-state transformation mechanism.* Journal of Solid State Chemistry, 1996. **123**(1): p. 168-182.